DEVELOPMENT OF A NOVEL MULTIMODAL ADAPTIVE SUPER RESOLUTION AND CONFOCAL MICROSCOPE

Liyana Valiya Peedikakkal

Thesis submitted in partial fulfilment for the award of the degree of

DOCTOR OF PHILOSOPHY

The University of Sheffield
Faculty of Science
Department of Physics and Astronomy
December 2018

I, Liyana Valiya Peedikakkal, affirm that the work presented in this thesis is my own. When information has been derived from other sources, this has been duly acknowledged in this thesis.

Liyana Valiya Peedikakkal

Thesis Overview

Existing optical microscopy techniques compromise between resolution, photodamage, speed of acquisition and deep imaging. This often confines a technique to a certain biological system or process. Ideally one would want to follow a biological process using a multitude of imaging techniques each suited to different parts of the process. To achieve this goal, a versatile imaging system is presented in this work which can adapt to the needs of a wide range of sample types and switch between imaging modalities with sub millisecond transition times. In modern microscopy, the mode of illumination and the mechanism by which the emitted light is detected play a crucial role in image resolution and photodamage to the sample.

In this work, a Digital Micro-mirror Device (DMD) based illumination and detection system is utilized to deliver a versatile-imaging system which can switch between imaging modalities at sub millisecond transition allowing us to combine low power widefield, structured illumination-based imaging and high-power single molecule localization microscopy into a single microscope. Imaging modalities implemented in this work are, digital pinholing confocal microscope, background corrected confocal microscope, rapid confocal microscopy running at 350 confocal scans per second imaging speed, background corrected confocal based structured illumination microscope, reconfigurable confocal for deep imaging, AiryImaging, selective illumination and localization microscopy.

Confocal microscopy development in this work can be classified into six categories. First is digital pinholing by rejection of out-of-focus light digitally during post processing. Second is background corrected confocal microscope built by collecting in-focus and out-of-focus light coming back from the sample in two separate cameras after physical pinholing from DMD micromirrors. This is followed by weighted subtraction of out-of-focus emission light from in-focus emission light by efficiently utilizing the data collected in in-focus and out-of-focus cameras. Third is the development of a Super Resolution Background Corrected Microscope by combining resolution enhancement image scanning microscopy algorithm with the background corrected confocal microscope. Fourth is the rapid confocal modality development by the rejection of out-of-focus light by physical pinholing to render the final confocal images in the camera at sub millisecond transition. This is followed by running the data through deconvolution or super resolution reconstruction algorithms to enhance the resolution.

Fifth is an reconfigurable confocal microscope built to change the pinhole size and the interpinhole distance in confocal imaging as a function of depth in the sample. This modality allows for deep imaging which can change between different confocal patterns during image acquisition to maximize the rejection of out-of-focus light. This reveals the localization of stromal lamella in plant chloroplast at high resolution deep into the sample. Sixth is Airyimaging mode which allows the user to perform AiryScan equivalent imaging with multifocal illumination patterns, increasing the speed of AiryScan. This is performed by replacing a GaAsP detector of AiryScan with an sCMOS camera. DMD projection codes for confocal and targeted illumination, reconstruction algorithms for all confocal imaging modalities mentioned previously and codes for DMD camera calibration methods are also provided with this work.

Rapidly switching between low light epi-fluorescence, high resolution structured illumination microscopy or localisation based super-resolution microscopy allows us to follow biological processes. The capabilities of this Versatile Imaging Platform (VIP) are demonstrated by visualizing the dynamics of early mitotic division in drosophila embryogenesis under low photo-toxicity epifluorescence and higher resolution confocal.

Localization based super resolution images of a biological sample is generally achieved by using high power laser illumination with long exposure time which unfortunately increases photo-toxicity of a sample, making super resolution microscopy, in general, incompatible with live cell imaging. Furthermore, the limitation of photobleaching reduces the ability to acquire time lapse images of live biological cells using fluorescence microscopy. A simple illumination system based on a digital mirror device which allows for fine control over the power and pattern of illumination is also presented. Spatial and temporal patterning of illumination is acheived by controlling the DMD pixel by pixel. The DMD allows the control of power and spatial extent of the laser illumination. This is applied to localization microscopy (LM), specifically stochastic optical reconstruction microscopy (STORM). It is shown that we can reduce the power delivered to the sample to allow for longer time imaging in one area while achieving sub-diffraction STORM imaging in another using higher power densities. Using this targeted STORM, we were able to image a selected area of a labelled cell without causing photo-damage to the surrounding areas of the cell. The protein co-localization of NrCAM in specific cellular compartments of NIH-3T3 cells is shown by combining low power LED based widefield with high power single molecule localization in dual colour.

Publications and presentations

Publications

1. ‘Development of Targeted STORM for Super Resolution Imaging of Biological Samples using Digital Micro-mirror Device’, **Liyana Valiya Peedikakkal**, Victoria Steventon, Andrew Furley, Ashley Cadby; Optics Communications, https://doi.org/10.1016/j.optcom.2017.06.055 (2017).

   ‘Development of Targeted STORM for Super Resolution Imaging of Biological Samples using Digital Micro-mirror Device’ identified as ‘a key scientific article contributing to excellence in science and engineering research’ by Advances in Engineering magazine. An article about the paper is featured online in AIE magazine, ‘https://advanceseng.com/development-targeted-storm-super-resolution-imaging-biological-samples-using-digital-micro-mirror-device/’.

2. ‘Controlled power delivery and super resolution imaging of biological samples using Digital Micromirror device’**, Liyana Valiya Peedikakkal**, Ashley Cadby; Proc. SPIE 10117, Emerging Digital Micromirror Device Based Systems and Applications IX, 101170E (February 20, 2017); https://doi.org/10.1117/12.2266678.
3. ‘A Multimodal Adaptive Super Resolution and Confocal Microscope’, **Liyana Valiya Peedikakkal**, Andrew Furley, Ashley Cadby; manuscript in the final stages of internal reviews for submission.

Selected Presentations

1. ‘Development of a Novel DMD Based Microscope to Combine Confocal, SIM and STORM to Study Biological Samples’ (Talk emphasises Multimodal adaptive imaging with Super Resolution-Background Corrected Microscope (SR-BCM)), **invited talk** in **Focus on Microscopy (FOM)** 2018, Singapore, 25th-28th March 2018.

2. ‘Development of physical pinholing in confocal microscopy and targeted STORM of biological sample using a Digital Micro-mirror Device’ (Talk emphasises combining confocal and STORM in one field of view with achievement of overall reduction in photobleaching with targeted STORM), **invited talk** in **Microscience Micrscopy Congress (MMC)** 2017 in Manchester, UK, July 04th – 07th 2017.

3. ‘Development of physically pinholed confocal microscopy and targeted STORM of biological sample using a Digital Micro-mirror Device’ (Talk emphasises targeted STORM and targeted gradient STORM), **invited talk** in **Focus on Microscopy (FOM)** 2017, Bordeaux, France, April 09th – 12th 2017.

4. ‘Controlled power delivery and super resolution imaging of biological samples using Digital Micro-mirror Device’, Liyana VP, Ashley Cadby, **invited talk** (**remote video call)** at the Emerging Digital Micromirror Device Based Systems and Applications IX at the **SPIE Photonics West 2017** held in San Francisco, California, USA, Jan 28th – 2nd Feb 2017.

5. ‘Selective illumination for STORM using Digital Micro-mirror Device’, **image poster presentation** in STORM symposium 2017, University of Sheffield, UK.

6. ‘Development of targeted illumination for STORM and epi-fluorescence using Digital Micro-mirror Device’, **poster presentation** in Imagine: Imaging Life launch symposium, University of Sheffield, UK.

7. PhD project proposal talk at the Imaging Life 2015 PGR symposium, University of Sheffield, UK.

Acknowledgements

I would like to extend my deepest and most sincere thanks to my PhD supervisor Dr Ashley Cadby for his support and guidance throughout my PhD work. When I started my PhD work, I had never used a high-end optical microscope. Ashley taught me and guided me through everything, from aligning simple optics to developing probably 'the most versatile microscope'. Ashley gave me the confidence to build anything and make it work. I am going to miss running to Ashley's office when getting stuck. During my PhD tenure, Ashley gave me the opportunity to travel around the world to see the world of science. Most importantly, Ashley taught me how to get excited with a research problem and how to find solutions.

I would like to thank my biology supervisor Prof. Andrew Furley, for his constant encouragement and for helping me much to gain an insight in biology. My special thanks to Victoria Steventon, research assistant in Furley lab, for teaching me the intricacies of cell culture. I also thank everyone at Cairn Research for the collaborations, kind hospitality during my visits and for the amazing Cairnfocal. Special thanks to Dr Martin and Jeremy for helping me understand the optics of the Cairnfocal.

Thanks for Cadby lab members, Adrien, Amy, Dan, Nicola C, Nicola R, Olivia, Raveen, Sam, Tanya and Yin for many great social meetings and food. I also thank my office mates, Mina, Subhadip, Tom and my friend Haia for their company during tea breaks. Special thanks to Nicola C for reading some chapters. I would like to thank Dr Christa and Dr Darren of LMF for letting me pick their brain to understand the practical difficulties when using conventional commercial microscopes. I also thank Dr Imene Bouhle (University of Cambridge) of the Conduit lab for Drosophila sample preparation, Dr Jason King's lab (University of Sheffield) for Amoeba sample preparation and Dr Sam Barnnett (University of Sheffield) of the Hunter lab for the leaf disk sample preparation. I thank the Imagine:Imaging Life, the University of Sheffield for funding the project.

I would like to thank Prof. Suckjoon Jun of the University of California, San Diego (UCSD) for his encouragement and guidance during my visiting graduate studentship in UCSD. Thanks to all the members of Jun lab, especially Sarah, JT, Dongyang, Mike, Xintian, Fangwei and Steve for their kind concerns and hospitality. I would also like to thank Dr Ricardo Henriques from University College London for giving me the opportunity to visit his lab, for critically proof reading my papers and for the insightful suggestions after my conference presentations. I also thank Prof Jörg Enderlein (Georg-August University, Göttingen) for providing CSD-ISM code

I would like to thank my former teachers, especially, Prof. P. Predeep, Dr Raghu C, Dr Ravi Varma and Dr Shivaji Reddy of National Institute of Technology, Calicut (NITC), India.

Finally, my family, my dad who ignited my love for research by doing small physics experiments with me at home when I was a little girl, my mom's hard work to give me the best of everything in life and my role model siblings who have parental control over me. I do not have words to thank you all for your love and support. If I have any degree of success in my life, it is because of my brother Thaj. Nizam, my loving life partner, for whom no thanks will be enough for putting up with my tantrums during the end of my PhD work. As I am finishing this thesis, a new journey awaits us. I feel so blessed that you are by my side.

Table of Contents

List of Figures

Abbreviations

AF	Alexa Fluor
ALP	Accessory Light Modulation Package
AOD	Acousto Optic Deflector
AU	Airy Unit
BCCM	Background Corrected Confocal Microscope
BPAEC	Bovine Pulmonary Artery Endothelial Cell
CFM	Comprehensive Fluorescence Microscope
CSM	Comprehensive Sensing Microscope
DC	Dichroic Mirror
DLP	Digital Light Processing
DMD	Digital Micromirror Device
DMEM	Dulbecco's modified eagle's medium
DPBS	Dulbecco’s Phosphate Buffered Saline
FCS	Fluorescence Correlation Spectroscopy
FPALM	Fluorescence Photoactivated Localization Microscope
FRAP	Fluorescence Recovery After Photobleaching
FRC	Fourier Ring Correlation
FRET	Förster Resonance Energy Transfer
GFP	Green Fluorescent Protein
GUI	Graphical User Interface
Ic	Conjugate Image
Inc	Non-conjugate Image
iSIM	Instant Structured Illumination Microscope
ISM	Image Scanning Microscope
LCoS	Liquid Crystal on Silicon
LM	Localization Microscope
LSCM	Laser Scanning Confocal Microscope
MEA	Monoethanolamine
MSB	Most Significant Bit
MSBHE	Modified Scrambled Block Hadamard Ensemble
MSIM	Multifocal Structured Illumination Microscope

NDS	Normal Donkey Serum
NGS	Normal Goat Serum
NIH 3T3	National Institute of Health 3-dat transfer (inoculum $3x10^5$)
OR-PAM	Optical Resolution Photo Acousto Microscope
OTF	Optical Transfer Function
PALM	Photoactivated Localization Microscope
PAM	Programmable Array Microscope
PBS	Phosphate Buffered Silane
PBST	Phosphate Buffer Saline and 0.05% Triton
PDMS	Polydimethylsiloxane
PFA	Paraformaldehyde
PMT	Photomultiplier Tube
PRS	Pseudo Random Sequence
PSF	Point Spread Function
PWM	Pulse Width Modulator
ROI	Region of Interest
rrx	Rhodamine Red
s/n	Signal to Noise ratio
SD	Standard Deviation
SIM	Structured Illumination Microscope
SLM	Spatial Light Modulator
SR-BCM	Super Resolution Background Corrected Microscope
SRRF	Super Resolution Radial Fluctuations
STED	Stimulated Emission Depletion Microscope
TFMEM	Temporal Focussing Multiphoton Excitation Microscope
TIRF	Total Internal Reflection Fluorescence

Chapter 1

Introduction

1.1. Early History of Microscopy

The first model for investigating objects which are invisible to the unaided eye is thought to be established by Robert Hooke and his contemporary Antonie Van Leeuwenhoek. Robert Hooke illustrated various biological and non-biological samples by his drawings in his famous book ‘Micrographia’ published in 1665 [Hooke, 1665]. Antonie Van Leeuwenhoek made several hundreds of microscopes around the 1670s, using small convex lenses and discovered bacteria, vacuole, spermatozoa and so on [Leeuwenhoek, 1816].

1.2. Diffraction Limit

Ernest Karl Abbe proposed in 1873 [Abbe, 1873] that two point objects could not be distinguished if they were separated by less than half the wavelength of light used to illuminate them. His findings had such high impact on light microscopy research that it took more than a century to surpass this diffraction limit defined by him. Parallel microscopic techniques by using electrons instead of photons were developed as electron microscopy. But the ability to break the diffraction barrier and visualize dynamic cellular process in nanometre scale remained as a big challenge since then until recently. The development of super resolution optical microscopy opened whole new possibilities and immensely enhanced the scope for the study of biomolecular complexes.

Abbe diffraction limit is given by the formulae,

$$dx, y = \frac{\lambda}{2N.A} = \frac{\lambda}{2nsin\theta} \tag{1}$$

$$dz = \frac{2\lambda}{N.A^2} \qquad (2)$$

where λ is the wavelength of illumination light in nanometres and $nsin\theta$ is the numerical aperture N.A of the objective lens. N.A is the function of the angle of cone formed by the focussed light. Here, $d_{x,y}$ is the lateral resolution and d_z is the axial resolution. There are other definitions of resolution limit, which include Lord Rayleigh's definition that two adjacent point objects are termed 'resolved' if the sum of their point spread function is less than 80% of the maximum intensity [Rayleigh, 1903]. Sparrow's definition is that two points are no longer resolved if there is no intensity dip between two adjacent point emitters [Hecht *et al.*, book, 2016].

When imaging a point object in the microscope, instead of obtaining an infinitely small point at the detector, we observe a diffraction pattern with concentric rings called the Airy disk formed owing to diffraction of emission light travelling through the finite aperture of the objective lens [Airy, 1835]. The intensity profile as a function of distance of this point spot gives the Point Spread Function (PSF). The Fourier transform of this PSF gives the Optical Transfer Function (OTF) of the optical imaging system indicating the spatial frequencies allowed through the aperture of the objective.

1.3. Fluorescence Microscope

The diffraction limit of resolution indicates that, as the wavelength decreases, smaller features can be resolved as given by equations 1 and 2. In 1904, August Kohler at Zeiss microscope company built the first ultraviolet microscope and observed that the emission light from the sample was in a different wavelength. With the help of this observation, Oskar Heimstadt built a fluorescence microscope [Heimstädt, 1911]. At that time, the requirement for transmitted illumination and the use of darkfield condensers to increase the contrast of autofluorescence in the sample were the major limitations of fluorescence microscopy. The use of exogenous fluorescent probes to enhance the contrast of imaging in epi-fluorescence technique and invention of dichromatic mirrors led to further developments in the field in fluorescence microscopy. Fluorescence microscopy combines the magnifying abilities of microscopy with fluorescence.

1.3.1. Fundamental Principles of Fluorescence

This section describes the electronic arrangements in a molecule and the conditions for fluorescence. When a photon is absorbed by a fluorophore, electrons in the stable lower energy ground state get excited to higher energy states S1(first excited state) or S2 (second excited state) as indicated by blue absorption arrows in **figure 1.1** [Jabłoński, 1933]. Each energy level indicated as S0 (ground state), S1, S2 *etc* has vibration energy levels associated with it. It is worth noting here that the possibility of an electron to get excited to any one of the vibrational energy level broadens the spectrum of wavelength at which the molecule can absorb a photon. This same logic applies to the emission spectrum of the molecule.

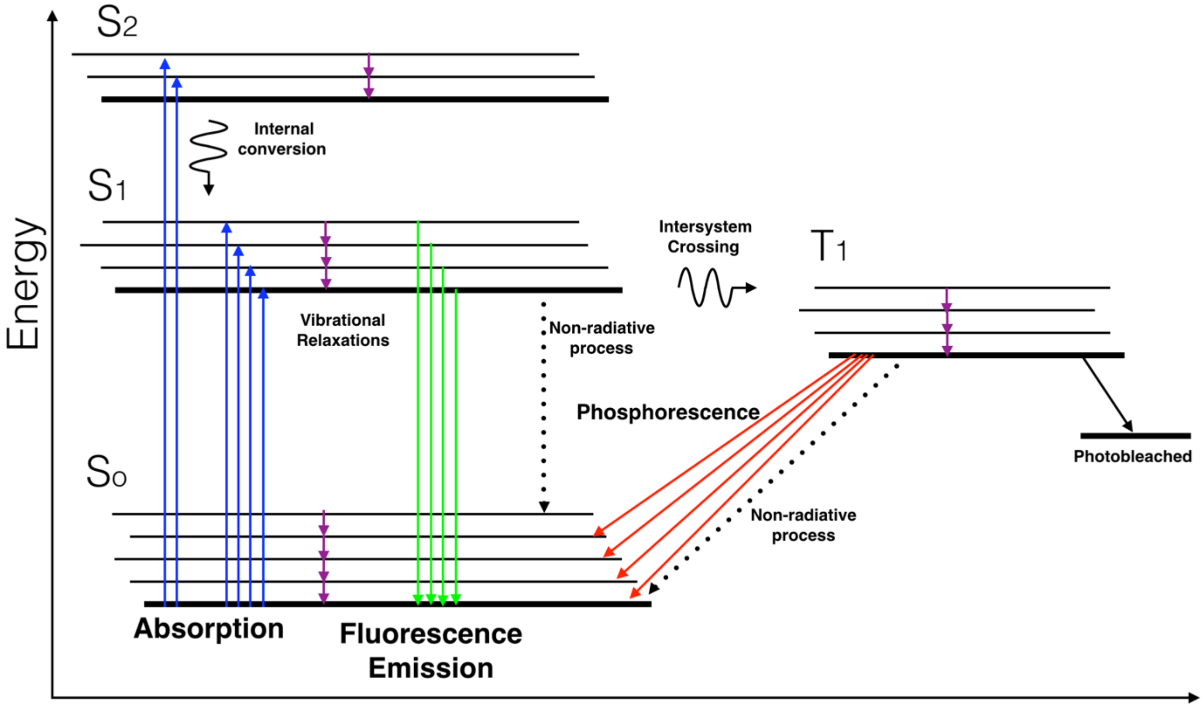

Fig. 1. 1. Jablonski diagram representing transitions of a fluorescent molecule. The diagram shows electron transfers during absorption, emission, phosphorescence, non-radiative decays, internal conversions, vibrational relaxations, non-radiative processes and photobleaching.

Depending on the spin change of electrons, photoluminescence can be classified into fluorescence (10^{-9} sec – 10^{-6} sec) and phosphorescence (10^{-3} sec – 1 sec). Spontaneous decay of electron from the excited singlet state to the ground state is termed as fluorescence emission as shown in green arrows. Delayed decay of electrons from triplet state to ground state is termed phosphorescence as shown in red arrows in **figure 1.1**. If the electron is absorbed from the ground state to a higher vibrational energy level of the excited state, it relaxes to the lowest vibrational energy level of this excitation state represented by purple arrows. Due to this internal conversion, the energy difference between the initial and final energy state of absorptions is higher than the difference between initial and final energy state of fluorescence decays owing to the Stoke shift of emission light with its wavelength higher than excitation wavelength. Since S2 is a highly unstable state compared to S1, when the electron excites from S0 to S2, it immediately deexcites to S1 through internal conversions in a time scale faster than florescence emission and with the release of heat energy.

Singlet state is defined as a molecular electronic state when all the electrons are paired, and the state does not split when the molecule is exposed to magnetic field. For singlet excitation states, an electron moves to the excited state with same spin orientation as it was in the ground state. For triplet excitation states, an electron moves to the excitation state with an opposite spin orientation as it was in the ground state. An electron in the singlet excited state may move to a triplet. This transition is ‘forbidden’ due to spin selection rule (no change in overall spin, conservation of spin). But spin orbit coupling can aid this singlet to triplet transition. Spin orbit coupling scales with nuclear mass and occurs in heavy atoms or fluorophores containing a heavy atom. Electron in the triplet state can have many options. One is that it decays to the ground state termed ‘phosphorescence’ [Lewis and Kasha, 1944], which is a radiative process. The probability of this transition is low as the electron spin in triplet excited state and singlet ground state are the same and the transition between them requires a change in spin multiplicity making the transition ‘forbidden’. The second is that it can decay to the ground state non-radioactively which competes with photoluminescence. One of the examples for non-radiative transition are quenching, which is the transfer of energy between molecules when absorption spectra coincides with the emission spectra of the molecule. Another example is energy transfer between the molecules when they collide with each other. The third option for the electron in the triplet state is intersystem crossing to the lowest singlet excited states. The electron then deexcites to the ground state. This process is called ‘delayed fluorescence’. Fourth is when the molecule covalently bonds with oxygen turning the molecule to a photobleached state [Borden *et al.*, 2017]. In this thesis, we are concerned about the fluorophores in condensed phase or in solution. Absorption and emission spectra not only depends on the electronic arrangements in the molecule, but also on the environment of the molecule and solvation effects in the solution state [Valeur *et al.*, book, 2002].

1.3.2. Labelling Techniques in Fluorescence Microscope

There are various labelling techniques to visualize biological complexes. Enzymatic labelling can be used if the location of a single protein or structure in a cell needs to be visualized (e.g. Horseradish Peroxidase, which converts a transparent soluble substrate to an insoluble colour that can be seen in visible light). The advantage of enzymatic labelling is that that stained cells can be stored for a long time. Visualizing multiple proteins and structures in a cell is not common in enzymatic labelling and resolution of the images with this labelling cannot compete with immunolabelling. Immunogold (gold-labelled antibodies) labelling can be used for electron microscopy and gives the highest resolution but are highly sample invasive. Fluorescence is important in bioimaging for two key reasons. First, it allows to visualise multiple epitopes at the same time. Fluorescent labelling of biological specimens use multiple fluorophores enabling the monitoring of multiple different proteins simultaneously. Fluorescence labelling allows to visualise living cells, either at cell surface molecules labelled with fluorescent antibodies, or by using fluorescent proteins.

Selection of fluorescent probes to label samples is crucial for the study of specific structures or dynamics of biomolecular complexes. Fluorescent probe selection is linked with the optical implementations such as selection of illumination source, imaging technique, detector *etc*. Two major categories of fluorescent labelling techniques are immunofluorescence and use of genetically encoded fluorescent proteins. There are two classes for immunolabeling: (i) primary/direct labelling in which the antibody which is chemically linked to a fluorochrome is attached to the target antigen molecule of the sample and (ii) secondary/indirect labelling in which the antibody is attached to the target sample antigen in the first step followed by attaching the fluorochrome as secondary antibody in the second step [Barbierato *et al.*, 2012]. Many secondary antibodies attach to one primary antibody in indirect labelling giving it higher fluorescence intensity. Impermeability of antibodies which are macromolecules, through the cellular membrane makes immunolabelling difficult on living cells, unless the sample target antigen is in the surface of the cell. This is solved by using fluorescent proteins which are isolated from animals such as jellyfish. These fluorescent proteins are used as protein tags *in vivo* enabling live cell imaging. These proteins are genetically encoded so that we can genetically alter the cell (or animal) so that it ‘expresses’ the protein in the living tissue, either on its own, or as a tag added genetically to another protein so that the tagged protein can be followed directly. Green Fluorescent Protein (GFP) isolated from jellyfish fluoresces when expressed in cells. Genetic mutations of GFP to make it more photostable, brighter and shifting their absorption and emission spectra gave rise to a strong tool to investigate live cells. This was recognized in the 2008 Nobel Prize in Chemistry, awarded for the discovery of GFP [Chalfie *et al.*, 1994].

1.3.3. Other Fluorescence Imaging Developments

Developments of fluorescence microscopy for optical sectioning and super resolution are described in detail in the coming sections of this chapter. This section briefly describes other main stream imaging techniques enabling the understanding of various biological processes. Some of these techniques include, Fluorescent Correlation Spectroscopy (FCS) [Magde *et al.*, 1972], Fluorescence Recovery After Photobleaching (FRAP) [Axelrod *et al.*, 1976], Fluorescence Lifetime Imaging microscopy (FLIM) [Jovin *et al.*, 1995], Förster Resonance Energy Transfer (FRET) [Fernandez *et al.*, 1976] *etc*. FCS enables the understanding of the kinetics of chemical and biological reactions, diffusion and flow by recording the stochastic movement of fluorophores in and out of the focussed laser beam. FCS can measure the diffusion of membrane protein while FRAP can give a better understanding for the movement of proteins in and out of the cellular membrane at micron scale resolution. FRAP photobleaches a region of the sample and records the rate of recovery of fluorescence intensity to study the kinetics of diffusion inside or between subcellular components. FRET microscopy can record protein-protein interactions when molecules transfer energy from a donor molecule to an acceptor molecule when they are separated by 8-10 nanometres. FLIM maps the fluorescence lifetime of various fluorophores in the sample. When FLIM is combined with FRET, fluorescence lifetime measurement of the donor molecules in the presence and absence of the acceptor molecules, we can estimate the distance between proteins [Peter *et al.*, 2004]. Recently, FLIM was used to map temperature variations between various structures in a cell. It has been shown, for instance, that there is a local heating around mitochondria after the treatment of mitochondria to inhibit ATP production [Kohki *et al.*, 2012].

1.4. Phase Microscope

Fluorescence microscope needs staining of the specimen. A phase microscope can visualise transparent or translucent specimens without compromising resolution. Frits Zernike received the Nobel Prize in 1953 for building a phase contrast microscope which allowed the visualization of ‘invisible’ or transparent cellular structures which need not be stained by fluorescent probes. Light from an illumination source is modified by an annulus to a ring-shaped beam of light illuminating the sample. When light interacts with the sample, due to the differences in refractive indices, a part of the light gets scattered. Both the un-scattered and scattered light are refocussed by an objective lens. A phase plate inserted between the objective lens and the detector generates an additional phase difference. Scattered light is phase shifted when it passes though the thicker part of the phase plate. This paves the way for background or un-scattered light and scattered light to destructively interfere to form a dark contrast of the sample structure at the detector [Zernike, 1942].

1.5. Developments of Techniques to Achieve Optical Sectioning

In a standard widefield microscope, an excitation light beam is focused on to the pupil or Fourier plane of the microscope. The excitation light beam illuminate areas other than the focal plane of the sample volume. Schematic diagram of an epi-fluorescence microscope is given in **figure 1.2(a)**. Ideally, we want the in-focus plane of the sample to be infinitesimally thin to obtain an optically sectioned image. The airy disk diffraction pattern produced by the objective not only extends in the lateral direction, but also extends in the axial direction. This leads the sample volume of a few micrometres thick to be in-focus rather than an infinitesimally thin in-focus plane. This depth of field is formulated by the equation [Bass *et al.*, Handbook of Optics],

$$d = \frac{\lambda * n}{N.A^2} + \frac{n}{M * N.A} * e \qquad (3)$$

where ‘d’ is the depth of field, ‘λ’ is the illumination wavelength in nanometres, ‘n’ is the refractive index of the medium, ‘N.A’ is the refractive index of the objective, ‘M’ is the magnification of the objective and ‘e’ is the smallest distance that can be resolved by a detector that is placed in the image plane of the microscope objective.

It has been shown that almost 90% of captured fluorescence from a sample in a fluorescence microscope is the out-of-focus light which comes from the plane above and below the focal plane [Conchelle *et al.*, 2005]. Emission light arising from a single point emitter can illuminate other fluorescent molecules or light scattering objects in planes above and below the focal plane. This decreases the optical sectioning or increases the ‘blurriness’ of the image. This is when the depth of field extends beyond the axial resolution defined with equation 2.

There are many techniques to confine the excitation to a single plane of focus. There are many techniques based on rejecting the out-of-focus light efficiently to achieve an effective depth of field of light illumination to be equal to the axial resolution of the microscope. The most widely used technique is the confocal microscopy system which will be addressed towards the end of this section. Other main stream techniques which are successful in achieving optical sectioning are also discussed in this section.

1.5.1. Total Internal Fluorescence Microscope

Visualization of dynamic processes such as endocytosis, exocytosis, ion transport *etc*, in the cell membrane were deemed difficult with a conventional widefield microscope because the intensities of out-of-focus fluorescence emission could disrupt the signal from the in-focus plane. In 1981, Daniel Axelrod [Axelrod *et al.*, 1981] collected the scattered photons from total internally reflected excitation beam. Total Internal Reflection Fluorescence (TIRF) microscope constrains the field of illumination to a region close to the coverslip. This can be achieved by using a TIRF objective and setting the angle of incidence of excitation light beam to be higher than the critical angle defined by the refractive index difference between imaging media and coverslip. The light beam undergoes total internal reflection and travels back through the objective. When light reflects from the coverslip surface, photons travel through the coverslip, illuminating a very thin strip of the sample, which is in contact with the coverslip. An evanescent field is generated here, a phenomenon which was known since the late 1800s. The thickness of the sample illuminated by evanescent field is typically around 200 nm and the intensity of the field decreases exponentially along the optical axis. TIRF could selectively illuminate a thin layer of sample with high precision enabling the study of cell membrane dynamics.

1.5.2. Two-photon Microscope

Confocal microscopy is successful in rejecting the out-of-focus light by incorporating point based illumination and pinhole based detection. Even though confocal microscopy excitation confines the area of illumination in the sample to a point spot in the lateral direction compared to widefield which illuminates the whole sample, the excitation spot is not as much confined in the axial direction. This is the major source of out-of-focus scattering in sample. Two-photon microscopy is an elegant implementation to achieve optical sectioning with reduced photodamage compared to confocal microscopy. A schematic diagram of setup is shown in **figure 1.2(b).** Two-photon microscopy illuminates the sample with a wavelength twice than the normal excitation wavelength of the sample. Since energy is inversely proportional to wavelength, molecules will absorb two photons simultaneously.

The probability of fluorescence emission increases quadratically with illumination intensity which is delivered usually by femtosecond lasers for high excitation photon flux. Only the focal plane of the sample will have enough photon density to achieve simultaneous two photon excitation. Molecules in the out-of-focus planes do not absorb photons reducing out-of-focus blur. A mode-locked femtosecond pulsed laser are employed to achieve two photon excitations. Lower energy excitation reduces the photodamage in the sample. This technique provides intrinsic three-dimensional resolution in confocal, making it an ideal technique to observe specific structures inside thick biological tissues [Denk *et al.*, 1990].

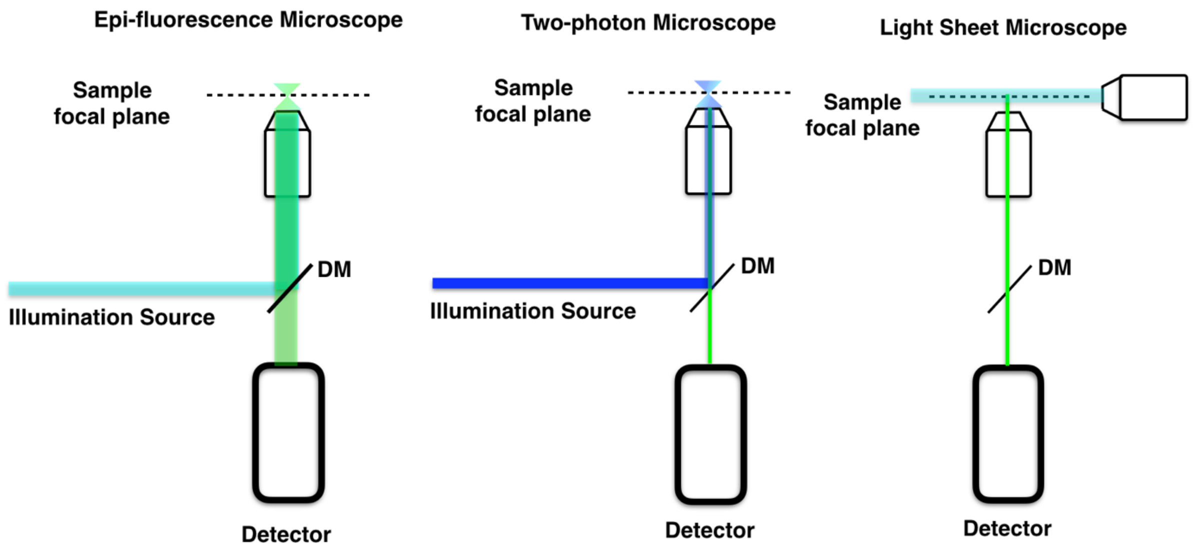

Fig. 1. 2. Schematic diagram of microscopes. (a) Epi-fluorescence. **(b)** Two-photon Microscope. **(c)** Light Sheet Microscope.

1.5.3. Light Sheet Microscope

Light sheet microscopy provides another solution for optical sectioning by selective plane illumination by employing a separate illumination pathway with a cylindrical lens. A schematic diagram of the setup is shown in **figure 1.2(c).** As only one plane of the sample is illuminated, photodamage is reduced compared to a confocal microscope. The lateral plane resolution of the system depends on the scattering of the sample while the axial resolution depends on the thickness of the light sheet with which the sample is excited [Voie *et al.*, 1993, Huisken *et al.*, 2004]. It is mentioned by Engelbrecht *et al.* in 2006 that the axial extent for the PSF of a light sheet microscope is 2.5 times smaller than a fluorescence microscope, 2 times smaller than a conventional confocal microscope and 3 times smaller than a two-photon fluorescence microscope.

1.5.4. Deconvolution Microscope

In an optical system, the image collected in the detector is a convolution of the PSF of the microscope with the ground truth. This process adds light from out-of-focus intensities to be collected in the 2D image acquired. Deconvolution process reassigns the out-of-focus intensity to its expected 3D positions by convolving the raw image with the inverse of the PSF of the optical system. Deconvolution operation is performed in the Fourier space. Fourier space makes handling convolutions easy as the convolution of two functions is simply a Fourier transform of the multiplication of these functions in Fourier space.

When deconvolving a widefield image, it is essentially removing the ‘blur’ of the image assuming that all objects are convolved with a PSF. Deconvolution is thus one of the ways to improve the optical sectioning of the image without the need of specialized optical components such as physical apertures in the optical pathway. Having said that, deconvolution algorithm is still useful to run on confocal images. Physical apertures in confocal microscopes reject the low frequency out-of-focus components. The image is still degraded by the high frequency out-of-focus components originating from the nearest planes to the focal plane. This cannot be rejected in conventional confocal systems owing to the finite size of the physical aperture. A deconvolution algorithm on confocal can therefore discard this out-of-focus light increasing the optical sectioning of the image [David *et al.*, 1983, Fay *et al.* 1989].

1.5.5. Laser Scanning Confocal Microscope

A confocal microscope is successful in rejecting these out-of-focus lights to obtain an optically sectioned image, opening the scope for three-dimensional imaging [Minsky, patent, 1961, Egger *et al.*, 1967, Shepphard *et al.*, 1981]. Optical sectioning in confocal microscopy can be achieved with several optical implementations as discussed below.

Laser Scanning Confocal Microscope (LSCM) is a very popular single aperture biological imaging technique where a laser is used to scan through the sample compromising the speed of acquisition of data. The illumination laser beam passes through a physical aperture and gets focused by the objective to project a single focus on the sample focal plane. Since only a small volume of the sample is illuminated, the emission from out-of-focus planes is hugely reduced with less scattering compared to a widefield microscope. The emission spot from the sample is collected by the objective and a physical pinhole in the emission pathway rejects the out-of-focus light which is in the exterior of the Airy disk. The excitation spot is scanned across the sample in a raster fashion in lateral direction to image the complete field of view and generate a confocal image. A Photomultiplier Tube (PMT) is a typical detector in a confocal microscope. Cameras are also used which allow further processing of the collected data, which is discussed in detail in the following chapters. This pinhole based setup increases the optical sectioning ability of the microscope. A schematic diagram of the LSCM is given in **figure 1.3(a)**.

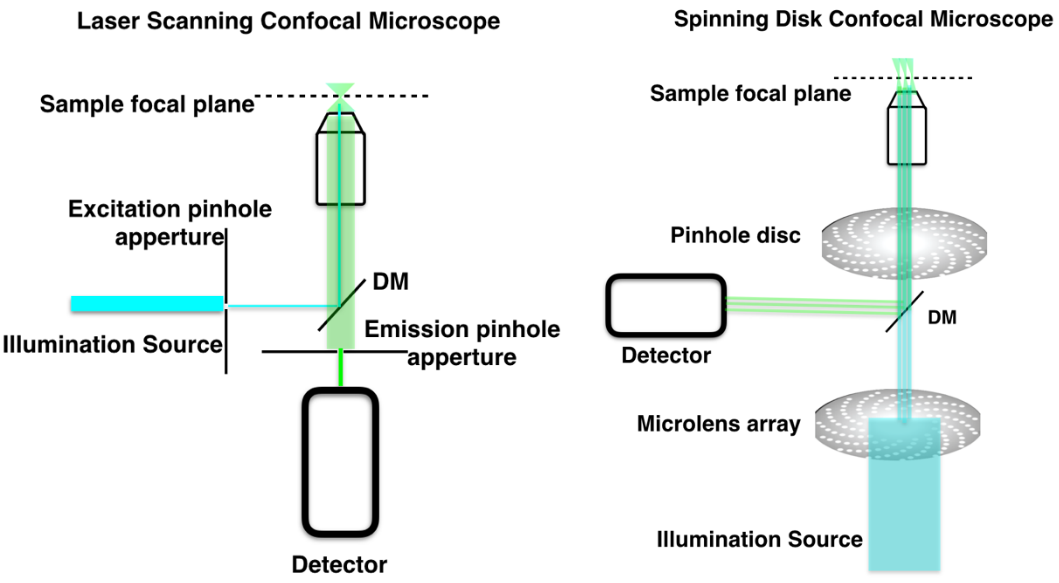

Fig. 1. 3. Schematic diagram of conventional confocal microscopes. (a) Laser Scanning Confocal Microscope. **(b)** Spinning Disk Confocal Microscope.

1.5.6. Scanning Disk Confocal Microscope

Since LSCM is a single point based illumination and detection system, speed of image acquisition is low. Speed of imaging is crucial to study the dynamics of live biological specimens. Nipkov disk based multi aperture confocal microscopes were developed which considerably increased the speed of acquisition of images [Masters *et al.*, 2006, Cox *et al.*, 2007]. Laser light is passed through a rotating disk with fixed pinholes acting as apertures and the out-of-focus light from the specimen is rejected by these pinholes. Nipkov disk is used in both excitation pathway for point illumination and emission pathway for out-of-focus rejection. Transmission efficiency of these disks are very poor, and backscattering of illumination light severely degrades the image quality. Yokogawa spinning disk microscope employs a microlens array between the illumination source and the Nikov disk. This improves the transmission efficiency of light enhancing the image quality. A schematic diagram of a typical spinning disk microscope is shown in **figure 1.3 (b).** Photobleaching of the sample is generally less in spinning disk compared to a LSCM because low intensity excitation beam can be used in spinning disk microscopes because emission intensity are collected in high quantum efficiency cameras. The major drawback of a scanning disk confocal microscope is that the size of pinholes and the distance between pinholes are fixed.

1.5.7. Programmable Array Microscope

Next stage in the evolution of confocal microscopy is the use of Programmable Array Microscope (PAM) using physically fixed Spatial Light Modulators (SLM) such as twisted nematic or ferroelectric Liquid Crystal on Silicon (LCoS) and Digital Micromirror Device (DMD). The user can achieve precise control over the illumination pattern and intensity. This enables selective light detection from the specimen. The major advantage of using SLM based PAM is the possibility of using an incoherent illumination source for confocal microscopy. Although these varieties of available SLMs are quite similar in their function of projecting patterned light on to the sample, DMD may be better compared to its counterparts because of better contrast over larger spectral range, higher speed, pixel quality *etc*. The DMD allows us to programmably control the source and the detection aperture in 2D to achieve the best signal and to reduces the crosstalk noise between the point sources [Verveer *et al.*, 1998, Hanley *et al.*, 1999, 2005, Heintzmann *et al.*, 2001, Křížek *et al.*, 2012].

1.6. Digital Micro-mirror Device (DMD)

In 1987, Larry J. Hornbeck designed the first Digital Micromirror Device (DMD) in Texas Instruments using photolithography [Hornbeck, patent, 1987]. The first commercial product using DMD is a printer of 1991. Since then, DMD found its application in various fields such as holographic data storage, maskless lithography, microscopy, spectroscopy, *etc* [Dudley, 2003].

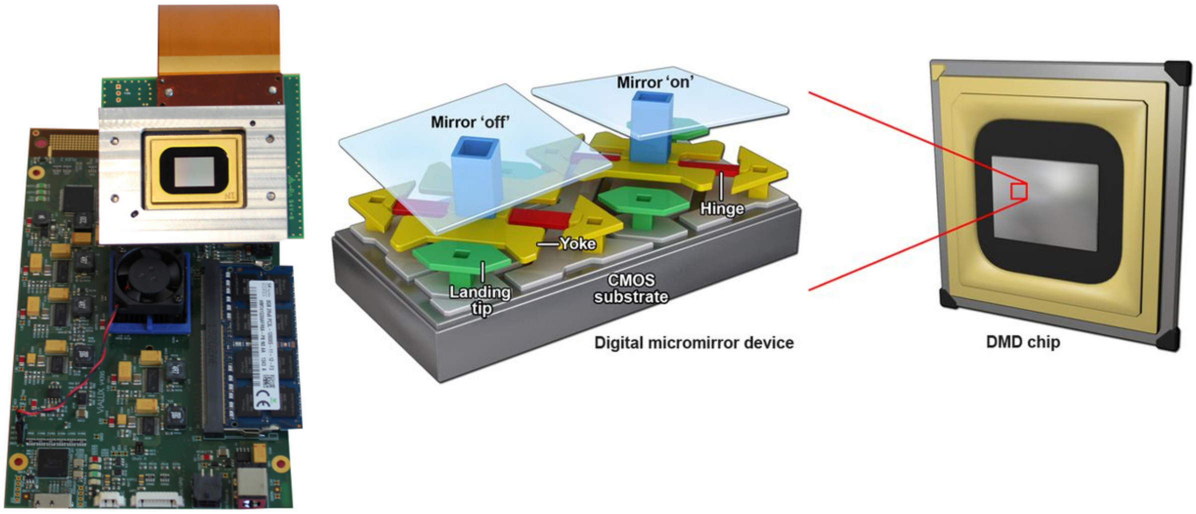

Fig. 1. 4. DMD used in this work. (a) Vialux Germany, V-7001Super speed DMD chip with FPGA [Vialux, Germany]. **(b)** Two micromirrors are illustrated which are deflected to two directions termed as 'ON' and 'OFF' [Allen, 2017].

A DMD chip consists of an active array of size of approximately 13.9 mm x 10.4 mm with around 8 million micromirrors arranged in regular rectangular array. Each micromirror is attached to a yoke and a support post connecting it to the complementary meta-oxide semiconductor (CMOS) substrate. Each micromirror is 13.6 µm and have two stable positions +12° and -12° (size and angle can vary with different models). Each micromirrors can be controlled individually which can generate countless number of patterns.

1.7. Key Research Literature of DMD based Patterned Illumination for Microscopy

Key literatures for the application of DMD in microscopy are detailed in this section. This forms a foundation of this specialized area. With this discussion, I intend to give the reader a better outlook for the work presented in the following chapters of this thesis.

1.7.1. Phase 1

The first incorporation of DMD in microscopy was in 1997 by Krause and co-workers as shown in **figure 1.5** where an attempt was made for the first time to define precisely a confocal pattern period without losing confocality and reasonable speed. They achieved a 6.25x times enhancement in light utilization efficiency and confocal frame rate when compared to its contemporary Nipkov disc based confocal systems [Liang *et al.*, 1997].

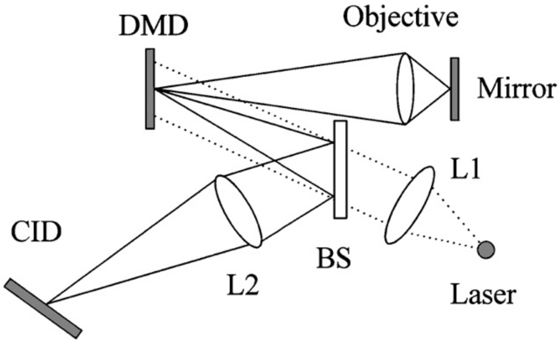

Fig. 1. 5. First incorporation of DMD in microscopy. L1 is the projection lens and L2 is the collection lens [Liang *et al.*, 1997].

The Jovin group announced in 1999 their first generation PAM based on DMD, shown in **figure 1.6.** Formerly, DMD technology was immature with poor reflectivity of DMD and underdeveloped electronics to drive the system. Moreover, in generation I PAMs, the need for two cameras for image acquisition resulted in Moire Beat pattern due to slight misalignments [Heintzmann *et al.*, 2001]. The team established that optical sectioning ability and signal to noise (s/n) ratio can be considerably enhanced by simultaneously collecting light from both conjugate and nonconjugate paths of emission light using a pseudo random pattern and the image collected in the conjugate pathway was regarded as an ‘analog’ of a conventional confocal microscope [Verveer *et al.*, 1998], [Hanley *et al.*, 1999, 2005].

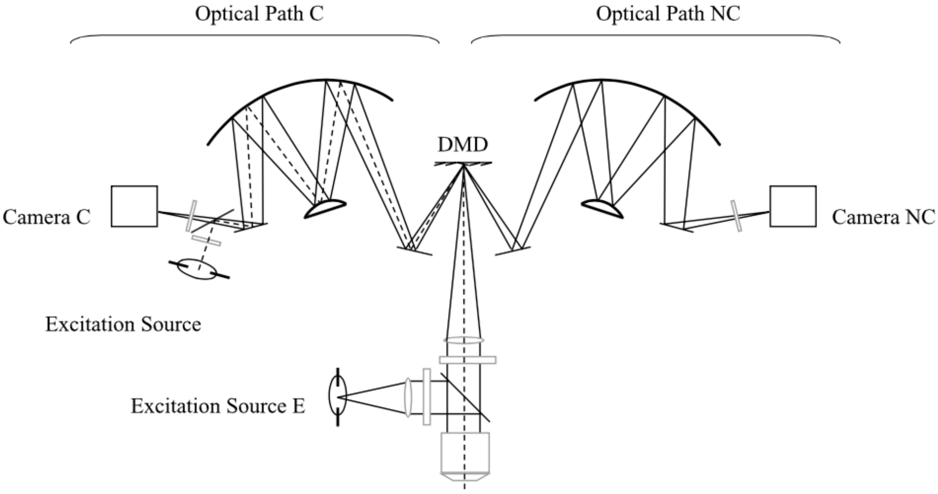

Fig. 1. 6. Dual path PAM for both illumination and detection. Use of Offner Triplet arrangement allowed the projection and collection of both conjugate and non-conjugate light pathways [Heintzmann *et al.*, 2001].

The theory of DMD based PAMs for confocal imaging was addressed in detail [Verveer *et al.*, 1998] and was experimentally established by several groups. In a dual path PAM system, a weighed subtraction of the non-conjugate image (Inc) from conjugate image (Ic) renders an optically sectioned image with the added advantage of superior noise characterisation and enhanced fluorescence emission light utilisation than single path systems.

Apart from various illumination techniques such as dot scanning, line scanning *etc*, a pseudo random sequence (PRS) illumination for optical sectioning was also employed in PAM systems [Heintzmann *et al.*, 2001]. The conjugate image consists of the 'confocal' component of fluorescence emission since we can reason that the 'ON' pixels act as pinholes to reject the out-of-focus light from the sample. With this reasoning, the conjugate image can be used as such without the removal of offset. A weighed subtraction of either widefield image or Inc from Ic can result in an optical sectioning. Yet another way is to utilise both Ic and Inc using deconvolution for the reconstruction of image [Verveer *et al.*, 1998, 1999]. These imaging techniques vary only by the noise characteristics and speed of imaging.

During 2004, attempts were made to use DMD just for detection of light from the sample alone to overcome the issue of slowness of the galvanometer driven mirrors which had a settling time of approximately 1 ms. Rapid spot illumination was employed using Acousto-Optic Deflectors (AOD) which allow concurrent optical recordings of user-selected sites of interest at high frame rates. These are operated in Bragg regime which block the higher order diffraction increasing the total power loss. Since AOD is based on diffraction, detection/de-scanning of Stroke shifted emission light from sample cannot be performed using AOD. Moreover, AOD has only 50% diffraction efficiency and therefore, DMDs which are based on reflection were preferred for detection [Bansal *et al.*, 2004, Bansal *et al.*, 2006].

To detect precisely the subcellular localization of the fluorescent signals from FRET between cyan and yellow mutants of green fluorescent protein [Takashi *et al.*, 2007], a DMD system was attached to an inverted widefield microscope to obtain optically sectional images. Tunability of optical sectioning using fringe pattern projection was explored by the same team in 2003 [Takashi *et al.*, 2003]. SIM using DMD has also been explored for the application in endoscopy. Because of its fast imaging with adjustable fringe size or sectioning strength, the system is adaptable to various biological samples [Wong *et al.*, 2006].

1.7.2. Phase 2

In 2007, LCoS SLM based PAM systems offered faster confocal imaging with lower exposure time than DMD based systems. Around this time, development of DMD in microscopy showed a decline [De Beule *et al.*, 2011]. Around 2010, the developments in Texas Instruments DLP DMD technology with high contrast, reduced pixel pitch, better efficiency and higher control of electronics gave rise to further developments on dual path PAMs.

DMDs were also used in the speckle-illuminated fluorescence microscopy by Jiang and Walker [Jiang *et al.*, 2010, 2009]. In this technique, computer generated binary laser speckle patterns were used to illuminate and encode a sample and a set of reference speckle illumination patterns were used to decode the image. This is a non-scanning imaging technique which is not suitable for live cell imaging because the processing of recording frames happens off-line. Using DMDs improved the mechanical stability of the system replacing conventionally used far-field speckle patterns by rotating diffuser. Two optical arrangements were implemented in 2009 [Jiang *et al.*, 2009] and 2010 [Jiang *et al.*, 2010] by the same group to realise this system. The first arrangement had only one CCD camera to collect fluorescence emission light from the sample but a second arrangement could collect the average of the fluorescence frames modulated by both correlated and anti-correlated speckle patterns in two separate cameras as shown in **figure 1.7(a)** and **(b).** The second arrangement reduced the data acquisition time by half because the former setup require two exposure times for complete acquisition of the final image. Imaging speed is dependent only on the specifications of the employed DMD technology. Higher frame rates and greater on-board RAM (number of speckle patterns which can be stored) can increase the speed and efficiency of image acquisition.

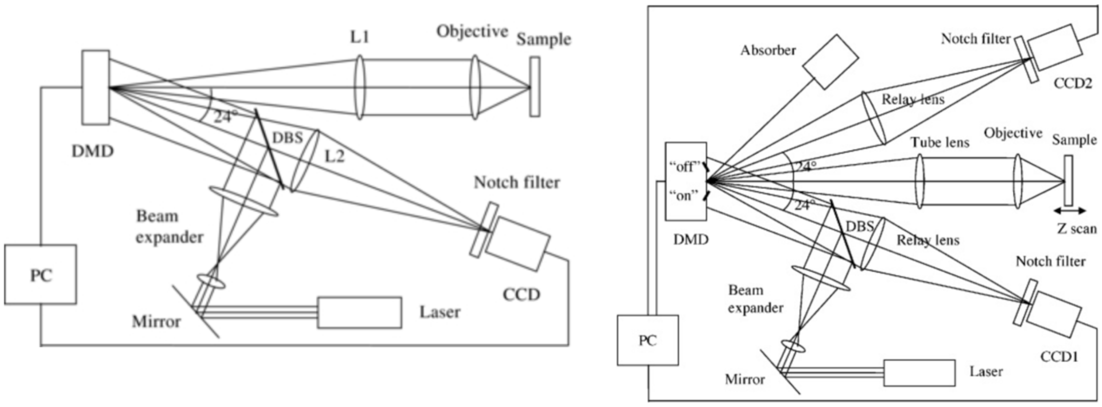

Fig. 1. 7. DMD for speckle illumination microscopy. **(a)** Single sided speckle illumination microscopy. **(b)** double sided speckle illumination microscopy [Jiang *et al.*, 2009, 2010].

In a conventional PAM based confocal microscope raster scanning is used to collect a set of images using CCD cameras. They are reconstructed to obtain a single optically sectioned image. Alternatively, out-of-focus light can be eliminated before the image reaches the CCD camera. Non-scanning Comprehensive Sensing Microscopy (CSM) exploits this idea by projecting an incoherent illumination pattern using DMD. Modified Scrambled-Block Hadamard Ensemble (MSBHE) comprehensive sensing measurement pattern has a sparse distribution of ON pixels which can efficiently obtain an optically sectioned image. A single pixel detector can be used to collect the fluorescence in-focus light with a higher efficiency in comparison to light collected by PAM systems [Wu *et al.*, 2010]. The schematic diagram of CSM is described in **figure 1.8.**

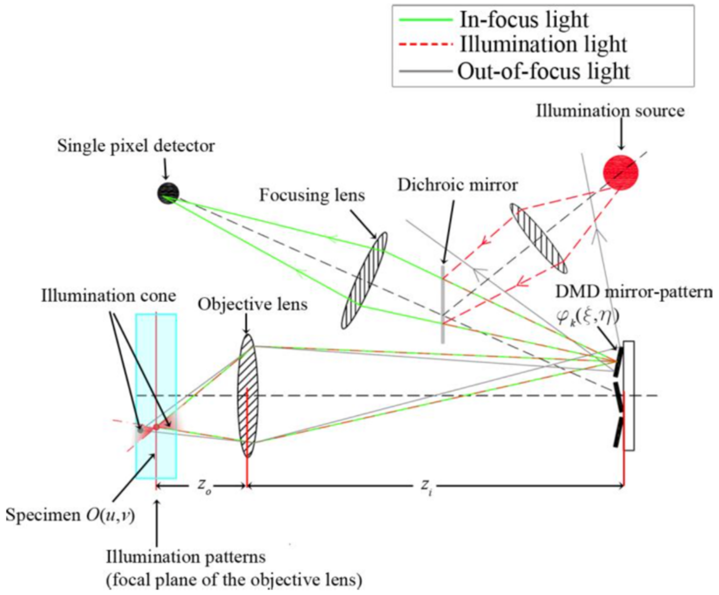

Fig. 1. 8. Optical sectioning comprehensive sensing microscope. Non-scanning comprehensive sensing microscope with sparse illumination [Wu *et al.*, 2010].

1.7.3. Phase 3

The Jovin group now has their generation III dual path PAM with telecentric relay optics and image plane tilt correction optics which consist of a concave mirror and two lenses on both conjugate and nonconjugate pathway as shown in the **figure 1.9** [de Vries *et al.*, 2015, De Beule *et al.*, 2011].

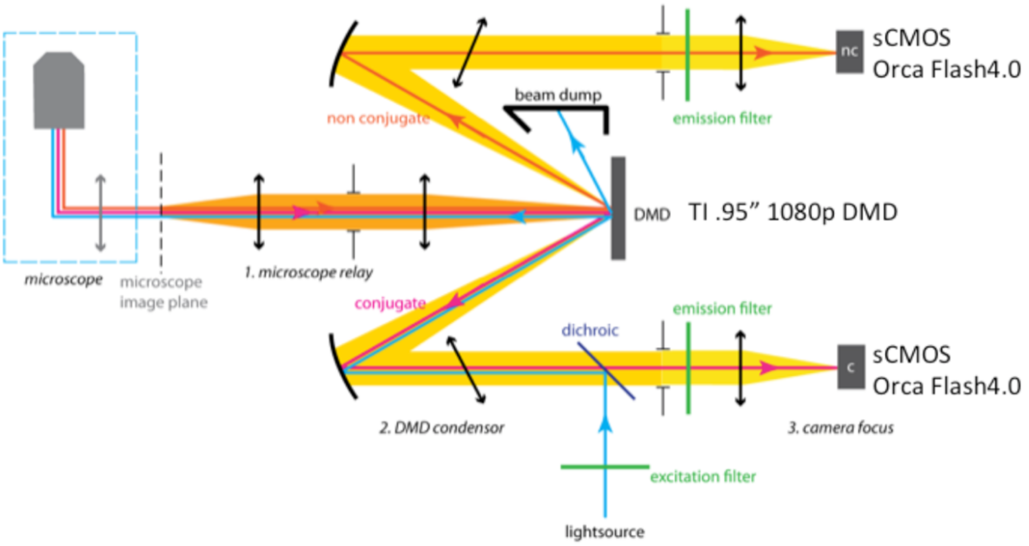

Fig. 1. 9. Generation III dual path PAM. Generation 3 dual path PAM employs Offner triplet arrangement to simultaneously collect conjugate and non-conjugate pathways of fluorescence emission [De Vries *et al.*, 2015].

The system collects images from conjugate and nonconjugate path simultaneously by employing an image combiner thus surpassing the Moire Beat pattern due to misalignments in their generation III dual PAM systems using DMD. In a dual path PAM system, a weighed subtraction of the Inc from Ic renders an optically sectioned image with the added advantage of superior noise characterisation and enhanced fluorescence emission light utilisation than single path systems. The system has also been used to control the light exposure with patterned illumination to reduce the overall photodamage in the sample [Caarls *et al.*, 2010].

N.A. Hartell and co-workers in 2012 commercialised DMD-SLM based high spatial and axial resolution microscope which operates in frame rates limited only by speed of the camera and opened the scope for imaging fast biological events using DMD technology [Martial *et al.*, 2012]. The distance between two pinholes and their sizes determine the sectioning ability and imaging speed for a specific illumination pattern. One of the major advantages of DMD based ‘confocal’ imaging is that we can precisely control the size of each pinhole and the distance between them. Reducing the distance between two spots can result in crosstalk between them decreasing the optical sectioning and signal to background ratio of the image. Increasing the distance increases the optical sectioning ability and the number of image frames needed for reconstruction. This in turn increases the time required for reconstruction of the image. The best option is to choose an optimal distance compromising on the sectional ability of the system. A modified Offner Triplet arrangement consisting of two concave mirrors and a convex mirror is used to collect the emission light reflected from DMD as shown in **figure 1.10**. This non lens system in the emission pathway can avoid the inherent astigmatism in DMD systems caused by angled reflection [Hartell *et al.*, patent, 2016].

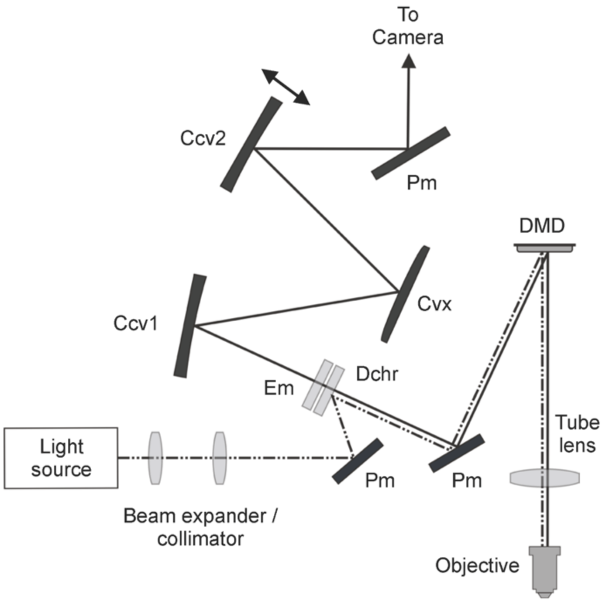

Fig. 1. 10. Modified Offner Triplet arrangement in emission pathway. Double headed arrow at concave mirror 2 indicates the changing magnification region [Martial *et al.*, 2012].

1.7.4. Phase 4

The Imaging Scanning Microscope (ISM) was first theoretically developed by Shephard and co-workers in 1980s [Shepphard, 1988] and experimentally implemented by the Enderlein group in 2010 [Müller *et al.*, 2010] using a LSCM. This first ISM setup projects diffraction limited confocal spots using a laser beam and emission light from the sample passes through a pinhole to reject the out-of-focus light and is collected in a camera. The key element of ISM is that the camera is used to reassign photons and improve resolution, where camera acts as second pin hole. Although this technique generates optically sectioned images of 150 nm lateral resolution, its popularity was limited by the speed of image acquisition because only a single point was illuminated at a time. The major disadvantage of ISM was that it was slow, similar to a conventional LSCM with single illumination spot.

Multifocal Structured Illumination Microscopy (MSIM) has a parallelization of ISM by projecting many focal illumination spots on to the sample at the same time considerably decreasing the image acquisition time. Shroff's group [York *et al.*, 2012] implemented ISM using a DMD which increased the speed and doubled the resolution when compared to a widefield image. Schematic of the MISIM setup is shown in **figure 1.11**.

Instead of a single laser spot, multifocal illumination spots were projected using a DMD to scan across a sample. This MSIM technique post processes the data with digital pinholing to reject the out-of-focus noise followed by 2x scaling and summing all the frames to get a MPSS image. This image is deconvoluted to double the resolution. Digital pinholing by postprocessing, 2x scaling, summing and deconvolution were done to generate MSIM images with improved resolution and contrast compared to a widefield image. Spots were aligned in equilateral triangles which is the best pattern as it allows the maximum density of spots in an area while keeping maximum distance between two spots in order to reduce crosstalk.

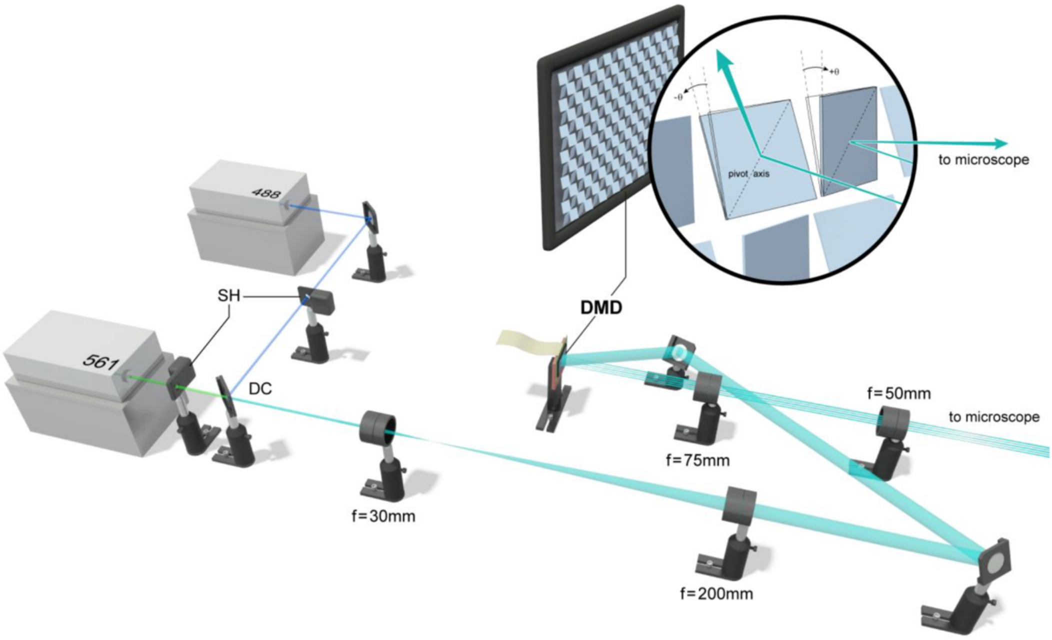

Fig. 1. 11. Multifocal Structured Illumination Microscopy setup. DMD is used to project illumination patterns to increase the speed of ISM. There are no physical pinholes to reject the out-of-focus light in this optical setup. Out-of-focus light is rejected by digital pinholing by multiplying the emission spot with a Gaussian mask. The standard deviation of the Gaussian mask applied determines the optical sectioning of the microscope [York *et al.*, 2012].

Developing MSIM has the added advantage of relatively easy implementation where an economical DMD is attached to a widefield microscope to achieve high switching speed of illumination spots with no mechanically moving parts. MSIM using DMD rendered 145 nm FWHM in biological samples improving the lateral resolution by two-fold when compared to widefield microscopy. This system was fast enough to be able to image live biological samples of thickness level eight-fold higher than conventional SIM because of digital pin holing. Although 3D SIM had the ability to render images with double the resolution of the classical limit, its optical sectioning ability was confined to thin samples. Using a micro-lens array [York *et al.*, 2013], multiphoton excitation [Winter *et al.*, 2014], total internal reflection microscopy [Guo *et al.*, 2018] *etc* have further opened new scopes for imaging using MSIM.

It has been shown that ISM can be implemented with a conventional spinning disk confocal microscope. By collecting the raw data in a camera and post processing with 2x scaling, summing and deconvolution, the resolution of the final image is doubled. One of the disadvantages of MSIM and its spinning disk equivalent is that the need for post processing techniques takes additional time making it difficult to get final images in a camera instantaneously.

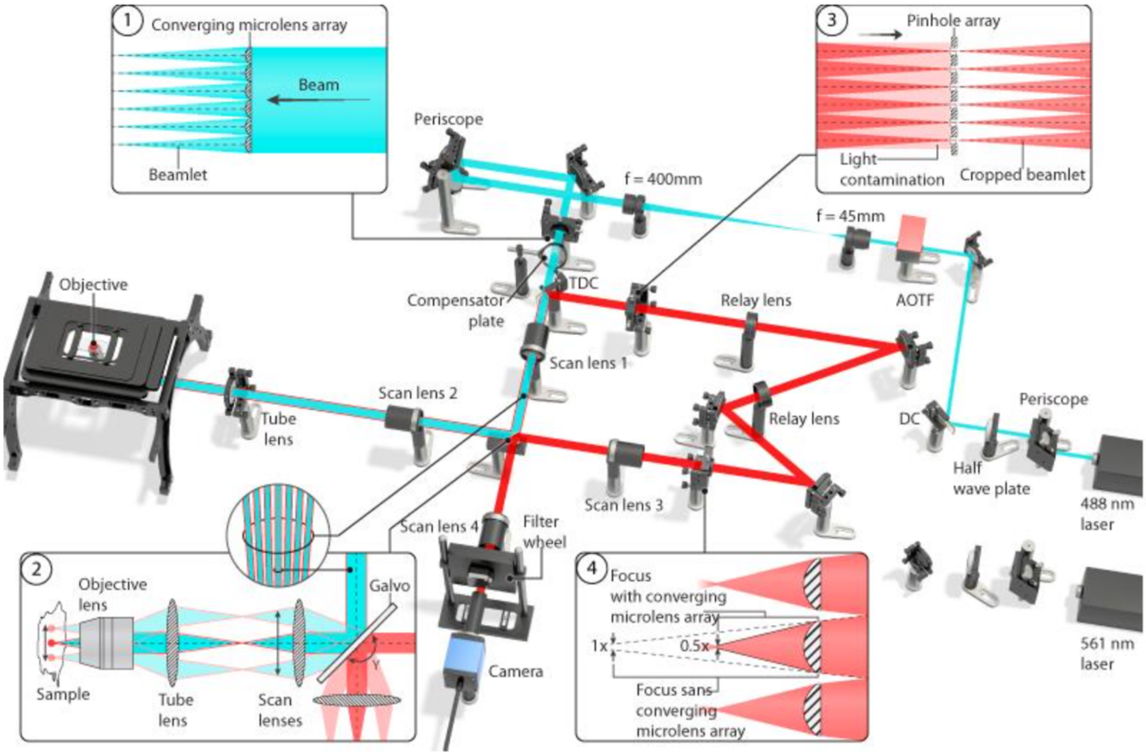

Fig. 1. 12. Optics of Instant Structured Illumination Microscopy. iSIM increased the speed of imaging from MSIM implementation by obtaining resolution doubling using microlenses. iSIM does not require post processing which will enable the visualization of fast biological processes instantaneously [York *et al.*, 2013].

Instant Structured Illumination Microscopy (iSIM) [York *et al.*, 2013] implements ISM using lenslet arrays for confocal structured illumination and another pair of lenslet arrays to focus each emission spot on the detector in such a way that it does the 2x scaling required by ISM when projected on to the camera chip. iSIM can image live biological samples instantaneously, potentially at 100 frames per second. It is worth noting here that iSIM uses a pinhole array to reject the out-of-focus light from the sample.

The iSIM optical setup as shown in **figure 1.12** is not based on DMD. But it is described in this section by considering it as an extension of MSIM. ISM has been implemented with a

GaAsP detector in AiryScan [Huff, 2017]. Another most recent ISM implementation is with a SPAD detector from Vicidomini group [Marco *et al.*, pre-print, 2018] which is an upgradation for the existing LSCM microscope without compromising on any of its functionalities.

1.8. Other significant applications of DMD in microscopy

Physiological manipulation of neuronal activity with micrometre spatial and sub millimetre temporal precision was done by integrating a DMD system into a multiphoton epifluorescence microscopy. The DMD based system allowed single neuron resolution optogenetics compared to previously used widefield methods which stimulated a population of neurons synchronously. R.W. Friedrich and group developed a system in 2012 which could conveniently switch between multi photon or epifluorescence microscopes as shown in **figure 1.13.** Two different configurations were implemented which could be easily changed from one another depending on whether the neurons to be focussed were in one plane or in a curved region in an ex vivo zebrafish brain [Peixin *et al.*, 2012].

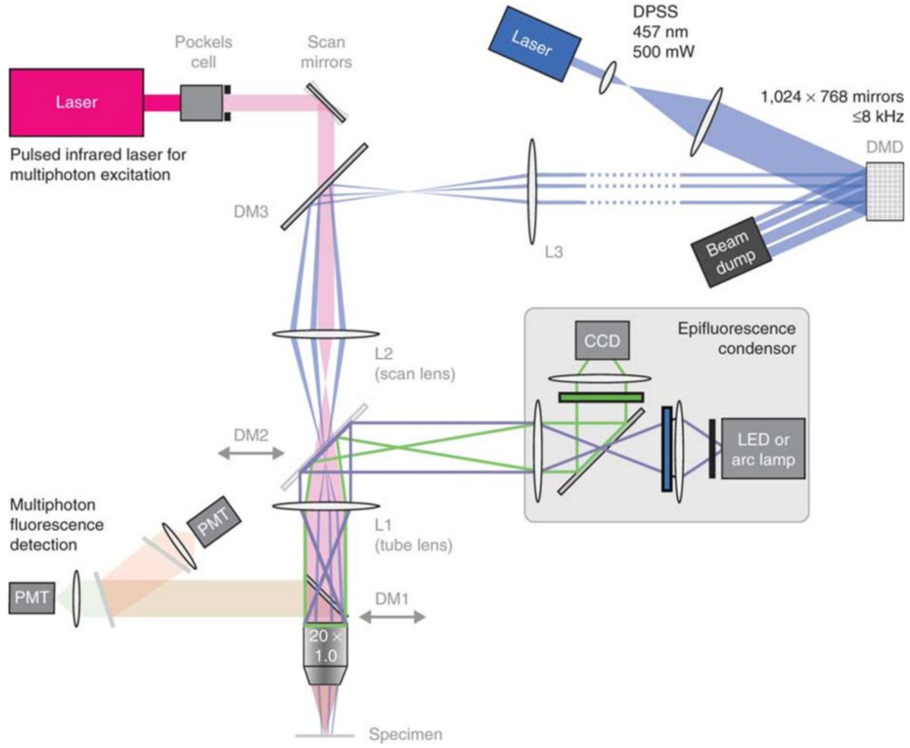

Fig. 1. 13. Integration of DMD in a multiphoton epifluorescence microscope. DMD is incorporated to implement multiphoton excitation for optogenetic applications. Imaging is switched between widefield imaging using LED or arc lamp and multiphoton excitation [Peixin *et al.*, 2012].

The conventional diffraction grating used for temporal focussing in a Temporal Focussing Multiphoton Excitation Microscopy (TFMPEM) can be replaced by a DMD acting as a diffraction component separating the frequencies and refocussing at the focal plane of the objective lens to project structured illumination [Yih *et al.*, 2014]. In 2014 a setup using a DMD as shown in **figure 1.14** was developed by the Shean-Jen Chen is group to project second order nonlinear structured illumination pattern on to the sample to enhance the resolution of TFMPEM laterally by 2.4 times and axially by 1.9 times [Cheng *et al.*, 2014].

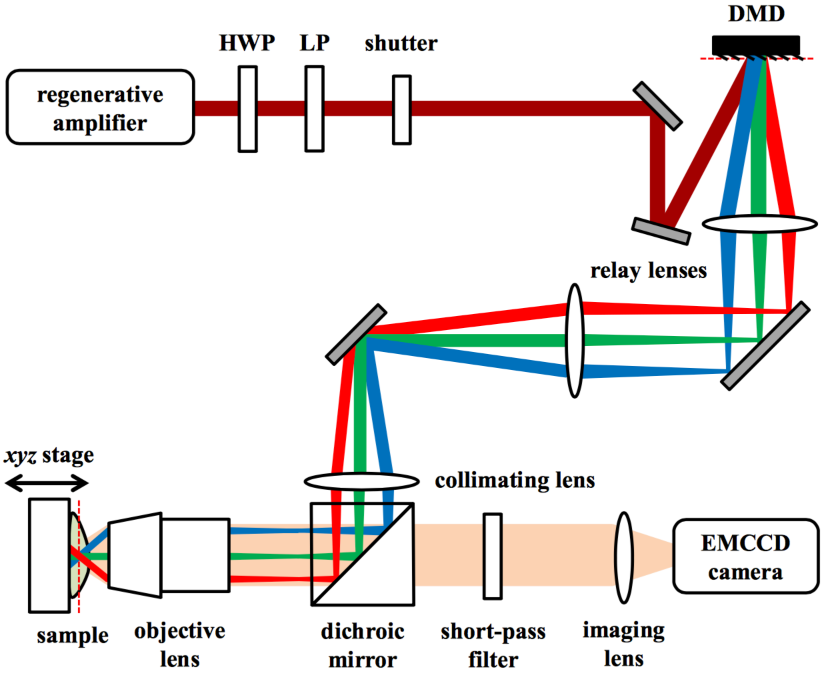

Fig. 1. 14. Temporal Focussing Multiphoton Excitation Microscopy (TFMPEM). DMD replacing a conventional diffraction grating in TFMPEM [Cheng *et al.*, 2014]**.**

Recently, a random access Optical Resolution Photo Acoustic Microscopy (OR-PAM) [Liang *et al.*, 2013] and Compressive Fluorescence Microscopy (CFM) [Vincent *et al.*, 2012] for biological and hyperspectral imaging were also developed using DMD.

In 2013, Dan Dan *et al.* showed a very compact implementation of DMD to the development of a SIM system using incoherent light source as shown in **figure 1.15**. Here, the minimum period of fringe projection is only limited by the Abbé diffraction limit set by the objective lens whereas it’s contemporary competitor system, which utilizes laser interference for fringe projection needs a higher and higher NA microscope objective to increase the convergence angle which in turn contributes to the minimum period of fringe projection. This clearly indicates that DMD based structured illumination for SIM system has greater scope of achieving higher lateral resolution. But for axial resolution, since the projection of structured light is in 2D for a DMD, it is limited by the point spread function of the objective lens. That being the case, illumination pattern formed by three laser interferences can obviously have a better potential for higher axial resolution. Having said that, there are various biological applications where there is a need for low cost, speckle noise free, easily switchable excitation source wavelength, high speed DMD based SIM systems with the added advantage of the ability to image non-fluorescent specimens. This system could achieve 90 nm lateral resolution and 120 µm penetration depth with 930 nm sectioning length. Imaging in 2D and 3D modes are easily interchangeable, and speed of imaging is limited only by the speed and sensitivity of the CCD camera used [Dan *et al.*, 2013, 2014, Jia *et al.*, 2015].

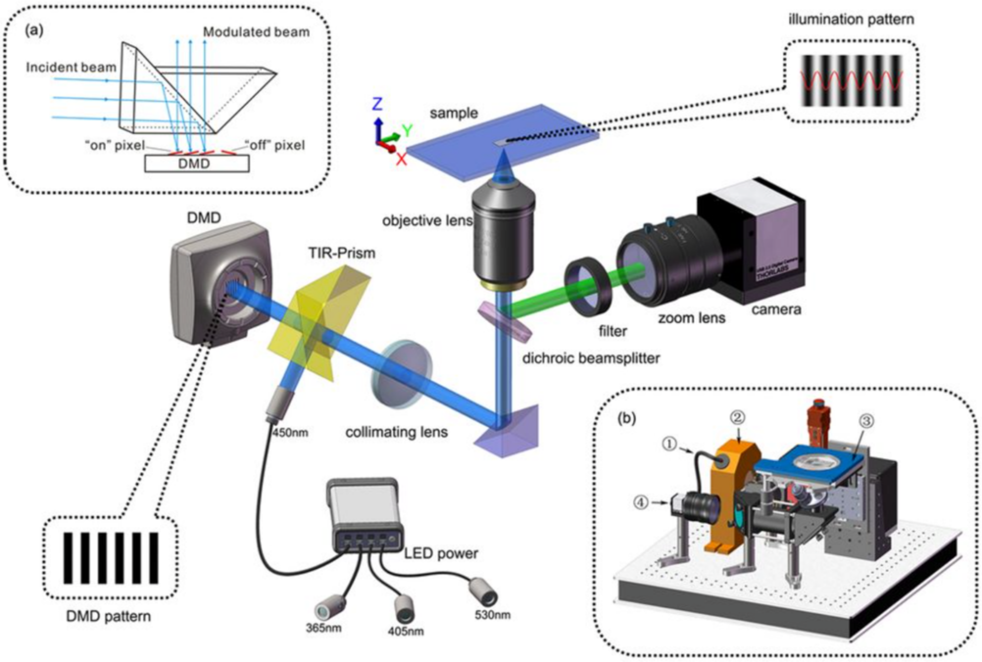

Fig. 1. 15. DMD based SIM using incoherent illumination. This optical setup is very compact and employs SIM with incoherent illumination [Dan *et al.*, 2013].

1.9. Physical and Digital Pinholing in Confocal Microscopy

We can classify the optical implementation of confocal microscopy into systems which perform out-of-focus light rejection by physical pinholing or digital pinholing. In this work, physical pinholing refers to the out-of-focus light rejected by physical apertures such as in

LSCM and spinning disk microscopes. Digital pinholing systems refer to optical implementations which collect the full emission spot without any physical apertures between the sample and the detector. Out-of-focus light rejection in these systems are performed by multiplying the emission spot with a Gaussian mask with the desired standard deviation (SD). The SD of the gaussian mask determines the optical sectioning ability of the system. This is analogous to increasing or decreasing the size of a pinhole to change the sectioning ability of the confocal microscope. **Figure 1.16 (a)** is the schematic for a physically pinholed rejection of out-of-focus light. The red ellipse highlights the emission pinhole aperture. In digital pinholing, optical sectioning is achieved during post processing of the acquired data by multiplying the full emission spot with a Gaussian mask as represented in **Figure 1.16 (b)**

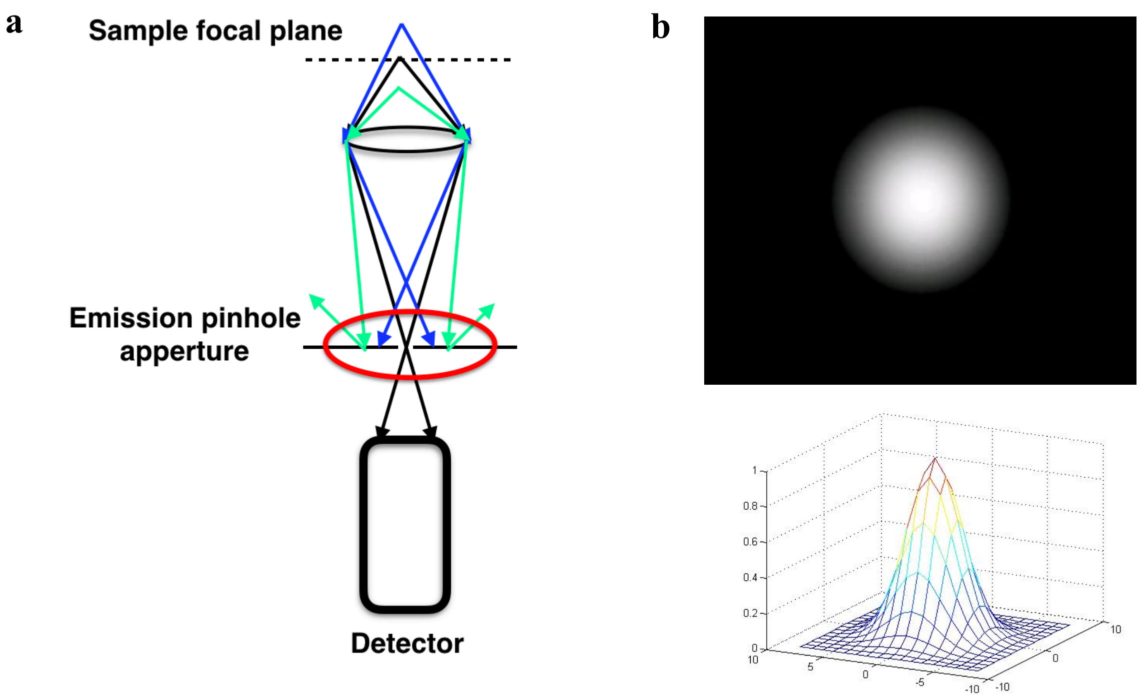

Fig. 1. 16. Schematic of physical and digital pinholing techniques for out-of-focus light rejection. (a) Schematic of physical pinholing. Blue line represents ray from above the focal plane. Green line represents rays from below the focal plane. Black line represents ray originating from the focal plane. **(b)** Digital pinholing multiplies a Gaussian mask to the emission spot collected in the detector.

1.10. Super Resolution Microscopy

In an optical microscope, as light passes through different media, it diffracts, and a single point emitter is captured as if it were to come from a larger volume. Thus, a conventional optical microscope is called a ‘diffraction limited’ system. Because of this reason, it was unable to visualize biomolecular complexes which were less than around 200 nm. Since many intriguing cellular structures and dynamics happen in a scale which is well below 200 nm, there were many independent attempts to break the diffraction limit of light microscopy and to understand life in a nanoscopic scale.

In recent years, the Abbe limit restricting the resolution of optical systems to the diffraction limit has been overcome [Eugene *et al.*, 2016, Hell et al, 2015, Huang *et al.*, 2010]. There have now been many independent solutions to this century old puzzle and these include, but are not limited to, Stimulated Emission Depletion Microscopy (STED) [Thomas A.K *et al.*, 2000], Localization Microscopy (LM) [Betzig *et al.*, 2006, Michael J.R *et al.*, 2006, Bates *et al.*, 2006] [Hess *et al.*, 2006] and Structured Illumination Microscopy (SIM) [Gustafsson *et al.*, 2000, 2005]. LM and STED was awarded 2014 Nobel Prize in Chemistry.

1.10.1. Structured Illumination Microscopy (SIM)

Gustafsson published his work in 2000 on Structured Illumination Microscopy (SIM) in which the resolution limit was reduced from diffraction limit down by a factor of two. SIM uses widefield patterned illumination and scanning across the sample in various orientations followed by reconstruction operations in Fourier domain to double the resolution compared to a wide field image [Gustafsson *et al.*, 2000].

SIM projects down sinusoidal fringe patterns by inserting a movable diffraction grating in the way of the excitation laser beam. This sinusoidal pattern of known frequency interferes with the sample frequency to generate Moiré fringe patterns. The higher unknown spatial frequencies of the sample are coupled to that of the known illumination pattern frequency allowing higher frequency information of the sample to be brought into the frequency domain of the optical system. This allows the higher frequency sample information to pass through the objective lens. To illuminate all the areas of the sample and to reconstruct the full image, patterns are translated three times. To reconstruct a high resolution SIM image, conventionally, nine raw images are taken by rotating the sinusoidal pattern three times and recording three translations for each rotation. SIM reconstruction brings the high frequency sample information to a resolvable range in the Fourier space as shown in **figure 1.17**.

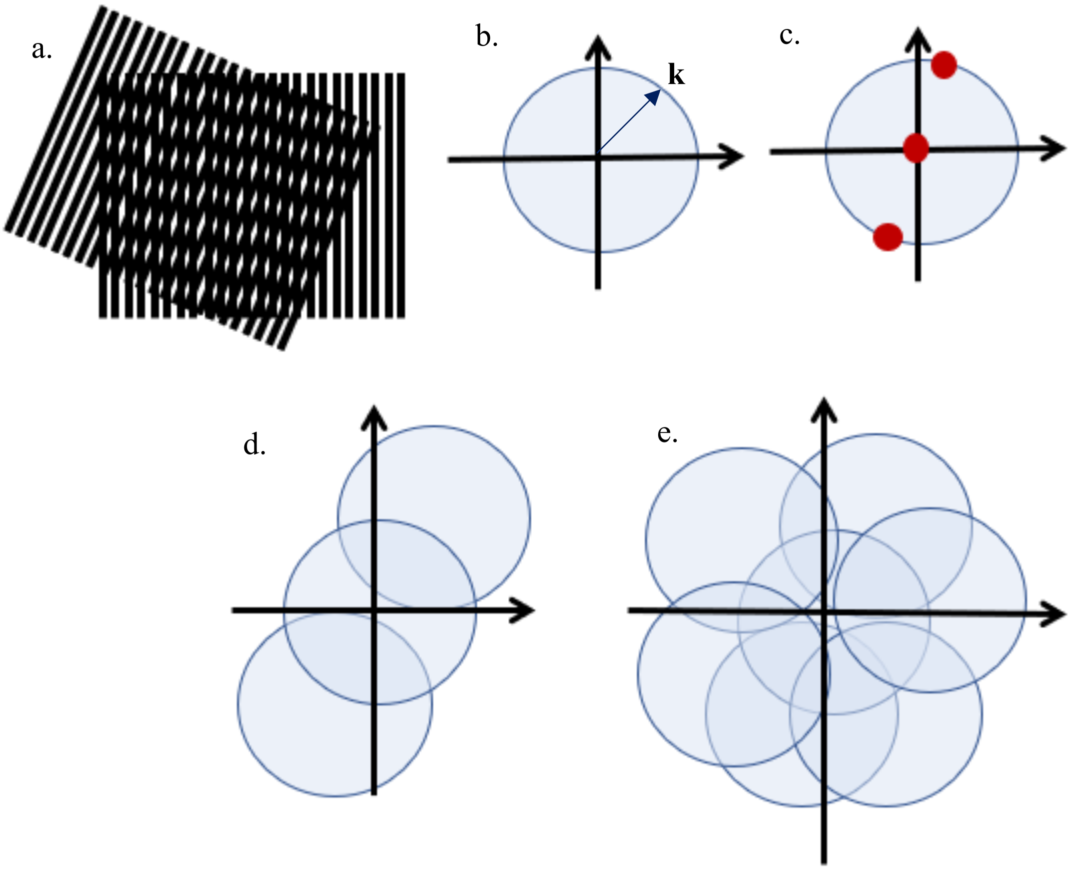

Fig. 1. 17. Schematic of SR-SIM. (a) Frequencies of illumination and sample forming Moire fringe pattern. **(b)** Fourier plane demonstrating the resolvable frequencies given by circle of radius k=1/d, where d is the resolution limit. **(c)** red spots indicate the frequency of line based illumination pattern. **(d)** The line based illumination pattern is scanned across the sample for uniform illumination covering the two circles in Fourier plane. **(e)** The line pattern is rotated three times to bring the higher frequency information on to the resolvable regime of Fourier space.

The nonlinear dependence of fluorescence emission rate to the illumination intensity due to the saturation of excitation state was exploited to establish that SIM could theoretically achieve ‘unlimited’ resolution while practically it was limited only by photobleaching [Gustafsson *et al.*, 2005]. Neil *et al.* used in 1997 the same method of projecting sinusoidal fringe pattern and laterally shifting the patterns three times to yield an optically sectioned image in real time [Neil *et al.*, 1997]. This grid based illumination increases the speed of imaging for attaining optical sectioning compared to confocal based point illumination by reducing the number of raw images needed for reconstruction. Super resolution SIM by acquiring nine raw images, and optical sectioning SIM by acquiring three raw images, are similar in their optical configuration but differ in data processing algorithms. Conventional SIM is limited by resolution doubling.

Sensitivity of SIM to the optical imperfection and aberrations of the sample, makes it technically challenging. In future, with further explorations, SIM could have the greatest impact in live cell super resolution imaging because of its advantage of low power and fast imaging over other super resolution techniques.

1.10.2. Localization Microscopy (LM)

The ability to temporally localize a single fluorescent molecule gave rise to further recent breakthroughs in the field of sub diffraction resolution light microscopy called Localization Microscopy (LM). The most common LM techniques are Stochastic Optical Reconstruction Microscopy (STORM) [Bates *et al.*, 2006], and Photoactivated Localisation Microscopy (PALM) [Betzig *et al.*, 2006], Fluorescent Photoactivated Localisation Microscopy (FPALM) [Hess *et al.*, 2006], which can give 10-30 nm lateral resolution.

Initially, a high laser power is used to bleach all the fluorophores into a dark state followed by switching 'ON' a small subset of fluorophores usually with ultraviolet illumination. Localization microscopy achieves super resolution by switching the fluorescent state of immunolabeled exogenous molecules in a cell (STORM), or photoactivable fluorescent proteins (PALM) in such a way that only a subset of molecules is turned ON per imaging frame. During data acquisition, the background intensity is determined by the small fluorescence intensity emitted from the bleached molecules and also by the contrast of this background intensity with the intensity of the ON fluorophores. These blinkings are fitted to the known point spread function of the microscope and a super resolution image is reconstructed. The error of fitting is given by,

$$\sigma_{x,y} \approx \frac{s}{\sqrt{N}}$$

where 'S' is the standard deviation of the PSF and 'N' is the number of photons detected. Use of imaging buffers can help in tuning the switching between fluorescent states and increase the photostability of fluorophores [Betzig *et al.*, 2006]. Multicolour imaging can be acquired using LM by separating the emission spots from two spectrally separated fluorophores using a dichroic mirror [Shroff *et al.*, 2007].

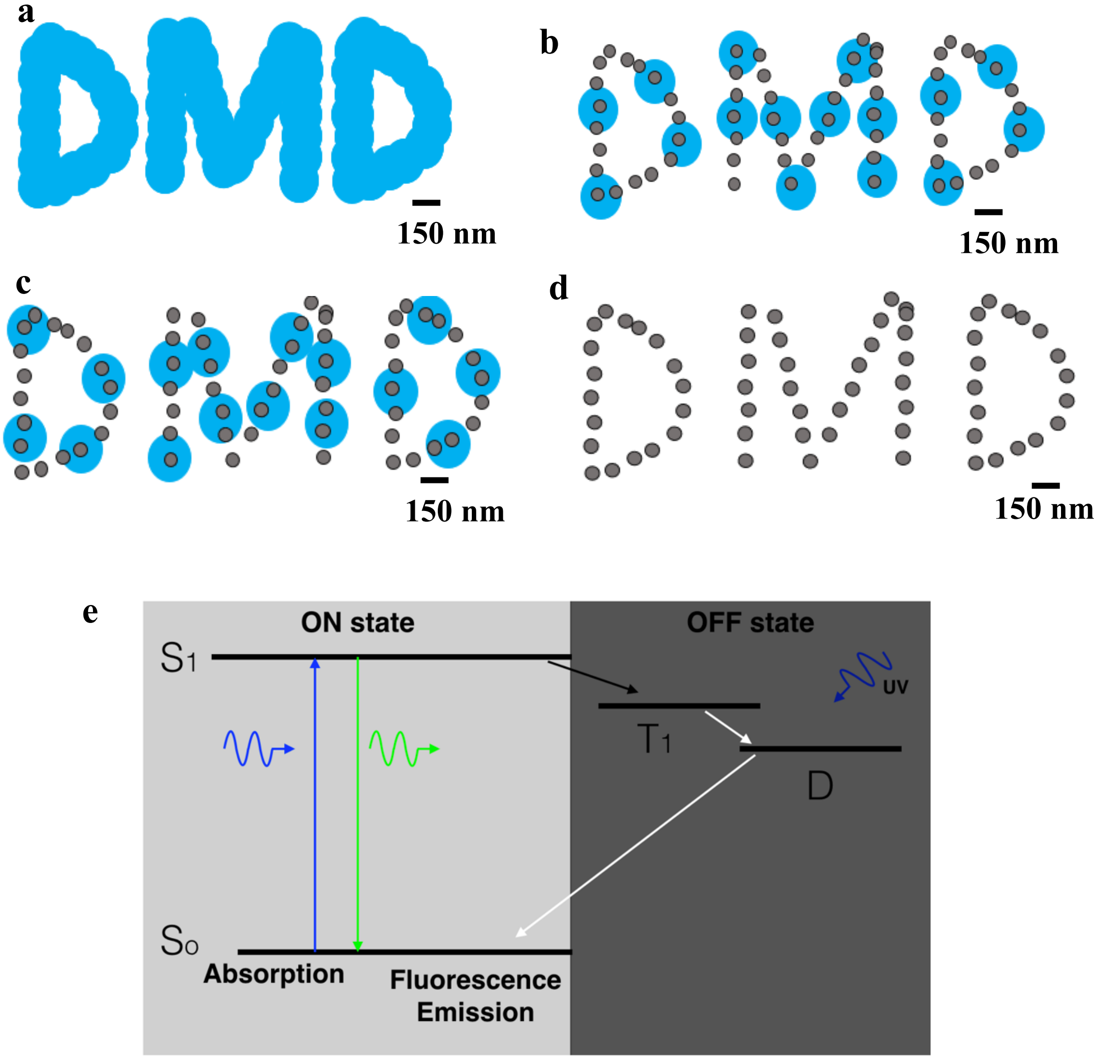

Fig. 1. 18. Principle of LM. (a) Densely populated fluorophores which are point emitter forming a diffraction limited conventional fluorescence image. (b) & (c) are raw LM frames in which a subset of molecules is ON to temporally localize the molecules. Sequential activation of fluorophores and time resolved localization of photoswitchable fluorophores generating a high resolution image in (d). Scale bar is approximately 150 nm. (e) Jablonski diagram for electron transitions in LM.

Figure 1.18(a) is a representation of an image acquired in a diffraction limited microscope. **Figure 1.18(b)** and **(c)** are the raw LM frames collected with a subset of fluorophore molecules in the 'ON' state. The majority of the fluorophores are in the 'OFF' state enabling spatial localization of individual molecules. After acquiring thousands of LM raw data sets followed by time resolved localization of molecules, a high resolution image is generated as represented in **figure 1.18(d). Figure 1.18(e)** is the Jablonski diagram representing electron transition in LM. Molecules in the ON state undergo fluorescence emission. Due to redox reactions, electrons jump to a dark state with life time ranging from milliseconds to several minutes.

Electrons move from excited state to triplet state with intersystem crossing where the lifetime of electron triplet state is in the range of microseconds. UV radiation can initiate the transition of electron from dark state to the ground state of the molecule and turning the molecule ‘ON’. When electrons are in either ground state or singlet excited state, molecules are ‘ON’ or they fluoresce. When electrons are in either triplet state or the long lived dark state, molecules are ‘OFF’ or they do not emit photons. Transition from ‘ON’ state to ‘OFF’ state can be controlled by controlling the redox reactions mediated by oxidants or reductants that can be present in imaging buffers.

Imaging buffer constituents used in this work include, glucose oxidase, glucose, catalase and β-Mercaptoethylamine in phosphate buffered saline (PBS) buffer [Ha *et al.*, 2012]. Oxygen is a triplet state quencher. It helps the molecules to move to the ground state from the triplet state. Without this quenching, blinking time of molecules can take upto several seconds which is not desirable for a STORM experiment. But oxygen radicals assist the molecules to bleach. An oxygen scavenger system containing glucose oxidase, glucose and catalase (glox buffer) is used to eliminate oxygen. Reducing agent MEA are added as triplet state quenchers to control the blinking of fluorophore molecules, as a replacement for oxygen [Vongelsang *et al.*, 2008]. Catalase is added to remove hydrogen peroxide formed as a by-product during the oxidation reaction which converts glucose to gluconic acid. The enzymatic system of glox constituents leads to acidification of the buffer over time [Shi *et al.*, 2010]. This acidification affects the photophysics of fluorophore molecules. The imaging buffer is efficient only for 3-4 hours after sample preparation. STORM imaging needs to be performed immediately after mounting the sample for better results.

Long imaging time to acquire enough localizations to obtain sufficient information of the structure, drift during imaging due to thermal perturbations and air currents in the room and UV activation laser photobleaching the sample are the major drawbacks of LM microscopy. To overcome the long exposure time which restricts the visualization of dynamic processes, post processing algorithms such as DAOSTORM [Seamus *et al.*, 2011] and 3B [Cox *et al.*, 2011] can reconstruct the sample structure with data sets having high ‘ON’ fluorophore density. Trajectory of drift can be calculated and corrected by employing fiducial markers which are bright fluorescent beads in the field of view. One of the methods to reduce the photobleaching in the sample is to target specific regions of interest and obtain high resolution image from the targeted areas without photobleaching other areas of the sample as detailed in Chapter 5 of this work.

There are different methods to calibrate the resolution of an LM image. Some commonly used methods include the calculation of the smallest resolvable distance between two known objects or determining the size of a known structure such as actin. Another method is the Fourier Ring Correlation (FRC) by Nieuwenhuizen [Nieuwenhuizen *et al.*, 2013] which divides an image into two parts and finding the statistical correlation between the outer ring pixels of a constant spatial frequency in the Fourier transform of these two images. At higher frequency or resolution, correlation is one and at lower frequency or resolution, correlation is zero. Resolution of an image is defined with this method as the value at which the correlation drops below a threshold of $1/7 \approx 0.143$.

There is always a compromise between temporal and spatial resolution of the system. Developments in new switchable organic dyes, fluorescent labels, labelling strategies and algorithms for fluorescent molecule localization have not only increased the resolution but also enabled fast, multicolour, three-dimensional and *in vivo* imaging [Bates *et al.*, 2007].

1.10.3. Stimulated Emission Depletion Microscopy (STED)

In recent years the light microscopy community witnessed some major breakthroughs to surpass the diffraction limit which opened tremendous scope for biological research. Stefan W. Hell and his co-workers developed STED microscopy by exploring stimulated emission.

In fluorescence, an electron excites to a higher energy level and relaxes back to the ground state by releasing a photon. In stimulated emission, the excited electron is stimulated to fall back to the highest vibrational energy level of the ground state as shown in the inset of **figure 1.19**. The stimulated emission photon is more red shifted than fluorescence emission enabling their differentiation. STED beam to induce stimulated emission requires a power density of approximately 100 MW/ cm^2 in the sample plane [Keller *et al.*, 2006]. The high photon intensity requirement of stimulated emission can cause photobleaching in samples.

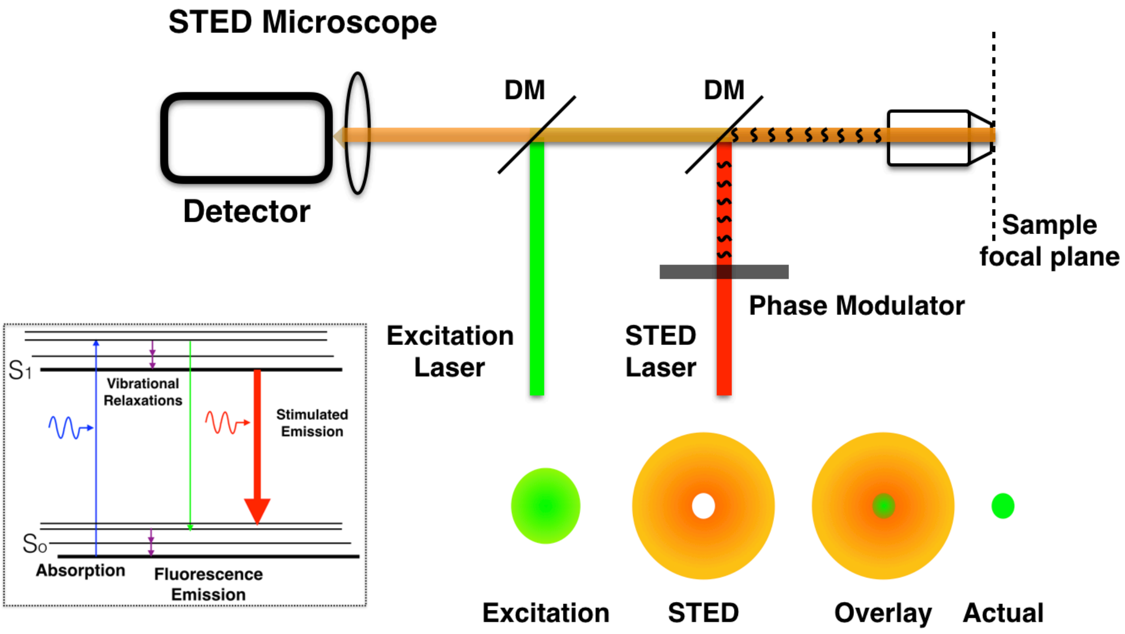

Fig. 1. 19. Schematic of STED microscope. Excitation laser projects a diffraction limited fluorescence excitation spot. STED projects an annular excitation spot which depletes the fluorescence from the outer ring of the excitation spots effectively reducing the actual excitation PSF illuminating the sample.

STED projects an excitation laser spot on the sample overlapped by an annular (doughnut) shaped depletion laser spot which effectively decreases the size of illumination spot to turn ON a very small subset of fluorophores. A doughnut shaped laser is used to de-excite the fluorophores in the outer ring effectively reduced the focal spot [Thomas A.K *et al.*, 2000]. The doughnut shaped laser beam suppresses the florescence with stimulated emission in the outer ring of the excitation spot. The shape of the STED beam is tuned with a vortex phase plate and the 'hole' in the centre of the STED laser beam determines the resolution of the image with lower 'hole' diameter increasing the resolution. This beam is scanned across the sample similar to a confocal microscope to achieve a super resolution image.

The resolution limit redefined for STED microscopy is given by,

$$d \approx 0.45 \frac{\lambda}{n\ sin\theta \sqrt{1+\frac{Imax}{Isat}}}$$

where λ is the excitation wavelength in nanometres, I_{max} is the maximum intensity of the STED laser and I_{sat} is the intensity required to deplete 1/e or 1/2 fluorescence intensity with the STED laser beam [Westphal *et al.*, 2005]. Theoretically, STED can achieve unlimited resolution by increasing the illumination laser intensity to infinity or using fluorophores with high quantum yield, photostability, long fluorescent lifetimes *etc*, decreasing saturation intensity values. Apart from the difficulty to build a STED microscope, the major disadvantage of STED is the high STED illumination intensity to achieve 100% depletion. The major advantage of STED is instantaneous image acquisition without the requirement of post processing like in LM and SIM. The maximum STED resolution achieved in fixed samples is approximately 30 nm [Keller *et al.*, 2006] and on live samples it is approximately 50 nm [Hein *et al.*, 2008].

1.11. Conclusion

This chapter starts with the discussion of a brief history of microscopy followed by a general discussion of fluorescence microscopy, its fundamental principles and labelling techniques for bioimaging. To enhance the axial resolution of fluorescence microscopy and to render 3D images of biological samples, many optical sectioning microscopes were developed as discussed in section 1.5. Among these techniques, confocal microscopy is the technique chosen for the work in this thesis. This is because, even with the recent developments of super resolution techniques, confocal is still the most widely used microscopic technique for biological imaging. Work in the following chapters is based on a DMD based programmable array microscope. Many critically important developments of DMD in microscopy, specifically in confocal and super resolution imaging have been discussed to help the reader understand where the work presented in the following chapters stands in this specialized area of research and technology. Depending on the out-of-focus rejection mechanisms followed, this thesis classifies the current confocal imaging technology into two, physical pinholing and digital pinholing confocal systems as described in section 1.9. Lastly, the 2014 Nobel prize in Chemistry, super resolution techniques were discussed in section 1.10.

1.12. Aims of this study

This thesis is the development of a novel multimodal adaptive super resolution and confocal microscope for versatile imaging. In Chapter 2, I will present the development of a confocal microscope with a PAM system through digital and physical pinholing confocal microscopic techniques. This chapter also discuss the general hardware implementations of the system and the development of software which are used throughout this thesis. Chapter 3 details the theory and experimental developments of a novel imaging technique, Super Resolution-Background

Corrected Microscope (SR-BCM) to enhance the signal to noise ratio and resolution of confocal imaging. Chapter 4 discuss the development of a targeted illumination system and implementation of STORM. Chapter 5 combines the two implementations of chapter 4, for the development of targeted STORM to selectively illuminate specific regions of interest without photobleaching other areas of the sample. Chapter 6 combines all the imaging developments described in other chapters to develop versatile imaging to study the dynamics of phagocytosis in amoeba and drosophila embryogenesis. The chapter also details the development of an reconfigurable confocal microscope for deep imaging.

Chapter 2

Development of a Digital and Physical Pinholing Confocal Microscope

2.1. Introduction

The Cairnfocal Generation I optical setup was the system employed during the first year of the work in this thesis. Various issues encountered with the Cairnfocal Generation I optical setup detailed in the Section 2.2 of this chapter led to further developments in the optical setup. The constant interactions and collaborations with the optics company Cairn Research, helped to understand the issues in the optical system. Rectifications of the optical issues led to the development of Cairnfocal Generation II [M. Thomas, patent, 2017]. The Cairnfocal optical setup presented in this work is analogous to the dual path Programmable Array Microscope (PAM) [J. Thomas, patent, 2002]. The Cairnfocal employs a Schwarzchild configuration and Jovin system employs an Offner triplet arrangement.

The optical design allowed us to define an 'ON' and 'OFF' path with each path being associated with a camera and an illumination source. Light from the illumination source on the 'ON' side is directed by 'ON' pixels on the DMD towards the image plane of the microscope, while 'OFF' pixels on the DMD direct light from the 'ON' path to a beam stop. In contrast, light from the 'OFF' side is directed to the microscope by 'OFF' DMD pixels while 'ON' pixels are sent to a beam stop. When the sample is illuminated, in-focus light from sample follows the 'ON' path or a conjugate pathway (same path as the illumination source) and gets reflected off from 'ON' DMD pixels and is collected on the conjugate camera. Light from out-of-focus regions of the sample is reflected by the 'OFF' pixels and follows an 'OFF' path or non-conjugate pathway to get collected on the non-conjugate camera.

The major issue with the Cairnfocal Generation I was in the collection pathway of the system. Images formed at the camera suffered high degree of astigmatism. This led to the development of digitally pinholed confocal microscopy in which emission light from the sample was collected using a camera at the back port of the microscope as detailed in Section 2.3. Out-of-focus light was rejected digitally during post processing of the data. Corrected optics in Generation II Cairnfocal system, enabled the development of physically pinholed confocal microscopy in which out-of-focus light was rejected physically by the micromirrors acting as an analogue of an aperture in a conventional confocal microscope.

There were six major stages during the development of confocal microscope presented in this work. The first stage was the development of a digitally pinholed confocal microscope by using DMD as an illumination setup and collecting emission light using a camera at the back port of the microscope followed by post processing to digitally subtract the out-of-focus light. Second was the development of a Background Corrected Confocal Microscope (BCCM) which was also based on the projection of multifocal illumination spots on to the sample using the DMD. Two separate cameras were employed for collection of in-focus and out-of-focus emission spots. On the emission pathway, DMD micromirrors were used as physical pinholes. Mapping of in-focus and out-of-focus emission spots were performed at high precision and advanced post processing techniques were employed to obtain a background corrected confocal image with higher signal-to-noise ratio. BCCM is detailed in Section 2.8 of this chapter. The third method was a rapid confocal technique in which confocal images were acquired seamlessly in the camera with speed which can potentially reach up to 350 confocal scans per second. Fourth method was the implementation of Image Scanning Microscope (ISM) algorithm to build an advanced confocal based structured illumination microscope, Super Resolution-Background Corrected Microscope (SR-BCM). Rapid confocal and SR-BCM are discussed in Chapter 3. Fifth was the development of AiryScan equivalent algorithm to establish AiryImaging with a camera based acquisition and point based illumination microscope. Sixth was the development of reconfigurable confocal microscope for deep imaging detailed in Chapter 6.

The digital pinholing confocal system, BCCM, SR-BCM and AiryImaging involve post processing of the raw data to get the final image. For any processing which involves a DMD and camera, a precise calibration of the DMD pixels with camera pixels is mandatory. The camera and DMD pixel calibration detailed in Section 2.7 of this chapter can achieve a precision of 130 nm (2 camera pixel or 1 DMD pixel).

The code for calibration provided in Appendix 4 can be adopted even for a non-confocal experiment which involves DMD illumination and camera detection. This chapter also details the optical setup and software development. The Graphical User Interface (GUI) to project multifocal illumination spots in the DMD using a DLP controller, various multifocal binary and Most Significant Bit (MSB) patterns corresponding to different pinhole sizes, optical sectioning ability of the confocal microscope and different algorithms written for post processing techniques for this Chapter are provided in Appendix 1-5.

2.2. Cairnfocal Generation I

One of the major issues in the Cairnfocal Generation I was that, the DMD plane was not focused perfectly on to the camera sensor. A 4x/0.13 NA air lens on a chroma fluorescent slide was used to test the system. When multifocal spots were projected on to the DMD as shown in **figure 2.1(a)**, the image formed in the camera attached to the Cairnfocal is shown in **figure 2.1(b)**. Relay optics to correct the inherent tilt of the image formed by DMD micromirrors, such as concave mirror, convex mirror and two fold mirrors in both pathways in Generation I system caused the image to tilt with respect to the camera sensor plane. The camera in the system was positioned at an angle due to the orientation of the fold mirrors. Spots above the diagonal area were stre*tc*hed vertically. Spots below the diagonal area were stre*tc*hed horizontally. Spots were focussed along the diagonal and spots above and below the diagonal suffer astigmatism due to the slanted incidence of light in the camera sensor. This was due to the incorrect orientation of fold mirrors causing the image to focus at an angle in the camera sensor.

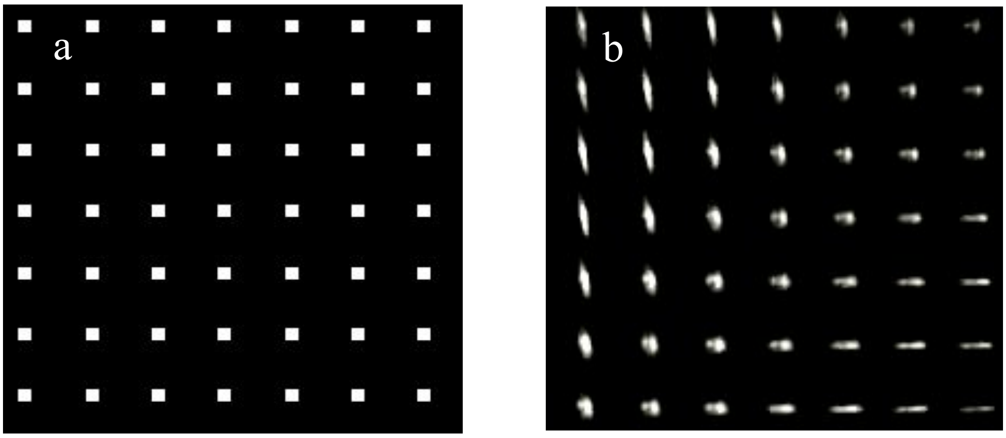

Fig. 2. 1. Multifocal spot collection in Cairnfocal Generation I system. (a) Multifocal spots projected in DMD. (b) Emission confocal spots collected in the conjugate path camera.

2.2.1. Illustration of the issue with collecting emission light on conjugate camera

The issue of collecting emission light in conjugate camera was illustrated with the comparison of a widefield image collected using a camera at the back port of the microscope and the camera on the conjugate side of the system. Widefield images of 200 nm beads with maximum absorption at 505 nm and emission at 515 nm were taken. 470 nm LED was used with 470/40 filter for illumination and 535/50 filter for emission. **Figure 2.2(a)** shows a widefield image of beads in the camera on the back port of the microscope and **figure 2.2(b)** shows beads imaged using the camera on the conjugate side of the microscope. We observe that the image in Cairnfocal conjugate camera suffered from astigmatism during imaging. Images were taken using Andor Zyla 4.2 sCMOS camera at 3x3 camera binning. **Figure 2.2(a-b)** are 682x682 pixels and each pixel is 3x65 nm in size.

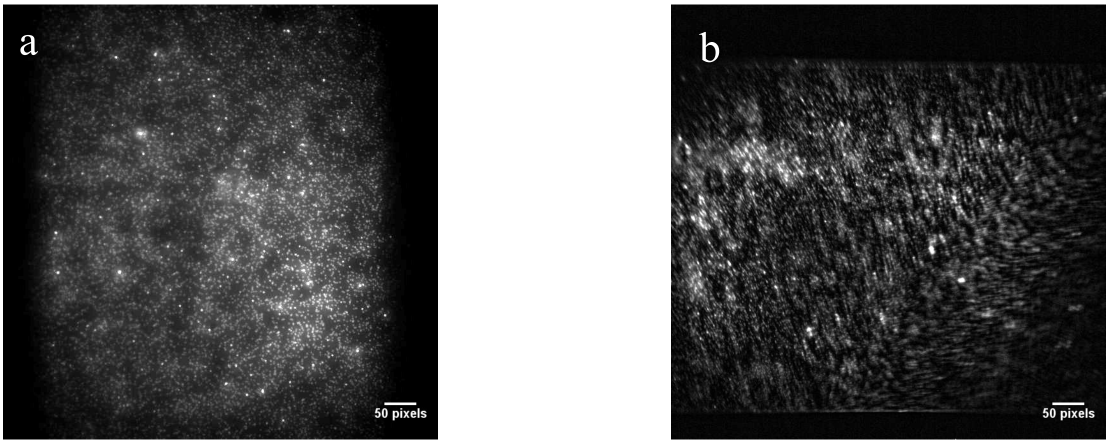

Fig. 2. 2.. Beads image collection in Cairnfocal Generation I conjugate camera. (a), Widefield image of beads with camera on the back port of the microscope. **(b),** Widefield image of beads with camera on Cairnfocal Generation I conjugate pathway.

A temporary solution and a long-term solution were planned for this issue. The temporary solution was to collect the emission light using a camera at the back port of the microscope and develop a digital pinholing confocal system. The results pertaining to this were discussed in Section 2.3. The long term solution for this issue was to upgrade the Cairnfocal Generation I to the next generation DMD based illumination and detection system. Correcting the orientation of fold mirrors which were causing the tilt in the image plane was corrected in Cairnfocal Generation II. Generation II DMD based illumination system began to be used from October 2016.

2.3. Development of digital pinholing confocal microscopy

The temporary solution to bypass the issues caused by fold mirrors was either to image only the middle area on the camera in which the projected confocal points were not blurred, or moving the camera to the back port of the microscope. Using a short pass dichroic filter before the objective, it was possible to illuminate the sample with light from the DMD and collect the light from the sample on the back port of the microscope, i.e. negating the return path via the DMD. It was more useful to have the camera on the back of the microscope which initiated the developments of the digital pin holing confocal microscope discussed in this section and the *E. coli* selection system discussed in Chapter 4.

A Nikon Ti-E inverted microscope was used as the base for the system. In the digital pin holing confocal microscopy setup, various multifocal spots were projected on to the sample by using the DMD for patterned illumination. The illumination system focuses the DMD image at the external focal plane of the microscope. Images projected at this plane are then relayed to the sample via the objective lens which de-magnifies the image by the combination of tube lens and the microscope’s objective lens. Fluorescent light coming from the sample was collected on the camera at the back port of the microscope followed by post processing of the acquired data to subtract the out-of-focus light. Post processing for digital pinholing requires precise mapping of each DMD pixel to its corresponding camera pixel in the camera. This calibration allows us to go to each camera spot and map it back to calculate which DMD pixel was ON to illuminate that camera spot.

2.3.1. Calibration for digital pinholing

For calibration, the DMD can be back illuminated through the microscope or a flat fluorescent sample can be used instead. Fluorescein dye was embedded on a thin layer of polymer to get a homogeneously thin fluorescent sample. Fluorescein was dissolved in 1:1 water and ethanol solution, mixed with Polydimethylsiloxane (PDMS) and spin coated on a wilko dish. This sample was used for testing and calibration

For digital pinholing calibration, the flat fluorescently labelled sample was illuminated through the ON pathway of the DMD system. Fluorescence emission from the sample was collected with a camera at the back port of the microscope. A 100x/1.45 NA TIRF oil objective was used. Initially, for calibration, two coefficients A and B were calculated which correspond to translation, rotation and scaling using three reference DMD and camera points. These three reference camera and DMD points were obtained by turning on three random DMD pixels and projecting these three spots on to the sample followed by acquiring a camera frame. From this camera frame and the known DMD pixels which were projected, three known camera pixels with its corresponding DMD pixels were found to fit a 2-D linear curve. This linear equation was generated to map any DMD pixel to its corresponding camera pixel.

It was observed that there was a distortion factor which moves the expected illumination spot from the actual illumination spot. It was also observed that the expected spot was close to actual spot at the three reference points taken for fitting the equation. To overcome this, one DMD frame was divided into 25 squares. Coefficients A and B were found for each square separately. This reduced the shift of actual spot from expected spot. Even in this case, the shift was higher than a diffraction limited spot and thus this distortion could not be ignored. Next step in this particular method of calibration would be to incorporate another coefficient C which corresponds to the distortion factor of the system. Deviation needs to be reduced to as low as possible to get a perfect calibration.

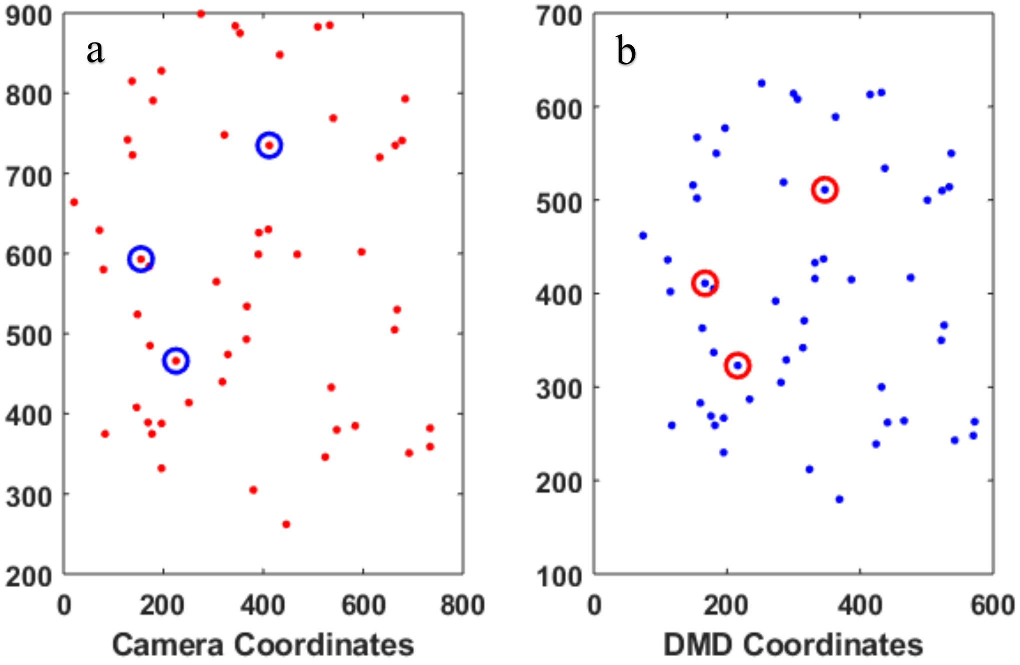

Fig. 2. 3. Calibration plot of DMD and camera coordinates. (a), 100 random pixels in camera coordinates marked in red dots, selected three points highlighted with blue circles. **(b),** 100 random pixels in DMD coordinates marked in red dots, selected three points highlighted with red circles.

Instead of finding C, an easier and more accurate method of calibration was found. 100 random DMD points were projected on to the sample and the corresponding camera points were taken as reference and these points were fitted to a polynomial. Thus, any camera pixel can be conveniently mapped to its corresponding DMD pixel. The expected point in the calibration method showed only a maximum of 4 - 5 camera pixels off from the actual spot which were manually corrected by changing the coefficients of the polynomial. A 2.5x magnifier in between the Cairnfocal system and the microscope could further reduce this deviation to less than three camera pixels. This is because, with a magnifier in the setup, light passes through the centre of the objective lens reducing spherical aberration effect by the objective. **Figure 2.3(a-b)** shows the 100 random points plotted in DMD plane and camera plane.

2.3.2. Post processing for digital pinholing

In Section 2.7, when the DMD was used for detection of emission light, out-of-focus light was rejected by physical pinholing at the DMD. In the setup in which emission light was collected with camera on the back of the microscope, out-of-focus light does not go through the system or the DMD for out-of-focus light rejection. There was a need for digital pinholing during post processing of camera frames to reject the out-of-focus light and to obtain confocal images of the sample.

Post-processing of images for digitally pinholed confocal microscopy was tried using different reconstruction methods to get the best possible final image. The reconstruction method employed in this technique highly depends on the emitted fluorescence intensity of the sample. For each DMD pixel in the square grid of the multifocal illumination pattern, its corresponding camera spot was calibrated using the above calibration method. After finding the expected camera spots, a square selection area around each spot was cut for all the illumination spots in every frame and was saved separately in such a way that each selection area had its expected camera spot in the centre. Cut width for these selection areas are chosen in such a way that intensities associated with only one illumination spot were covered in the selection area as represented in the black square in **figure 2.16.**

2.3.2.1. Gaussian Filtering

Optionally, before recording intensities from selection area, each spot can be multiplied with a Gaussian mask of standard deviation 2 which determines the sectioning strength of the confocal image [Chakrova *et al.*, 2015, A.York et al, 2012]. Gaussian filtering all the frames with standard deviation 20 and subtracting it from frames of Gaussian filtering with standard deviation 2 can considerably reduce background of the image.

2.3.2.2. Reconstruction

Method 1. The first method for reconstruction was to record the intensity at the expected spot position and allot this intensity to the corresponding DMD pixel. A zero matrix of size equal to the size of DMD chip (1,024x768 pixels) was made to allot the recorded intensities. When this process is repeated for all the spots in all the frames, a digitally pinholed reconstructed confocal image was obtained.

Method 2. Since the calibration used for mapping DMD and camera pixels for digital pinholing does not include the secondary calibration (implemented in physical pinholing post processing) as described in Section 2.7, for some spots, the calibrated camera spot may not exactly coincide with the maximum/centre intensity of the actual camera spot and might be 3-5 pixels off. In this case, recording the exact intensity at the expected calibrated spot might give error in the final reconstruction. The second method is recording the maximum intensity or average intensity of each selection area and allotting that value to the corresponding DMD pixel for reconstruction. Each selection area can be optionally multiplied by a Gaussian mask which can determine the pinholing mask.

Method 3. In some samples with low fluorescence emission intensity, to get better contrast for reconstructed images, each cut section can be multiplied with a mask and all the intensities inside a selection area can be summed and allotted to the corresponding DMD pixel. This process is repeated for all selection areas in all the frames to obtain a digitally pinholed reconstructed confocal image.

2.3.3. Digital pinholing confocal microscopy in bead samples

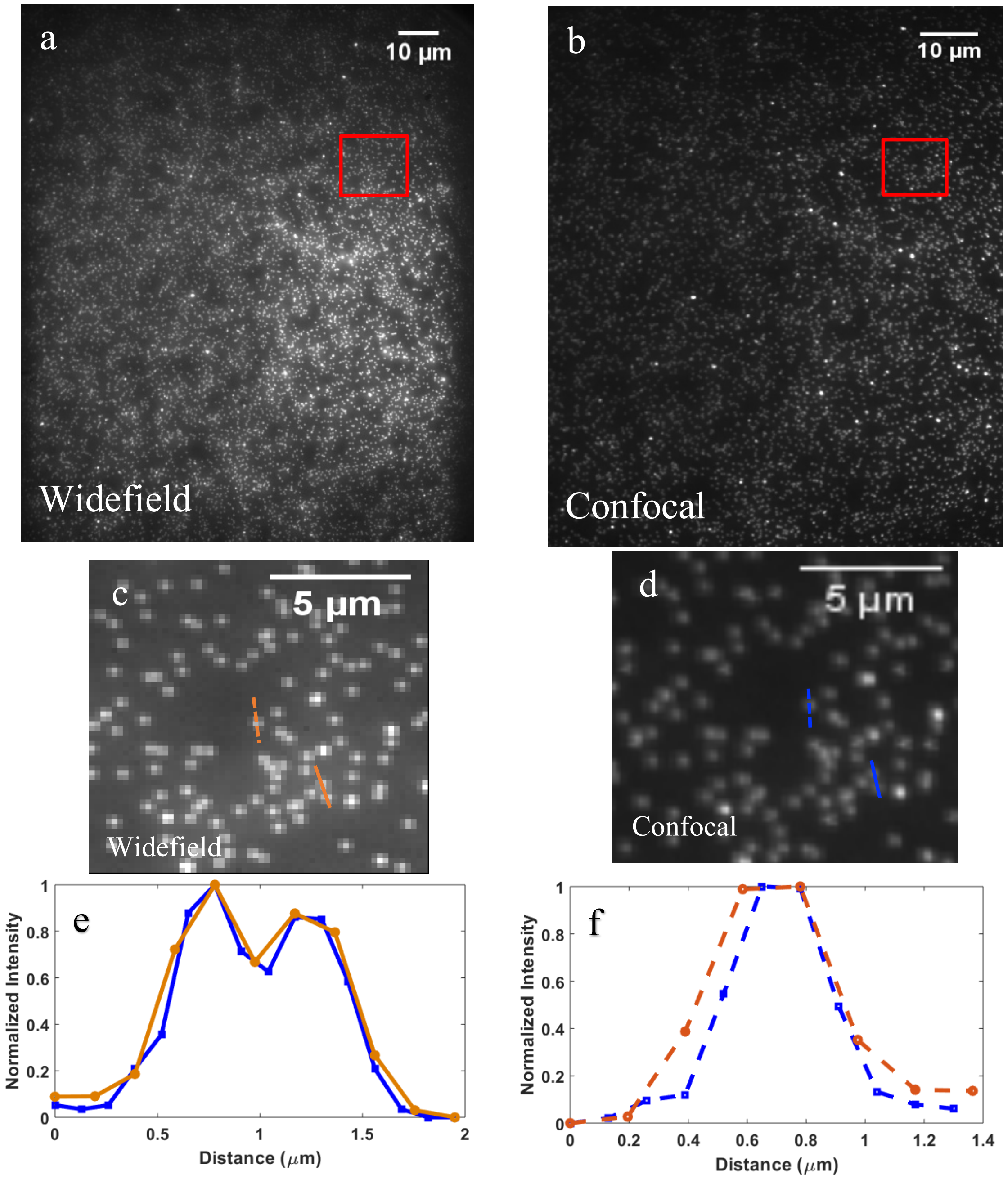

Fig. 2. 4. Imaging 200 nm beads with digital pin holing confocal microscopy. (a), Widefield image of 200 nm beads. **(b)**, Digitally pinholed confocal image of 200 nm beads. Both images are formed in the camera at the back port of the microscope. **(c)**, Zoomed-in area of widefield image marked with red square. **(d)**, Zoomed-in area of confocal image marked with red square. **(e)** Line profile plot of 200 nm beads widefield and confocal images through the solid line in **figure (c-d)**. **(f)**, line profile plot of 200 nm beads widefield and confocal images through the dotted line in **figure (c-d)**. FWHM of widefield is 500 nm and FWHM of confocal is 400 nm.

Digitally pinholed confocal image of 200 nm beads with illumination at 505 nm and emission at 515 nm. A widefield image of the same sample area was also acquired. A 470 nm LED is used with 470/40 filter for illumination and 525/50 filter for excitation. The confocal image in **figure 2.4(b)** has 1,024x768 pixels, the same size as a DMD chip and each pixel in a DMD chip is 13.6 µm in size.

In this experiment, a 1x1 pinhole was used with 20x1 DMD pixels gap between each pinhole to have minimum cross talk between adjacent illumination spots. A total number of 20x20=400 frames were recorded in the camera of pixel size 65 nm with 3x3 camera binning at 40 msec exposure time. Syncing of DMD frames with camera frames for this experiment was done using NI 6341-USB DAQ. Details of syncing DMD frames with camera frames and triggering modes are given in Section 2.6. With this exposure time, it takes 16 seconds to completely scan through one DMD frame and to render a confocal image.

Figure 2.4(a) is a widefield image taken at 3x3 camera binning and one camera pixel is 3x65=195 nm. **Figure 2.4(b)** is a reconstructed confocal image. **Figures 2.4(c)** and **2.4(d)** are zoomed-in area of **figure 2.4(a)** and **2.4(b)** respectively. There is an improvement in signal-to-noise ratio for confocal image which results from the rejection of out-of-focus noise during the post processing. When comparing the line profile plot of confocal image and widefield image in **figure 2.4(f)**, we can observe a slight improvement in resolution. Two adjacent beads can be distinguished slightly better in the digitally pinholed confocal image **(figure 2.4e)** but the distinction is not substantial. Out-of-focus emission light changes throughout the sample due to the high inhomogeneity of the samples, especially when imaging biological samples. Digital pinholing generally does not take this into account when masking or when subtracting the emission spot with a Gaussian mask of constant standard deviation. Discussion of this is given in Chapter 3.

2.3.4. Digital pinholing confocal microscopy in *E. coli* sample

Widefield, phase and confocal images of *E. coli* bacteria expressing GFP and embedded in agarose containing growth medium were acquired. For this experiment, a 3x3 pinhole was used with 20x3 DMD pixels gap between each pinhole to have minimum cross talk between adjacent illumination spots. A total number of 20x20=400 frames were recorded with 3x3 camera binning. To increase power with which sample is excited, a 2.5x magnifier was attached between the system and the microscope. This reduced the effective area of illumination in the sample. Without the magnifier and with a 100x objective, each DMD pixel illuminates 136 nm x 136 nm area in the sample. With the magnifier the same amount of power was used to illuminate (136/2.5) 54.4 nm x 54.4 nm which is a much smaller area. Diffraction limited spot (or the actual illumination spot in the sample plane) for a 100x /1.45 NA TIRF oil objective with 470 nm illumination will be 162 nm. 1x1 pixels on for confocal pinholes without magnifier come under a diffraction limited spot. With a magnifier, 2x2 and 3x3 pinhole also comes under a diffraction limited spot which means even more power on one illumination spot.

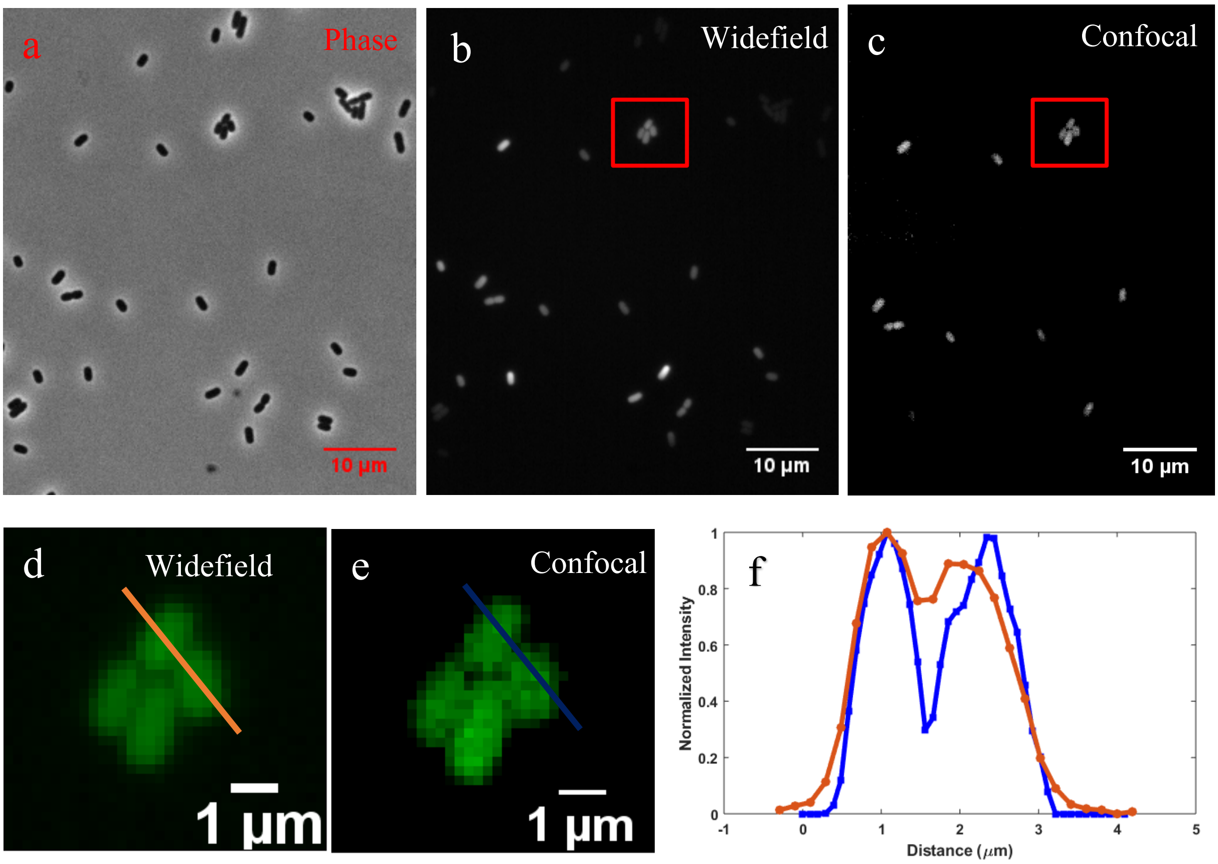

Fig. 2. 5. *E. coli* cells imaged with digital pinholing confocal microscope. (a) Phase image of *E. coli*. **(b)** Widefield image. **(c)** Confocal image. **(d)** Zooming in area of interest in a widefield image, **(e)** Zooming in area of interest in a confocal image, **(f)** Line profile plot through widefield and confocal shows a slight improvement in resolution in the confocal image.

Figure 2.5(a-c) shows *E. coli* cells imaged using phase, widefield and digitally pinholed confocal microscopic imaging techniques. **Figure 2.5(d)** and **2.5(e)** show zoomed-in images of selected area from **figure 2.5(b)** and **2.5(c)** respectively. The line profile shows a slight improvement in resolution of adjacent *E. coli* cells as shown in **figure 2.5(f)**.

2.3.5. Conclusion

This part of the work was done during the visiting graduate studentship in the University of California, San Diego (UCSD). The issues with collection optics in Cairnfocal Generation I led to the development of digital pinholing confocal microscopy in which illumination spots were projected by the DMD and emission spots were collected using a camera at the backport of the microscope. Although this was useful for a short term to develop the software for projection and simple reconstruction codes, final images did not have substantial resolution improvements.

2.4. Cairnfocal Generation II

Cairnfocal Generation II was employed for most of the work in this thesis. Various microscopic techniques were built into the system and various biological systems were studied as detailed in the next chapters. This section includes the general instrumentation, software developments, laser relay setup, Z-stage controls, DMD-camera calibration and BCCM development.

In Cairnfocal Generation II setup, when the sample is illuminated by patterned illumination from the DMD, fluorescence light from the sample collected by the objective lens was directed back along the conjugate path (illumination path), or the non-conjugate path using the DMD and collected with one of the cameras. Light from the ‘ON’ and ‘OFF’ paths was collected by two Andor Zyla CMOS cameras, one on each path. Here it is worth noting that the fluorescence from sample, because of light projected using the ‘ON’ path, will be imaged using the ‘ON’ camera. ‘OFF’ pixels direct fluorescence light towards the ‘OFF’ camera in such a way that the ‘ON’ camera will only contain fluorescence from the ‘ON’ pattern projected on to the sample.

Collection of in-focus and out-of-focus light in two cameras are shown in the schematic diagram in **figure 2.6.** When the illumination patterned light falls on the sample after reflection from the DMD, the fluorescence emission light from the ‘in-focus’ plane of the sample follows the illumination path and forms a conjugate image (Ic). The emission light which is reflected off from the OFF pixels of DMD micro mirrors forms a nonconjugate image (Inc). Interestingly, light from ‘out-off-focus’ planes are reflected off by ON and OFF pixels to contribute to both Ic and Inc (primarily Inc) while light from in-focus plane contributes only to

Ic. In this work, the collection of out-of-focus light in ON camera is termed as ‘blead through’ intensity which is detailed in the next sections.

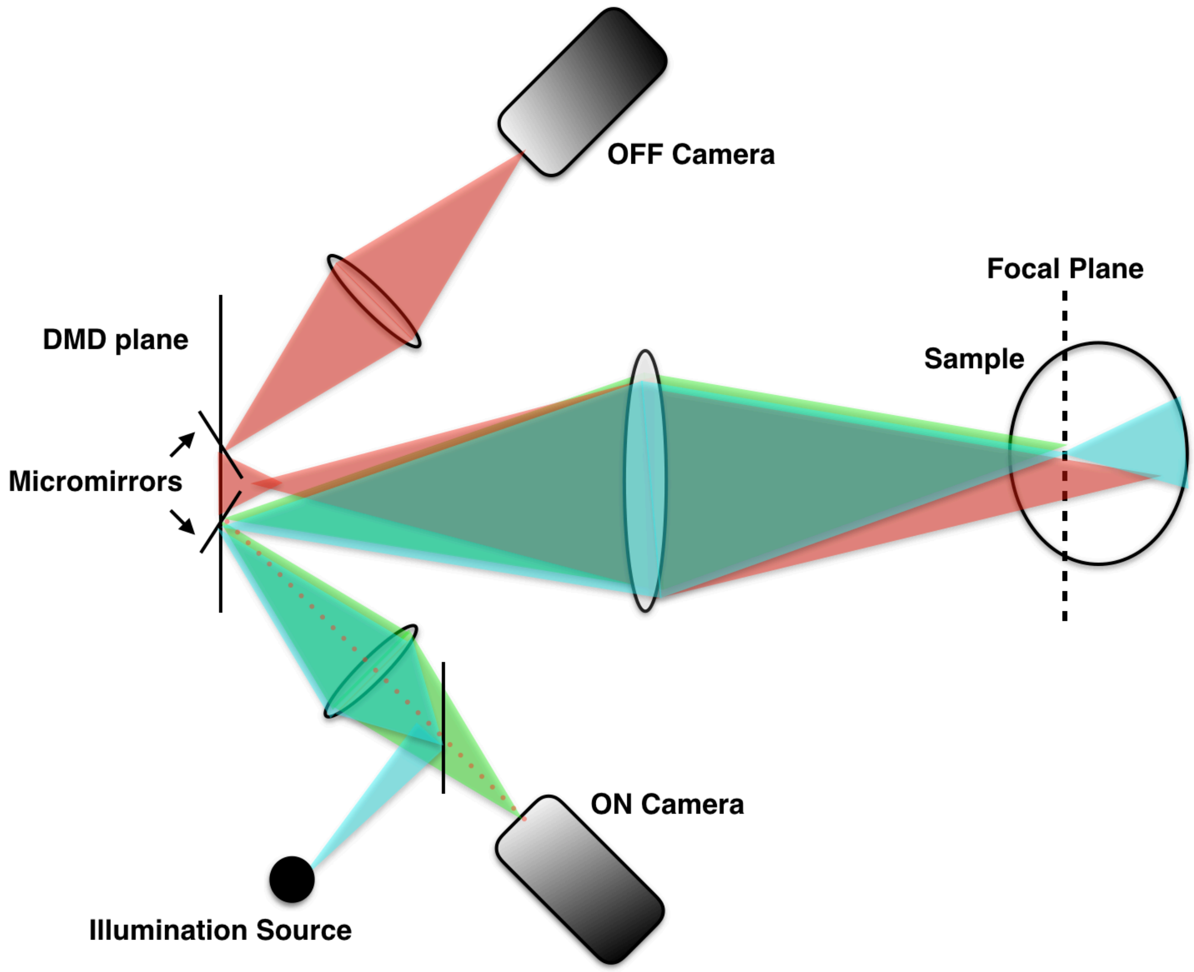

Fig. 2. 6. Schematic diagram at in-focus and out-of-focus data collection with two cameras. Diagram shows the collection of in-focus and out-of-focus light in two separate cameras. Light from in-focus plane is collected only in the ON camera. Light from out-of-focus planes is collected in OFF camera primarily, but are also collected in the ON camera.

2.4.1. Digital Micromirror Device

The system is based on Digital Light Processing (DLP) which can be used to generate patterns of illumination on the sample. At the heart of DLP technology is the DMD. A DMD chip has on its surface several hundred thousand microscopic mirrors which can be turned on and off allowing light to be sent to the sample plane of the microscope to control the power and pattern of illumination pixel by pixel. Texas Instruments DLP7000 chipset with FPGA controller and SDK was purchased from Vialux [Vialux, Germany].

The DMD is a bi-stable device with around eight million micromirrors mounted on a CMOS memory cell arranged in 768 rows and 1,024 columns. Apart from binary (ON/OFF) images, DMD can also project down grey scale images by flipping between the two stable mirror positions at pulse width modulation of around 23 kHz with 8 bit precision giving an effective frame rate of 290 Hz, enabling precise control over the power with which sample is illuminated.

A DMD device consists of an array of mirrors which can be switched between two states. In the DMD used in this work, one state sets a mirror at +12° to the normal axis of the DMD chip and the other state sets the mirror to −12° to the normal. This allows light incident on a mirror to be reflected at either +12° or −12°. For this work we defined the +12° state as being ‘ON’ and the −12° state as being the ‘OFF’ state.

2.4.2. Optical setup

All optics were fixed in a 195 cm x 120 cm x 80 cm optical table (Thor Labs) to minimize mechanical vibrations. Nikon Eclipse Ti microscope base held all the objectives including, Nikon 100x Apo SR TIRF oil and 60x Apo VC 1.2 NA water objectives. A Z-stage piezo (Prior Nano Scan Z) was used to move along the axial direction of sample. The DMD system was relayed to the side port of the microscope. An Andor iXon EMCCD/Photometrics 95B camera was attached to the backport of the microscope which can be used to collect data without physical pinholing or the emission optical pathway passing through the DMD. The two filter cube holders in the microscope were kept empty when imaged using the ‘ON’ / ‘OFF’ cameras or an appropriate dichroic mirror or beam splitter can be used to image with the camera at the back port of the microscope. Obis coherent 488 laser, coherent sapphire 561 and Necsel multi-colour RGB NovaLum 1200 lasers were relayed to one illumination path and LED light source (Cairn OptoLED) was attached to the second illumination path which allows easy swapping between laser and LED illumination. Two illuminators can be used simultaneously in the two independent pathways of the setup.

Illumination light after passing through excitation filter and dichroic filter, passes through a relay optics consisting of a convex mirror (focal length = -100 mm, AR coating between 425 nm to 875 nm), and a concave mirror (focal length = +250 mm, AR coating between 425 nm to 875 nm). Two fold mirrors were incorporated between the concave mirror and the DMD in order to make the system more compact, and all mirror profiles were within L/4 per 25mm. For illumination, light was introduced into the infinity space prior to the convex mirror, but offset from the Schwarzschild optical axis by a distance so as to arrive at the DMD at an angle of 24 degrees. Light falling on pixels tilted by 12 degrees in this same direction was thereby orthogonally reflected and relayed to the microscope objective. For confocal detection, light from the microscope followed the reverse pathway through the Schwarzschild mirrors and was then focussed to form the camera image by conventional lens optics. Imaging light falling on the 'OFF' pixels of the DMD was similarly collected and sent to a second camera by the other Schwarzschild mirror pair. The refocussing lenses were similarly offset from their Schwarzschild optical axes, so as to form standard orthogonally focussed images at the camera, at or close to diffraction-limited quality [M. Thomas, patent, 2017], rather than the 24 degree tilted focus produced by previous DMD-based confocal systems, and which has discouraged their more general use.

The second plane fold mirror which reflects illumination light to the DMD and collects emission light from the DMD, is aligned at +24/- 24 degrees for ON and OFF optical pathways respectively. The +12/-12 degree orientation of micromirrors define the DMD patterns.

A custom made MATLAB [Matlab, Mathworks] GUI was used to generate and load the desired patterns to the FPGA memory of the DMD. For confocal imaging, multifocal patterns were generated instead of single illumination spots to increase the speed of imaging. For widefield or STORM imaging, a uniform illumination pattern was used. Codes for projecting various patterns using DMD and codes to build all the patterns used in this work in the format which are ready to be loaded on to the DMD are available in Appendix 1 and 3 respectively. Light from the illumination pathways forms a pattern at the DMD and is reflected along the optical axis perpendicular to the DMD face. Light from the DMD is collected and relayed to the side port of the microscope using two lenses (triplet lens with focal length 160 mm). There is a 1:1 magnification of the beam between DMD to microscope side port. The light beam is de-magnified using an objective (for most of the experiments in this work, a 100x oil TIRF objective was used) before illuminating the sample.

The emission light coming back from the sample was collected by the same objective. It passes through the two relay lenses and is projected on to the DMD. In confocal imaging, when multifocal patterns are projected, each DMD micromirror acts as a physical pinhole to direct the in-focus and out-of-focus light from the sample into two pathways in the system. Emission light from the in-focus plane of the microscope follows the same pathway as the illumination light and is reflected to the ON pathway, while out-of-focus light is reflected to OFF pathway and is collected in separate ON and OFF cameras respectively. Andor Zyla 4.2 sCMOS cameras which have a 6.5 µm pixel size were used for detection in the pathways. In the ON pathway, the illumination beam and emission beam were separated at the dichroic. The emission light passed through the dichroic is collected and focused to the camera sensor by a lens (triplet lens with focal length 160 mm) and a plane mirror. A detailed layout of optics is illustrated in **figure 2.7**.

2.4.3. Detailed Optical layout

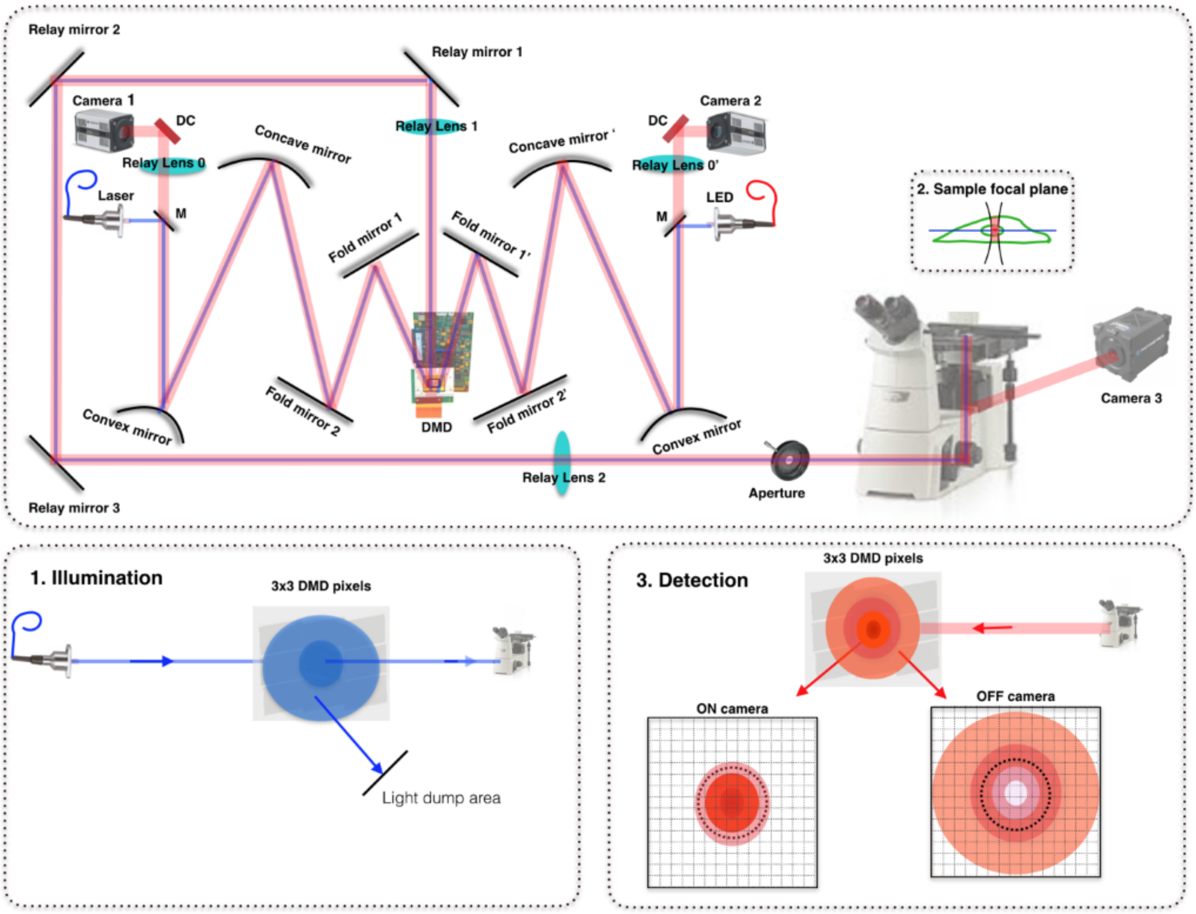

Fig. 2. 7. Detailed optical layout. Optical layout of the system showing the two illumination pathways. All the relay optics and cameras are mounted on the same optical bench as the microscope. Illumination pathway and emission pathway at the DMD is given separately in parts 1 and 3 of the figure. Inset of the figure shows the sample illumination.

As mentioned previously, there are two illumination pathways and two detection pathways in the system. Illumination light from one of the light sources, passes through an excitation filter and a dichroic filter (DC), hits a convex mirror of focal length -100 mm and is reflected to a concave mirror of focal length +250 mm before projecting on to the DMD. There are two fold mirrors on each pathway between the concave mirror and the DMD to make the system compact. When light is projected on to the DMD, ON pixels (at +12 degrees) reflect light to a projection lens and OFF pixels (at -12 degrees) reflect light to a dump area inside the system **(figure 2.7, part 2**). When the sample is illuminated **(figure 2.7, inset**), light from the sample passes through the system and the DMD micro-mirrors act as a physical pinhole. The major advantage of this system is that the in-focus and out-of-focus light returning from the sample can be collected separately in two separate cameras enabling the advanced post processing techniques with this data.

Emission light collected in ON and OFF cameras is shown in **figure 2.7, part 3**. In-focus light coming back from the sample follows an in-focus pathway (same path as the illumination light) and gets collected in an in-focus camera (camera 1). Out-of-focus light coming back from the sample follows an out-of-focus pathway and gets collected in an out-of-focus camera (camera 2) as described in the figure. The dotted circle marked in the emission light collected in ON and OFF camera **(figure 2.7, part 3**) is the virtual pinhole diameter, equivalent to a conventional aperture based physical pinhole confocal microscope. The system is more compact with a 3D arrangement while it is drawn as 2D for easy understanding of the optical setup. The number of optical elements is accurate but the angle, orientation and relative spacing between the optics are changed to emphasise the simplicity of the instrumentation.

2.4.4. Ray diagram of the light path in the optical setup

Figure 2.8 illustrates the ray diagram of the optical path in the setup. Light from the illumination source hits a convex mirror of focal length -100 mm and reflects to a concave mirror at an angle 39.4° with respect to the incident ray to hit the concave mirror of focal length +250 mm. Centres of curvature of the two mirrors coincide and are placed at 165 mm from the DMD. Light is reflected from the concave mirror at an angle of 7.7° with respect to the optical axis and hits the DMD. Micro-mirrors which are turned at an angle 12° with respect to the optical axis towards the light path from the concave mirror reflect the light from concave mirror hitting the DMD at 24° along the axis perpendicular to the DMD chip is relayed on to the side port of the microscope.

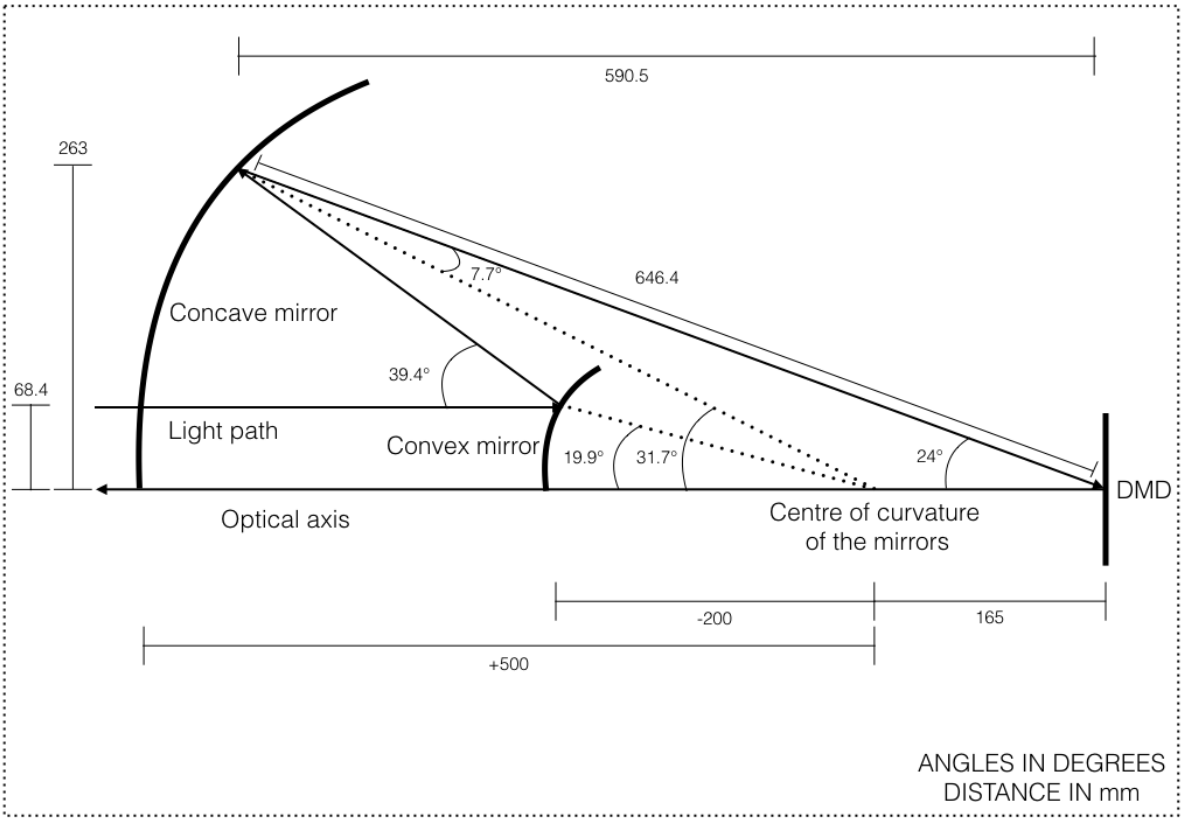

Fig. 2. 8. Ray diagram of light path in the optical setup. This ray diagram shows the light path hitting the convex mirror, concave mirror and reflected towards the DMD. Patterned light from the DMD forms an image at the image plane of the microscope.

2.4.5. Lasers and LEDs

In the optical setup, a laser illumination was setup in the ON pathway and an LED illumination was setup in the OFF pathway. To project maximum laser power on to the sample, the laser beam in the ON pathway is focused on to a small portion in the centre of the DMD (about 1/6th of the active area of the DMD). Lasers used are Necsel multi-colur RGB NovaLum 1200, Obis 488 laser and coherent sapphire 561. OptoLED light source from Cairn Research is used for 488 nm, 505 nm, 647 nm and white LEDs. Thor labs laser pointer was used for alignment. Simple optics arrangement was employed to relay the 488 and 561 lasers through a fibre and launched into the 'ON' pathway of the system. This optical arrangement is given in **figure 2.9**. There is 55-60% power loss inside the Cairnfocal system. This is calculated by measuring the power of the laser before going into the Cairnfocal (at the optical fiber) and after it goes through the system with all DMD pixels ON. This loss is primarily because the higher diffraction orders of light diffracted by DMD micromirrors are not collected with the lens placed in front of the DMD [Texas Instruments, 2008, Chen *et al.*, 2012].

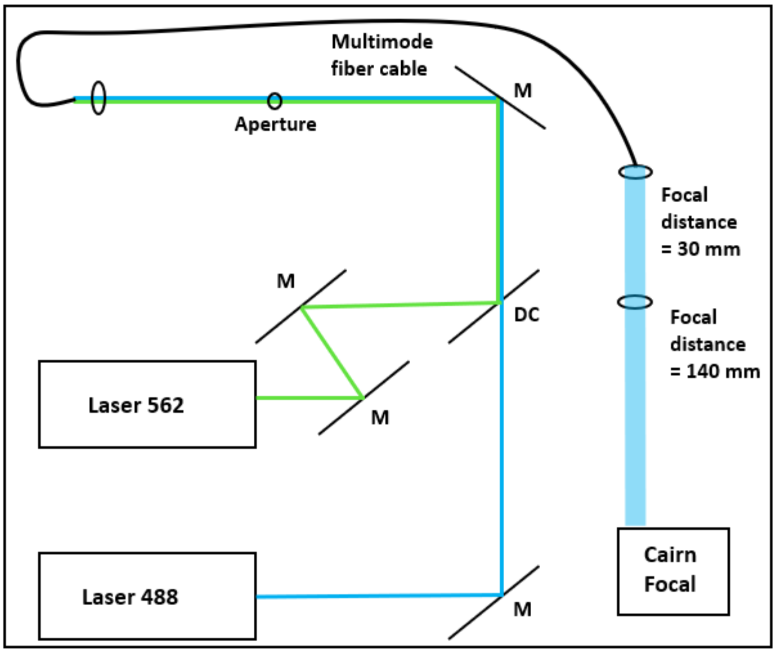

Fig. 2. 9. Optical arrangement for laser illumination. 488 laser and 562 laser relayed through a fiber to the Cairnfocal laser pathway.

2.4.6. Alignment of optics

General outline for the alignment of the optics is given below,

1. The Cairnfocal and the microscope should be secured independently to a common optical table for precise alignments.
2. Back illuminate the system through the microscope.
3. There is an aperture between the microscope and the Cairnfocal. Close the aperture half way.
4. Adjust the two lenses between the DMD and the microscope to produce a sharp image of the aperture on the DMD.
5. Aperture image at the DMD is positioned in the centre by adjusting the three mirrors between the two relay lenses.
6. Project a square pattern on to the DMD. Turn on the laser. Turn on both the ON and the OFF cameras. A flat fluorescent sample was used for alignment or the system can be back illuminated through the microscope to perform the following steps.

7. Position of the camera can be adjusted by rotating the camera and moving the camera vertically. Rotate the camera and fix its position in such a way that the edge of the DMD plane is parallel to the edge of the camera plane. Move the position of the camera vertically to focus the image of the square pattern projected in the DMD, imaged in the camera.
8. Align the optical path between the DMD and cameras by adjusting the concave, convex and the two plane mirrors. The two conjugate and non-conjugate pathways need to be aligned independently. There are coarse and fine adjustments for these mirrors. For coarse adjustments, fix the mirrors to the vertical support. Their correct position can be identified with the help of the camera image. Fix the coarse position of the mirrors in such a way that the image of the square pattern is in-focus at the camera.
9. For fine adjustments, there are three springloaded screws in each mirror. For fine adjustments, it is better to project a multifocal pattern with single spot size equal to one DMD pixel. Springloaded screws in each mirror need be to adjusted in such a way that the multifocal spots are focused without any astigmatism.
10. During the coarse and fine adjustments of the mirrors, illumination light should hit all the mirrors at the centre and also hit the DMD at the centre.

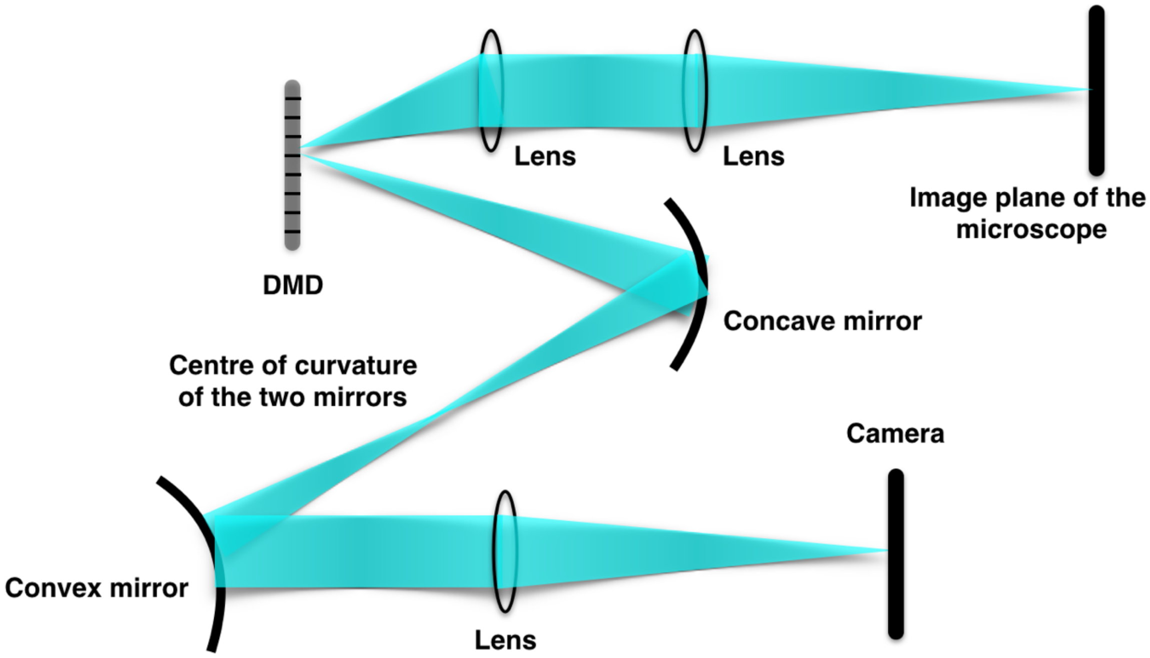

Fig. 2. 10. Optical pathway showing real planes and Fourier planes of the system. 3D arrangement of the setup is drawn in 2D for easy representation. Angles and distances are given in **figure 2.8**.

Figure 2.10 represents the optical pathway showing real planes and Fourier planes of the system. Light path where the rays focus are real planes and regions where light path is parallel are Fourier planes. Centre of the two mirrors coincides when the system is perfectly focussed. It is this condition which makes the alignment of the optics very difficult. The concave and convex mirrors together act as a single lens with effective focal length of 165 mm. There are two fold mirrors between the concave mirror and the DMD. They are not shown in this figure for the easy understanding of the optics. Angles and distances are given in **figure 2.8**.

Steps described above are a general structure which can be followed for alignment. It might require many trial and error methods during each alignment sessions to get perfect alignment. The system is perfectly aligned when the following conditions are achieved in both the optical pathways

1. A multifocal pattern with 1x1 DMD pixel pinhole size, is focused in the camera without astigmatism.
2. Light from the illumination source hits all the mirrors, lenses and the DMD at the centre.

2.5. Software development

Custom application GUI is programmed in MATLAB using Accessory Light Modulator Package SDK (ALP-4). The basic step-by-step operation of this code includes, initializing the device, allocating a sequence of images, defining the display mode and timing of the sequence, loading the sequence into the onboard memory, displaying the sequence, stopping the display of the sequence, freeing the sequence from memory and then freeing the device as shown in **figure 2.11**.

Using this GUI, data can be simultaneously loaded on to the memory, while DMD is displaying a different sequence. The GUI allows us to conveniently and seamlessly swap between two preloaded sequences in binary format or MSB format. For each sequence, there are two projection modes. Single projection in which the projection stops after projecting the last frame and continuous projection which continuously projects the sequence until stopped. When a sequence is stopped while running in continuous projection, it completes the projection of all the frames in that sequence before stopping. It does not stop projection in a middle frame of the sequence which makes rapid confocal imaging very efficient as detailed in Chapters 2 and 6.

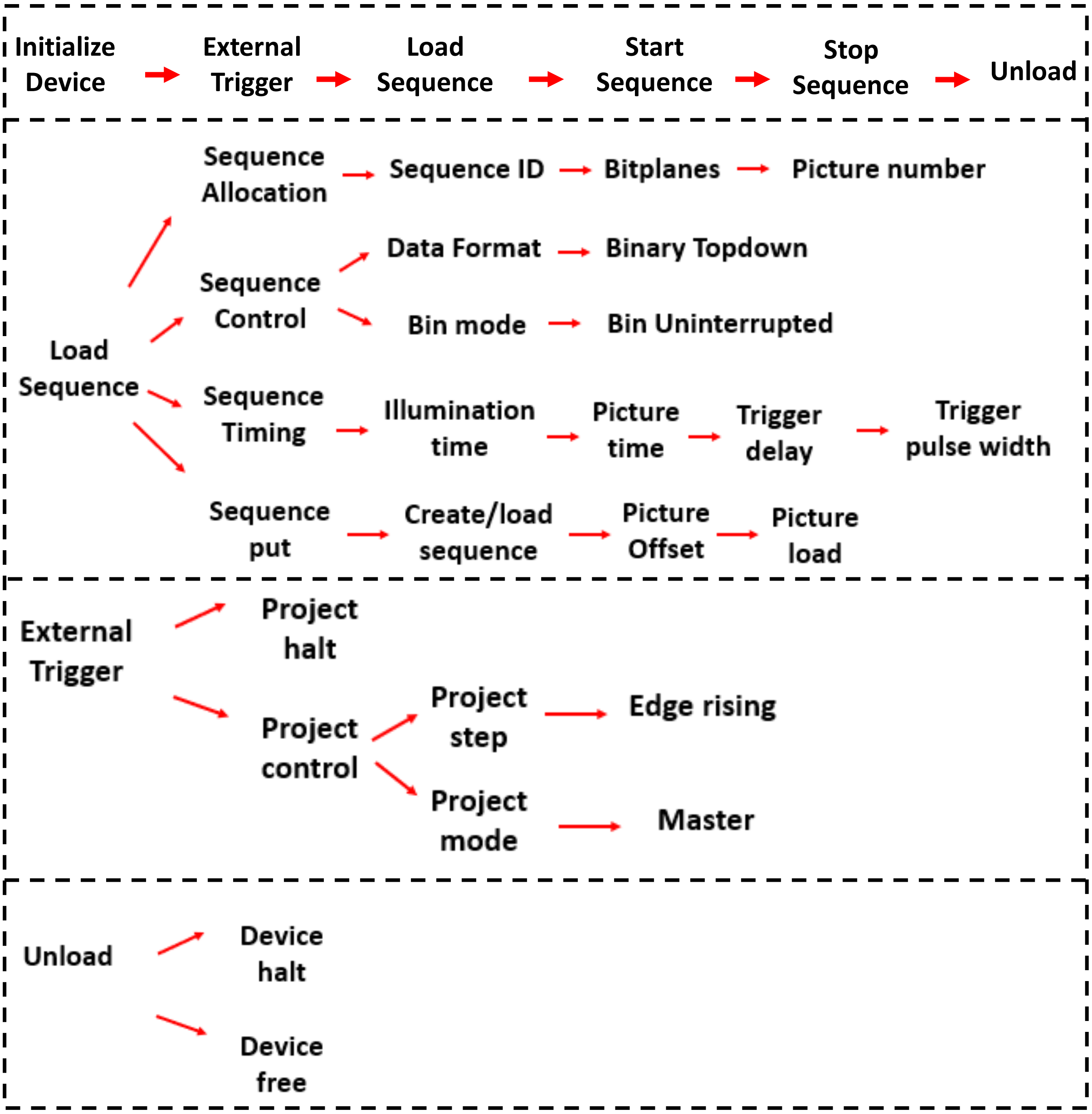

Fig. 2. 11. Flowchart for DMD projection software development. Main sections for the software include initialisation of the device, external trigger, loading sequence, starting sequence, stopping sequence and unloading the device.

The GUI has an ‘External Trigger’ button which can be used when the user wants the frame transition to be triggered externally. The user can select between two projection modes: slave mode and master mode, which decide whether the frame display is triggered by external or internal timings respectively. This is described in the API description provided by Vialux company. We found that DMD can be triggered externally with both slave and master mode settings. But slave mode waits for the first trigger to project the first DMD frame from the loaded sequence, while master mode projects the first frame on to the DMD and waits for the first external trigger to change to the second frame. For example, when external triggering mode is set to master mode and when 'Start Seq' button is pressed, the DMD displays the first frame in a sequence and waits until an external trigger is detected at Multi-Purpose I/O connector TRIGGER_IN input (pin 7).

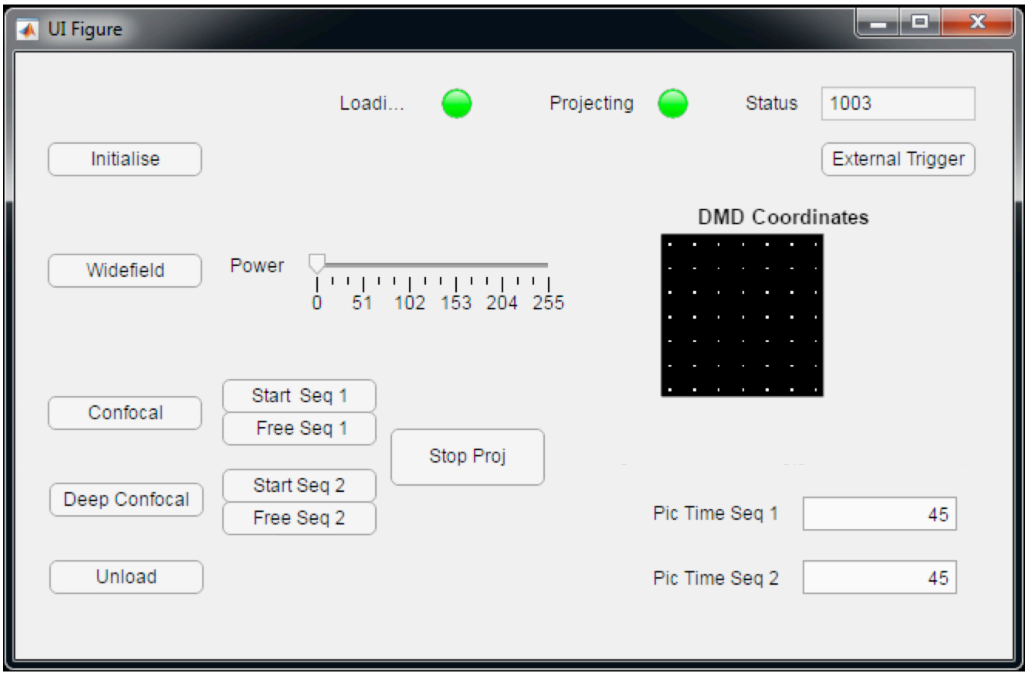

Status 1003

Pic Time Seq 1 45

Pic Time Seq 2 45

Fig. 2. 12. MATLAB GUI for controlling the DMD. Three patterns were loaded in this GUI. Widefield, and two confocal patterns. First confocal sequence was set in binary and second sequence was set in MSB format**.**

An example of a GUI created for reconfigurable confocal is given in **figure 2.12.** Reconfigurable confocal is described in Chapter 6. **Figure 2.12** has widefield and two confocal patterns which can be easily swapped between each other at sub millisecond transition. 'Initialise' button initialises the DMD and 'widefield' button projects a uniform MSB pattern. The power of this pattern can be controlled by changing the 'power' slider. The 'Confocal' button loads a 3x3 pinhole size, 3x5 inter pinhole distance confocal pattern on to the onboard memory of the DMD. 'Deep Confocal' loads a 3x3 pinhole size, 3x10 inter pinhole distance confocal pattern on to the onboard memory of the DMD. There are two buttons: 'Start Seq' and 'Free Seq', for each pattern to start projecting and to free the sequence from the memory respectively. 'Stop Proj' stops the projection of the sequence displaying. It is to be noted that when 'Stop Proj' command is given, DMD stops the projection of the sequence after completing the projection of all the frames in that sequence. 'DMD coordinates' display the pattern which is projecting. When ‘External Trigger’ button is clicked, DMD waits until an external trigger is detected before displaying each frame in a sequence. ‘Pic Time Seq’ is set to 45 μsec which is the smallest time for a binary sequence. This can be changed by giving the desired picture display time at the ‘Pic Time Seq’ section for each sequence.

2.5.1. Format of image loaded on to DMD

An image which is to be projected on to the DMD is made as a 1,024x768 ‘uint8’ array with numbers from 0 to 255 for MSB format or 768x128 ‘uint8’ array with number 0 or 1 for binary format. When loading images in binary format with bitplane depth one, the display is uninterrupted surpassing the dark time 44 μs which is the time required for flipping the mirror positions between two consecutive images. In binary format, a maximum of 87,380 images can be stored in the 64 Gbit onboard RAM and displayed at 22,727 Hz. For confocal imaging, external triggering is preferred so that the DMD frame transition is in sync with the camera frame rate. Although using MSB format is easier, binary format allows the user to have more control over the bitplane depth and is faster. Codes to make MSB and binary format sequences are given in Appendix 3.

2.6. Control scheme for Z-stage, ON Camera, OFF camera, DMD and laser illumination

To allow post processing with data from the two cameras, each DMD frame in a confocal sequence needs to be in perfect sync with the corresponding frame of the ON camera and OFF camera. NI DAQ is used to control and synchronize the image acquisition with a custom made LabView program.

Rapid confocal microscopy is configured to achieve the maximum speed by setting the DMD to trigger using an internal timer and is set to 44 msec per frame which is the minimum reset time for DMD micromirrors. The camera exposure time can be set depending on the sample brightness and desired signal-to-noise ratio of the image. To obtain a z-stack using the rapid confocal modality, the z-stage is controlled externally using a DAQ and the ON camera is run in internal/external exposure mode which is also triggered by the DAQ synchronized to the z-stage movement.

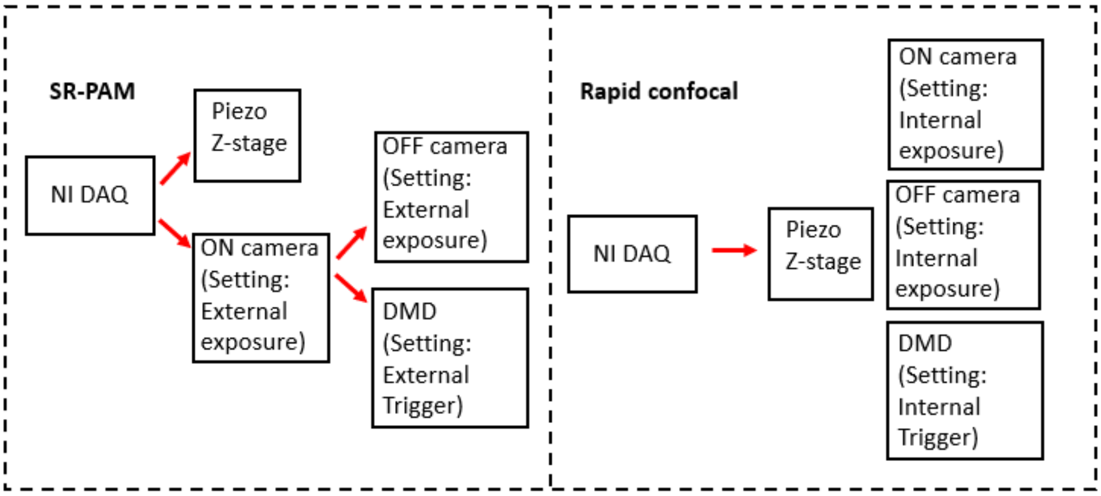

Fig. 2. 13. Frame change control scheme. Frame change control scheme for SR-BCM and rapid confocal.

In SR-BCM modality, the NIDAQ is used to trigger z-stage and the ON camera. The ON camera is then used to trigger the OFF camera and the DMD frame change. The DMD in this modality is run in external trigger mode. **Figure 2.13** describes the frame change control scheme for SR-BCM and rapid confocal. **Figure 2.14** describes the z-stage control scheme of image acquisition in rapid confocal and SR-BCM demonstrated as a voltage vs time graph.

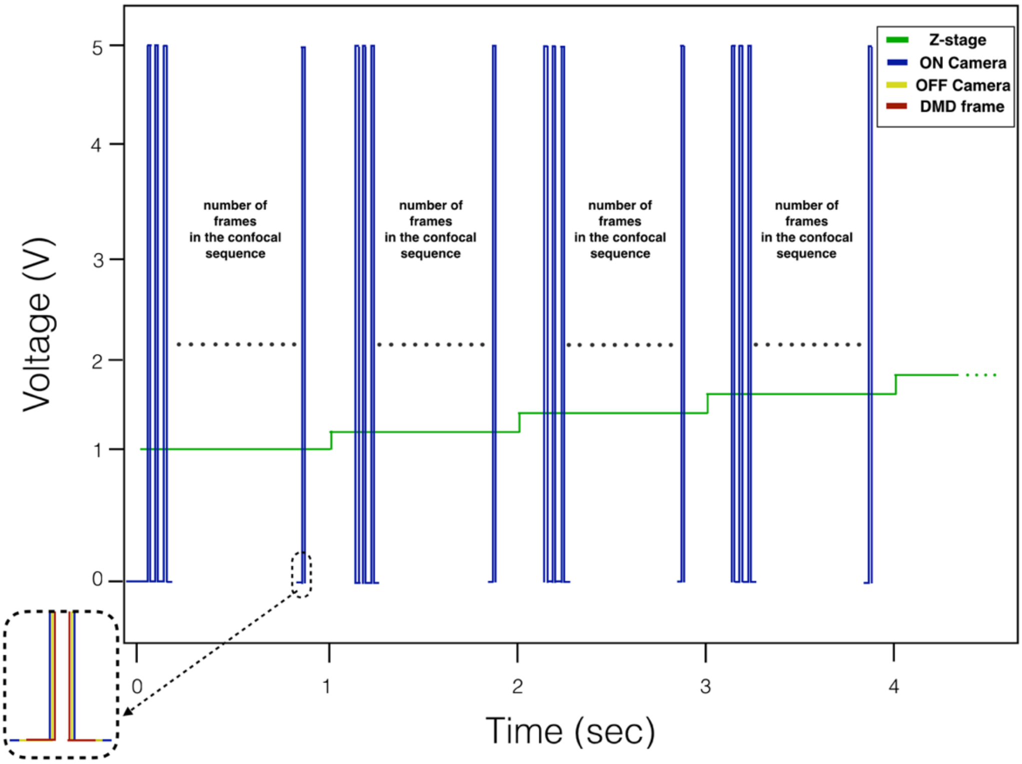

Fig. 2. 14. Z-stage control scheme for acquiring in-focus and out-of-focus data in ON and OFF cameras separately**.**

2.7. Calibration for physical pinholing confocal

There are many DMD and camera based techniques developed recently for many applications including optogenetics and particle tracking. They need a highly precise calibration of DMD pixels with the corresponding camera pixels. DMD-camera calibration code presented here can be adapted even for a non-confocal work which requires DMD and camera calibration and achieves a 130 nm precision reported in this work.

For physical pinholing, both cameras in ON and OFF pathways need to be calibrated with the DMD. Since there is around 55% intensity loss in the system, using flat fluorescent sample for calibration is not preferred. The best way to do calibration in this case is to back illuminate the DMD using a white bright LED light source through the microscope without the objective. Calibration for physical pinholing is done in two steps, primary calibration and secondary calibration.

2.7.1. Primary calibration

Post processing for physical pin holing confocal system involves subtraction of out-of-focus OFF camera data from in-focus ON camera data as described in BCCM Section 2.8. It requires precise mapping of each DMD pixel to its corresponding camera pixel in camera A and camera B. For taking calibration data, DMD can be back illuminated through the microscope with a bright light source without the objective in place. The following procedure is followed for primary calibration,

1. Primary calibration is done by collecting N(N=100, in most of the calibration experiments) frames of one random known DMD pixel ON per frame and corresponding image stack is collected in camera A and camera B.
2. The known DMD and camera points from the above data are used to find the translation vector to translate all the pixels in DMD plane to the corresponding pixels in camera plane.
3. To decrease the error of mapping, a rotation angle is added to the translation vector. Expected camera pixels calculated from the translation vector are rotated to find the

angle of rotation which gives minimum separation between expected and actual camera spots.

4. This angle of rotation which gives the minimum deviation of expected DMD spots from actual DMD spots is recorded and used to rotate all the expected DMD spots with this angle to give the new expected DMD spots.
5. These translation and rotation parameters are saved. These parameters are used to translate DMD coordinates to the camera coordinates in the reconstruction algorithms developed in this work.

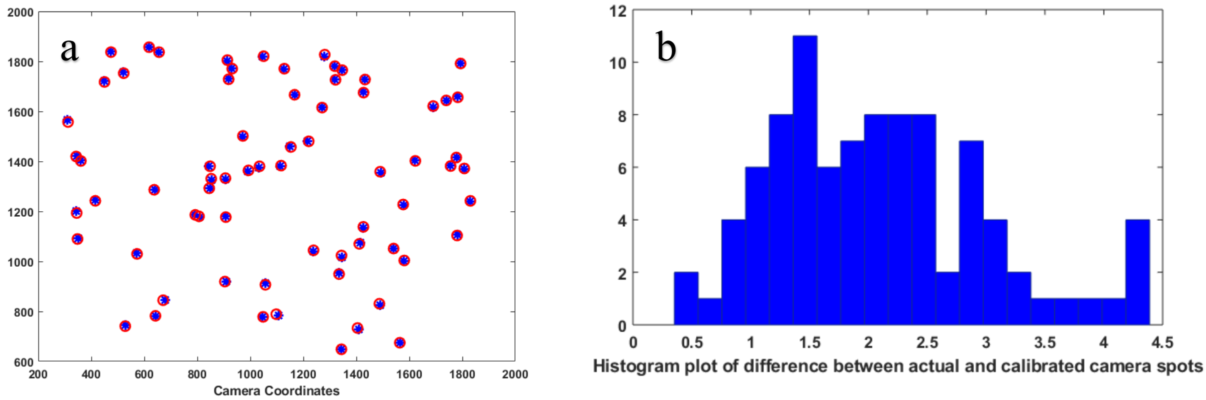

Fig. 2. 15. Primary calibration. (a) Plot of all 100 frames collected using the above method with one DMD pixel ON in each frame. Blue (*) and red (o) denote expected DMD points and actual DMD points respectively. Coordinates of the plot are the camera coordinates. **(b)** Histogram plot of difference between actual and calibrated camera spots. X axis is the camera coordinates and Y axis is the number of camera pixels.

2.7.2. Secondary calibration

Non-linear deviation of the expected DMD pixels in camera from the actual camera points and the requirement of the mapping precision to be less than a diffraction limited spot, calls for a secondary calibration. This is achieved by collecting 100 frames of 1x1 ON pixels with 10 pixels inter pinhole distance multifocal patterns scanned across the DMD. These data are collected for both camera A and camera B. For each DMD pixel in the known multifocal pattern, expected spot positions in camera are calibrated using the primary calibration method as described above. For each illumination spot in the camera, a square area is cut out around this expected camera spot in the multifocal camera data as shown in **figure 2.16**. The pixel corresponding to the maximum intensity in the cut out square area is saved as the exact camera spot when that particular DMD pixel is illuminated. These exact illumination spots are recorded and saved for all the 1,024x768 DMD pixels for both cameras separately. This gives a calibration precision with a maximum deviation of not more that two camera pixels in an Andor sCMOS zyla 4.2 camera which is equivalent to less than 130 nm in sample coordinate with a 100x objective. These are saved for further post processing applications as DMD lookup tables.

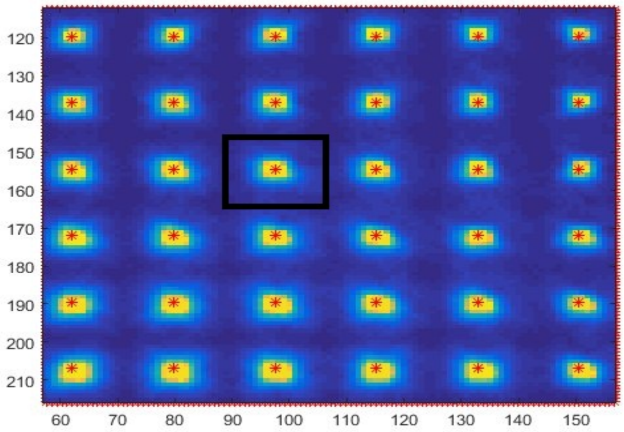

Fig. 2. 16. Second Calibration. Actual illumination spots are marked in yellow and expected illumination spots are marked in red asterisks. Image is in camera coordinates.

2.8. Background corrected confocal microscope

Confocal microscopy was implemented by physical pin holing using DMD micromirrors, to achieve superior background rejection mechanism. The Jovin group [Heintzmann *et al.*, 2001] elegantly built a dual PAM system to collect in-focus and out-of-focus light in separate cameras by using an SLM. PAM found applications in imaging techniques such as FRET and conventional confocal microscopy. In the paper [Heintzmann *et al.*, 2001], confocal imaging was shown using two different types of modulation patterns. Multifocal and pseudo random patterns were utilized. With multifocal excitation, data collected in the ON camera/conjugate camera are regarded as an analogue of a confocal image. Data collected in out-of-focus is a conventional image minus confocal image. With pseudo random pattern projection, data collected in conjugate camera are regarded as a conventional image plus confocal image. Data collected in non-conjugate camera are regarded as a conventional image minus confocal image. The paper also discusses the point that the conjugate camera has intensities collected from in-focus and out-of-focus planes of the sample, but the non-conjugate camera collects only the intensity from out-of-focus planes.

We employ multifocal excitation on to the DMD to collect conjugate and non-conjugate images on two different cameras. Instead of considering in-focus intensity collected in conjugate camera as a final confocal image, this work utilizes the intensity from out-of-focus plane to render a background corrected confocal microscope. This increases the signal-to-noise ratio of the image and slightly improves the resolution.

BCCM developed here can change between the pinhole size and inter pinhole distances conveniently by creating different patterns. Depending on the sample characteristics which determine the resolution required, speed of imaging and optical sectioning, various patterns can be employed. For thick samples, larger inter pinhole distances can reduce the collection of scattered light from out-of-focus planes to pass through the pinholes. Large inter pinhole distance can also reduce the cross talk between the pinholes for thick samples. As the inter pinhole distance increases, the optical sectioning ability of the microscope also increases. Smaller inter pinhole distance reduces the number of frames required for performing a complete scan. This increases the speed of imaging which may be more suitable for visualizing the dynamics in live cell imaging.

Another key factor considered here is the size of the pinhole. When the size of pinhole is small, for example, when 1x1 DMD pixel is used as one pinhole, the intensity of light projected, and the intensity of light collected through the pinhole are less. This is shown as the green curve in **figure 2.17 (d).** With a medium sized pinhole, for example, when 2x2 DMD pixels are used as one pinhole, the intensity of light projected, and the intensity of light collected through the pinhole are higher than 1x1 DMD pixel pinholes as shown as the red curve in **figure 2.17 (d)**. 3x3 DMD pixels when used as a pinhole, projected higher excitation intensity on to the sample. This also collects higher emission intensity from the sample. Emission intensity of 3x3 DMD pixels pinhole is shown as blue curve in **figure 2.17 (d).** This is ideal for samples with low fluorescence emission intensity. In theory, while using a 100x objective, 1x1 projects 136 nm size spot, 2x2 projects 272 nm size spot and 3x3 projects 408 nm size spot in the sample plane ignoring the diffraction limited. Due to the diffraction limited system, a point emitter will have ($\frac{\lambda}{2*NA} = 168$ nm) diffraction spread with widefield illumination.

Figure 2.17 is a comparison of different confocal projection patterns employed in this work. Three different multifocal illumination patterns were projected on to a bead sample and the intensity collected for each pinhole was compared. **Figure 2.17(a)** is 1x1 DMD pixel with inter pinhole distance 1x10. **Figure 2.17(b)** is 2x2 DMD pixels with inter pinhole distance 2x5.

Figure 2.17(c) is 3x3 DMD pixels with inter pinhole distance 3x5. **Figure 2.17(d)** is the intensity profile of line though the data collected with three different patterns. The intensity of emission light collected increases as the pinhole size increases. FWHM of 1x1 emission pinhole is 160 nm, 2x2 is 250 nm and 3x3 is 370 nm.

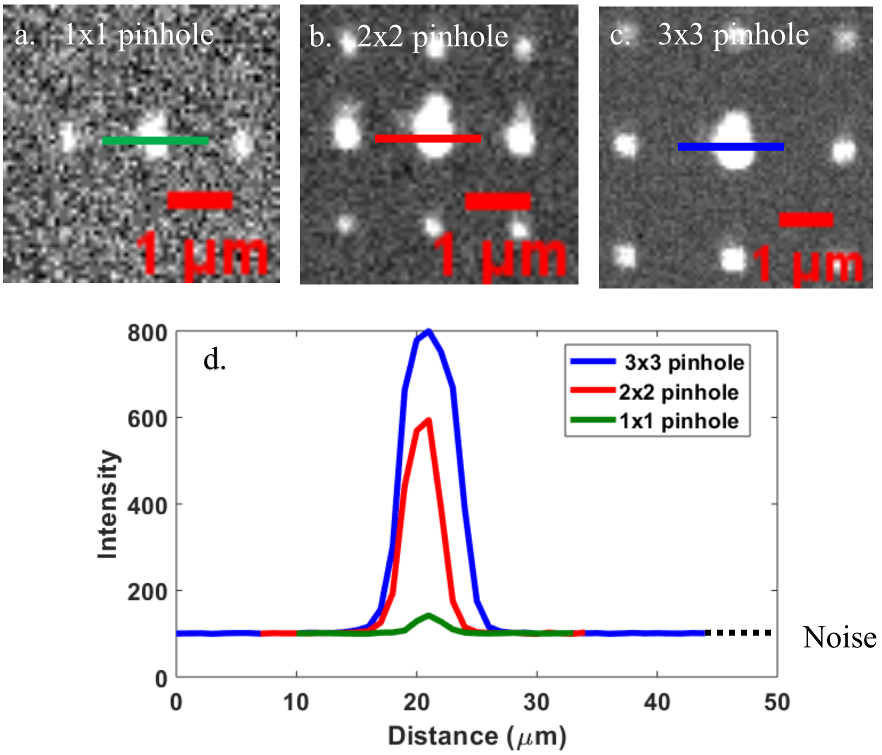

Fig. 2. 17. Comparison of emission intensity with different confocal projection patterns. (a) 1x1 pinhole with inter pinhole distance 1x10. **(b)** 2x2 pinhole with inter pinhole distance 2x5. **(c)** 3x3 pinhole with inter pinhole distance 3x5. **(d)** Intensity profile of line through 1x1, 2x2 and 3x3 pinholes.

2.8.1. BCCM post processing

Data for BCCM is collected by projecting multi focal patterns on to the DMD and involves reconstruction of the data using post processing algorithm described in this section. It is to be noted that each frame in a multifocal pattern needs to be collected frame by frame with perfect syncing of DMD frames with camera frames as detailed in Section 2.6. Even if there is a slightest syncing issue, the reconstructed image will have aberrations and will not produce a perfect background subtracted confocal image. This is an essential condition which needs to be met with hardware syncing. This will enable the collection of all the frames of ON and OFF camera separately. Before taking the data, calibration of camera pixels and DMD pixels need to be performed as detailed in the previous section. This allows the mapping of DMD camera emission spots with its correcting spots in the DMD which will enable high level control over each emission spot collected in each frame of the multifocal pattern.

The following are the main steps for post processing,

1. Load both ON and OFF camera data.
2. Using the DMD coordinates of the multifocal patterns projected, we can go to the camera coordinates for each emission spot using the calibration lookup tables.
3. A square section is cut around the expected ON and OFF camera pixels. We now have the ON and OFF cut section of each emission spot of each frame separately for ON and OFF camera data.
4. Invert the OFF PSF with the equation,

   $$\text{OFF\_cutSection\_new} = (\text{OFF\_cutsection} * (-1)) + \text{MAX}(\text{OFF\_cutsection}) + \text{MIN}(\text{OFF\_section})$$

   This inverts the intensity collected in the ring towards the centre. This inverting is crucial for subtracting the blead through intensity. Simulation of blead through intensity is given in Chapter 3.
5. Create a matrix (mask) with a zero array of size equal to cut section. Make a centre square with pixel value one. The size of the centre square equals the number of pixels in the camera expected to collect the emission spot from one DMD confocal pinhole. For example, if 3x3 DMD pixels are used as the pinhole size, camera area corresponding to this is 6x6 camera pixels. This is for Andor sCMOS Zyla 4.2 camera employed in this work which has 6.5 µm pixel size which is approximately half of the DMD pixel size. 6x6 pixels is the size of the centre square of the mask. Masking rejects the scattered light intensities collected in pixels outside the expected spot size. Multiply this mask with ON and OFF cut sections.
6. Subtract 1/10th of the OFF section from ON cut section. This will give the new background corrected cut section. Discussion of the chosen weight ‘1/10’ is discussed in detailed in Chapter 3.
7. This new cut section is multiplied with a Gaussian mask of standard deviation 1.5.
8. There are two methods to stitch all the cut sections together to form the final image.
   a. Make a zero array with size equal to the size of the DMD. Sum all the intensities inside the cut section and assign the value to the corresponding DMD pixel.

Size of the final image formed with this method will be equal to the size of the DMD, and size of each pixel in the image will be the size of each DMD pixel which is 136 nm in sample space.

b. Make a zero array with size equal to twice the size of DMD. This is to get each pixel in the array with half the size of a DMD pixel. It is worth noting that each camera pixel is half the size of each DMD pixel. Add the cut section to the corresponding DMD pixel. This builds up the final image with twice the number of pixels as in previous method (a). Size of the image will be equal to the camera size and size of each pixel will be equal to the size of a camera pixel, which is 65 nm in sample space.

2.8.2. BCCM imaging of actin sample

To demonstrate the background subtraction with BCCM, microtubules were imaged. A multifocal pattern with 3x3 pinhole size and 3x5 inter pinhole distance was projected on to the sample to collect in-focus and out-of-focus data in two separate cameras as described in the previous section. **Figure 2.18 (a)** and **(f)** are the sum of all the frames collected in ON camera and **figure 2.18 (b)** and **(g)** are the sum of all the frames collected in OFF camera. **Figure 2.18(c)** and **(h)** are the BCCM image. It can be seen in the BCCM image that, it shows higher background subtraction with microtubule structures more prominent. **Figure 2.18 (d)** and **(e)** are intensity profiles through ON and OFF images as shown by blue and red lines in **figure 2.18(a)** and **(c)** respectively. Black arrows indicate the places where there is a higher signal-to-noise ratio or higher distinction of adjacent structures. **Figure 2.18 (f), (g)** and **(h)** are the zoomed-in images of areas in **figures 2.18 (a), (b)** and **(c)** marked as shown by white squares. Line profile through one microtubule structure in ON, OFF and BCCM image was taken as shown in **figure 2.18(i).** FWHM of microtubule width obtained in ON image is 360 nm, OFF image is 410 nm and BCCM image is 350 nm.

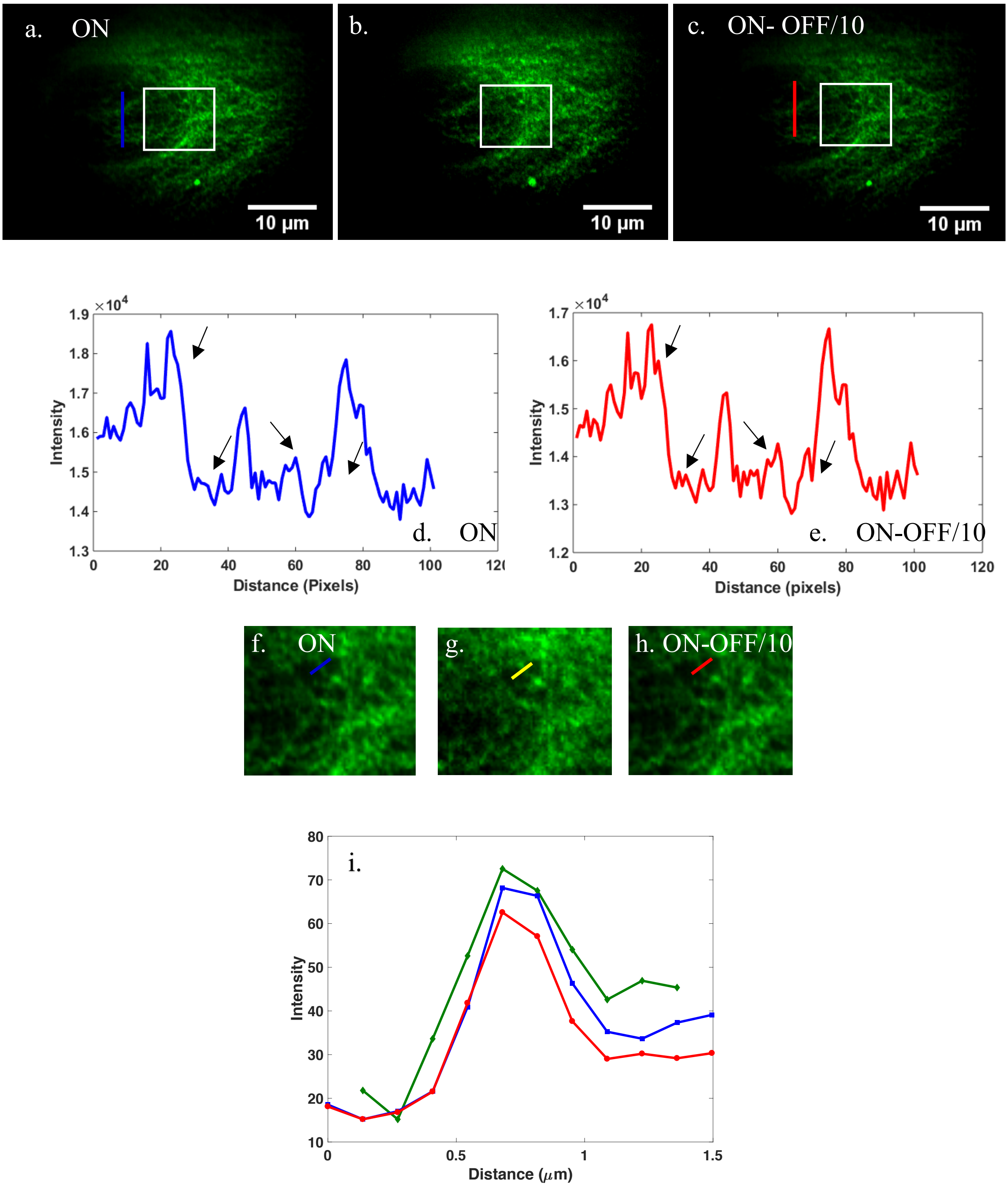

Fig. 2. 18. BCCM imaging on microtubules. **(a)** Sum of all the frames collected in ON image. **(b)** Sum of all the frames collected in OFF image. **(c)** Image reconstructed with BCCM algorithm. **(d)** Line profile through ON image. **(e)** Line profile through BCCM image. **(f), (g), (h)** Zoomed-in areas of figure **(a), (b), (c). (i)** Normalized intensity profile of lines through one microtubule in ON, OFF and BCCM.

2.8.3. Dual colour BCCM

To explore the potential of BCCM for dual colour imaging with Z stacks, microfilaments of bovine pulmonary artery endothelial (BPAEC) cells were imaged. Samples were labelled with Texas Red-X phalloidin for F-actin. Anti—bovine α-tubulin mouse monoclonal 236-10501 in conjunction with BODIPY FL goat anti—mouse IgG antibody was labelling microtubules. The prepared slide was purchased from Thermofishers (product number-F14781). This is the same sample used for the images in the Section 2.8.2.

Multifocal patterns with pinhole size 3x3 DMD pixels and inter pinhole distance 3x5 DMD pixels were employed. ON and OFF data were collected for five slices. The sample stage is moved axially to change the z position of the sample by controlling the stage using piezo z-stage controller with LabView. Each slice was taken by moving the stage by 500 nm. Reconstruction was done with each colour separately and combined using ImageJ. **Figure 2.19 (a)** is the dual colour microtubules and actin reconstructed with BCCM. **Figure 2.19 (b)** is the red square zoomed-in.

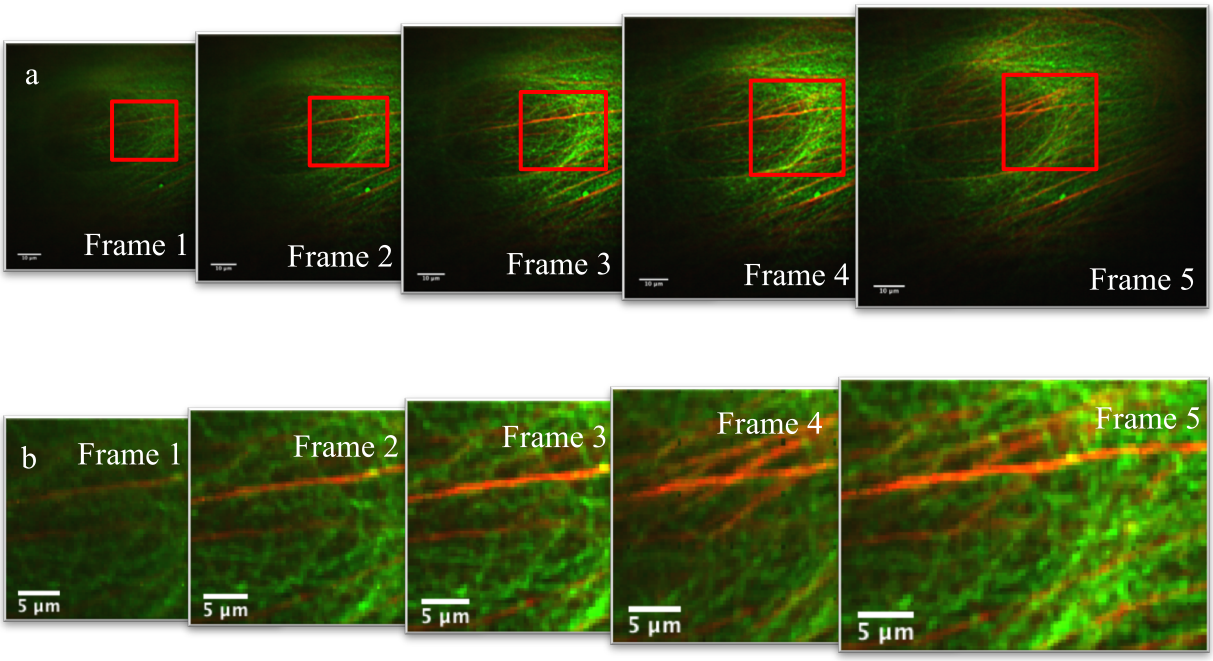

Fig. 2. 19. **Dual colour microtubules and actin z-stack. (a)** Frame 1 to 5 combined BCCM image. **(b)** Frames 1 to 5 red square zoomed-in.

2.9. Discussion

During the initial phase of the systems development, issues pertaining to the optics caused emission intensity collection in conjugate and non-conjugate cameras difficult. Digital pin holing confocal microscope was developed to bypass the emission pathway through the DMD. Images of beads and *E. coli* shown in this chapter demonstrates an improvement in signal-to-noise ratio with digital pin holing compared to a widefield image.

Optical issues were identified to upgrade the system to the next generation which allowed the collection of emission pathway through the DMD. This gave rise to further developments in confocal microscopy by using DMD as a physical pinhole to reject the out-of-focus light. Detailed optics of the Cairnfocal Generation II system is discussed. Alignment of the system is very crucial for all imaging experiments with this system. Alignment has proved to be extremely strenuous due to the various adjustments for every mirror and lens in the system. Although alignment involves many trial and error methods each time, a generalized alignment procedure for the optics which can be used as an outline for the alignment procedure has been detailed. Emission light coming back from the sample was physically pinholed by the DMD pixels in the work presented in the second part of this chapter. Physical pinholing confocal microscopy development can be classified into BCCM, rapid confocal, SR-BCM, AiryImaging and reconfigurable confocal. BCCM is presented in this chapter with detailed discussion of its post processing method. Images using BCCM demonstrated on microtubules and actin show improved background subtraction to distinguish the biological structures in the sample with higher signal-to-noise ratio and slightly improved resolution.

This chapter also includes the basic software development to control the DMD patterned projections. All the custom softwares used for various applications in other chapters are the modified version of the GUI presented in this chapter. Hardware settings for calibrations and imaging are also detailed. Calibration of DMD pixels with camera pixels can achieve a precision of less than 130 nm (two camera pixels). Calibration methods and codes described in this work can be adopted with any DMD and camera based experiments even for non-confocal implementations. Codes for DMD projection and digital pinholing confocal algorithm presented here can be integrated easily with any microscope even without the need for collection optics through DMD increasing the wide adoptability of the techniques.

There are many possibilities for future developments. One of the major issues with the system is power loss due to diffraction. This can be improved by replacing the relay lens and mirrors between the DMD and the microscope with optics that have larger dimensions to collect higher diffraction orders. Camera can be controlled using its SDK in MATLAB and integrated with the DMD GUI. Real time pattern generation and projection can be developed in the future depending on the biological experimental needs. Real time image analysis, automated pattern generation and automated pattern projection can be implemented for long term imaging or photo-manipulations in biological systems. In conclusion, depending on the biological experimental needs, the system can be easily transformed using the optical and software developments presented in this chapter.

Even though digital and physical pinholing confocal system improve the signal-to-noise ratio of the image, resolution improvement is not substantial. A conventional confocal microscope has the ability to get $\sqrt{2}$ resolution improvement with spot scanning frequency mixing. To extract this resolution from the image and to develop a super resolution confocal microscope with enhanced background correction was the goal for the work presented in the next chapter.

Chapter 3

Development of Super Resolution-Background Corrected Microscope

3.1. Summary

The development of SR-BCM presented in this work is the confocal based structured illumination microscope with superior out-of-focus rejection mechanism compared to other recently developed Sheppard summing based techniques. Detailed implementation and post processing techniques of SR-BCM are detailed in this chapter supported with theory and simulation. The algorithm for SR-BCM reconstruction is also provided with this work. A method for obtaining AiryScan equivalent images termed in this work as AiryImaging, for easy integration into any camera based setup is also presented in this chapter.

3.2. Introduction

Optical microscopy has played a significant role in biological research due to its non-contact, minimally invasive nature enabling *in vivo* investigation. Diffraction limit theory states that two point objects cannot be distinguished if they are closer than half of the wavelength used to image them. This finding had high impacts on the developments of optical microscopic techniques and it took around a century to find loopholes to surpass this limit. STimulated Emission Depletion Microscopy (STED) [Hell *et al.*,2007], Localisation Microscopy (LM)

[Betzig *et al.*, 2006, Bates *et al.*, 2006] and Structured Illumination Microscopy (SIM) [Gustafsson. M *et al.*, 2000] are independent super resolution microscopic techniques which can render images with resolution beyond the diffraction limit. Imaging techniques are highly dependent on sample characteristics making each imaging technique applicable only for specific biological applications.

Confocal microscopy is the most widely used microscopic technique for biological studies and has become the workhorse of biological imaging. Obtaining super resolution images using confocal microscopy was first theoretically studied in 1988 by Sheppard and co-workers [Shephard et.al, 1988] and experimentally achieved as Imaging Scanning Microscope (ISM) by Muller *et al.*, [Muller et. al., 2010]. It has been shown that a conventional confocal microscope with a point detector can achieve higher resolution by decreasing the size of detection pinholes [Voort *et al.*, 1990]. Theoretically, confocal can achieve √2 times better resolution when the size of the pinhole is zero. Decreasing the size of pinhole considerably reduces the signal-to-noise ratio of the image. ISM employs an imaging detector rather than a point detector to capture emission from the sample. When the camera pixel size is really small, they act as individual pinholes. In this case, signal-to-noise is retained as the photons are not rejected by a very small physical pinhole, but all the possible photons are collected in the camera chip. The original ISM setup projects diffraction limited confocal spots using a laser beam and emission light from the sample passes through a pinhole to reject the out-of-focus light and is collected in a camera [Muller et. al., 2010].

The major disadvantage of the original ISM was that it was really slow as a conventional laser scanning confocal microscope with single illumination spot. York *et al.* [York et. al., 2012] implemented ISM using a DMD which increased the speed and doubled the resolution when compared to a widefield image. Instead of a single laser spot, multifocal illumination spots were projected using a DMD to scan across a sample. This Multifocal Structured Illumination Microscopy (MSIM) technique post processes the data with digital pinholing, to reject the out-of-focus noise followed by 2x scaling and summing all the frames to get a multifocal-excited, pinholed, scaled and summed (MPSS) image. This image is deconvoluted to double the resolution and render an MSIM image. [Ward *et al.*, 2017]

It has been shown that ISM can be implemented with a conventional spinning disk confocal microscope. By collecting the raw data in a camera and post processing with 2x scaling, summing and deconvolution, resolution of the final image is doubled [Schulz *et al.*]. One of the disadvantages of MSIM and its spinning disk equivalent is that the need for post processing techniques takes additional time making it difficult to get final images in a camera instantaneously. Instant Structured Illumination Microscopy (iSIM) [York et. al., 2013, Curd *et al.*, 2015] implements ISM using lenslet arrays for confocal structured illumination and another pair of lenslet arrays to focus each emission spot on the detector in such a way that it does the 2x scaling required by ISM before projected on to the camera chip. iSIM can image live biological samples instantaneously and potentially at 100 frames per second. It is worth noting here that iSIM uses a pinhole array to reject the out-of-focus light from the sample.

It is shown that almost 90% of captured fluorescence from a sample in a fluorescence microscope is the out-of-focus light which comes from the plane above and below the focal plane [Jose Angel *et al.*, 2005]. One of the crucial elements when building a confocal based structured illumination microscope is the rejection of out-of-focus light. The current state of the art techniques for obtaining higher resolution in confocal based structured illumination microscopy lack the ability to control the out-of-focus light rejection. In this chapter, the next generation confocal structured illumination based Super Resolution-Background Corrected Microscope (SR-BCM) is presented. SR-BCM has a superior out-of-focus rejection method followed by deconvolution to get higher resolution images.

The theory of confocal illumination and detection reveal that emission light that passes through the pinhole is the light from the in-focus plane and the light incident outside this pinhole is the light from planes above and below the focal plane [Pawley, book, 2006]. Even when collecting light from just the pinhole, there will be blead through of intensity from areas outside the pinhole. This is demonstrated with a model in Section 3.4.4. SR-BCM imaging modality presented in this work incorporates three tiers of out-of-focus light rejection. Emission light from the sample is physically pinholed using DMD micromirrors which act as a conventional pinhole such as in a spinning disk microscope. This is followed by an optional digital masking in which each detection spot is multiplied by a mask to subtract the background.

Instead of discarding the out-of-focus light completely, SR-BCM employs maximum utilization of the emission light from the sample by collecting the in-focus and out-of-focus light coming back from the sample in two separate cameras using a Schiefschild telescope optical setup. Third tier of out-of-focus rejection is by subtracting a masked in-focus spot with a masked out-of-focus spot. These subtracted spots are shrunk two times, summed and deconvoluted to get a high resolution image.

Two modalities of confocal development are presented in this chapter. The second development is the rapid confocal imaging with can run up to approximately 350 confocal scans per second. In rapid confocal, out-of-focus light is rejected by physical pinholing of DMD micromirrors. Images are processed through a deconvolution algorithm or super resolution reconstruction algorithms such as Super Resolution Radial Fluctuations (SRRF) [Gustafsson. N *et al.*, 2016] algorithm to get higher resolution when compared to a widefield image. The confocal system presented here which includes rapid confocal and SR-BCM enable the control over the compromise between optical sectioning, resolution and speed of image acquisition. In SR-BCM, signal-to-noise ratio was increased in an image after subtracting the bleed through of intensity (calculated from out-of-focus data) from in-focus data. Bleed through intensity was calculated from the out-of-focus planes. The theory of SR-BCM is detailed in Section 3.4.3. A method to obtain AiryScan equivalent images termed in this work as AiryImaging is presented in Section 3.4.11. Post processing algorithms for SR-BCM and AiryImaging are given in appendix 6 and 7 respectively.

3.3. Methods and Developments

This section briefly discusses the data acquisition and post processing methods for SR-BCM and rapid confocal. The techniques are tested on fixed cells. Detailed description of the development of these techniques are given in Section 3.4.

3.3.1. Data acquisition

For confocal imaging development in this chapter, the system was set to operate in two modalities. First is SR-BCM which has an advanced out-of-focus subtraction mechanism. Second is rapid confocal which can run potentially at 355.11 confocal scans per second. For rapid confocal imaging, camera and DMD were running in its internally defined timings which allow us to change the camera exposure time depending on the sample brightness. For SR-BCM, NI DAQ (USB-6341) was used to trigger the Z stage and ON camera. In this setting, the ON camera is configured to trigger the DMD frame change and the OFF camera exposure time as discussed in Chapter 2. It is worth noting here that these triggering settings are very crucial to get each camera frame to be in perfect sync with DMD frame changes achieving high level precision and control over each in-focus and out-of-focus emission frames. The Z stage moves to the next axial level only after projecting all the confocal frames in one sequence.

3.3.2. Data processing

In all optical setups with point based illumination and a physical pinhole based out-of-focus light rejection such as in LSCM, spinning disk, iSIM *etc*, there is an intensity blead through from the out-of-focus planes which are always collected in the detector. In other optical setups which are based on digital pinholing to subtract out-of-focus light by multiplying the full emission spot with a Gaussian mask, the out-of-focus bleed through intensity is not subtracted. Moreover, out-of-focus intensity change throughout the sample due to the high inhomogeneous nature of biological structures which make digital pinholing systems not fully efficient. SR-BCM collects both in-focus and out-of-focus light in two separate cameras and calculates the intensity bleed through from the collected OFF camera data during post processing and subtracts this from the ON camera data.

Post processing is performed with custom software, written in the MATLAB programming language. Post processing includes: (i) two-tier DMD calibration with the ON and OFF cameras to achieve not more than two camera pixels or 130 nm precision mapping between DMD and camera pixels, (ii) weighted subtraction of bleed through intensity from each ON emission spot using the corresponding OFF emission spot to get the corrected PSF, (iii) pixel reassignment of the corrected PSF to account for ISM with √2 improvement in resolution and stitching all the spots to construct the final image and (iv) deconvolution of the final image to double the resolution. Data processing for SR-BCM is detailed in Section 3.4.8. DMD camera calibration code for SR-BCM is same as for BCCM and is given in Chapter 2.

Rapid confocal does not require any specific post processing, as the image acquired in the camera is physically pinholed at the DMD to reject the out-of-focus light. Optionally, deconvolution and super resolution reconstructions can be employed as discussed in the next section.

3.3.3. Deconvolution and super resolution reconstructions

Fast confocal data can be run through a deconvolution algorithm to restore the image and improve the resolution. We use AutoQuant (Media Cybernetics) with 10 iterations using adaptive PSF (Blind) method. For rapid confocal imaging in **figure 3.2**, the final data were deconvoluted with Huygens deconvolution (SVI) using Classic Maximum Likelihood Estimation which improved the quality and restored the final image. Even though our detection of confocal emission light is based on DMD with micromirrors acting as physical pinholes, even with the unavoidable loss of higher diffraction orders, we get enough signal-to-noise ratio to run the data through super resolution reconstruction algorithms such as 3B, SOFI *etc*, with the most recent Super Resolution Radiant Fluctuations (SRRF) algorithm to get super resolution images from the rapid confocal imaging mode.

3.3.4. Fixed cellular samples

Actin samples used in this chapter are bovine pulmonary artery endothelial cells (BPAEC) labelled with Texas Red-X phalloidin for F-actin. A prepared slide was purchased from Thermofisher Ltd. (product number-F14781).

3.4. Results

3.4.1. ON and OFF PSF of various pinhole sizes

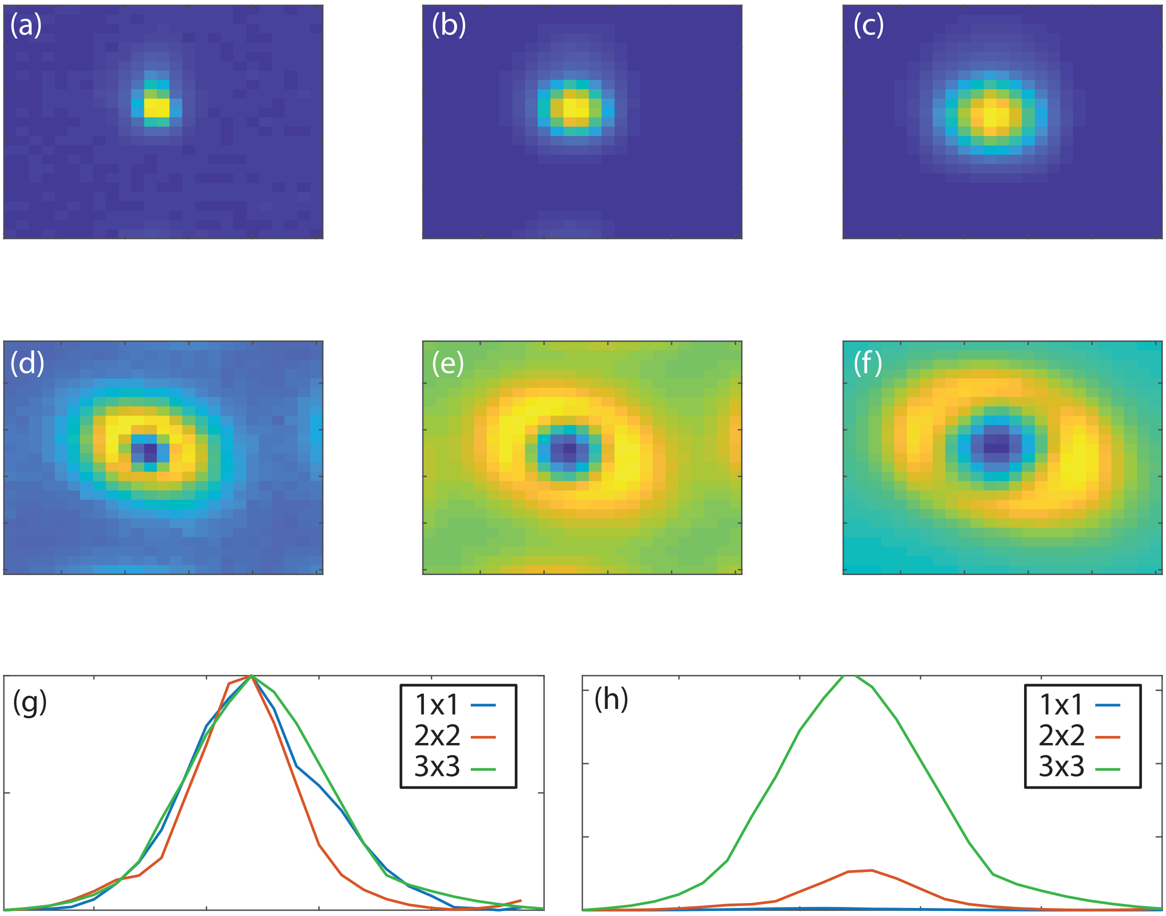

Fig. 3. 1. On and OFF PSF of various pinhole sizes. **(a-c)** ON PSF of 1x1, 2x2 and 3x3 respectively. **(d-f)** OFF PSF of 1x1, 2x2 and 3x3 respectively. (g) Normalized line profile through (a-c) indicating that 2x2 pinhole size confocal patterns can give the best resolution. (h) Line profile through (a-c) indicating that 3x3 pinhole size confocal patterns give maximum intensity.

For comparison, PSF collected with 1x1, 2x2 and 3x3 pinhole size is compared in **figure 3.1** with data collected used the corresponding modulation patterns. The data were taken on a bead sample. **Figure 3.1(a-c)** is the sum of all ON cut sections in 1x1, 2x2 and 3x3 data respectively. **Figure 3.1(d-f)** is the sum of all OFF cut sections in 1x1, 2x2 and 3x3 data respectively. **Figure 3.1 (h)** is the line profile through **figure 3.1 (a-c)**. **Figure 3.1 (g)** is the normalized line profile through **figure 3.1 (a-c). Figure 3.1 (g)** shows that minimum FWHM and maximum resolution is obtained using 2x2 pinhole size confocal pattern. **Figure 3.1 (h)** shows that 3x3 gives the maximum intensity than 2x2 and 1x1 pinhole size confocal patterns. We can infer that for bright samples, 2x2 pinhole size confocal patterns will be suitable and for less bright samples, 3x3 pinhole size confocal patterns will be suitable.

3.4.2. Rapid confocal imaging

For rapid confocal imaging, the DMD was configured in the optical setup to act as a physical pinhole to reject the out-of-focus light rapidly and to achieve high speed. In this mode, the DMD is set to run at the fastest possible frame rate which is 44 µsec per frame. For example, if a 100 frame confocal pattern is used, it acquires one confocal image in 4.4 msec. The speed of imaging is limited only by the speed of the camera and the fluorescence emission intensity (brightness) of the sample. When running the system in rapid confocal mode, the ON camera collects data which are equivalent to that collected in a spinning disk setup. Multifocal patterns are continuously projected, and camera acquires and integrates these pattern in one camera frame. Camera exposure time equals the number of times all the patterns for one scan is projected multiplied by the time to project all the patterns for one scan.

The speed of the DMD allows us to image at frame rates of 355.11 confocal scans per second (when using 64 frames at 2x2 DMD pixels as pinhole size and 2x4 DMD pixels separation between pinholes). Confocal scans per second can be varied depending on the distance between the pinholes and the size of the pinholes. It can be varied from 101.01 (when using 225 frames at 3x3 DMD pixels as pinhole size and 3x5 DMD pixels separation between pinholes) to 280.58 (when using 81 frames at 3x3 DMD pixels as pinhole size and 3x3 DMD pixels separation between pinholes). 2x2 confocal pinhole which projects a 272 nm spot on the sample plane (with 100x objective) is the ideal pinhole size. We also use 3x3 pinhole size to deliver higher illumination intensities for a less bright sample.

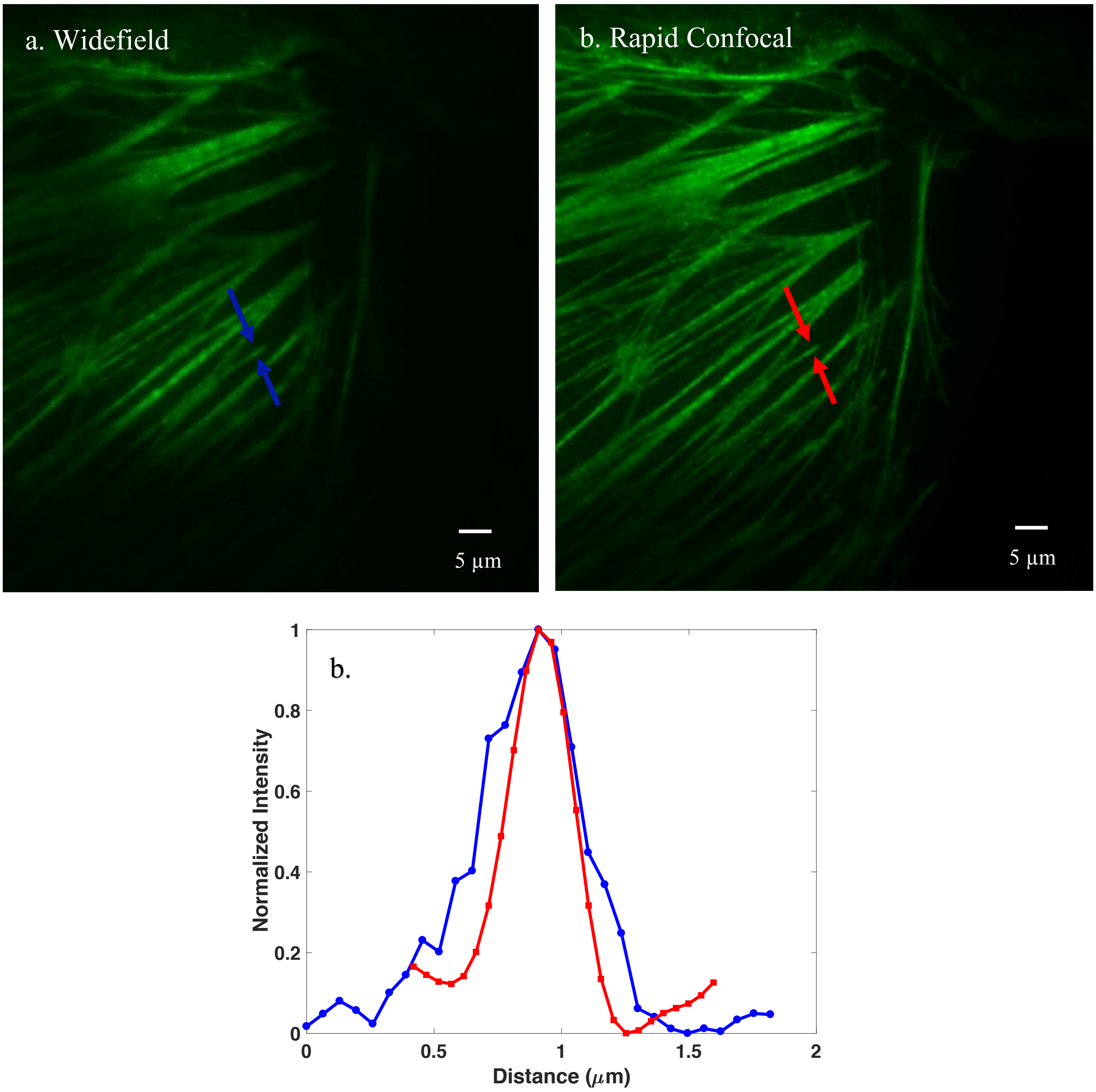

Fig. 3. 2. Comparison of widefield and rapid confocal of F-actin filamements. (a) Widefield, **(b)** Rapid confocal. Multifocal pattern used for acquiring this data is 2x2 DMD pixels pinhole size and 2x5 DMD pixels inter pinhole distance. **(c)** Intensity profile through an actin filament to compare the resolution improvement. FWHM of the selected actin filament in widefield and rapid confocal are 500 nm and 350 nm respectively.

When running the system in fast confocal mode, the ON camera collects the data which are equivalent to the data collected in a spinning disk setup and much faster with approximately 350 confocal scans per second. **Figure 3.2 (a)** shows widefield images. **Figure 3.2 (b)** is rapid confocal which is running at 227 confocal scans per second. Multifocal pattern used for acquiring these data are 2x2 DMD pixels pinhole size and 2x5 DMD pixels inter pinhole distance. These data are collected at 30 millisecond camera exposure time. If the sample is bright, fast confocal data acquisition is limited only by the maximum speed of the camera mounted in the DMD system. FWHM of the selected actin filament in widefield and rapid confocal in **figures 3.2 (a)** and **(b)** are 500 nm and 350 nm respectively as shown in **figure 3.2(c)**. This resolution improvement can depend on the deconvolution software applied. We used Huygens deconvolution and found that it gave the best resolution improvement. In this figure, rapid confocal is reconstructed with Huygens software (classical maximum likelihood estimation) with 10 iterations. PSF is calculated by the software theoretically when pixel size, objective specifications and imaging mode are given as input to the software.

As described previously, patterned illumination confocal imaging presented in this chapter has two major modes of operation which can be switched depending of the sample characteristics and imaging requirements. Rapid confocal can potentially run at 355.11 confocal scans/second enabling rapid live biological imaging. In rapid confocal, out-of-focus light from the plane above and below the focal plane is rejected physically by micro-mirrors. Each in-focus camera frame collects several complete confocal images. This is performed by summing each pinhole intensity of all the frames of the several confocal scans in one camera frame. Final image can be deconvoluted to restore the resolution. This image can be run through deconvolution or super resolution reconstruction algorithms to enhance the resolution.

3.4.3. Modulation Pattern and Rapid Confocal Post Processing

Modulation pattern for SR-BCM and rapid confocal is a square grid of ON and OFF pixels as shown in **figure 3.3**. The distance d between two adjacent pixels can ideally vary from 8 to 12 DMD pixels depending on which, the number of frames for reconstruction also varies. If the pinholes are close, there will be intensity cross talk between the pixels and this decreases the optical sectioning ability of the system. If the pinholes are far apart, it can increase the number of frames required for reconstruction, increasing the speed of imaging. To illuminate the whole area of one frame, this pattern is repeated d^2 times and the image is recorded in the camera.
The size of the pinhole of a confocal pattern can be changed by changing the number of ON pixels in the DMD as 1x1, 2x2, 3x3 and so on. Abbe diffraction limited spot size for 488 nm illumination light source is in theory is approximately, $\lambda/2NA = 168$ nm. Each DMD pixel size is 13.6 µm x 13.6 µm and a 100x/1.45 NA objective is used for imaging. Ignoring the diffraction limit, one DMD pixel should illuminate 136 nm x 136 nm area of the sample. We find that using 2x2 or 3x3 ON pixels in square grid pattern can give the optimal signal-to-noise

ratio and optical sectioning of the sample. A 2x2 and 3x3 pixels DMD spot theoretically illuminates 272 nm x 272 nm and 408 nm x 408 nm in sample plane respectively.

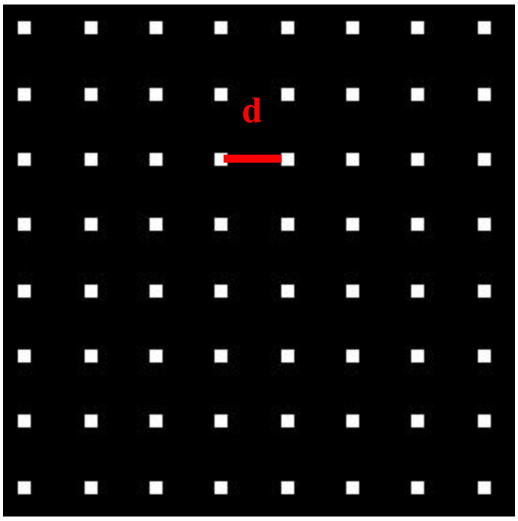

Fig. 3. 3. Modulation pattern. Distance 'd' masked in red is the inter pinhole distance. Number of DMD pixels ON per spot determines the size of the pinhole.

3.4.4. SR-BCM Theory

The theory of SR-BCM is derived as an extension of PAM and ISM interpretations pioneered by Jovin Thomas in around 1990s and Sheppard in around 1980s respectively. A PAM system is based on patterned illumination projection and patterned emission collection positioned in the same physical location, the SLM plane. The major advantage here is that the excitation and collection planes coincide in such a way that there are no alignment issues. Conventional PAM system has found its applications in many fields such as FRET, conventional confocal microscopy, SIM, selective photoreactions and so on [Heintzmann *et al.*, 2001, Jiang *et al.*, 2010, Wu *et al.*, 2010, Martial *et al.*, 2012, Křžek *et al.*, 2012, Fulwyler *et al.*, 2005]. In the conventional PAM system, the image collected in the ON camera is interpreted as an 'analog of a confocal image' as it is used without processing [Verveer *et al.*, 1998]. Considering the simulations in Section 3.4.4, the raw data for SR-BCM were obtained by doing a weighted subtraction of the data collected in ON and OFF images to subtract the intensity bleed through from out-of-focus planes of the sample. This was achieved with the collection and mapping of each illumination and emission spot to give high level control enabling superior out-of-focus light subtraction and the ability to do other point based illumination techniques such as MSIM and Airyscan.

When imaging a sample in a microscope with uniform widefield illumination, the image formed on the detector is a convolution of the sample and the excitation PSF of the microscope. Expression for the image formed at the detector is given by,

$$I_{w} = \int H_{em}\ (xc - u, yc - v, w)\ S\ (u, v, w)\ du\ dv\ dw \qquad \textbf{(1)}$$

where, Hem is the PSF formed on the camera (camera coordinates represented by xc, yc) if there is a point detector at position (u, v, w) in the sample S.

When using patterned projection, the image formed in the camera is modified with respect to the illumination pattern. Here, an illumination pattern G is projected on to the DMD plane and de-magnified on to the sample plane with a magnification factor M. The Modulation pattern used in this work is a multiple square pattern as shown in Section 3.4.3. An image is collected on the DMD. ON pixels reflect light on to the ON camera and OFF pixels reflect light on to the OFF camera. An in-focus or conjugate image is formed in the ON camera and out-of-focus or non-conjugate image is formed on OFF camera. Here we consider DMD coordinates (xd, yd) as the detector coordinates. The conjugate image is given by,

$$I_{c,G}\,(x_d, y_d, z_s) = \frac{T}{nx\,ny} \iiint_{-\infty}^{+\infty} \mathrm{Hem}\left(\frac{xd}{M} - u, \frac{yd}{M} - v, w\right)$$

$$* \; I_G\left(u - \frac{xd-\phi x}{M}, v - \frac{yd-\phi y}{M}, w\right) * S\,(u, v, w\text{-}z_s)\ du\ dv\ dw \qquad \textbf{(2)}$$

where, Hem is the emission PSF, ϕx, ϕy is defined as xd, yd mod η, η is the size of the DMD pixel, Zs is the axial direction depth of field, T is the total integration time, S is the density function of the emitter, I_G is the total illumination function given by,

$$I_G\,(x_o, y_o, z_o) = \iint_{-\infty}^{+\infty} G\ (Mu, Mv) * H_{ex}\,(x_o\text{-}u, y_o\text{-}v, z_o)\ du\ dv \qquad \textbf{(3)}$$

where G is the modulation pattern defined by equation (4) and which follows the condition (5),

$$G\ (x_d, y_d) = G\ (x_d - pn_x\eta\ , y_d - pn_y\eta) \qquad p, q \in N \qquad \textbf{(4)}$$

$$\sum_{a=0}^{nx-1} \sum_{b=0}^{ny-1} G\,(x_d - a\eta\,, y_d - b\eta) = 1 \tag{5}$$

where, (nx, ny) are the number of columns and rows in the DMD and **a** and **b** are pixel numbers with limits $0 \leq \mathbf{a} \leq nx$ and $0 \leq \mathbf{b} \leq ny$.

The non-conjugate image is given by substituting modulation pattern G by 1-G,

$$G_{nc}\,(Mu, Mv) = 1 - G\,(Mu, Mv) \tag{6}$$

Substituting equation (6) and equation (3) in equation (2) gives the non-conjugate image as,

$$I_{nc,\,G}\,(x_d, y_d, z_s) = \frac{T}{nx\,ny} \iiint_{-\infty}^{+\infty} \mathrm{Hem}\,\left(\frac{xd}{M} - u, \frac{yd}{M} - v, w\right) * (1 - G\,(Mu, Mv)) * \mathrm{Hex}\,(u, v, w) * S\,(u, v, w - z_s)\; du\, dv\, dw \tag{7}$$

For obtaining the SR-BCM image, we subtract the bleed through of out-of-focus intensity of each emission spot on the conjugate image by using the non-conjugate image followed by pixel reassignment to increase the resolution of the image by √2. We can deconvolve this image with the ‘real’ PSF to obtain the final image. By ‘real’ PSF we mean that we need not rely on the theoretical PSF or calibrated PSF (generally calibrated using beads), we can obtain the ‘real’ PSF from the image by doing,

$$PSF_{real} = PSF_{ON} - \mathrm{invert}(PSF_{OFF})/\Phi \tag{8}$$

where Φ is the scaling constant which can be varied depending on the thickness of the sample. The value of Φ used in the next sections is 10 which is modelled in Section 3.4.4. Before pixel reassignment, the raw SR-BCM data are given by the equation,

$$\mathrm{Raw}\ I_{SR\text{-}BCM} = Ic - Inc/\,\Phi \tag{9}$$

Substituting (2) and (7) in equation (9) we get,

$$\text{Raw I}_{\text{SR-BCM}}(x_d, y_d, z_s) = \frac{T}{10*nx\,ny} \iiint_{-\infty}^{+\infty} \text{Hem}\left(\frac{xd}{M} - u, \frac{yd}{M} - v, w\right) * (11 * G\,(Mu, Mv) - 1) * \text{Hex}\,(u, v, w) * S\,(u, v, w\text{-}z_s)\, du\, dv\, dw \quad \textbf{(10)}$$

New I_G for the raw $I_{\text{SR-BCM}}$ can be given as,

$$I_{Gnew}(x_o, y_o, z_o) = \iint_{-\infty}^{+\infty} (11 * G\,(Mu, Mv) - 1) * \text{Hex}\,(x_o\text{-}u, y_o\text{-}v, z_o)\, du\, dv \quad \textbf{(11)}$$

and raw $I_{\text{SR-BCM}}$ can be derived as,

$$\text{Raw I}_{\text{SR-BCM}}(x_d, y_d, z_s) = \frac{T}{10*nx\,ny} \iiint_{-\infty}^{+\infty} \text{Hem}\left(\frac{xd}{M} - u, \frac{yd}{M} - v, w\right) * I_{Gnew}\left(u - \frac{xd-\phi x}{M}, v - \frac{yd-\phi y}{M}, w\right) * S\,(u, v, w\text{-}z_s)\, du\, dv\, dw \quad \textbf{(12)}$$

We can simplify this by setting DMD coordinates (xd, yd, zs) to **s** and sample coordinates (u, v, w) to **r'**. The raw SR-BCM image can be obtained by integrating the above equation (12) with xd and yd (or s).

$$\text{Raw I}_{\text{SR-BCM}}(r, s) = \iint \text{Hem}\,(s - r' + r) * I_{Gnew}(\,r - r' - f(s)) * S\,(r')\, ds\, dr' \quad \textbf{(13)}$$

where f(s) is a function of s defined by substituting s for xd in $\frac{xd-\phi x}{M}$**.** Each pixel in the DMD is considered as an independent detector. Raw SR-BCM image is processed by pixel reassignment to increase the resolution. Pixel reassignment shifts the displaced pinhole by half the distance towards the optical axis. Thus SR-BCM image can be represented as,

$$I_{\text{SR-BCM}}(r, s) = \iint \text{Hem}\left(\frac{s}{2} - r' + r\right) * I_{Gnew}\left(\,r - r' - f(s) - \frac{s}{2}\right) * S\,(r')\, ds\, dr' \quad \textbf{(14)}$$

The function f(s) in the excitation PSF represents the pinholes in excitation pathway projecting the intensity spot and in emission pathway collecting the intensity spot. The effective PSF of SR-BCM system can be written as,

$$\text{PSF}_{\text{SR-BCM}}(r) = \int \text{Hem}\left(\frac{s}{2} + r\right) * I_{Gnew}\left(\,r - f(s) - \frac{s}{2}\right) ds \quad \textbf{(15)}$$

3.4.5. Simulation

When acquiring a confocal image with any type of physical apertures, there is an intensity blead through from out-of-focus planes in the in-focus camera. A PSF using Born and Wolf 3D Optical Model (PSF generator ImageJ plugin was used) were simulated to estimate the weighing factor for the subtraction of non-conjugate image from conjugate image. The PSF of in-focus (**figure 3.4(a)**) and out-of-focus (**figure 3.4(b)**) pixel PSF is calculated with pixel size in x,y as the size of the camera pixel 65 nm, z step as 300 nm, N.A 1.4 and refractive index 1.5. Estimated depth of field (which is higher than the axial resolution due to diffraction limited optics) for 100x 1.45 oil objective is estimated as 500 nm.

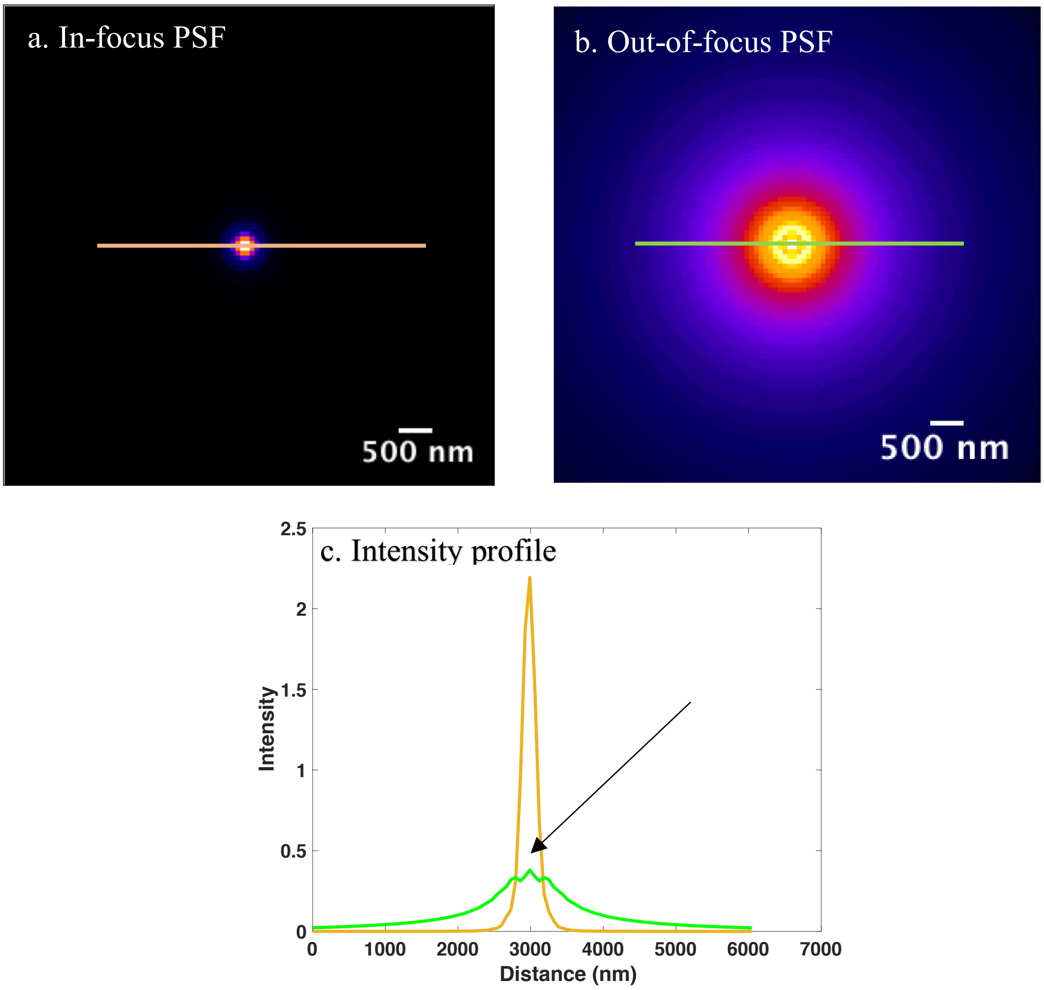

Fig. 3. 4. Modelling the point spread function. (a). In-focus PSF. **(b).** Out-of-focus PSF. **(c).** Intensity profile graph of line profile through in-focus and out-of-focus PSF represented as yellow and green curves respectively.

Figure 3.4(c) is the intensity profile of in-focus and out-of-focus PSF. Black arrow in **figure 3.4(c)** indicates the blead through intensity from out-of-focus planes in the in-focus image. The contribution of '1/10' out-of-focus intensity to the final SR-BCM raw data comes from here. It is to be noted that this intensity profile should not be confused with the actual intensity of emission light from in-focus and out-of-focus planes collected in both the cameras. Intensity of out-of-focus light for moderately thick sample is several times higher than light collected from the in-focus plane. It has been shown that almost 90% of emission light from the sample in an optical microscope is from planes above and below the focal plane [Jose Angel *et al.*, 2005]. A quantitative comparison of this with varying pinhole size in a point based illumination system is given in Section 3.4.9.

3.4.6. SR-BCM implementation

One of the crucial elements when building a confocal based structured illumination microscope is the rejection of out-of-focus light. Despite recent advances, implementations of ISM do not efficiently utilize out-of-focus light because they are based on either physical pinholes which reject light from being detected or digital pinholes which mix both in and out-of-focus light at ratios which change throughout the sample. Using a spatial light modulator to provide both illumination and detection allows the collection and separation of light passing through the confocal pinhole and light that would normally be rejected by the pinhole [Heintzmann *et al.*, 2001, Jiang *et al.*, 2010, Wu *et al.*, 2010, Martial *et al.*, 2012].

Here I present SR-BCM, where the in-focus light is collected on the ON camera, this is the same information as collected by a conventional laser scanning confocal microscope (LSCM) or spinning disk microscope and shown in **(Figure 3.5 a,c,e)**. Bleed through of intensity from out-of-focus planes in the in-focus camera is generally collected by a conventional confocal based setup with a physical pinholing aperture. The out-of-focus light is collected by the OFF camera. This contains the information which is usually rejected by a conventional confocal based setup **(Figure 3.5 b,d,f).**

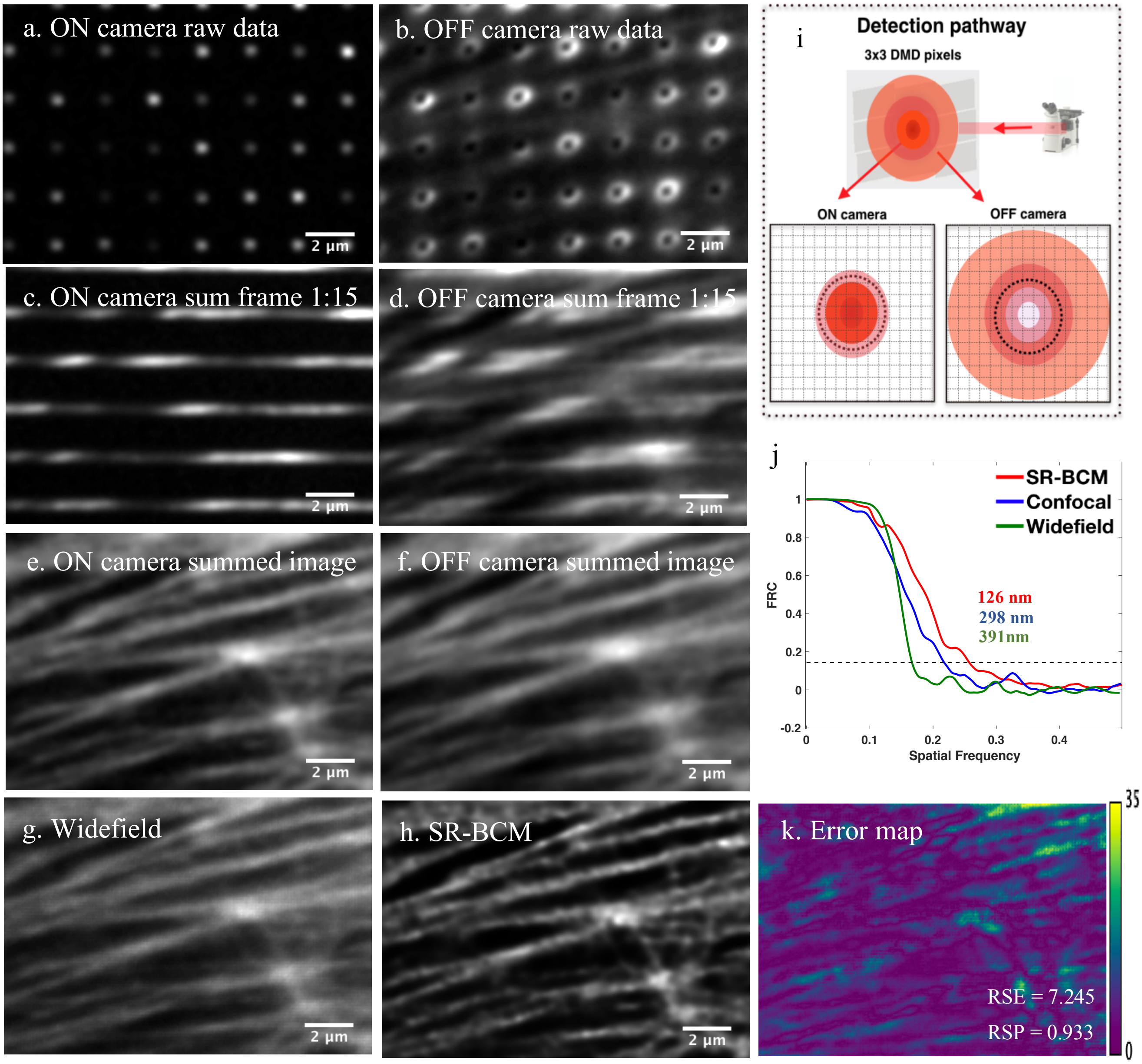

Fig. 3.5. Bovine Pulmonary Artery Endothelial Cells (BPAEC) labelled for F-actin filaments with phalloidin are visualized to demonstrate the enhancement in contrast and resolution in SR-BCM. (a) In-focus data collected with the ON camera with 3x3 DMD pixels as pinhole size and 3x5 DMD pixel distance between two pinholes. **(b)** Out-of-focus data collected with the OFF camera. **(c)** Sum of frames 1 to 15, ON camera. **(d)** Sum of frames 1 to 15, OFF camera. **(e)** Sum of all the 225 frames in ON camera. **(f)** Sum of all the 225 frames in OFF camera. **(g)** Widefield image. (h) SR-BCM image. **(i)** Optical pathway of detection of emission spots. **(j)** FRC map to compare the resolution of widefield, confocal and SR-BCM. FRC values are, widefield 391 nm, confocal 298 nm, SR-BCM 126 nm. **(k)** NanoJ SQUIRREL error map between widefield and SR-BCM.

In the schematic for the optical pathway **figure 3.5 (i)** one DMD pixel is turned ON (+12 degree) and is surrounded by OFF (-12 degree) pixels, the ON pixel directs the light towards the microscope. A single DMD pixel translates to 136 nm at the sample plane of the microscope. Light returning from the sample, after diffraction spreading, hits the ON pixel and the surrounding OFF pixels. The ON pixel acts as an analogue of a pinhole in a conventional confocal system and the in-focus light from the sample is collected on the ON camera. The out-of-focus light collected in the surrounding OFF pixels, which would be rejected by a conventional confocal microscope, is directed towards the OFF camera. The black dotted circle **(Figure 3.5i)** on both cameras represents the size of the equivalent pinhole in a conventional confocal system.

Using the data collected on the OFF camera, which would normally be rejected by the confocal pinhole, a background correction of the image can be performed efficiently to improve the signal to noise ratio. For SR-BCM, we subtract a portion the out-of-focus PSF from in-focus PSF to remove the background light and to achieve a higher s/n. This makes the most efficient use of the collected light from the sample. The out-of-focus PSF subtraction method (Section 3.4.8) is supported with detailed theory (Section 3.4.3) and simulation (Section 3.4.4) to calculate the weight of correction.

The resulting corrected PSF is then used along with a Sheppard summing algorithm to increase the resolution. When a low frequency multifocal illumination pattern mixes with the sample frequency, higher frequency sample information is collected in the objective due to Moire effect. Reducing the size of the collection pinhole in the image plane increases the collection of this high frequency information from the objective's Fourier plane. The goal is to extract this high frequency information which is collected by a conventional confocal microscope. For this, a displaced point detector technique is employed to collect all the emission intensity without the loss of signal due to reduced size of pinhole. This is followed by pixel reassignment to bring the intensity of the displaced pinhole back to the optical axis to enhance the resolution of the image. The resolution enhancement is achieved using Sheppard summing and is shown and compared with a widefield **(Figure 3.5 e)** and the confocal image **(Figure 3.5 g)** in **figure 3.5 (j)** and error map using NanoJ SQUIRREL is shown in **figure 3.5 (k)**. The collection of the conjugate and non-conjugate planes allows enhanced background rejection which improves the signal to noise ratio and resolution (Section 3.4.10) we then apply Sheppard summing to achieve twice the resolution improvement when compared to a widefield microscope. The SR-BCM theory is an extension of the conventional PAM [Verveer *et al.*, 1998] and ISM [Schulz *et al.*, 2013] detailed in the previous sections.

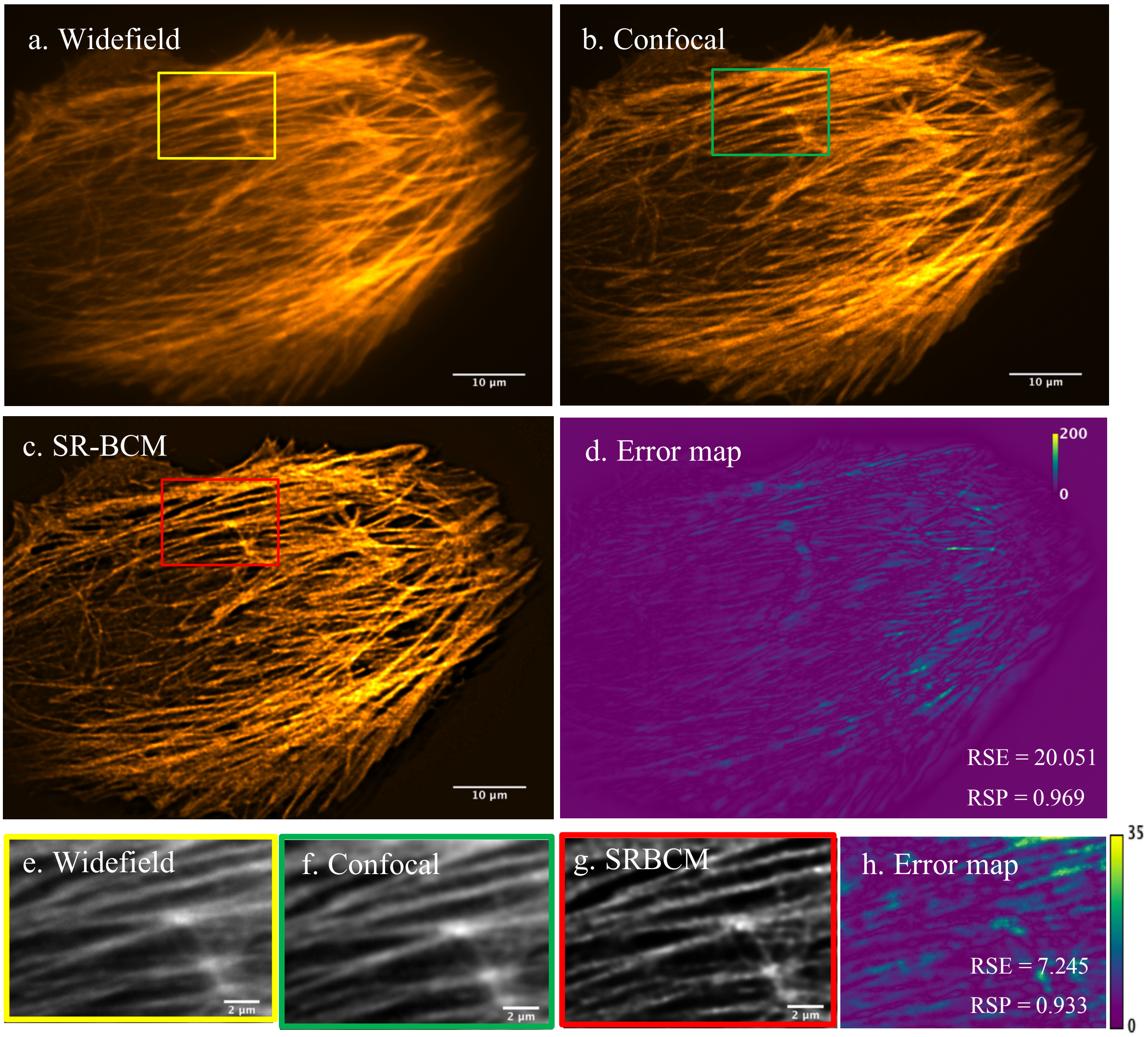

Fig. 3.6 shows the NanoJ SQUIRREL error map for an area scanned and reconstructed using SR-BCM. (a) is the widefield image, **(b)** is the confocal image collected in ON camera, **(c)** is the SR-BCM image and **(d)** is the NanoJ error map generated with widefield image as reference frame and SR-BCM image as super resolution frame. The global RSP with indicate that there is a high correlation between these images calculated using Pearson correlation method and low global error indicated by the RSE value calculated using NanoJ SQUIRREL ImageJ plugin. **(e), (f)** and **(g)** are zoomed in selection area of widefield, confocal and SR-BACM respectively. **(h)** is an error map between **(e)** and **(g)**.

The collection of conjugate and non-conjugate planes allows for enhanced background rejection which improves the signal-to-noise ratio while allowing Sheppard summing to achieving $\sqrt{2}$ times resolution improvement when compared to a widefield microscope. This image is further deconvoluted to double the resolution compared to a widefield image. **Figure 3.6 (a)** is a widefield image, **figure 3.6 (b)** is confocal and **figure 3.6 (c)** is an SR-BCM post processed image after deconvolution. Figure 3.6 (d) is the error map obtained using NanoJ SQUIRREL.

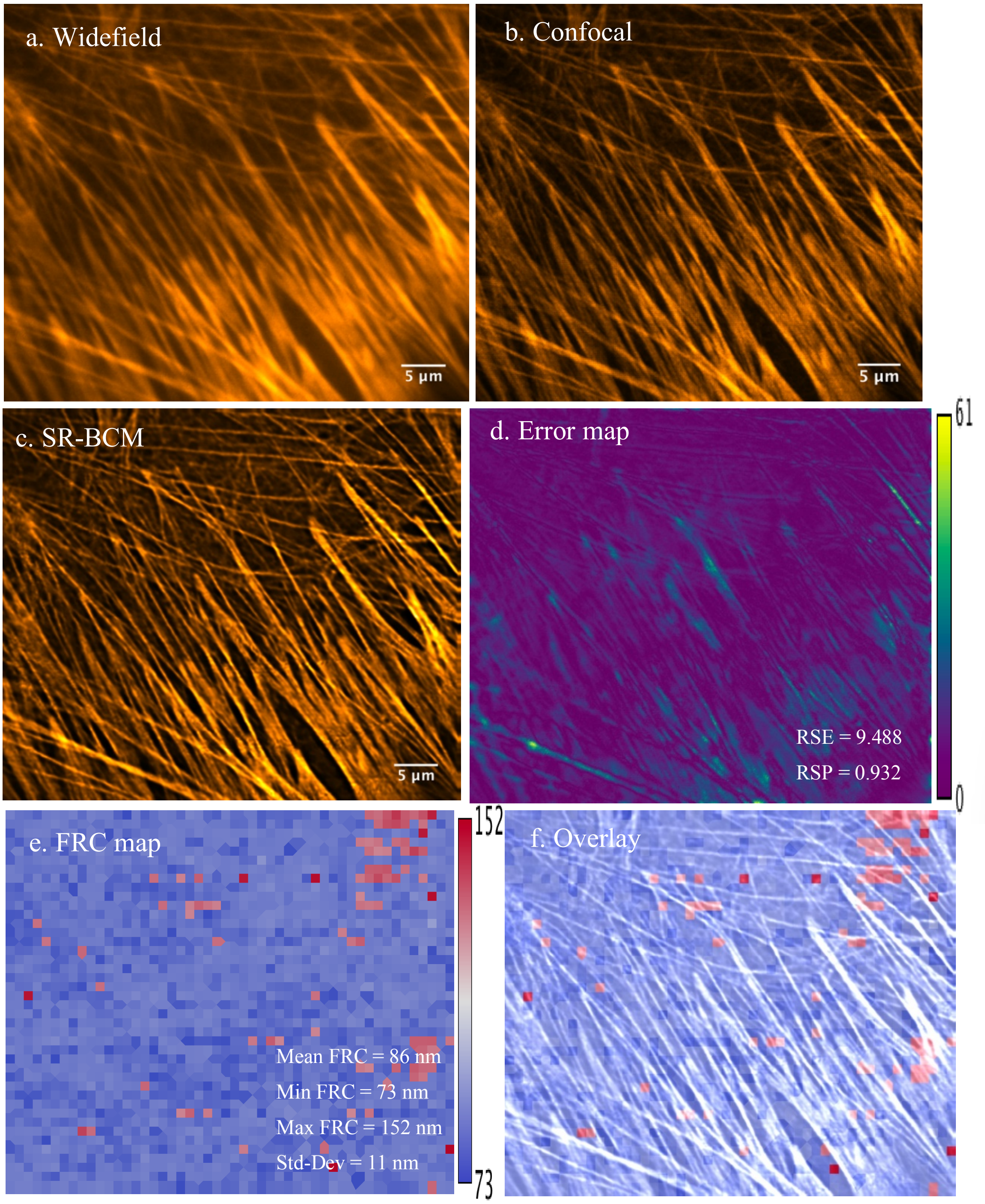

Fig. 3.7. shows the NanoJ SQUIRREL error map for an area scanned and reconstructed using SR-BCM. (a) is the widefield image, **(b)** is the confocal image collected in ON camera, **(c)** is the SR-BCM image and **(d)** is the NanoJ error map generated with widefield image as reference frame and SR-BCM image as super resolution frame. **(e)** is the FRC map generate by reconstructing two SR-BCM images generated by two sets of SR-BCM raw data acquired consecutively. Mean FRC is 86 nm. **(f)** is the overlay of FRC maps and SR-BCM image.

Figure 3.7 shows the resolution improvement of SR-BCM compared to widefield and confocal using FRC map generated using NanoJ SQUIRREL. The software splits an image into several sections and computes the FRC value for each section. Mean FRC of 86 nm is obtained for this image.

3.4.7. Comparison of SR-BCM with software based ISM

We now compare our implantation of ISM, SR-BCM, with conventional confocal microscopy and a software-based ISM to demonstrate the superior background rejection afforded by using the DMD in both the collection and excitation pathways. The ISM compared to in this work is the CSD-ISM implementation which has elegantly applied resolution enhancement with a spinning disk optical setup using a stroboscopic method to capture individual frames [Schulz *et al.*, 2013].

In the SR-BCM optical setup, data collected on the ON camera is equivalent to a conventional confocal system with the DMD micromirrors acting as an analogue of a conventional confocal aperture. **(figure 3.8a)**. Data collected on the ON camera can then be used to obtain the software-based ISM image (figure 4b). The ISM processing used in **figure 3.8(b)** requires an initial step to identify the confocal spots using localization software's such as ThunderSTORM [Ovesný *et al.*, 2014] or RapidSTORM [Steve *et al.*, 2012]. This localization requires a threshold, which can be used to limit the out-of-focus light and is discussed **in figure 3.8**. This thresholding method can be inefficient as confocal spots with low intensity can be missed. SR-BCM does not require any thresholding as emission spot finding is based on calibrating the exact expected emission spot pixels in both ON and OFF cameras. This is achieved by precisely mapping the DMD pixels with both ON and OFF camera pixels. Our DMD-camera calibration technique which achieves a precision with an error of less than 130 nm (2 camera pixels). This to our knowledge is the best achievable DMD to camera mapping algorithm. The resultant background corrected SR-BCM image can be seen in **figure 3.8(c)**. This SR-BCM image is deconvoluted using AutoQuant software as given in **figure 3.8(d).**

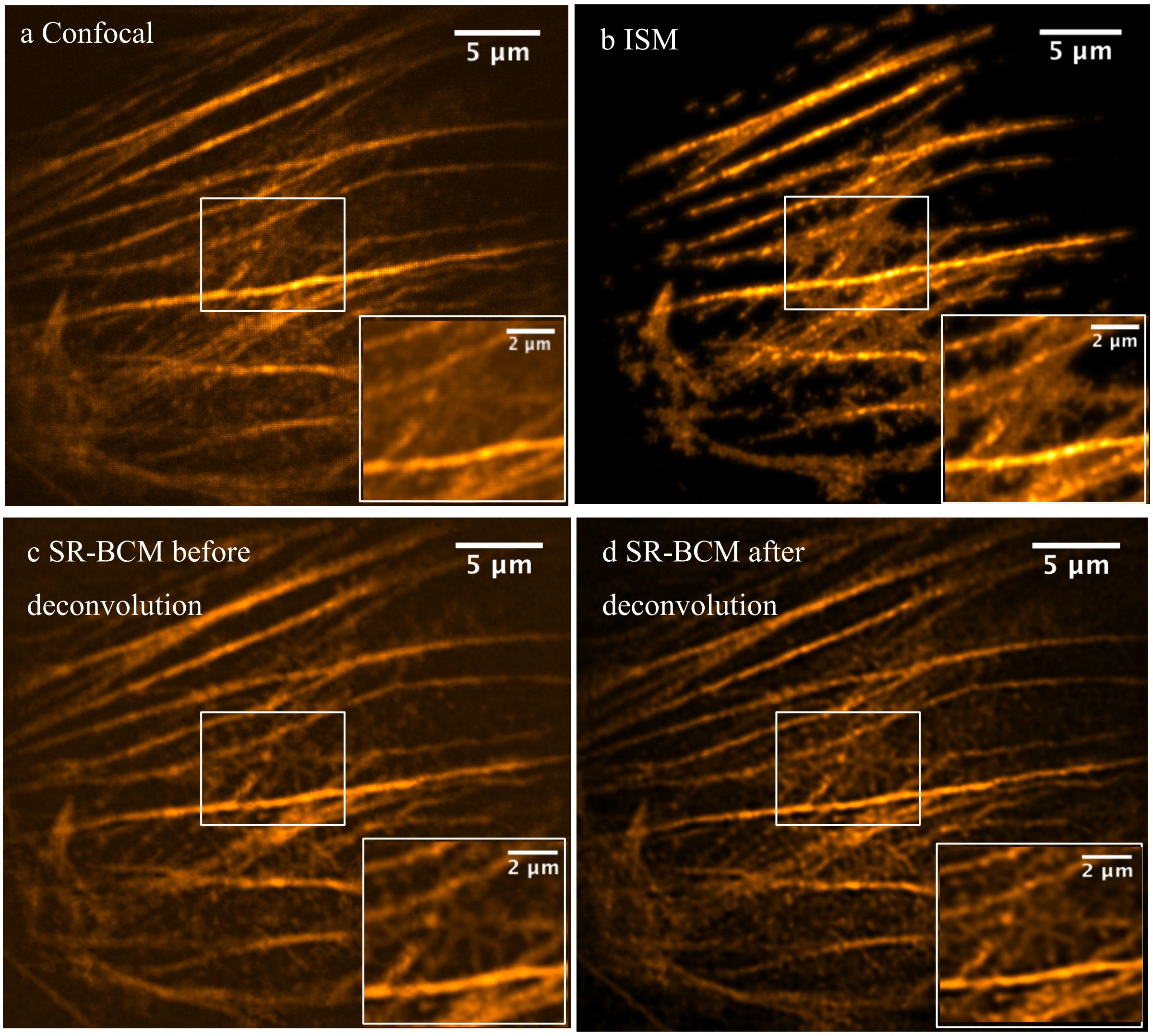

Fig. 3.8. A comparison of confocal, CSD-ISM (algorithm) and SR-BCM on BPAEC labelled for F-actin filaments with phalloidin. (a) The confocal image, data collected on the ON camera using the DMD as a physical pin-hole. This is a maximum value projection of the 225 frames collected, one frame for each DMD pattern. **(b)** The CSD-ISM algorithm image calculated on the single frames from **(a)**, the position of the confocal spots was calculated using Thunderstorm, this requires the selection of a threshold. **(c)** The SR-BCM image is calculated using the methods outlined in this work. Mapping the DMD to the cameras allows for a background correction without the need for thresholding. **(d)** The SR-BCM image after deconvolution with Huygens deconvolution with classic maximum likelihood deconvolution. Insets magnified for clarity.

The SR-BCM optical setup also allows us to obtain MSIM and AiryScan equivalent images which are based on collecting the full emission spot without physical apertures to reject out-of-focus light. SR-BCM performs this by adding the ON and OFF emission spots collected in the two cameras to restore the full PSF followed by employing MSIM and AiryScan (section 3.4.11) equivalent algorithms (provided with this work). A resolution comparison of SR-BCM is performed on 100 nm bead samples and compared with resolutions achieved using widefield imaging, confocal and MSIM (section 3.4.10).

Figure 3.8 is effect of thresholding on a plant leaf tissue sample. Thresholding increases from (a) to (j). As thresholding increases, background signals are subtracted making the image blurry.

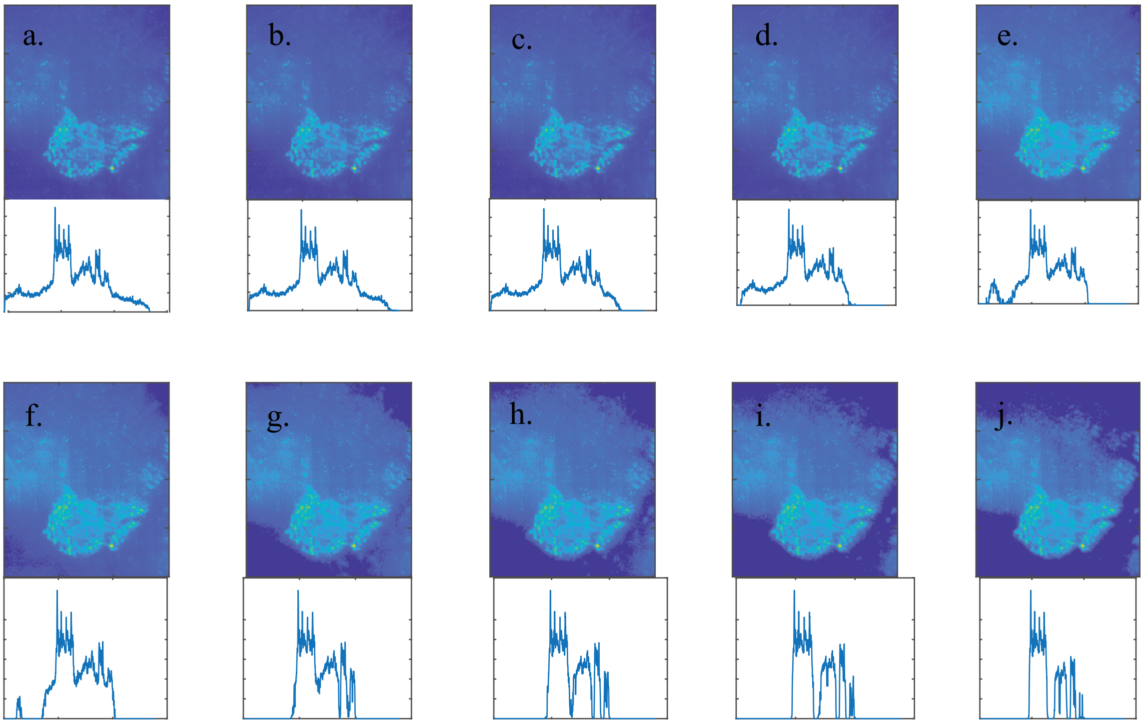

Fig. 3. 9. Effect of thresholding on a plant leaf tissue sample. This figure describes the effect of thresholding of an image. Graph represents a line profile through the corresponding image. Scale of thresholding increases from (a) to (j). As thresholding increases, background signals are subtracted making the image blurry.

3.4.8. SR-BCM data running in ON and OFF camera

Individual multifocal raw data frames collected from the camera can be deconvoluted before running the data through SR-BCM post processing. This does not make substantial differences in the final image. But the square spot collected in the cameras due to the square shape of DMDs can be resolved by running the raw data through deconvolution. **Figure 3.10 (c)** and **(d)** are videos of simple summed reconstructions of the data in ON **(figure 3.10 (a))** and OFF **(figure 3.10 (b))** camera respectively. **Figure 3.10 (e)** and **(f)** are the final summed image for the data collected in ON and OFF camera respectively. **Figure 3.10 (g)** is the corresponding SR-BCM image. **Figure 3.10 (h), (i)** and **(j)** are line profiles through ON, OFF and SR-BCM images. Higher intensity of **figure 3.10 (i)** compared to **figure 3.10 (h)** indicates higher intensity originating from out-of-focus planes of the sample. **Figure 3.10 (j)** indicates approximately 7 times higher signal to noise ratio after background correction of SR-BCM.

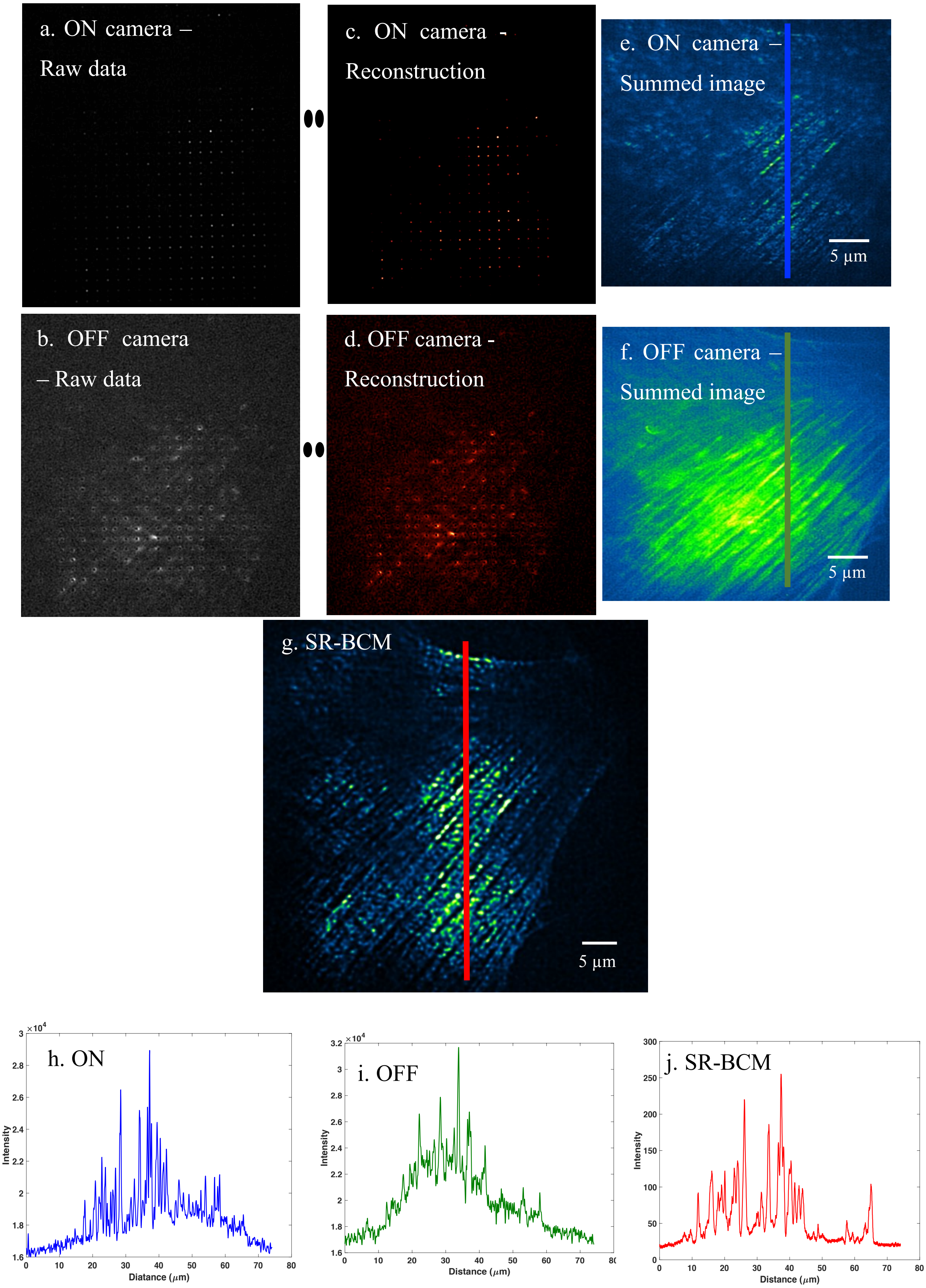
a. ON camera –
Raw data
c. ON camera -
Reconstruction
e. ON camera –
Summed image
5 µm
b. OFF camera
– Raw data
d. OFF camera -
Reconstruction
f. OFF camera –
Summed image
5 µm
g. SR-BCM
5 µm
h. ON
×10^4
3
2.8
2.6
2.4
2.2
2
1.8
1.6
Intensity
0
10
20
30
40
50
60
70
80
Diatance (µm)
i. OFF
×10^4
3.2
3
2.8
2.6
2.4
2.2
2
1.8
1.6
Intensity
0
10
20
30
40
50
60
70
Distance (µm)
j. SR-BCM
300
250
200
150
100
50
0
Intensity
0
10
20
30
40
50
60
70
80
Distance (µm)

Fig. 3. 10. SR-BCM data running in ON and OFF camera. (**a**) Video of in-focus data collected in ON camera with 3x3 DMD pixels as pinhole size and 3x5 DMD pixels as distance between two pinholes. (**b**) Video of out-of-focus data collected in OFF camera. (**c**) Video of reconstruction in ON camera. (**d**) Video of reconstruction in OFF camera. Red LUT is given for reconstruction video. (**e**) Sum of all the 225 frames in ON camera. (**f**) Sum of all the 225 frames in OFF camera. (**g**) SR-BCM image. **(h)** Line profile through (e). **(i)** Line profile through (f). **(j)** Line profile through (g).

3.4.9. SR-BCM post processing

Confocal based structured illumination microscopy imaging, SR-BCM, described in this work with post processing collects in-focus and out-of-focus PSF separately to make the efficient use of the fluorescence emission from the sample. SR-BCM is slow compared to rapid confocal as there is a need to collect all the illumination frames of confocal ON and OFF data in two separate cameras frame by frame and then running the data through the reconstruction code to get a weighed subtraction of out-of-focus plane emission intensities from in-focus plane intensities to improve the signal-to-noise ratio.

Point illumination based techniques use either a physical pinhole or a digital pinhole to reject the out-of-focus light. Physical pinhole is a physical aperture to block the out-of-focus light such as in conventional laser scanning microscope and spinning disk microscope. This can reduce the intensity of the signal collected because the aperture blocks a major part of the emission intensity. In digital pin holing, the emission spot is fitted to a Gaussian mask. Out-of-focus light changes throughout the sample as the structures in biological samples are highly inhomogeneous. SR-BCM out-of-focus subtraction is advanced in this regard as it is solely optical with no requirement of digital pin holing or the assumption of out-of-focus PSF being constant throughout the sample.

Raw data are collected using either 3x3 pin holing with 225 frames or 2x2 pin holing with 100 frames in ON camera and OFF camera. The ON and OFF data are run through the reconstruction code. In the code, each DMD illumination spot is selected one by one and the position of each spot in the ON and OFF camera data was found using the calibration lookup table. Calibration lookup table was found by camera-DMD calibrating technique detailed in Chapter 2. A square area was cut around each illumination spot in all the frames. These cut sections were saved for ON and OFF data separately.

Following are the main steps involved in reconstruction,

1. Load both ON and OFF camera data.
2. Using the DMD coordinates of the multifocal patterns projected, we can go to the camera coordinates for each emission spot using the calibration lookup tables.
3. A square section is cut around the expected ON and OFF camera pixels. We now have the ON and OFF cut section of each emission spot of each frame separately for ON and OFF camera data. This increases the versatility of the system with the ability to build the final image using various modalities with post processing.
4. Invert the OFF PSF with the equation,

   OFF_cutsection_new = (OFF_cutsection * (-1)) + MAX(OFF_cutsection) + MIN(OFF_section)

   This inverts the intensity collected in the ring towards the centre. This inverting is crucial for subtracting the blead through intensity. Simulation of blead through intensity is given in Section 3.4.4.
5. Optionally, a mask can be multiplied with the square cut section around the subtracted cut section obtained for ON and OFF data. This can improve the signal-to-noise ratio of thick samples. Create a matrix (mask) with a zero array of size equal to cut section. Make a centre square with pixel value 1. The size of the centre square equals to the number of pixels in the camera expected to collect the emission spot from one DMD confocal pinhole. For example, if 3x3 DMD pixels are used as the pinhole size, camera area corresponding to this is 6x6 camera pixels. This is for Andor sCMOS Zyla 4.2 camera employed in this work which has 6.5 µm pixel size which is approximately half of the DMD pixel size. 6x6 pixels is the size of the centre square of the mask. Masking rejects the scattered light intensities collected in pixels outside the expected spot size. Multiply this mask with ON and OFF cut sections.
6. Subtract 1/10th of the OFF section from ON cut section. This will give the new background corrected cut section. Discussion of the chosen weight ‘1/10’ is discussed in detail in Section 3.4.4.
7. This new cut section is multiplied with a Gaussian mask of standard deviation 1.5.
8. Magnify this cut section with a magnifying factor (magnification factor used for this work is eight). Build a zero image matrix with size equal to 2*magnification

factor*number of pixels in camera. Add the magnified cut sections back to this image matrix.

9. Demagnify the image matrix by magnifying factor used in step 10. This step doubles the number of pixels in the final image. Data are acquired in Andor sCMOS zyla 4.2 camera which has a pixel size of 65 nm in sample plane, when using a 100x objective. Pixel size in an SR-BCM image will be 32.5 nm (65/2).
10. Deconvolve the matrix obtained in step 11 to get the final SR-BCM image.

3.4.10. Resolution calibration of SR-BCM and comparison with other point-based illumination techniques.

Fluorescent beads of 100 nm were used to calibrate the resolution of SR-BCM and it was compared with other point illumination based imaging techniques. A widefield image was obtained with all the DMD pixels ON. Confocal image was acquired with 2x2 DMD pixel pinhole size (272 nm in image space) and inter pinhole distance 2x5 DMD pixels (1,360 nm in image space). These confocal data were acquired in rapid mode without deconvolution. SR-BCM data were acquired using both ON and OFF camera with the same pattern as used for acquiring widefield and rapid confocal image. SR-BCM was reconstructed with the post processing algorithm (Section 3.4.8). Image acquired after running the data through the post processing algorithm of SR-BCM was not deconvoluted for this bead data to demonstrate the resolution improvement of the technique even without deconvolution.

MSIM image is reconstructed using the SR-BCM raw data. The original MSIM optical setup does not use a physical pinhole to reject the out-of-focus intensity, but it uses a digital pin holing process by multiplying the emission spot with a Gaussian mask of SD 1.5. In SR-BCM setup, emission spots acquired in ON and OFF camera were added to restore the full emission spot without any physical out-of-focus rejection, equivalent to MSIM optical setup. The spot is multiplied by a Gaussian mask of SD 1.5 followed by ISM procedure to enhance the resolution and render the MISM equivalent image using SR-BCM setup.

Figure 3.11 (b) is the normalized intensity plotted against distance for widefield, confocal, MSIM, and SR-BCM of 100 nm bead sample. **Figure 3.11 (a)** is the image of 100 nm bead SR-BCM image. FWHM of widefield is 400 nm, confocal is 317 nm, MSIM is 270 nm and SR-BCM is 261 nm. SR-BCM without deconvolution provides a resolution improvement of more than $\sqrt{2}$. This is attributed to the additional out-of-focus subtraction. Deconvolution further enhances the resolution. It is to be noted that none of the images in this section is deconvolved. This is to acquire and compare the resolution improvement of techniques without deconvolution and to demonstrate the resolution improvement of SR-BCM.

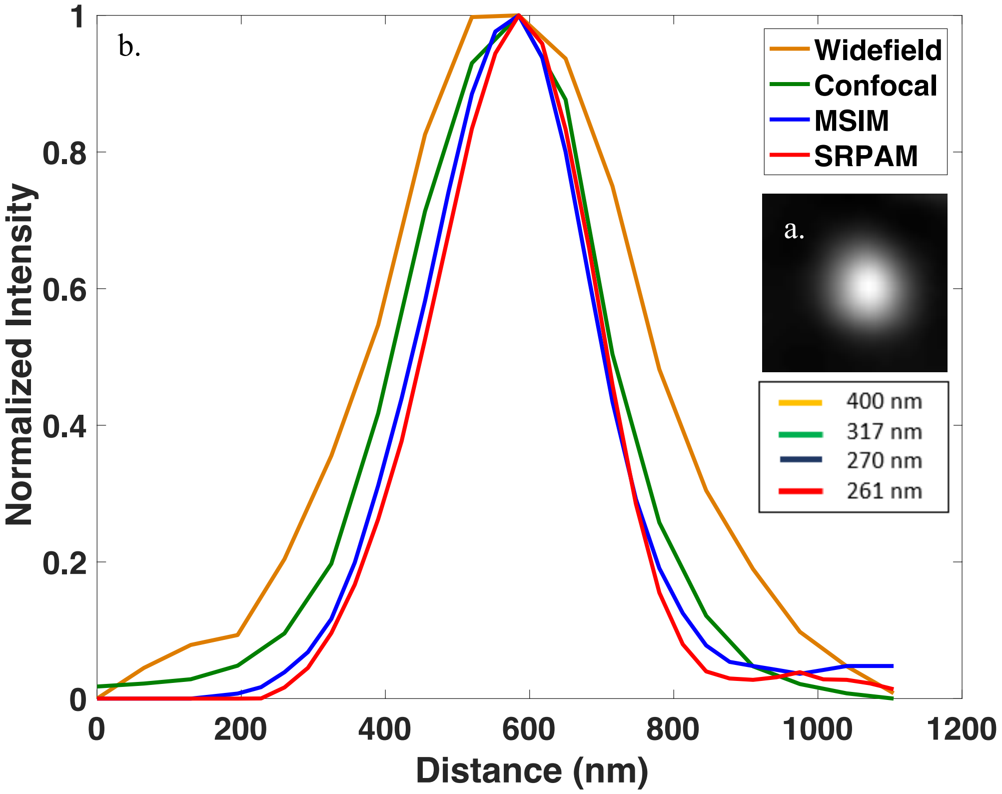

Fig. 3. 11. Resolution calibration of SR-BCM. (a) SR-BCM image of 100 nm fluorescent bead. **(b)** Normalised intensity comparison of data reconstructed using widefield, confocal, SR-BCM and MSIM.

3.4.11. AiryImaging

This section details a method and algorithm to obtain an AiryScan equivalent image using any camera based confocal setup. Image Scanning Microscopy was first theoretically developed by Sheppard in 1980s. AiryScan microscopy from Zeiss efficiently implements ISM by collecting the emission spot with a GaAsP detector followed by post processing based on Sheppard summing. The GaAsP has 32 detectors arranged in a hexagonal arrangement as shown in **figure 3.11(a)**. Diameter of the solid circle is 1.25 Airy Unit (AU) and diameter of the smaller circle is 0.2 AU. AU is the diffraction spread of a point emitter defined by,

$$\mathrm{AU} = \frac{1.22 \times \lambda}{2 \times \mathrm{N.A}} \qquad \textbf{(16)}$$

where λ is the wavelength of emission light in nanometres and N.A is the numerical aperture of the objective. The ISM implemented in the AiryScan is based on considering each small detector in a GaAsP detector acting as a displaced pinhole of a confocal microscope. There are four rings in the GaAsP detector structure, with the first detector/first ring in the centre or along the optical axis. Intensity collected in the other detectors located in 2nd, 3rd and 4th rings is equivalent to the intensity collected with a displaced pinhole, displaced from the optical axis. When the Airy disk of the emission PSF hits the detector, 32 images are generated with each image corresponding to the intensity detected by each small detector. Each of the 32 images is deconvoluted separately using Wiener deconvolution and then weighted summing of these 32 images results in an AiryScan image.

AiryScan equivalent image using a camera based confocal setup is generated by considering each pixel in the camera as an analogue of the small detectors in a GaAsP detector. Data can be collected using any multifocal confocal setup using a DMD or spinning disk or any single spot confocal setup using laser scanning can be used. We divide the rectangular camera detector arrangement into four rectangles (equivalent to the four rings in a GaAsP detector).

Due to the hexagonal arrangement of the GaAsP detector all the detectors in one ring are equidistant from the centre detector or optical axis while all the pixels in one rectangle are not equidistant from the centre or the optical axis. This is compensated with different weights for pixels depending on their location in the camera with respect to the optical axis. There are 49 displaced pinholes divided into 10 different weights, **figure 3.12 (b).** All the pixels which are numbered with the same number are displaced at same distance from the centre. Depending on the location of the pixels or displaced pinholes, its contribution to the final image is calculated. The emission wavelength is 505 nm with 100x magnification, 1.49 N.A oil objective for the data acquired to reconstruct the images in **figure 3.12 (c)** and **(d)**. In this setting, one AU is 212.44 nm. Andor sCMOS Zyla 4.2 camera is used in this optical setup which has a pixel size of 6.5 µm (65 nm for 100x objective). Detector area in this camera based AiryImaging is 7x7 pixels which is 455 nm and covers the full Airy disk of the emission PSF of a point emitter.

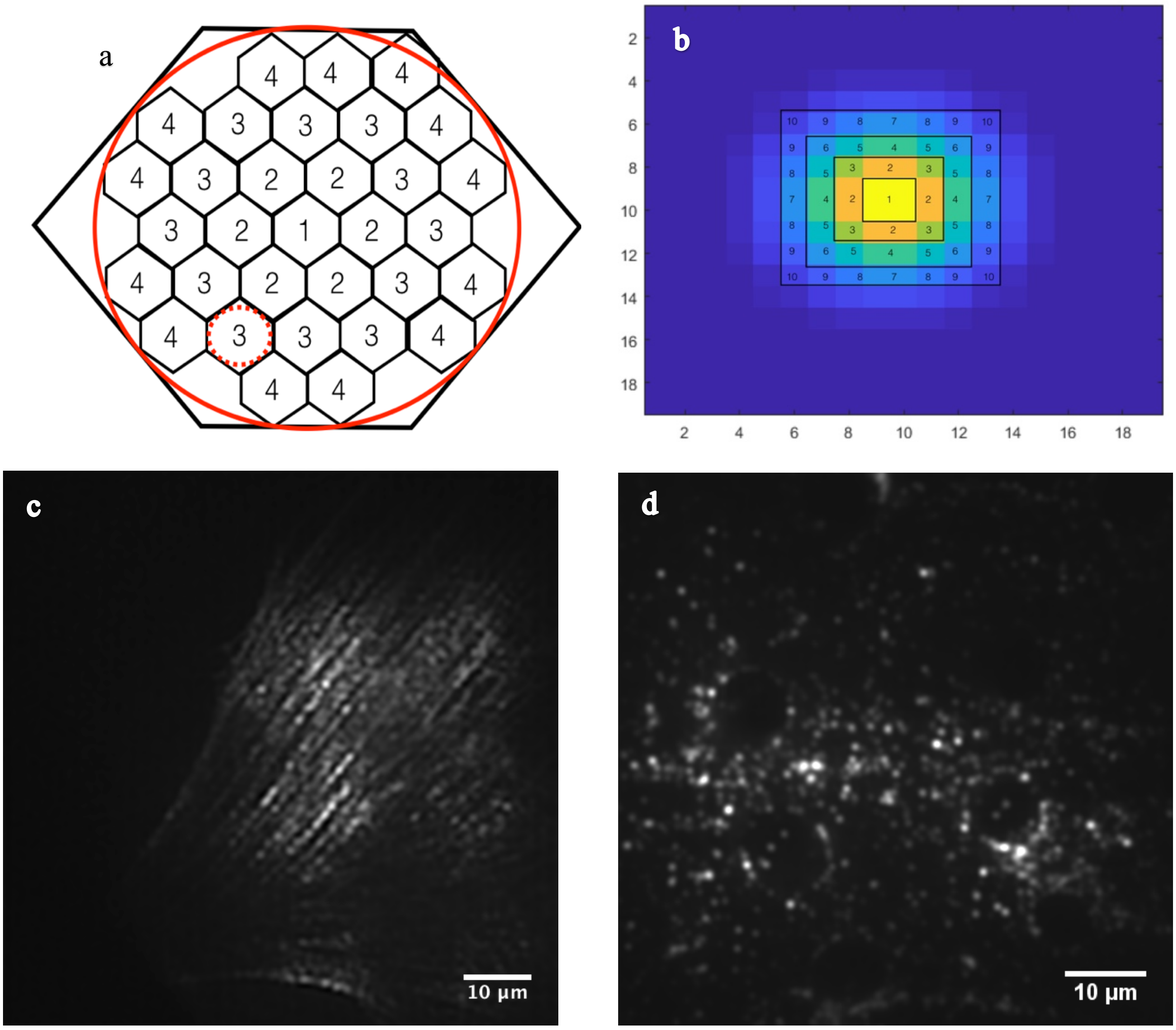

Fig. 3. 12. AiryImaging. (a) Hexagonal GaAsP detector arrangement of AiryScan detector. **(b)** Dividing the camera pixels to perform AiryScan equivalent algorithm. **(c)** AiryImage of 100 nm actin sample. **(d)** AiryImage of 100 nm fluorescent bead.

Here, it is worth recalling that SR-BCM optical setup collects both in-focus and out-of-focus emission spots in two separate cameras. In AiryScan, since there are no physical pinholes to reject the out-of-focus light in the emission pathway, we add the in-focus and out-of-focus emission spots to restore the complete emission spot and then run the data through our algorithm for camera based imaging to obtain the AiryImage. **Figure 3.12 (c)** and **(d)** are AiryImages obtained using this technique. This algorithm uses the DMD camera calibration method detailed in Chapter 2 to find the coordinates of each emission spot. For setups which are not based on DMD illumination such as a spinning disk or laser point scanning setups can also use the open source algorithms such as ThunderSTORM or rapidSTORM to find the emission spot coordinates in the camera and then run the data through AiryImaging algorithm presented here to get AiryImages. Codes for obtaining AiryImages with any confocal optical setup is provided with work and are given Appendix 7. Equivalently, an MSIM image can be obtained with the SR-BCM setup and applying the algorithm after summing the in-focus and out-of-focus emission spot and performing ISM followed by deconvolution as given in section 3.4.10.

3.5. Discussion

SR-BCM modality achieves resolution improvement like previous elegant implementations such as SIM, MSIM, iSIM *etc*. SR-BCM utilises the emission intensity effectively to improve the resolution and image quality by collecting out-of-focus light separately. Point based patterned illumination has been chosen in this implementation to increase the spatial frequencies passing through the objective and to combine it with the implementation of digital light processing by utilizing the out-of-focus emission information. Theory of SR-BCM is an extension of PAM and ISM imaging techniques.

Implementation of instant SIM increased the speed of imaging compared to MSIM and achieved 100 Hz scanning rate. Rapid confocal runs at 350 confocal scans per second. Resolution enhancement in rapid confocal is not instantaneous. Resolution enhancement in rapid confocal is based on deconvolution or super resolution reconstruction algorithm during post processing. Rapid confocal has been demonstrated to visualize the dynamics of cellular processes in drosophila embryogenesis and amoeba cells. This is discussed in Chapter 6.

For higher resolution imaging requirements, the system can currently perform post processed SR-BCM or LM (as discussed in Chapters 4 and 5). SR-BCM reconstruction codes are given in Appendix 6. The ability of the system to generate other point based illumination techniques such as MSIM was also explored in this chapter. The method and algorithm to perform an analogue of GaAsP detector based AiryScan with camera detector based AiryImaging is presented which can be easily adopted into any camera based point illumination microscope.

For future work, implementation of microlens arrays between the DMD and the cameras can optically provide higher resolution for rapid confocal. Another potential future development is in deconvolution. For deconvolution, PSF of the system is either theoretically calculated or experimentally calibrated using beads. With the system presented in this work, ‘real’ PSF is obtained with point-based illuminations. Further investigations and comparisons into whether this ‘real’ PSF can improve the image restoration of deconvolution processes will be interesting. Even though confocal imaging has been explored and widely adopted for biological imaging, its potential to give super resolution is currently limited to $\sqrt{2}$ fold improvement and 2 fold improvement with confocal combined with deconvolution. Exploring the nonlinearity of fluorophores with SR-BCM could be a potential extension of SR-BCM to get higher resolution. A combination of ISM frequency mixing concept with stimulated emission can be developed. STED microscope can be easily built into this system by projecting the excitation laser though one optical pathway of the system and depletion laser through the other optical pathway of the system. Machine learning techniques can be used for automation by training the system to switch between widefield and super resolution. For example, in a plant and bacteria sample, the system can be trained to do super resolution when bacteria move close to the plant cells. Using the development of imaging techniques and software presented in this work, the microscope can be transformed and adapted to the imaging requirements of various biological samples. Due to the complexity of biological systems in nature, such a versatile system could be very powerful in terms of the ability to adapt depending on the needs of biological investigations. Examples for this adaptation of the system is given in Chapter 6.

Chapter 4

Development of Targeted Illumination for Optical Microscopy and Implementation of Stochastic Optical Reconstruction Microscope

4.1. Summary

An epifluorescence targeted illumination system was developed which can selectively illuminate specific bacteria of interest from a group. In a mother machine [Wang *et al.*, 2010] when bacteria are lined up in various channels, bacteria of interest are illuminated without photodamaging other bacteria. One of the major advantages of epifluorescence targeted illumination is that it allows high power super resolution imaging on selective areas of interest without photobleaching other areas, as will be detailed in Chapter 5. Software for targeted illumination presented in this chapter can be widely adopted with any Digital Micromirror Device (DMD) based setup even without the need for the collected optics through a DMD. The power and pattern of light illumination are precisely controlled using the software. This chapter also includes the implementation of STochastic Optical Reconstruction Microscopy (STORM) microscopy into the system which expands the versatility of the system. The system is applied to study protein colocalization of NIH 3T3 cells. The two illumination pathways of the optical setup are used to switch between LED based widefield illumination and STORM in two colours to find the colocalization of protein in specific regions of the cell.

4.2. Introduction

Targeted illumination has been used in optical microscopy to manipulate and explore various cellular dynamics and structures. There are many techniques which exploit targeted illumination including optogenetics [Feng at al., 2006], Fluorescence Recovery After Photobleaching (FRAP) [Snapp *et al.*, 2001], photoactivation [Weiner *et al.*, 2009], ablation [Damisah *et al.*, 2017] and photo-conversion [Saberianfar *et al.*, 2015]. Development of targeted illumination software and its implementation into the optical setup described in this chapter is a tool which can be easily implemented and widely adapted to these applications.

This chapter outlines the development of the software written in MATLAB for targeted illumination system using Digital Light Processing (DLP) technology. The targeted illumination software was developed to selectively illuminate the regions of interest in a sample. To test the performance and establish the application of the system, the technique is applied for the selection of a single channel and to selectively illuminate specific bacteria of interest in a 'mother machine system'. A mother machine system is a microfluidic device to study generations of bacteria in balanced growth conditions for long term imaging [Wang *et al.*, 2010]. *E. coli* cells expressing GFP are imaged to demonstrate the capabilities of the system.

This chapter also details the implementation of STORM with the DMD based illumination system. In Localization Microscopy (LM), the inherent relative stabilities of the optically bright and dark states within a molecule are tuned to allow only a small subset of the molecules under study to be optically active at any point in time. This is then used to reduce the density of emitting molecules to the point where each emitting molecule is separated by a distance greater than the diffraction limit, essentially making the single molecule resolvable. By fitting the corresponding image of each emitting molecule to the point spread function (PSF) of the optical system, the location of the molecule can be determined to within a few nanometres [Hess *et al.*, 2006]. The emitting molecules are then returned to their dark state or a bleached state and a different subset of molecules is activated. This process is repeated until a substantial number of single molecules has been localized. The localizations are used to build a molecular map with nanometre resolution of all the molecules of interest. In this work, a STORM was built using DMD based illumination system. The system was tested on two different biological test beds: HeLa cells stained with Alexa Fluor (AF) 647 phalloidin to calibrate the resolution of the system and NIH3T3 cells transfected with DNA encoding the neural cell adhesion molecular NrCAM. The latter was labelled with antibodies and co-labelled with a marker of primary cilia, a membrane sub-organelle. The key objective was to test the ability of our system to determine the subcellular distribution of a specific protein.

NIH 3T3 cells [Todaro *et al.*, 1963] and HeLa cells [Scherer *et al.*, 1953] are immortal cell lines cultured and immunolabelled to test the system. 3T3 (3-day transfer, inoculum 3×10^5 cells) are an established cell line from NIH Swiss mouse embryonic fibroblast cells. They are applied for various cell based assays, DNA transfection studies, protein localization studies *etc*. HeLa cells are human cell line derived from cervical cancer cells. These are immortalised, and its stability has enabled different disease studies, development of vaccines, gene mapping *etc*. This chapter details the cell culture, DNA transfection, serum starvation to grow cilia and immunolabelling for various proteins and microfilaments.

NIH 3T3 cells are transfected to express the cell adhesion protein NrCAM, which plays an important role in cell-cell interaction in brain and peripheral nervous system and is labelled with AF647. Cells are serum starved on the second day from seeding cells to grow cilia. Arl13b is a protein known to exist in the cilium and these are labelled with rhodamine red (rrx). Arl13b is used to locate the position of cilia in the cell and STORM image is performed for NrCAM. Cilia and NrCAM are imaged in two colours by using the two independent illumination pathways of the system. This allows switching between two colour imaging, LED or laser based illumination and imaging modalities at sub millisecond transition .

4.3. Materials and Methods

4.3.1. Preparation of Test Samples

NIH 3T3-L (3T3) mouse embryonic fibroblast cells (obtained from Dr Frederic Charron, Montreal, Canada) are used for this work to build confocal, widefield, STORM and targeted STORM and to combine all these techniques to one single system. *E. coli* cells and HeLa cells are the different types of samples used for the work in this chapter.

4.3.2. Coverslip cleaning

For super resolution experiments, 22x22 mm size and 0.13 mm - 0.17 mm thick high precision coverslips are used. In this work, for super resolution experiments, coverslips were cleaned in 1M HCl for 30 minutes followed by cleaning in distilled water three times and then stored in 100% ethanol.

4.3.3. NIH 3T3 cell storage and growth media

NIH 3T3 cells were cultured, transfected and stained for different proteins and dyes to test and develop the system [Conacci *et al.*, 2002]. Cells are stored in cryogenic liquid nitrogen preservation chamber at -210°C – -196°C. Cells were grown on tissue culture dishes at 37°C in a humidified incubator gas-adjusted to 5% CO_2 in standard conditions (10% Fetal Bovine Serum in Dulbecco's Modified Eagle's Medium (DMEM, Gibco), 1% Glutamine (Gibco) + 1% Penicillin- Streptomycin (Gibco)).

4.3.4. Seeding cells

Cells are kept in growth medium (10%FBS + Pen/Strep + DMEM) at 37℃ incubators after thawing frozen cells. Confluency of cell culture is checked under the microscope until 90-100% of the plate is covered by cells. Old medium is removed, and cells are washed in Dulbecco’s Phosphate Buffered Saline (DPBS) to remove dead cells. After the wash, 1 ml of trypsin (0.25%, Calbiochem) is added to dissociate the cells into single cell culture suspension. Cells are put back in the incubator for 5 minutes followed by adding fresh growth medium into the cell culture. To count cells, trypan blue dye is added to distinguish viable cells (cells with intact cell membrane which excludes trypan and have clear cytoplasm) and non-viable cells (dead cells with blue cytoplasm). These are counted using haemocytometer counter to ensure approximately 1 million cells/ml of growth medium.

Cells are transferred to multi well plates (4-well round culture plates) containing coverslips (22 mm x 22 mm size and 0.13-0.17 mm thickness) in such a way that each well contains approximately 0.05 million cells per well for widefield, confocal or other non-super resolution experiments. For super resolution experiments, coverslips are cleaned according to the protocol given section 4.3.2, prior to transferring the cells. After transfecting the cells, the multi well plates are incubated overnight at 37°C to allow cells to attach to coverslips and grow.

4.3.5. Induction of primary cilia by serum starvation

Primary cilia are present on dividing cells in only one phase of the cell cycle (G1). However, this is very transient in rapidly dividing cells. Serum starvation makes the cells quiescent, increasing the number of cells in G1 and so increasing the proportion of cells bearing cilia [Tucker *et al.*, 1979]. Cells are taken from the incubator to the tissue culture hood. Old medium is taken off and the cells are cleaned with DPBS. Growth medium is made with 0.5% FBS in DMEM which contains 1% Glutamine and 1% Penicillin- Streptomycin. 200 µl - 1 ml (depending on the size of coverslip and multi well plates used) of this medium is added to the cells and the cells are put back in the incubator.

4.3.6. Transfection

Induction of NrCAM expression in NIH3T3 cells was achieved through transfection of an expression vector (pIRES1neo) containing an NrCAM cDNA tagged with a hemaglutinin epitope (NrCAM-HA) [Falk et al 2002, Davey et al 2005]. Before transfection, penicillin /streptomycin free medium is added to the cells after washing the cells using DPBS. Cells are kept in incubator for 20 minutes in 250 µl antibiotic free medium before adding plasmids. For transfection, NrCAM-HA plasmid [Davey *et al.*, 2005] was introduced using Lipofectamine-2000 (11668019, Invitrogen) according to supplier’s recommendation. Briefly, a DNA-lipofectamine mix was created by adding DNA to Optimem medium and keeping for 5 minutes at room temperature. This was then added to a solution of lipofectamine in Optimem in a dropwise fashion and allowing to sit at room temperature for 20 minutes. 50µl of this solution (containing ~500 ng of pNrCAM-HA plasmid DNA) is added to each well containing serum starved NIH3T3 cells, as detailed above. Wells are then incubated at 37ºC overnight, to allow the transfected plasmid to induce expression of NrCAM-HA protein before fixation on the following day.

4.3.7. Fixing the cells

The cells were fixed on the following day (after 18-24 hours at 37°C) using 4% Paraformaldehyde (PFA) in 0.1 M phosphate buffer at pH7. The wells are placed in a rocker for 20 minutes. PFA fix is removed and the wells are placed in the rocker for 5 minutes in PBST (Phosphate Buffer Saline and 0.05% Triton). 3% normal goat serum is used as blocking serum. Blocking serum is added to cells for 1 hour before immunolabelling. After this, cells are ready for staining [Dang *et al.*, 2012].

4.3.8. Immunolabelling

Immunolabelling was performed as described by [Davey *et al.*, 2005]. NrCAM tagged with HA was detected by anti-HA rat monoclonal (11867423001, Sigma Aldrich; 1:1,000 in PBS, 0.05%TX100, 3% normal goat serum (PBST/NGS)), which in turn was detected by AF647 Goat Anti-Rat IgG (A21247 - Thermo Fisher Scientific) secondary antibody (1:200 in PBST/NGS, incubated 1-2 hours in dark at room temperature).

4.3.8.1. Staining micro-cilia

Arl13b (11867423001, Sigma Aldrich; 1:1,000 in PBS, 0.05%TX100, 3% normal goat serum (PBST/NGS)) is used as the primary antibody to label cilia. Rhodhamine red (rrx) was used as the secondary antibody.

After taking off the blocking serum and adding primary antibody staining solutions, cells are stored at 4°C overnight. After 24 hours, the solution is taken off and the cells are washed three times in PBST while placing the wells in the rocker for 20 minutes after each wash. After all three washes, the secondary antibody solution is added, and the dish is wrapped using tin foil to minimize damage. Wells are placed in the rocker for 1-2 hours. Antibody solution is removed, and the cells are washed in PBST for three washes of 20 minutes each.

4.3.9. Cell culture for phalloidin staining

HeLa cells or NIH 3T3 cells are cultured and fixed as described in sections 4.3.3 and 4.3.7. Fix is removed, and coverslip is cleaned 2-3 times for 5 minutes each using PBS. After the last wash, PBST is added to cells for 3-5 minutes to permeabilize the membrane. PBST is removed and the coverslip is washed with PBS for 2-3 times for 5 minutes each.

PBS solution for staining is prepared by adding 1% BSA to PBS in 1:100 ratio. This PBS solution is added to the cells for 20-30 minutes. 1% BSA acts as a blocking reagent. AF647/AF488 phalloidin is used to stain F-actin of cells. AF647/AF488 phalloidin is added to the PBS solution which contains 1% BSA in 1:40 ratio and then added to wells for 20-30 minutes. Cells are washed 3 times with PBS for 5 minutes each. After the washing, coverslips are used for imaging after mounting on to microscope slides.

4.3.10. STORM buffer

For STORM imaging, coverslips need to be mounted over 2 or 3 drops of STORM buffer. STORM buffer for this work is prepared by mixing 100 millimolar monoethanolamine (MEA), 0.5 mg/ml glucosidase, 40 µg/ml catalase and 10% w/v glucose in PBS solution [Dempsey *et al.*, 2011].

4.3.11. Mounting coverslips on to microscope slides

Coverslips are taken from wells and gently placed over the slide. For STORM experiments coverslips were mounted on microscope slides using STORM buffer and imaged immediately. For widefield, confocal, STED and SIM experiments, coverslips were mounted in vectashield or ProlongGold. Experiments showed that vectashield was more stable to photodamage in these samples than ProlongGold. Vectashield without DAPI was used for STED experiment.

4.4. Results

This section starts with the discussion of targeted illumination development and moves on to the discussion of building STORM microscopy using the DMD based illumination system. The NIH 3T3 cells and HeLa cells detailed in the previous sections are used to test the STORM implementation. Samples of *E. coli* cells expressing GFP are used to build and test the targeted illumination system detailed in the first part of this section.

For the software development of the targeted illumination system, a DMD chip controlled through a Field Programmable Gate Array (FPGA) controller board was programmed using MATLAB. The combination of these elements allows us to display 1 bit 1,024 by 768 pixel images at frame rates of roughly 23 kHz and 8 bit greyscale frames at 300 Hz. In a 1 bit image each pixel is defined as ‘ON’ or ‘OFF’ as described in Chapter 1. For 8 bit images, the DMD works as a pulse width modulator (PWM) based optical modulator, allowing us to change the amount of power delivered to the sample, with the PWM ‘ON’ time of each mirror being defined by a value between 0 and 255, with 0 being 100% ‘OFF’ and 255 being 100% ‘ON’.

Here it is worth recalling that the fluorescence from the sample, because of light projected using the 'ON' path, will be imaged using the 'ON' camera and 'OFF' pixels will direct fluorescence towards the 'OFF' camera, in such a way that the 'ON' camera will only contain fluorescence from the 'ON' pattern projected on to the sample. This not only enables point illumination for confocal microscopy, but any pattern in binary or grey scale can be projected on to the sample.

4.4.1. Targeted pattern projection

AF647 is drop cast on to a coverslip and mounted on a glass slide to get intense fluorescence emission from the sample for tests and alignments. Using the DMD, any pattern can be projected on to the sample. For example, in **Figure 4.1** an image of a heart is displayed on the DMD. Light from the illumination source in the 'ON' path projects an image of the heart on to the sample plane of the microscope. **Figure 4.1 (a)** shows the image recorded by the camera on the 'ON' path. This is light collected from the sample which is reflected off the DMD and collected by the 'ON' camera. It should be noted that the image on the DMD acts as a spatial filter on the return path. As the DMD acts as a spatial filter, only light hitting the DMD's 'OFF' pixels is collected by the 'OFF' camera. Since the light hitting the sample comes from the 'ON' path, only out-of-focus or scattered light is detected on the 'OFF' camera. **Figure 4.1 (b)** shows the image collected by the camera on the 'OFF' path. It shows the light diffracted at the edge and scattering back. The patterned illumination at the sample plane is collected by the camera on the back port of the microscope and is given in **Figure 4.1 (c).**

Fig. 4. 1. Patterned projection. If the 'ON' path light source is turned on and an image is displayed on the DMD, for example a heart, an image is projected though the illumination optics on to the sample plane of the microscope. **Fig. 4.1 a, b,** and **c** show the images collected on the 'ON', 'OFF' and backport cameras respectively.

4.4.2. Gradient illumination intensity control

A thin layer of AF647 provided a uniform photoluminescence sample which can be used to quantify the patterns projected on to the sample. **Figure 4.2** shows an 8-bit gradient image. The gradient has value ranging from 0 to 255, where a 0 represents no power being projected to the sample, and 255 represents the full laser power being projected. Values between 0 and 255 represent an amount of time the sample is illuminated, with 127 illuminating the sample for 50% of the time. **Figure 4.2(A)** shows the 8-bit image projected on to the sample which consists of a rectangular gradient on a solid black background. **Figure 4.2 (B1- B2)** are the images collected from the 'ON' and 'OFF' paths, the patterns produced are similar to each other but inverse. The light collected on the backport **Figure 4.2(C)** is a direct measurement of the photoluminescence from the sample. The gradient in this image is replicated from the sample. Due to an astigmatism caused by the low pass dichroic filter being used, the image has a slight blur. The light collected by the camera on the 'ON' path is sharp and in-focus and it clearly shows the gradient. It should be noted that light from the sample is also reflected by the DMD. For a DMD pixel set to a value of 127, all the light from the sample reaches the ON camera because speed of light is much higher than DMD flipping time. These images demonstrate one of the disadvantages of the DMD system to be used for collection and illumination. With a DMD pixel set to a value of 255, 100% of the light (ignoring losses) is directed to the microscope and 100% of the light returned from the sample is directed to the camera. However, for a DMD value of 127, 50% of the light is directed to the sample, allowing us to lower the illumination and the light collected is directed to the 'ON' camera. It is worth noting that intensity gradient seen in 'OFF' camera (**figure 4.2 (B2)**) is the scattered light from the system and not the light from the sample.

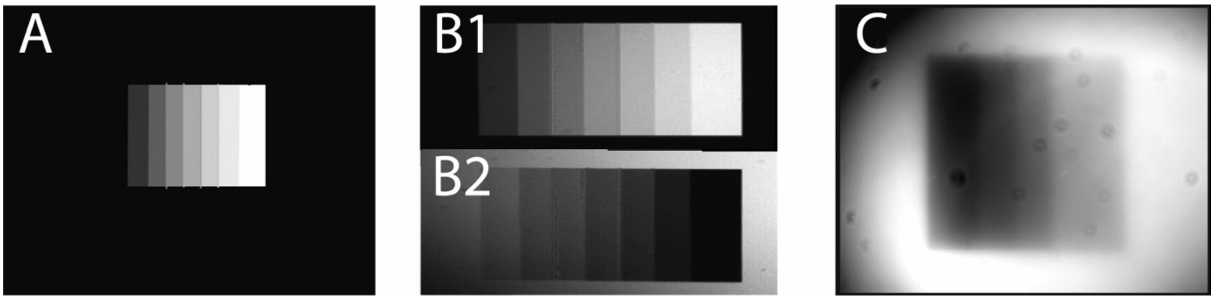

Fig. 4. 2. Gradient patterned projection. The ability to deliver controlled power is vital. **(A)** shows the pattern projected on to the DMD, illumination from the 'ON' path. **(B1 and B2),** the image captured by the camera on the 'ON' path **(B1),** and the 'OFF' path **(B2). (C)** is the image collected by the camera on the backport of the microscope.

4.4.3. Software development

This section outlines the development of the software written in MATLAB programming language for targeted illumination system using DLP technology. Software for targeted illumination presented in this section can be widely adopted with any DMD based setup without the need for the collection optics through the DMD. Power and pattern of light illumination are precisely controlled using the software. A custom made GUI was made for illuminating only a selected number of bacteria. The GUI in **figure 4.3** allows the user to illuminate only a selected area of interest in the sample. The circular shape is chosen considering the shape of the bacteria for investigation. The user can move the centre and radius of the circle to move the area of illumination along the field of view of the sample so that only the bacteria of interest are illuminated. Since the image loaded on to the memory of DMD is in MSB format, grey scale level of circles can be controlled. The user can also define the power with which the area is illuminated by changing the power slider from 0 to 255.

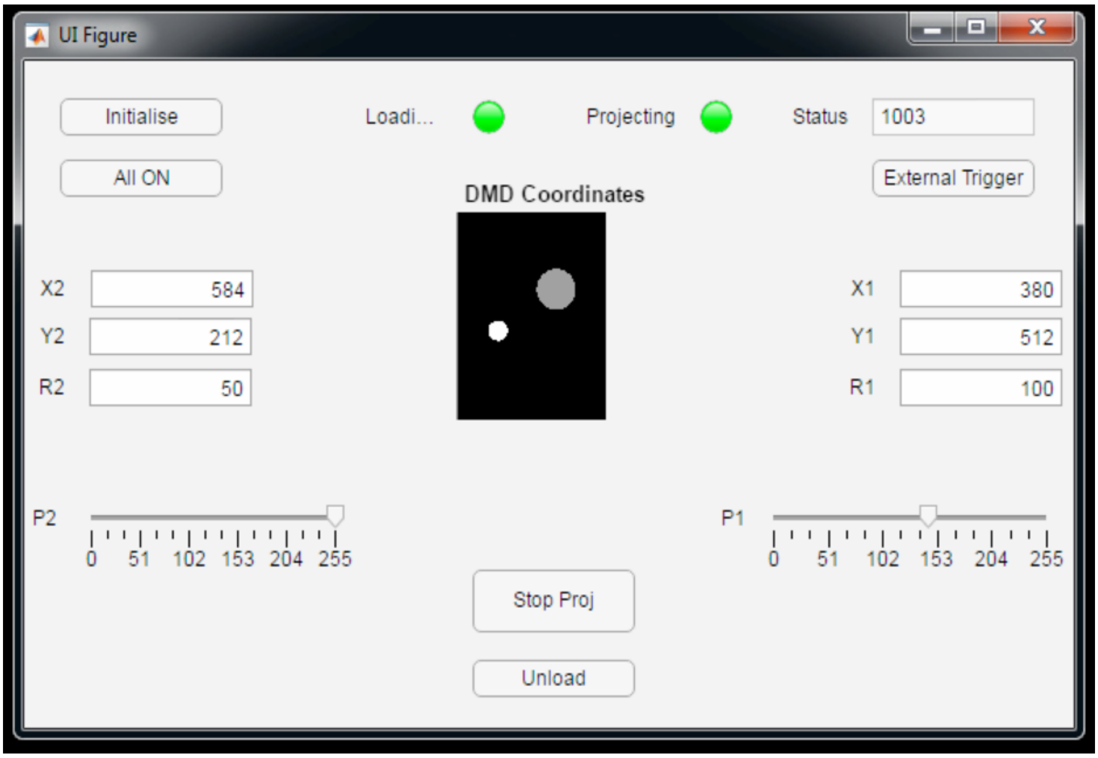

Status 1003

X2 584
Y2 212
R2 50

X1 380
Y1 512
R1 100

Fig. 4. 3. GUI for selecting specific bacteria of interest. GUI for patterned projection with two circles. Position, radius and power can be controlled.

For selected illumination of bacteria, it was important to determine its position in the camera. Initially, a phase image or a widefield image of the sample was taken and loaded into

MATLAB. The *E. coli* of interest were chosen, and its centroid MATLAB pixel coordinate was recorded. Alternately, the coordinates can be directly read from the camera. This pixel coordinates (x.y) was used as input in the GUI. The GUI converts the camera pixel position to DMD pixel position with the calibration polynomial/DMD lookup tables obtained when calibrating the camera (Chapter 2). The DMD projects a small circle with centroid of *E. coli* as the centre of the circle and the bacteria of interest were illuminated.

4.4.4. Application of targeted illumination

Development of targeted illumination was tested on *E. coli* cells expressing GFP. The size of an *E. coli* is approximately 0.5 µm in width and 2 µm in length. The smallest spot which can be projected on to a sample with a 13.6 µm pixel size DMD chip and 100x objective is ideally 136 nm, and with diffraction spread, it is approximately 160 nm. The size of an *E. coli* cell makes it a perfect candidate for testing targeted illumination. The performance of the system was tested by selective illumination of one of the daughter cells when a mother cell is dividing.

The single bacteria selection system and mother machine channel selection were built with the Cairn Focal Generation I system. The sample is illuminated through the ‘ON’ camera pathway using an LED and the fluorescence emission is collected using a camera at the back port of the microscope. Selective illumination of bacteria and control over the illumination power of cells are the major advantages of epifluorescence targeted illumination system. Live cell imaging of *E. coli* cells in mother machine channels were carried out.

For the development of targeted illumination, the DMD is setup as an illumination system to project down illumination power to an area of interest to achieve selective illumination on the sample. When light is projected on to the DMD system, it is oriented in such a way that illumination light reflected off the ‘ON’ pixels passes through a relay lens and on to the microscope. One of the major advantages of the DMD is that it can also project down grey scale images by flipping micromirrors to control the power with which the sample is illuminated.

4.4.5. Single bacteria selection system

As described in previous sections, in a single bacteria selection system, bacteria of interest were selectively illuminated using the GUI. The GUI used for this experiment is based on projecting two circles with the centre position and radius defined by the user. After taking the widefield image, camera coordinates for the centre of the circles and the desired radius of the circles to be projected were given as an input in the GUI. The circles can be loaded on to the onboard memory and projection can be started using the corresponding buttons in the GUI. Power of illumination intensity can be controlled by a sliding button. Power slider number 0 corresponds to the DMD in 'OFF' state or the micromirror turned to the pathway opposite to illumination, and 255 corresponds to the DMD in 'ON' state or the micromirror turned towards the illumination pathway directing 100% of the illumination light towards the microscope. When power slider number is changed between 0 and 255, micromirrors flip between +12 and -12 to control the intensity of light illumination.

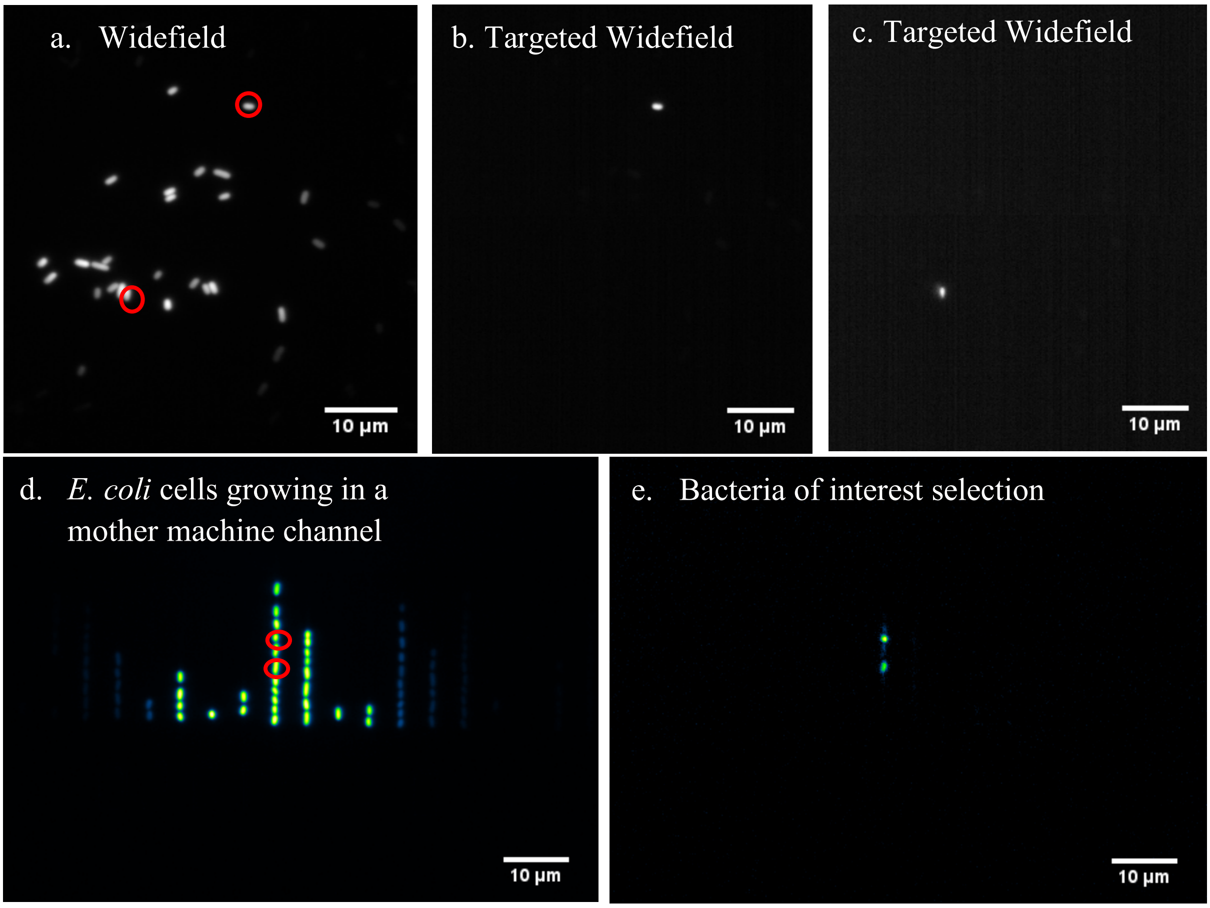

Fig. 4. 4. Targeted illumination of bacteria of interest in mother machine channels. (a) Widefield image of *E. coli*. **(b)** and **(c)** Selectively illuminating bacteria of interest. **(d)** Growing *E. coli* cells lined up in mother machine channels. **(e)** Two *E. coli* cells of interest are selectively illuminated.

Figure 4.4(a) is a widefield image of *E. coli* expression GFP illuminated with 470 LED along one of the illumination pathways of the system. **Figure 4.4(b)** and **(c)** are targeted widefield images of the bacteria of interest. **Figure 4.4(c)** shows that adjacent *E. coli* cells can be selected and illuminated efficiently using the system. **Figure 4.4(d)** shows a widefield image of bacteria lined up in various channels of mother machine and **Figure 4.4(e)** shows two *E. coli* cells in a channel are selected and illuminated.

4.4.6. Mother machine channel selection

By selectively illuminating a channel of interest in a mother machine system, it is demonstrated that not only circular patterns can be projected, but also any pattern depending on the biological experimental needs can be projected on to the sample. When only one channel in a mother machine is to be illuminated, the GUI was modified to illuminate the channel of interest. Channel position selection determines position of illumination. A rectangular pattern was determined by the position of the channel of interest and was projected on the DMD. Channel position can be changed to illuminate any channel of interest in a mother machine. **Figure 4.5(a)** shows *E. coli* cells growing in a mother machine channel and **Figure 4.5(b)** is the targeted illumination of a single channel.

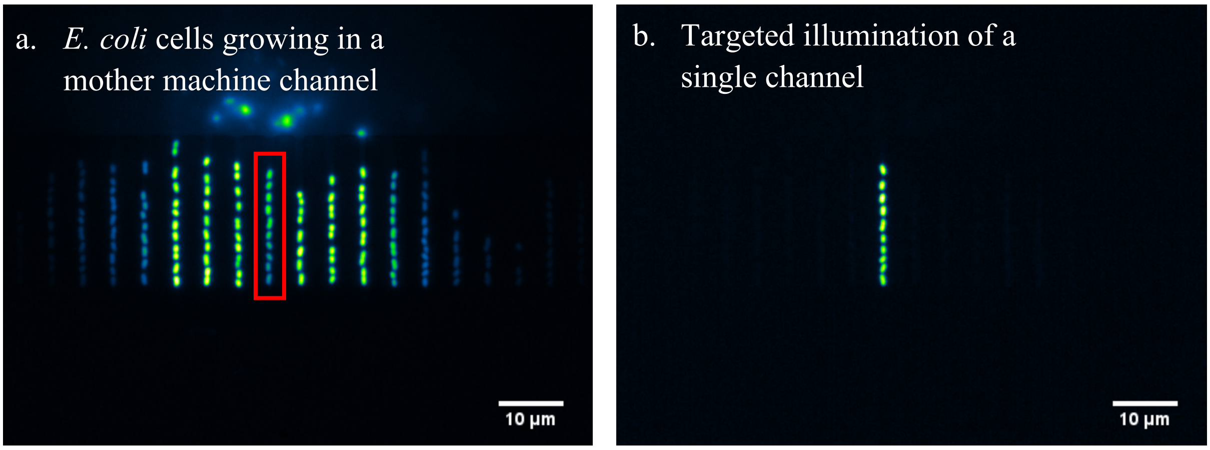

Fig. 4. 5. Selection of specific channels of interest in the mother machine system. (a) Widefield image of *E. coli* cells lined up in the mother machine system, **(b)** Single channel in mother machine selectively illuminated.

4.4.7. DMD based STORM implementation

STORM is implemented in the DMD based illumination system. A multiline laser set to project 647 nm is projected through the 'ON' illumination pathway of the system. Collimating optics consisting of two lenses of focal length 30 mm and 140 mm was built to minimize the power loss when projecting the laser and to fill a small fraction of area in the DMD to increase the illumination power intensity per volume. Maximum power is projected to a small area in the centre of the DMD. The figure shows the optical setup with two illumination pathways employed for the implementation of STORM experiments. Laser illumination is setup in one pathway and LED illumination is setup in the second illumination pathway as shown in **figure 4.6**.

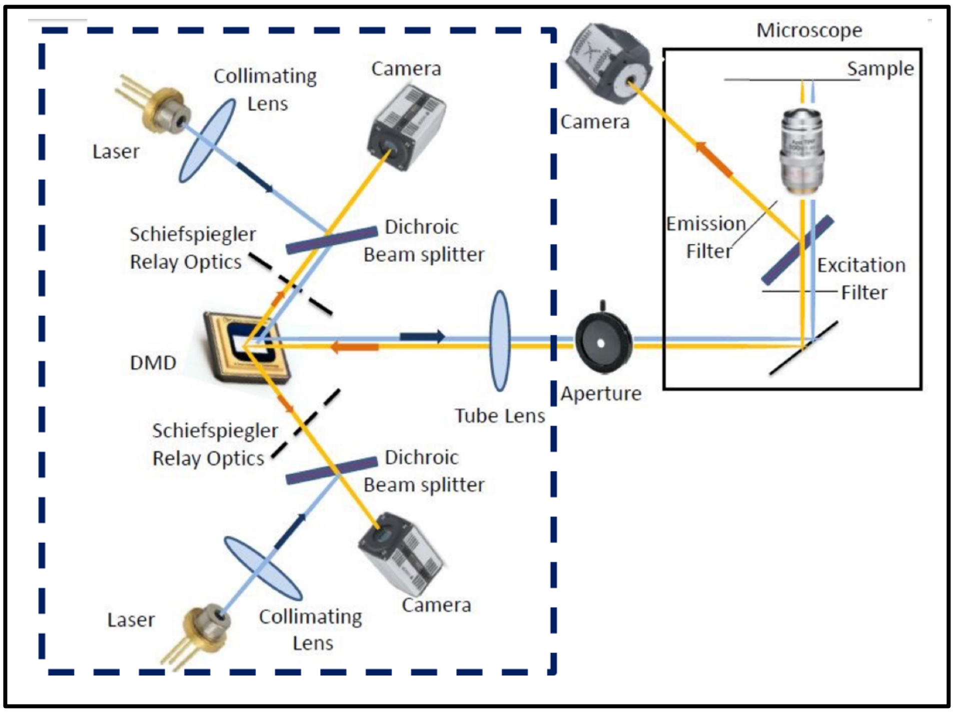

Fig. 4. 6. Schematic of the optical setup. Optical setup for the work in this chapter used a laser in 'ON' pathway and LED in 'OFF' pathway of the system.

4.4.8. Calibration of resolution

To calibrate the resolution of the system, HeLa cells are stained with AF647 phalloidin to visualize actin. The width of actin filament has been observed previously with high precision using electron microscopy [Niederman *et al.*, 1983] as 10 nm. This makes actin an ideal structure to calibrate the resolution of this imaging modality. When high laser power was projected on to the STORM sample, the molecules start to turn on and off their fluorescent state.

Widefield images of HeLa cells with low light intensity illumination is taken before starting to take STORM data as shown in **figure 4.7(a)**. **Figure 4.7(b)** is one STORM data frame with several individual blinks marked in white circles. The STORM image in **figure 4.7(c)** is reconstructed with 3,000 frames using ThunderSTORM ImageJ plugin [Oversny *et al.*, 2014]. **Figure 4.7(c)** is the reconstructed STORM image. **Figure 4.7(d)** is an area of interest zoomed-in. The red line represents the line profile drawn in **figure 4.7(e).** The width of actin filament is calculated by measuring the FWHM of the line plot in **figure 4.7(e)** and is calculated to be 90 nm.

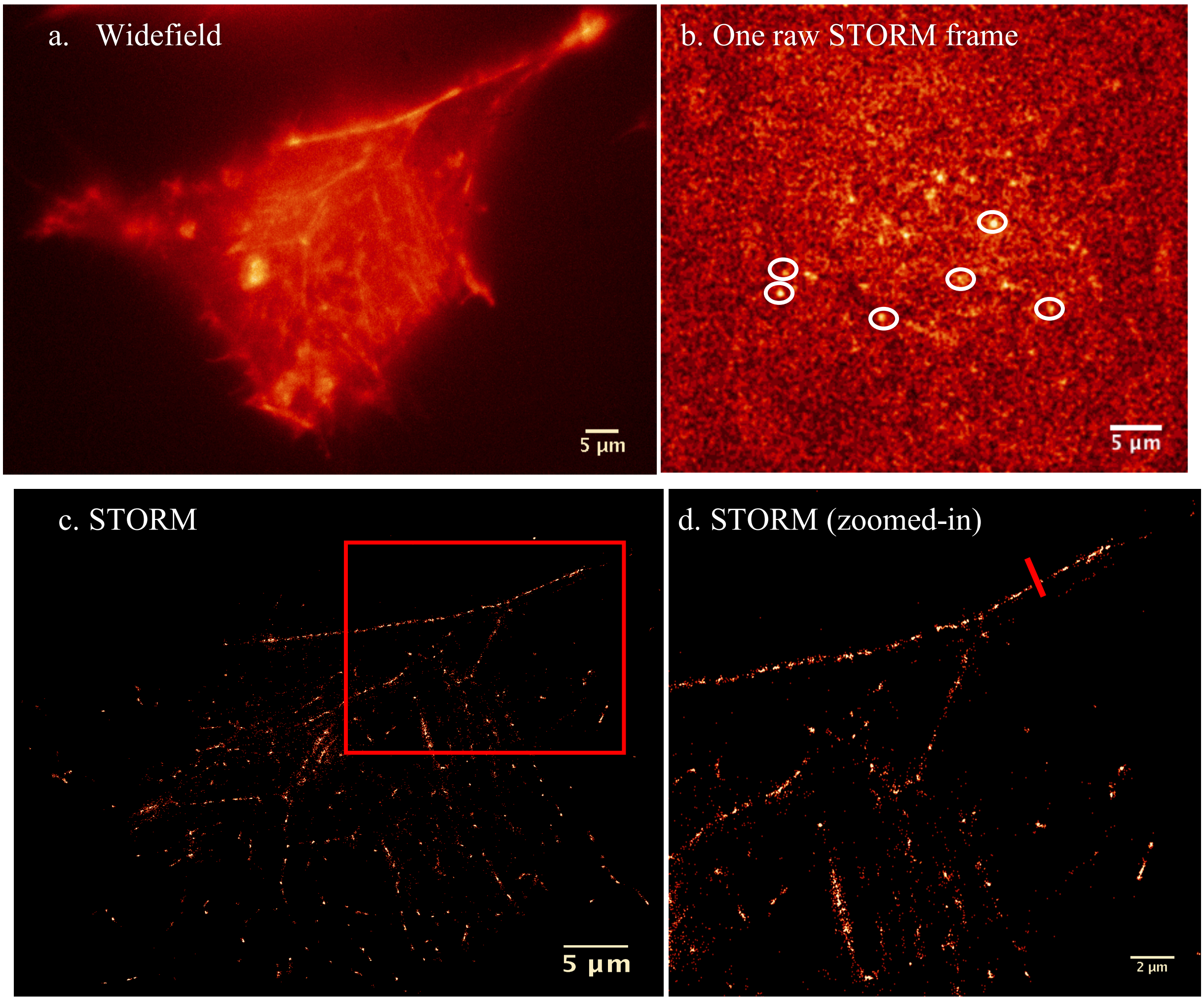

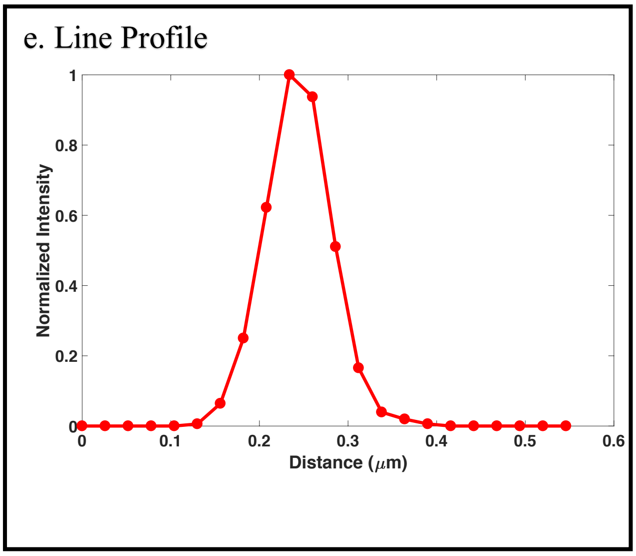

Fig. 4. 7. Resolution calibration. (a) Widefield image of HeLa cell stained with AF647 phalloidin, **(b)** One STORM frame with individual blinks. Selected blinks are highlighted in white circles. **(c)** STORM image, **(d)** Area marked by red square in (c) zoomed-in and line profile (marked as red line) selection to measure the width of actin, (**e)** Normalized intensity plot against distance in micrometer. FWHM is measured to be 90 nm.

4.4.9. Dual colour imaging

To establish the ability of the system to adapt to various biological investigations, LM microscope was built into the system. NIH 3T3 cells are imaged in dual colour with an LED based widefield imaging and STORM imaging to find the co-localisation of two proteins in the cells. Cells are transfected to express NrCAM protein which is labelled with AF647. NrCAM is a cell adhesion protein which plays an important role in cell-cell interaction in brain and the peripheral nervous system [Sakurai *et al.*, 2012]. An important question in understanding the role of NrCAM in intercellular signalling is whether the protein is located in primary cilia [Xenaki *et al.*, 2011], subcellular membrane organelles that regulate specific signalling pathways [Guemez-Gamboa, 2014]. Here we address this using dual colour imaging with the system by inducing cilia in NrCAM-HA transfected NIH3T3 cells, which are then double-labelled with a cilium marker (Arl13b protein) [Alberts *et al.*, 2002] with rhodamine red and with anti-HA labeled with AF647 to detect NrCAM-HA. The two independent optical pathways in the optical setup are used to launch an LED and a laser simultaneously in two colours. LED based widefield imaging is employed to image cilia and switched to laser by changing the angle of DMD micromirrors followed by STORM imaging for NrCAM to get super resolution localisation of NrCAM molecules in the cell.

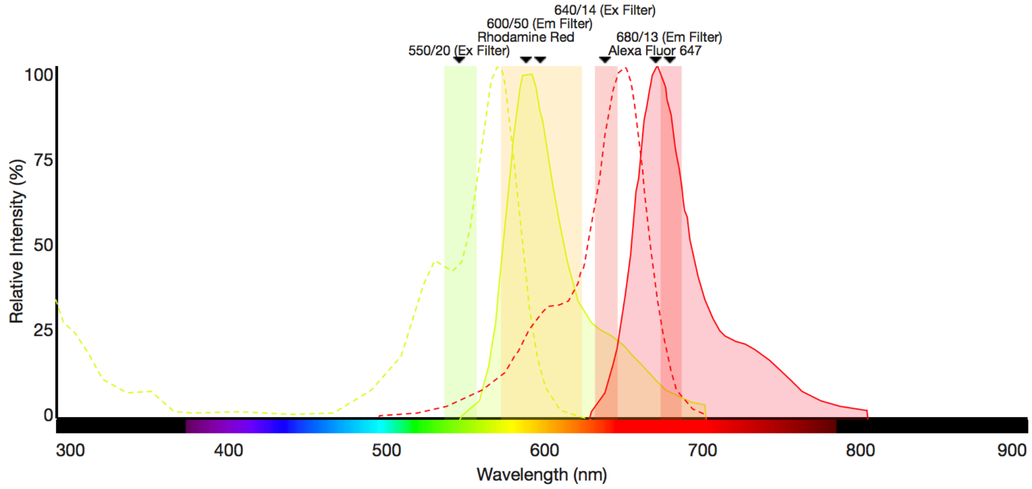

Fig. 4. 8. Relative intensity vs wavelength graph for the dual colour experiment. Excitation and emission spectra and filters used to image NrCAM and cilia labelled with AF647 and rrx [Thermofisher spectra viewer].

Dual colour imaging was implemented in this system to determine whether NrCAM is localized in cilia of 3T3 cells. The laser is setup in the ‘ON’ pathway to illuminate NrCAM molecules with 647 nm laser. 532 nm LED was setup in ‘OFF’ pathway to illuminate micro-cilia. In the ‘ON’ pathway, 649 dichroic was used with 640/14 filter for excitation and 680/13 filter for emission. In the ‘OFF’ pathway, 560 dichroic was used with 550/20 excitation and 600/50 for emission as shown in **figure 4.8**.

Initially, a widefield image was taken with 647 nm laser at low power. A uniform white image (value 255 for all the pixels) was projected on to the DMD to turn ‘ON’ all the DMD micro-mirrors. 100 frames were taken at 1x1 camera binning and 30 msec exposure time. Grouped Z maximum intensity projection of the data was taken to obtain the final NrCAM widefield image as shown in **figure 4.9(a)**. A uniform black image (value 0 for all the pixels) is projected on to the DMD to turn ‘OFF’ all the DMD micro-mirrors and LED based widefield image of cilia is acquired. 100 frames were taken at 1x1 camera binning and 30 msec exposure time. Grouped Z projection similar to the above NrCAM widefield data to get the final cilia widefield image as shown in **figure 4.9(b)**.

Figure 4.9(c) is the overlay of widefield image of NrCAM (green) and cilia (red) image. STORM image is taken by increasing the laser intensity until the molecules start switching fluorescent states. After taking a few frames and bleaching the molecules, the laser intensity was increased to a very high value to push more molecules to excited states and initiate a higher number of blinkings in the sample. Once the blinking starts, laser power is reduced and 10,000 frames of data are acquired at 30 msec exposure time and 1x1 camera binning. The image was reconstructed using QuickPALM [Henriques *et al.*, 2010] as shown in **figure 4.9(d)**. **Figure 4.9(e)** is an overlay of STORM image with widefield image of cilia.

This experiment gave insights to the colocalisation of NrCAM in cilia. This versatile imaging with super resolution localization reveals the vesicular transport of NrCAM molecules in the cell. Arl13b was used to locate the position of cilia in the cell at 532 nm LED widefield illumination and imaging was switched to 647 nm STORM laser illumination. These images indicate that there is no substantial NrCAM localization in cilia of the cell.

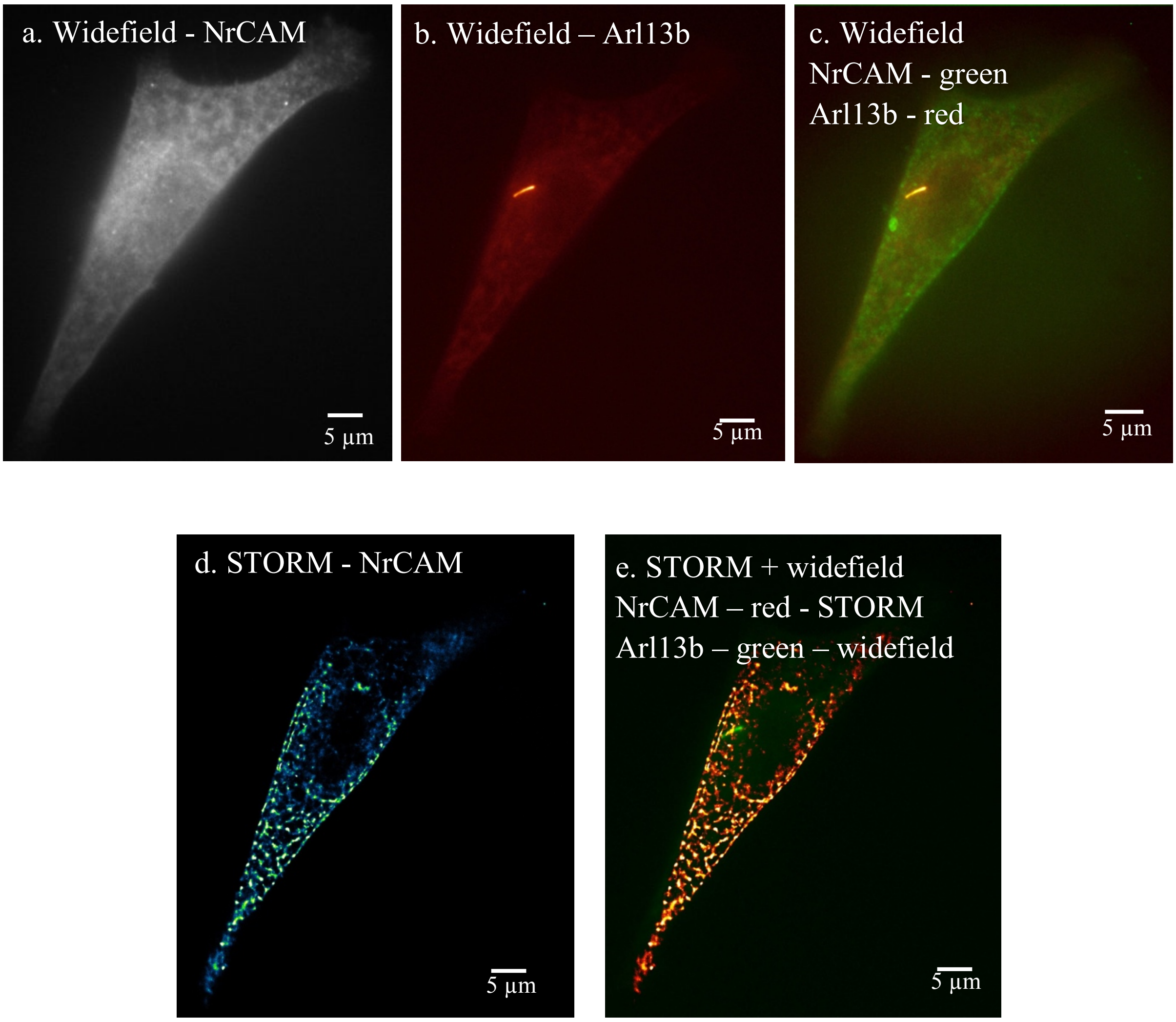

Fig. 4. 9. NIH 3T3 cells expressing NrCAM and Arl13b in widefield and STORM for super resolution localization of proteins at specific locations in the cell. (a) Widefield image of 3T3 cells expressing NrCAM stained with AF647, (b) Widefield image of cilia expressing Arl13b stained with rhodamine red (532), (c) Widefield image of NrCAM overlaid on widefield image of cilia, (d) QuickPALM reconstruction of STORM data, (e) Widefield cilia overlaid on STORM image.

The system can switch between the two pathways, light sources, imaging techniques, illumination wavelength and intensity, at sub millisecond timescale by changing the angle of reflection of the micromirrors. The experiment was repeated to ensure the reproducibility of biological experiment involving transfection, serum starvation, fixation, immunolabelling, STORM buffer preparations and imaging experiment involving two colour LED based widefield and high power STORM imaging.

Arl13b is used to locate the position of cilia in the cell at 532 nm LED widefield illumination (**figure 4.10(b-c)**) and at sub millisecond transition switching to 647 nm STORM laser illumination as in the previous experiment. These images indicate that there is no substantial NrCAM localization in cilia of the cell. **Figure 4.10(d)** also reveals the super resolution localization of vesicular transport of NrCAM molecules in the cell.

Unlike in a conventional LM technique in which the entire sample is illuminated with high power laser illumination, we are not limited by photobleaching the entire sample. Versatility of the system allows us to selectively illuminate only sections of interest to get targeted super resolution images as detailed in the next chapter.

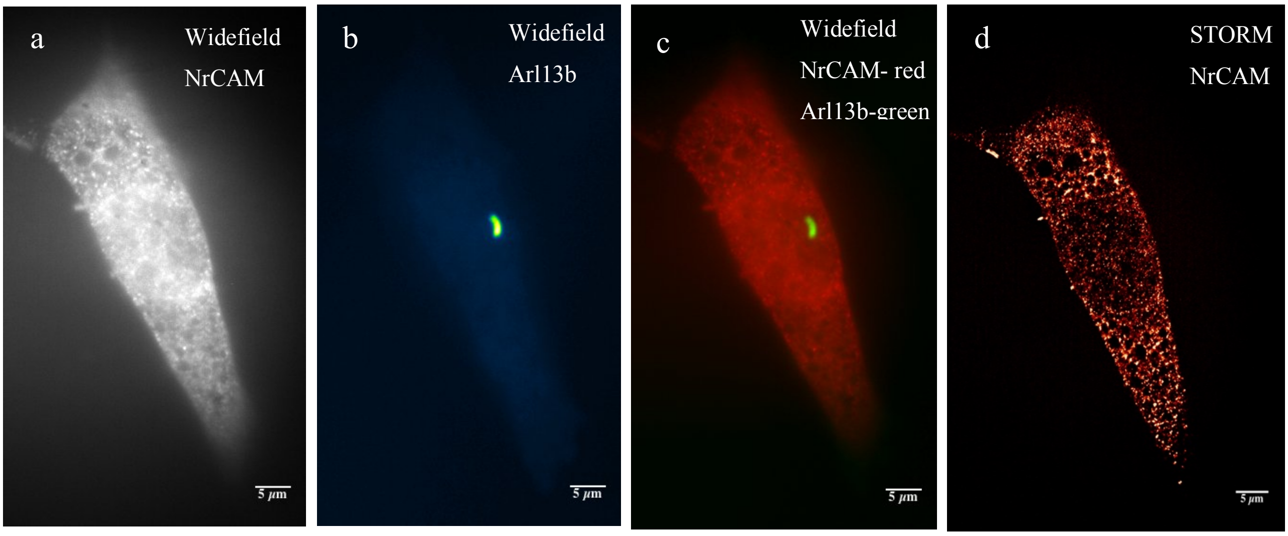

Fig. 4. 10. Dual colour imaging of NrCAM in cilia. (**a**) Widefield image of NrCAM with low power 647 nm laser in 'ON' optical pathway. (**b**) Widefield image of Arl13b in cilia with 532nm LED illuminated from the 'OFF' optical pathway. (**c**) Merged image of (**a**) and (**b**) to locate the position of cilia with respect to the localisation of NrCAM in the cell. (**d**) Super resolution localisation of NrCAM protein in the cell implementing STORM microscopy with high power 647 laser illumination from the ON optical pathway.

4.5. Discussion

To control the pattern and power of light projection on to the sample enabling targeted illumination is an advantage of the imaging system developed in this work. Targeted illumination is developed into the system which can selectively illuminate the regions of interest. The smallest region which can be illuminated using a DMD is equal to the size of one DMD pixel which is 13.6 µm in DMD space and 136 nm in sample space with a 100x objective. Diffraction limited system spreads this to around 160 nm.

E. coli cells embedded in agar and cells growing in mother machine channels are selectively illuminated to demonstrate the application of targeted illumination presented in this chapter. Specific channels of interest can also be selectively illuminated by projecting rectangular (instead of circular in the case of single cell selection) patterns on to the DMD. Software development of targeted illumination is discussed in this chapter and it is given in appendix 2. Projection of two circles with the control of their position, size and intensity is presented as an example. Any pattern can be easily integrated into this code depending on the experiment, opening the adoptability of the software for various other photomanipulation experiments. The ability of the DMD to project various patterns at various light intensities across the sample and collection of these in conjugate and non-conjugate cameras are discussed in more detail in Chapter 5.

STORM gives single molecule localization of biological structures which have gained a lot of attention and won the Nobel Prize in 2014. STORM is implemented into the system to study the NrCAM protein in NIH 3T3 cells and actin filaments by phalloidin staining in NIH 3T3 cells and HeLa cells. This chapter also includes the method followed for cell culture, serum starvation for cilia growth, transfection of NrCAM protein, fixation of the cell, immunolabelling *etc*. Dual colour imaging was performed to find the position of cilia and the localization of NrCAM in the cell. STORM system built into the setup was tested with a biological sample actin, which has a well-known structure and shape. The resolution of this system was calibrated by finding the width of an actin filament.

Building targeted illumination and STORM microscopy led to the development of targeted STORM as discussed in the next chapter. The ability to selectively illuminate regions of interest in a sample enabled the integration of various imaging modalities into one single setup to develop a versatile imaging system as discussed in Chapter 6.

Chapter 5

Development of Targeted Stochastic Optical Reconstruction Microscope

5.1. Summary

Selective illumination of a region of interest in the sample with a custom made GUI was presented in the Chapter 4. Localization microscopy (LM) projects high illumination intensity which can be invasive to most of the biological samples. Targeted Stochastic Optical Reconstruction Microscopy (STORM) presented in this chapter can select specific regions of interest without photobleaching other regions of the sample. Photobleaching is observed in the targeted areas after STORM and no photobleaching is observed in non-targeted areas of the sample by the development of the targeted STORM imaging.

Digital Micromirror Device (DMD) is used to project various power levels across one field of view. STORM was performed on a sample with gradient power illumination. Different resolutions were acquired for different regions in one field of view depending on the excitation laser power. Resolution degradation at low illumination powers was observed with gradient illumination and widefield image acquisition. By employing Super Resolution Radial Fluctuations (SRRF) [Gustafsson *et al.*, 2016] reconstruction algorithm, the image can retain the resolution throughout the gradient illumination. Targeted illumination was demonstrated on NIH 3T3 cells expressing NrCAM. Gradient illumination with widefield image acquisition for widefield and SRRF analysis is demonstrated on NIH 3T3 cells and HeLa cells labelled for F-actin. The width of an actin filament or the distance between two actin filaments was used to analyse the resolution. DMD based illumination enables the compromise between power and resolution in one field of view of the sample.

5.2. Introduction

LM along with the other super resolution techniques, has begun to provide novel insights into biological systems [Jones *et al.*, 2011]. However, in general, the increase in resolution comes with an increase of photo-toxicity, for example, LM which has the highest resolution of the techniques, requires very high laser power densities of the order of 15 kW/ cm^2. The increase in optical power has significant problems for imaging live cells due to increased photo-damage [Wäldchen *et al.*, 2015].

To follow the time progression of biological process using LM, researchers have used a variety of methods to follow natural processes in a living system. An elegant example is the work by [Holden *et al.*, 2014]. In that work, they developed a high throughput LM microscope which imaged hundreds of bacteria per super resolution frame, with each frame recorded at a different sample location. Furthermore, each frame was synchronized to the life cycle of the bacteria under observation. This allowed them to image over time, the nanoscale organization of the bacterial cell division protein FtsZ in a live system. While this work was incredibly useful at allowing LM to follow growth progression in a synchronized culture where changes over time in different cells can be assumed to represent the changes that also are occurring to a single cell, it is difficult to apply this technique to look at changes occurring within a single cell over time since continued imaging of the whole cell results in cell damage or death.

Super resolution images are generally obtained by projecting down high intensity laser power on to the sample. STORM exploits a photoswitchable property of fluorophore molecules with high laser power illumination to render super resolution images [Hess *et al.*, 2006, Michael *et al.*, 2006]. Photobleaching of samples poses a major drawback for this type of high resolution techniques. This limits the capability of STORM imaging to obtain time lapse images. As a large amount of power is needed for STORM microcopy, it would be ideal to identify a region of interest, such as single bacterium or a sub region of a eukaryotic cell. An experiment to locally image the region of interest (ROI) using a super-resolution technique, while leaving the surrounding regions unperturbed, requires a great deal of control from the illumination system used in the imaging platform. There are several ways to control the power delivered to a sample with the most commonly used in microscopy being a spatial light modulator (SLM) which is generally either a liquid crystal based device which modulates the phase [Hagen *et al.*, 2007] of the signal or a DMD which allows an ON/OFF modulation [Dan Dan *et al.*, 2013].

Selecting an area in a sample, controlling the illumination intensity in this area and delivering various amounts of power at different areas in one field of view using a DMD illumination system is the underlying approach of targeted STORM. This allows us, in real time, to select and acquire high resolution STORM images of an area of interest in a sample. For example, one bacterium of interest from a group of growing bacteria. The major advantage of this system is that there is only low light exposure on other parts of the sample and as such this technique can promise photo-toxicity for resolution. We can obtain a high resolution image of a selected area in a cell while acquiring long time imaging of the whole cell. Getting high resolution STORM images of small areas without illuminating or photobleaching other areas in a sample is highly advantageous and will open enormous possibilities in biological research. It can be applied to selectively imaging single cellular light sensitive organisms without photobleaching the entire field of view.

In this work, a novel technique of targeted STORM using a DMD based illumination system was developed. We used our system to deliver the high-power densities to specific areas of the sample plane to build a selective LM microscope. To demonstrate the capabilities of the illumination system, NIH 3T3 mouse fibroblast cells were imaged. NIH 3T3 cells express the cell adhesion molecule NrCAM [Davey *et al.*, 2005] through DNA transfection. NrCAM is tagged with an HA epitope recognized by anti-HA antibodies.

5.3. Results

5.3.1. Targeted STORM implementation

Targeted STORM is developed in this DMD based system by using both the ‘ON’ and ‘OFF’ pathways as shown in **figure 5.1**. Illumination light from a DMD is focused on to the sample. The light coming back from the sample has two options, depending on the dichroic mirror placed in the microscope. It can be either collected using a camera at the back of the microscope or the light can come back through the system, hit the DMD and get collected in one of these cameras on the system.

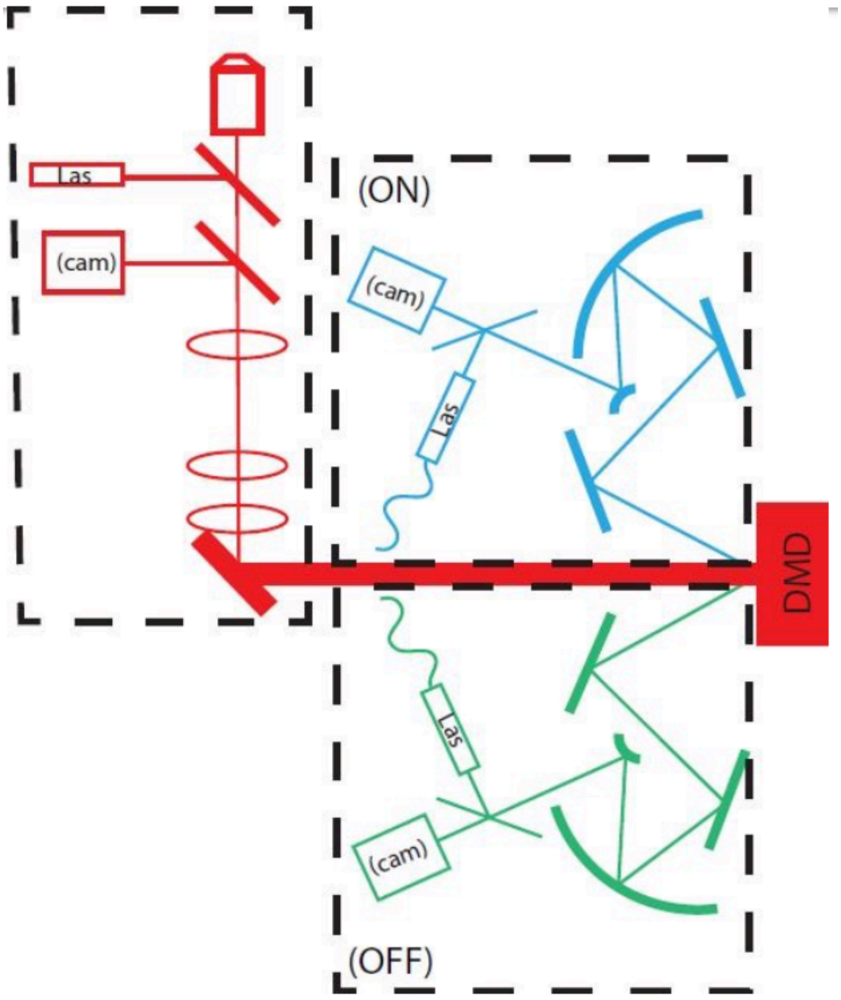

Fig. 5. 1. Optical pathway. The optical path for the DMD based illumination system. The ON (blue) and OFF (green) channels, are at +12° and −12° to the DMD. Each pathway contains both an illumination source and a camera. The red pathway depicts the optical path from the DMD to the sample. This pathway also contains a camera (cam) and illumination source (las) which can be either a laser or LED system.

5.3.2. Laser illumination to the DMD

As previously mentioned, STORM requires individual molecules to be isolated. This is achieved by placing most dye molecules into a dark state. This requires high illumination densities. As such the illumination source for STORM measurements requires a high-power light source. The power of the laser must cover a significant area of the DMD. As such a 7 W multi line laser from Cairn-Research was used. Up to 4 W of 635–645 nm light from the laser was focused on a 400 µm optical fibre. The light emitted from the opposite end of the fibre was collimated to give a 4 mm diameter circular illumination spot which was projected on to the DMD. The laser light was delivered to the DMD via the ‘ON’ optical path as discussed above.

The 4 mm laser spot does not completely cover the DMD. Although this limited the area of the DMD that could be used, this still covered 75,000 pixels (9.5% of DMD active area) and allowed a higher power density at the sample. The 4 mm diameter laser spot once projected on to the sample through a 100x Nikon SR lens produced a 40 µm diameter spot.

Once the area of the DMD containing the laser spot had been identified, it was possible to build a series of images which could be used to illuminate the sample. These patterns could be single value bitmaps used to control the laser power delivered to the sample. For example, to allow us to easily switch between a lower power mode for selecting sections of the sample of interest (epifluorescence) or high power for performing localization microscopy. However, the patterns could also be more complicated allowing different sections of the sample to be illuminated with different laser powers.

5.3.3. Pixel size considerations for targeted LM

Each pixel on the DMD is 13.6 µm. After being de-magnified on to the sample by the microscope, this would be 136 nm in size. As this is smaller than the diffraction limit, the resulting spot would be equivalent to the point spread function (PSF) of the microscope. For targeting power to the sample, we can excite the sample from any DMD pixel meaning that we can illuminate any sample feature down to the diffraction limit of the microscope. In this work, the limiting factor in the maximum size was the area of the laser spot on the DMD. The 130 nm effective pixel size for illumination means that a single pixel illumination could be used for confocal illumination. However, to define patterns on the sample using the DMD, the minimum feature size needs to be three DMD pixels corresponding to 390 nm.

For the two cameras attached to the DMD illumination system (the ON and OFF paths) the effective pixel size is 65 nm. Each pixel is 6.5 µm in size and the optical magnification of the system is 100x. For these cameras, the images were binned 2×2 to give effective pixel sizes of 130 nm. For the experiments in this chapter, an Andor iXon EMCCD is mounted in the back port of the microscope. The camera mounted at the rear illumination port of the microscope has a pixel size of 13 µm and with the 100x magnification the effective pixel size is 130 nm. The use of effective pixel sizes between 100 and 150 nm for STORM is common. With the PSF of the system being of the order of 300 nm, the signal from a single molecule is spread over several pixels. This allows the PSF to be fitted with a Gaussian function. If the effective pixel size is too big, the PSF would be confined to a single pixel and it would be impossible to fit the emission from a single molecule to a Gaussian. If the effective pixel size is too small, then the signal from a single molecule is spread over many pixels. Although this increases the number of data points and the Gaussian can be fitted to it. This reduces the signal-to-noise ratio for each pixel as the number of photons collected per pixel is reduced. It is common in localization microscopy to use effective pixel sizes at or around 100 nm.

5.3.4. Targeted STORM

Figure 5.2 shows targeted illumination of NIH 3T3 cells expressing NrCAM through transfection. Before starting to take STORM data, an epifluorescence image as shown in **figure 5.2(a).** The epifluorescence image was taken at 0.03 seconds exposure time with all DMD pixels ON illuminated with laser power at less than 0.1 W as shown in **figure 5.2(a)**. DMD pixels corresponding to the area marked in red circle was turned 'ON' to illuminate only that region. **Figure 5.2(b)** shows an epifluorescent targeted illumination of the area of interest. For the fluorophores to start blinking for STORM, the laser power hitting the sample plane is increased to 10-20 kW/ cm^2. There was around 30% power loss in the optical setup due to the loss of higher diffraction orders from the DMD.

DMD micromirrors corresponding to the area of interest on which targeted STORM is to be implemented are turned ON and other mirrors are turned OFF. Precise control of the area and intensity of laser illumination are implemented using custom made GUI through MATLAB. Illumination light from laser system is passed through a 642/20 excitation filter. When laser power of around 20 kW/ cm^2 was projected, the fluorophore molecules started to blink. On the emission pathway, a 676/29 emission filter is used. The camera video was taken at 0.03 seconds exposure time for 4,000 frames.

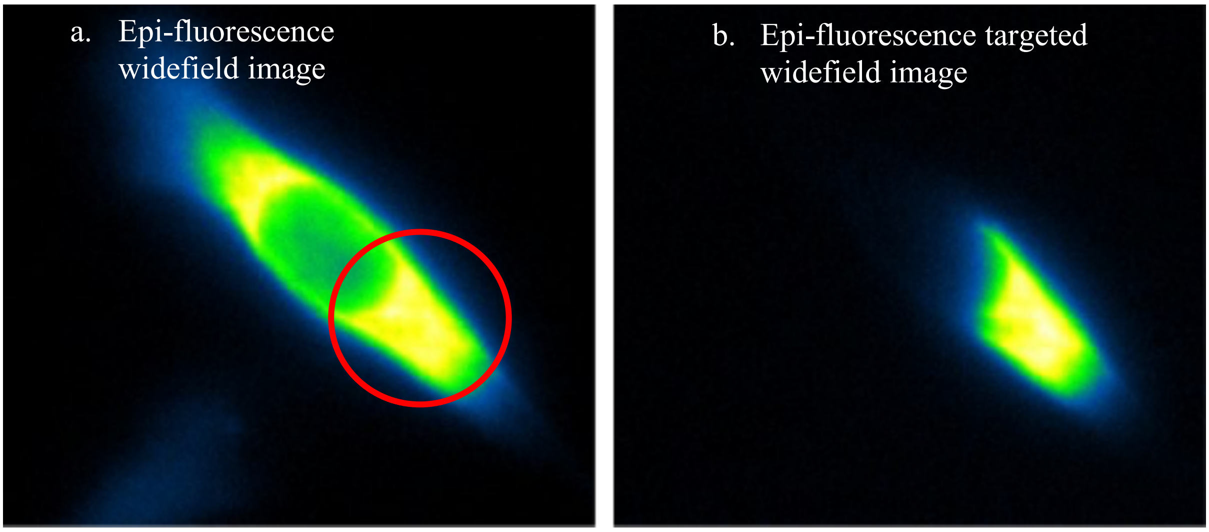

Fig. 5. 2. Targeted illumination of NIH 3T3 cells expressing NrCAM. (a) Epifluorescence image of a cell expressing NrCAM with all DMD pixels ON. **(b)** Epifluorescence targeted illumination of the same cell with DMD pixels ON in the targeted area.

The images were reconstructed using ThunderSTORM ImageJ plugin. It is to be noted that only the fluorophores inside the targeted area blink and reconstruction of the area outside targeted area does not form an image. **Figure 5.3(a)** is a single frame of the STORM data. **Figure 5.3(b)** shows the average grouped projection of STORM data. Although areas outside the targeted area are illuminated due to scattered light, its intensity is not high enough to damage the sample. **Figure 5.3(c)** shows the reconstructed STORM image of the targeted area expressing NrCAM. **Figure 5.3(d)** is the reconstructed STORM image overlaid on a widefield image. Using DMD for targeted illumination, high resolution image of the area of interest is obtained without photobleaching other parts of the cell expressing NrCAM. Using a DMD for targeted illumination, a high resolution image of the area of interest is obtained without photobleaching other parts of the cell.

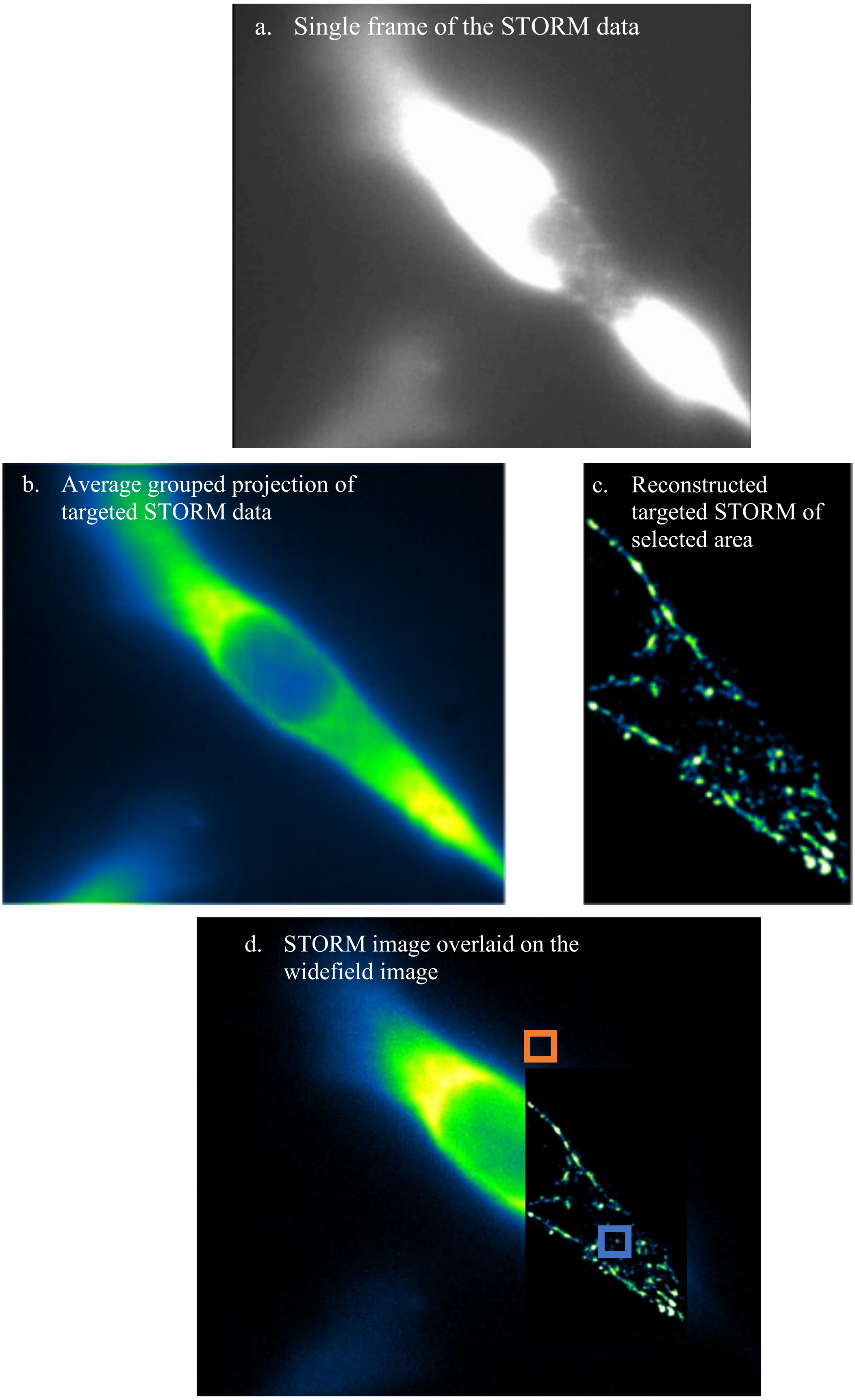

Fig. 5. 3. Targeted STORM on NIH 3T3 cells expressing NrCAM. (a) Single frame of the STORM data. **(b)** Average grouped projection of targeted STORM data. **(c)** Reconstructed targeted STORM of selected area. **(d)** STORM image overlaid on the widefield image.

Figure 5.4 shows the intensity comparison of an excited area and a dark area over the camera frames. The excited area and dark areas used are marked in blue and orange squares respectively in **figure 5.3(d).** The excited area is an area of interest which is excited using laser power. It can be seen that intensity of the excited area increases in the beginning due to illumination in this area. Due to photobleaching of the sample, intensity of targeted area decreases rapidly. There is also a slight elevation in the intensity of dark area due to the scattered light hitting the non-targeted area.

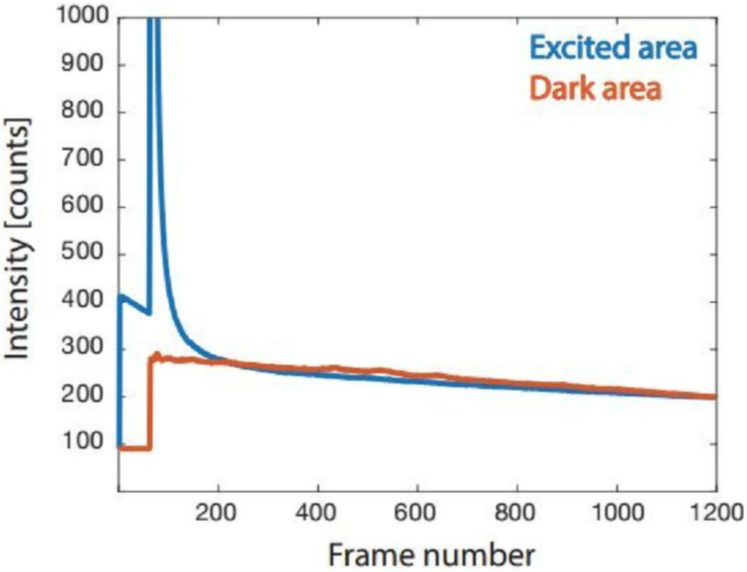

Fig. 5. 4. Intensity profile of excited area and dark area over the first 1,200 camera frames. Intensity of excited area increases due to high power STORM laser illumination. When the molecules jump to 'OFF' state, intensity rapidly decreases and there is single molecule blinking.

5.3.5. Multiple areas targeted STORM

A key goal is not only to control the power delivered to the sample but also the location of that power, specifically for high-resolution applications. For the data presented in **figure 5.5**, the DMD was addressed using 1 bit images, so the mirrors were either set to 'ON' or 'OFF', i.e. the power delivered to the sample was controlled directly by the laser power rather than the DMD which only controlled to position of the power delivered. **Figure 5.5 (A-B)** shows the images collected by the cameras on the 'ON' and 'OFF' paths respectively.

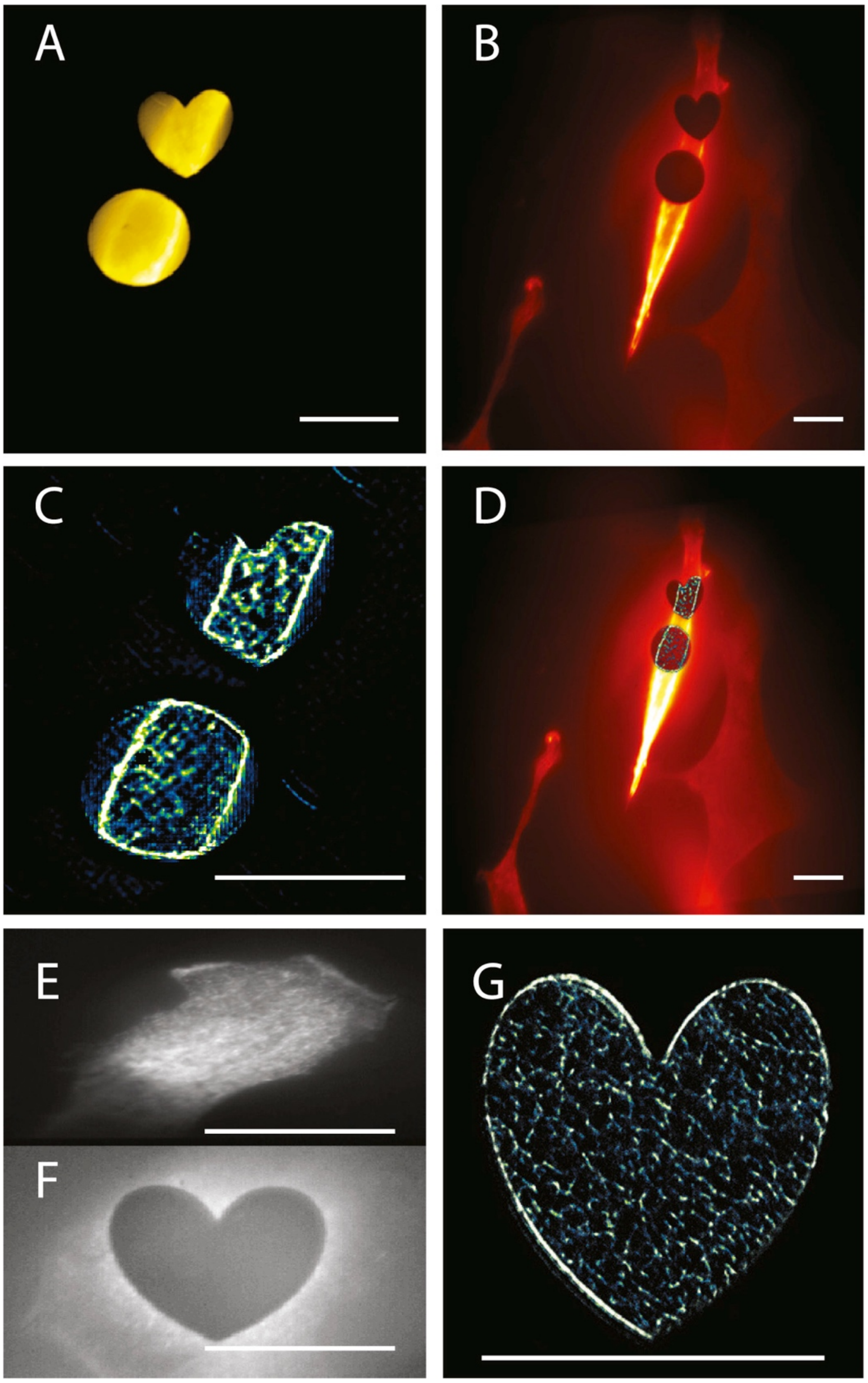

Fig. 5. 5. Targeted STORM on multiple areas of one cell. (A) A single frame widefield was taken before a STORM measurement was taken. The image was collected on the 'ON' path with a low intensity illumination source. The same image collected on the 'OFF' channel is shown in **(B)**. The laser power density is increased to take a STORM data set. After many STORM frames have been collected, the data was reconstructed using SRRF, and is given in **(C)**. Combining **figure(A)** and **(C)** gives the **figure(D)**. In **figure (E,F)** a 3T3 cell has been imaged using targeted STORM. **Figure (E)** shows the sample before illumination. **Figure (F)** shows the image collected by the OFF channel and **figure (G)** shows the STORM reconstruction of the area reconstructed using ThunderSTORM. The reconstruction shows the network structure associated with NrCAM. The scale bar in all images is 10 micrometres.

The sample was illuminated using the ‘ON’ path. For this work a circle and a heart were used for easy recognition. However, any shape could be used, including masks of single cells or subcellular structures. Although only light from the DMD ON pixels should reach the sample, there is some scatter which gives a small uniform background. **Figure 5.5 (B)** is the summation of 100 collected ‘OFF’ frames and the area of investigation can be seen showing several 3T3 cells, illuminated by scattered light. Since light collected from the sample is also reflected off the DMD, the two illumination areas defined by the heart and circle shapes are completely missing from the camera image because light from the sample at that point cannot reach the camera. As shown in **Figure 5.5 (B)** the sample receives light in areas not intended to be illuminated.

To reconstruct the STORM images in **figure 5.5**, 10,000 frames were collected. The areas defined showed the characteristic blinking of STORM whereas the areas not defined by the DMD as being ‘ON showed no blinking. The reconstruction from this is given in **Figure 5.5 (C),** while **Figure 5.5 (D)** shows an overlay of the high-resolution image on the data collected by the ‘OFF’ camera. A larger area of a 3T3 cell is imaged in **Figure 5.5 (E–G).** Here **figures 5.5 (E)** and **(F)** represent the ‘ON’ and ‘OFF’ respectively, with the image in **figure 5.5 (G)** showing the reconstructed STORM image. **Figure 5.5 (G)** was reconstructed using ThunderSTORM [Ovesny *et al.*, 2014], a common ImageJ plugin used for STORM reconstruction.

The STORM images shown in **Figure 5.5 (C-G)** show the high-resolution localization of NrCAM molecules inside the targeted area. Structures seen in the images can be attributed to the vesicular transport of NrCAM protein through the cell. A higher concentration of NrCAM near the nucleus were seen, which could be the presence of these molecules inside the endoplasmic reticulum, or in the vesicular network that will carry it to golgi apparatus en route to its normal location at the cell surface. This pattern of expression is typical of cells artificially stimulated to express high levels of exogenous protein after transient DNA transfection. It is worth noting that the reconstructed images show very few localization events from the area outside of excitation area as expected. In both reconstructions, using SRRF and ThunderSTORM, the frames of the fields of illumination were classed as structure by the algorithms. This is likely due to the sharp discontinuity of illumination.

5.3.6. After STORM photo bleach

Figure 5.6 (A–C) shows a 3T3 sample used in this work. Although the level of scattered light illuminating the non targeted area is low, it is still undesirable. To investigate the effect of stray light at the illumination powers used in STORM, low illumination light intensity images were taken before and after the storm imaging. **Figure 5.6(A)** is the image of the cell taken at low light levels before STORM. **Figure 5.6(B)** is taken during the STORM imaging using the OFF camera. **Figure 5.6(C)** is the same cell imaged after STORM imaging. **Figure 5.6(D)** shows the average signal level taken from two small areas of the sample taken during 50 frames of imaging. The blue line represents an area of the sample targeted to be illuminated (defined as 'ON') and the red from an area not targeted (defined as 'OFF'). In the first 20 frames, there is no laser illumination. The laser is turned on at the 20th frame. It can be seen in the log plot that light from the laser is reaching the regions of the sample defined as 'OFF'. The ratio between the 'OFF' and 'ON' intensities is of the order of 300. In this work, we apply about 0.5 mW of power per 'ON' pixel to the sample, the equivalent power supplied for an 'OFF' pixel is therefore roughly 2 µW.

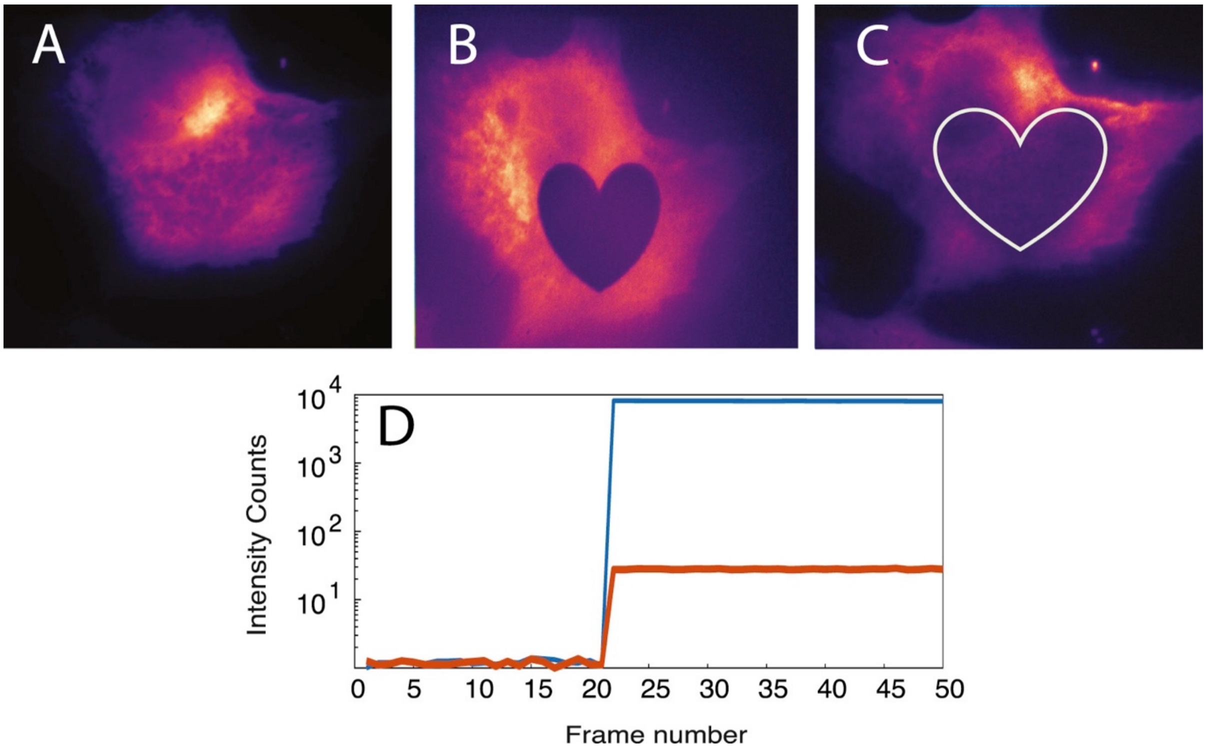

Fig. 5. 6. After STORM widefield image to demonstrate photobleaching. figure 5.6 (A) shows the sample illuminated under low power. The sample is illuminated under high power using a heart shape pattern, a single frame from the 'OFF' camera is given in **figure 5.6 (B).** After 10,000 frames of high illumination the sample was again re-imaged using low power widefield. This is given in **figure 5.6 (C).** Finally, **figure 5.6 (D)** shows the average intensity from a region of the sample during illumination for an 'ON' region (BLUE) and 'OFF' region (RED), showing that even the OFF regions are illuminated.

5.3.7. Gradient STORM

In previous sections, it is shown that, it is possible to deliver enough power to a sample to induce blinking. The next step is to introduce more control into the power delivered. It has been shown that several high-resolution adaptive algorithms can deliver different resolutions across an image. This can be dependent on the power delivered to the sample with higher power densities generally producing higher resolutions.

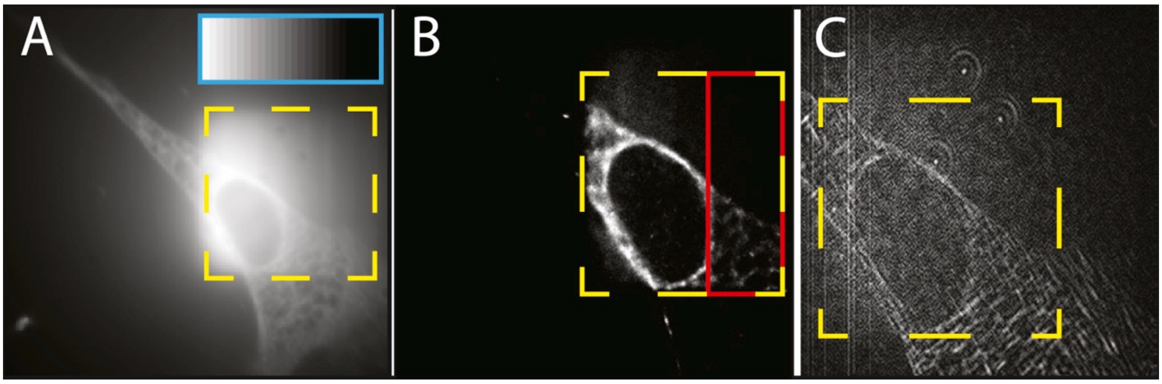

Fig. 5. 7. Targeted gradient STORM. (A) shows a 3T3 cell under illumination from the DMD illumination system, where the power from the system follows a gradient as shown in the inset of **figure (A)**. The STORM reconstruction and the SRRF are given in **figures (B)** and **(C)** respectively. The yellow box shows the area of excitation.

STORM images in **figure 5.7** were collected by illuminating the sample with a power density which changes across the sample. This is performed by projecting an 8-bit gradient using the DMD. **Figure 5.7 (A)** shows a 3T3 cell which has been illuminated using the gradient illumination. The gradient is given as an inset (top right) to the **Figure 5.7 (A).** The square of the sample illuminated using the gradient is highlighted by a yellow box in the figures. To maximize the signal collected from the sample the images were collected using the back port of the microscope. This bypasses the DMD on the return path, but as mentioned previously, it does add a slight astigmatism. The sample was imaged using conditions suitable for STORM imaging with the gradient of power applied and ten thousand frames were collected. The resulting frames were analysed using two different algorithms, ThunderSTORM shown in **Figure 5.7 (B),** and SRRF shown in **Figure 5.7 (C)**.

The data reconstructed using ThunderSTORM, which uses a classic LM approach, shows a good clear reconstruction for the area of high power illumination. The lower power region as highlighted in red still received power from the laser via the DMD, but at a lower intensity.

Here fewer events are seen as the reconstruction is quite poor. SRRF reconstruction which uses radial fluctuations shows a uniform reconstruction. However, the astigmatism of the system has imparted structure on to the image. SRRF could reconstruct all areas of the sample, including areas which were not directly illuminated (outside of the yellow box). These areas were excited by scattered light within the system. In these data, it was not possible to quantify the direct relationship between power and resolution for SRRF.

Two different reconstruction algorithms have been used: one based on localization microscopy (ThunderSTORM) and one based on radial fluctuations (SRRF). In the data analysed with localization microscopy, the change in power across the sample acts in a binary fashion, with regions above a certain power threshold producing single molecule blinking events which can be localized. Below this power very few events are localized. For the data analysed using SRRF we obtain a complete image with even regions outside of the illumination pattern having structures defined. This is due to a non infinite contrast ratio of the DMD.

To gauge the performance of gradient STORM, a structure with known shape and size was imaged at different power levels. HeLa cells were stained for F-actin using AF647 phalloidin. A gradient grey scale image with varying power levels as shown in **Figure 5.8(a)** inset, was projected on to the DMD. The laser power was setup to fill the area of the gradient pattern projected in the DMD. The laser was turned on at maximum power intensity. The DMD projected the pattern on to the sample. Eight different power levels were projected in the same field of view with the brightest region projecting 100% of laser power and darkest region projecting 0% of laser power on to the sample. Because of the non-infinite contrast ratio of the DMD, the dark region will also be illuminated. However, not with enough intensity to induce bleaching or to move the electrons in the fluorophore molecules to the dark state. Therefore, there are no or very few single molecule blinkings in this area.

The camera was binned by 2x2 pixels to increase the signal-to-noise ratio of the molecules. The data were reconstructed using ThunderSTORM. **Figure 5.8(a)** is the sum of 2,000 STORM frames and **figure 5.8(b)** is a single STORM frame. 100 frames of the actual STORM data are featured online in https://advanceseng.com/development-targeted-storm-super-resolution-imaging-biological-samples-using-digital-micro-mirror-device/. **Figure 5.8(c)** is the reconstructed STORM data. As the intensity of illumination decreases, the number of molecules transferred to triplet state decreases and fewer structures are imaged.

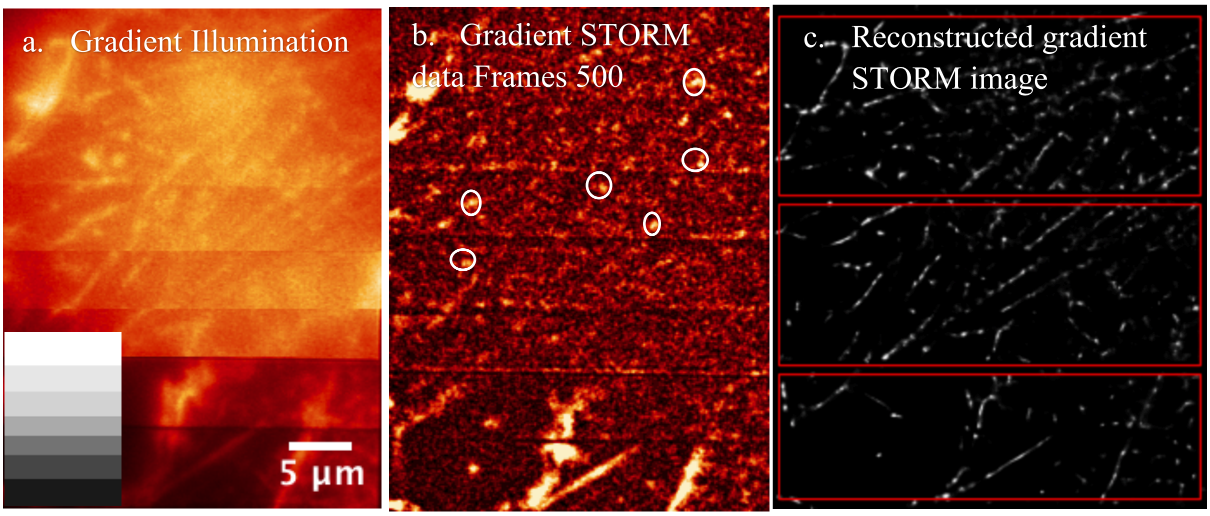

Fig. 5. 8. Gradient STORM on actin labelled HeLa cells. (a) Sum of 200 frames of STORM data. Gradient pattern projected on the DMD is given as an inset to **figure (a)**. **(b)** is one frame of the data and 100 frames are given as a video in supplementary video. A few selected blinkings are highlighted with white circles. **(c)** is the reconstructed STORM image.

5.3.8. Resolution control in one field-of-view with different power densities

The development of gradient STORM shown in the previous sections with gradient illumination using DMD can give different resolutions across one field of view using STORM microscopy providing the control of compromise between resolution and sample invasion. STORM projects high laser power to switch the molecules to triplet state or 'OFF' state which is not desirable for biological samples, especially in live cell imaging. Techniques such as SRRF are successful in terms of providing higher resolution images with widefield or confocal data. SRRF reconstruction is used to retain resolution at lower illumination power (**figure 5.10)**. SRRF is a fast threshold free algorithm comprising temporal analysis of a subpixel geometrical measure applied to an image sequence. Instead of point wise detection, it calculates the degree of local gradient convergence (radiality) across the entire frame. Image points have high degree of local gradient. To test the ability of SRRF to improve resolution, BPEC cells stained for F-actin with AF488 (Thermofishers prepared slide 1, catalog number F36924) were imaged. 100 frames with 30 milliseconds camera exposure time and 2x2 camera binning is taken by projecting a uniform illumination pattern on to the DMD to acquire a widefield image. The data were reconstructed with ImageJ SRRF plugin. **Figure 5.9(a)** is the grouped sum projection of the widefield data. **Figure 5.9(b)** is the reconstructed SRRF image. A normalized intensity line plot was drawn across an actin filament in widefield and SRRF image as marked in red and blue lines respectively in **figure 5.9(a)** and **(b)**. **Figure 5.9(c)** is the normalized intensity profile which shows the Full Width Half Maximum (FWHM) of the actin filament to be 0.64 µm in the widefield image and 0.43 µm in the SRRF image.

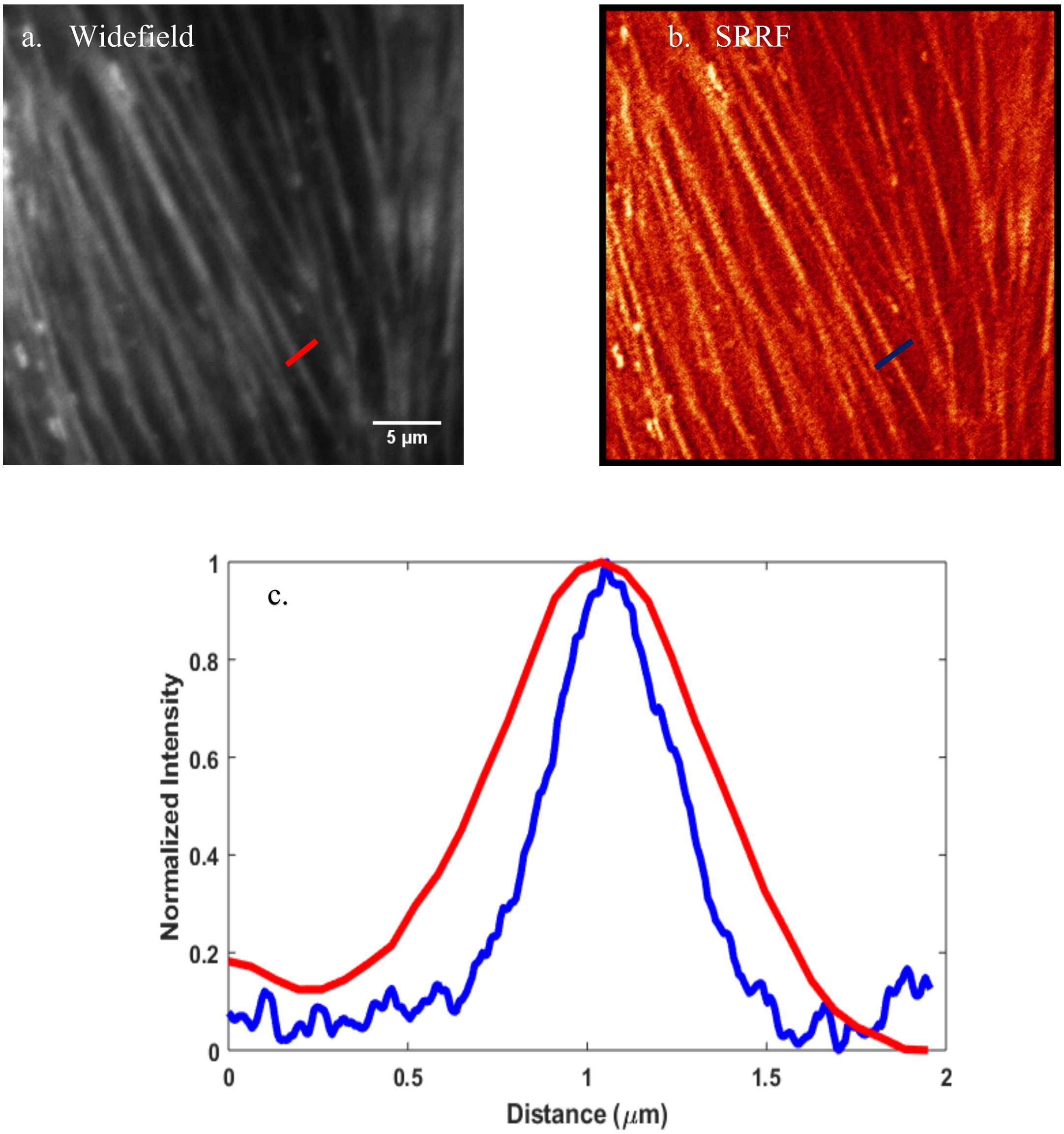

Fig. 5. 9. Demonstration of resolution improvement using SRRF reconstruction. (a) Widefield image. **(b)** Reconstructed SRRF image of **figure (a). (c)** Normalized intensity plot of the width of actin compared for widefield in red and SRRF in blue.

Various resolutions with gradient illumination were obtained using widefield illumination in **figure 5.10(a)**. Increase in the resolution when increasing the laser power, due to higher signal-to-noise ratio of the sample, was investigated. For example, gradient illumination was used to obtain widefield data at different power levels in one field of view. **Figure 5.10(a)** shows a widefield image with gradient illumination with 100%, 75%, 50% and 0% illumination intensity.

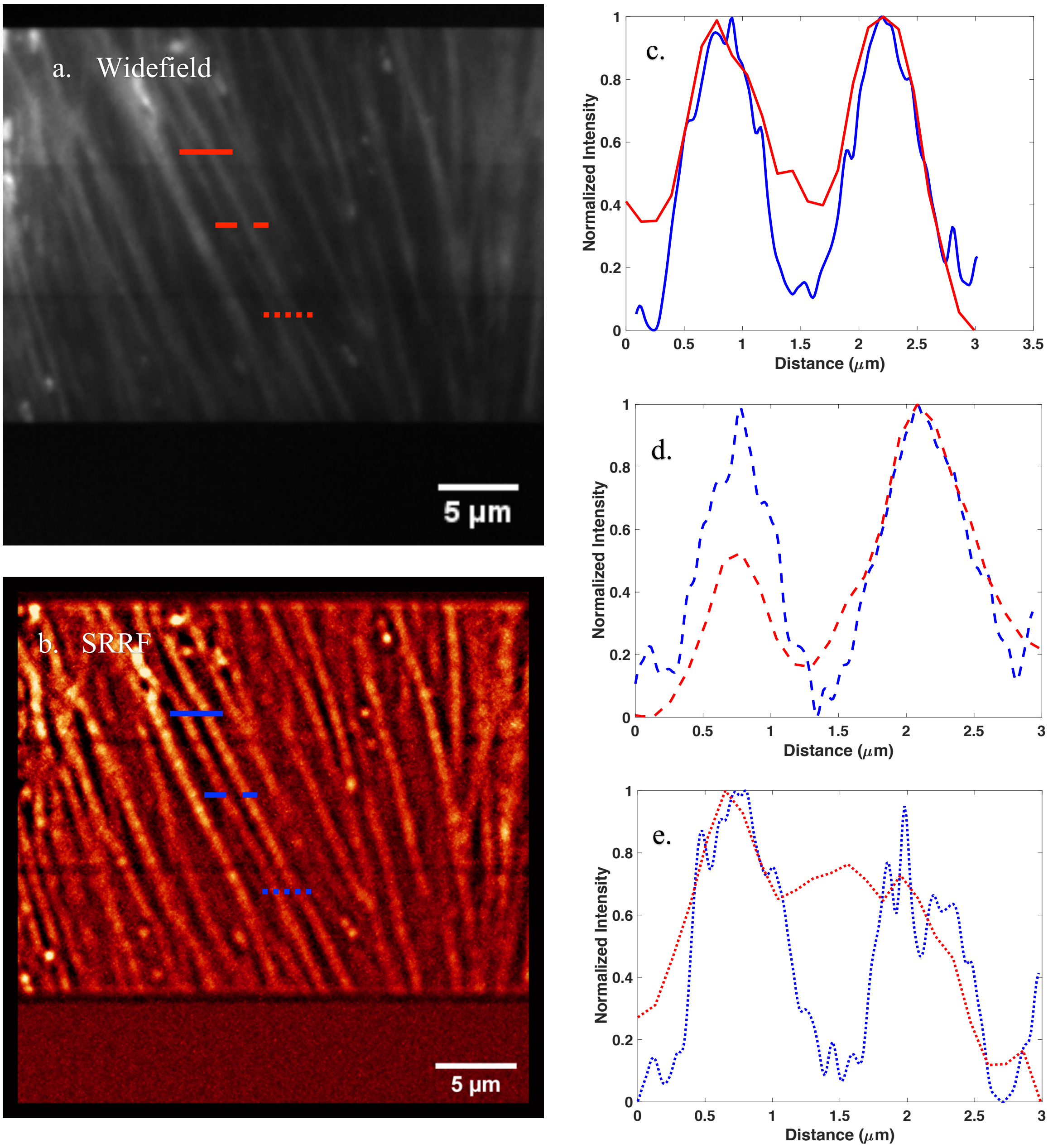

Fig. 5. 10. Demonstration of resolution compromises with illumination power in one field of view with widefield and SRRF imaging modes. Different power levels using gradient illumination in one field of view giving different resolutions in the widefield image. SRRF reconstruction maintains resolution at lower power levels. (a) Widefield image of actin at different illumination powers. (b) Reconstructed SRRF image of widefield data of figure (a). (c) Line profile of solid line at 100% illumination intensity across widefield and SRRF shown in red and blue respectively. (d) Line profile of coarse dotted line at 75% illumination intensity. (e) Line profile of fine dotted line at 50% illumination intensity.

100 frames with 30 milliseconds camera exposure time and 2x2 camera binning were taken. The sum of these 100 frames is shown in **figure 5.10(a).** These 100 frames were used to

reconstruct a SRRF image as shown in **figure 5.10(b)**. **Figure 5.10(c)** is the line profile of a solid line in 100% illumination intensity region. Red and blue lines represent line profiles on widefield and SRRF images respectively. This shows the two actin filaments resolved in both widefield and SRRF images. At 75% light intensity, coarse dotted line profile also shows the two actin filaments resolved. But the intensity of one filament is not high in widefield image as shown in **figure 5.10 (d)**. At 50% light illumination, fine dotted line profile shows that widefield cannot resolve the structures while SRRF still maintains the resolution. 0% light illumination does not show an image. It was shown in the STORM section previously that non targeted areas of the sample were also illuminated. Widefield projects low light intensities in the range of a few W/cm^2 while STORM projects 15-20 kW/cm^2 on to the sample. The signal from 0% or non-targeted area in widefield is equal to noise of the camera, thus showing no structures on the image.

5.4. Discussion

A targeted high resolution, STORM image is acquired for a small portion of a single NIH 3T3 mouse embryonic fibroblast cell, establishing a new method in biological imaging. Using this technique, high resolution images can be obtained from an area of interest while other areas are not photodamaged. The targeted area undergoes photobleaching while other areas of the sample are protected and the overall photobleaching of the sample is reduced. Development of this method has many applications and opens wide capabilities for biological studies.

The ability to target laser power to a sample with diffraction limited resolution can be used to selectively target areas of a sample for high-resolution imaging without damaging other areas of the sample. The application of DMD technology to STORM does not increase the speed of acquisition. It does allow the selection of specific regions of interest within the field of view, allowing us to isolate specific regions of the sample in space and time for study through STORM without damaging the rest of the sample with high illumination powers. However, it should be possible to apply techniques which measure the resolution of the image such as Fourier ring correlation (FRC) as described by [Nieuwenhuizen *et al.*, 2013] to the area targeted and stop imaging when a maximum resolution (or required) resolution is achieved. This may require different amounts of time across the image, depending on the sample geometry as discussed by [Fox Roberts *et al.*, 2017].

It has been shown that the resolutions obtainable with SRRF are not as power dependent as in widefield imaging. Applying different power densities to different areas of the sample were used in conjunction with SRRF to retain the imaging resolution against lowering the power of illumination.

The advantage of STORM over confocal microscopy is the increased resolution. However, there are significant disadvantages. These include reduced imagining speed and increased phototoxicity. Using a DMD based system it is possible to assign different regions of interest to different imaging modalities, performing STORM on one area of the sample and confocal based (SR-BCM) or line based structured illumination microscopy (conventional SIM) [Dan Dan *et al.*, 2013, 2014] to another region. A pathway for multimodal imaging to combine various imaging modalities are presented in the next chapter.

Chapter 6

Development of Versatile Imaging Platform by Advanced Light Processing

6.1. Summary

For the investigation of biological systems, there are many imaging techniques available, each suited to specific sample characteristics or biological investigations. In modern microscopy, the mode of illumination and detection of emission light plays a crucial role in image resolution and sample invasion. Widefield microscopy and Localization Microscopy (LM) use uniform illumination while confocal microscopy, Structured Illumination Microscopy (SIM) and STimulated Emission Depletion Microscopy (STED) use patterned illumination. In this work, a Digital Micro-mirror Device (DMD) based illumination and detection system were utilized to deliver a versatile imaging platform which can be used to combine various imaging techniques. The control over the mode of illumination can be divided into the ability to switch the pattern (structure of illumination light) and change the power of illumination.

We exploit this understanding to combine imaging modalities. Imaging modalities can be changed between each other at sub millisecond transition rate as demonstrated by changing between confocal and widefield imaging in section 6.3.1. The system allows us to combine low power widefield, high power single molecule localization and structured illumination based imaging modalities. To demonstrate the ability of the system to combine various imaging modalities in one field of view, widefield, confocal and STochastic Optical Reconstruction Microscopy (STORM) imaging are performed sequentially as given in section 6.3.2. The multimodal adaptive imaging platform developed was tested to study the early mitosis stage in

a Drosophila melanogaster embryogenesis. The ability to switch between modalities was applied to minimise photodamage in the embryo.

This chapter includes the final development of confocal microscopy presented in this work, reconfigurable confocal for deep imaging. The adaptive nature of the system allows us to solve the fixed pinhole limitation of a conventional spinning disk microscope. The ability to choose various confocal imaging parameters such as the pinhole size and the inter pinhole distance to suit a sample's brightness and thickness, followed by the ability to change these confocal imaging parameters during an image acquisition through the sample as a function of depth without substantial loss of resolution is a unique advantage of this adaptive system. Changing the size of pinholes and inter pinhole distances during acquisition for deep imaging helps to achieve control over image resolution and optical sectioning ability of the specimen. Development of reconfigurable confocal allows the visualization of stromal lamella in plant chloroplast for the first time using an optical microscope. This ability to adapt to a wide range of sample characteristics opens wide possibilities for designing adaptive biological investigations.

6.2. Introduction

The Abbé diffraction limit imposed huge constraints on the capabilities of optical microscopy for around a century to visualize biomolecular complexes. The developments of super resolution microscopic techniques could render images beyond this diffraction limit. Imaging techniques compromise between the ability to image deep into thick samples [Jan *et al.*, 2004], reduction in the level of photo bleaching in sample [Strickler *et al.*, 1990], fast techniques enabling live cell imaging [Gustofsson *et al.*, 2000] and most importantly the extent to which these can push the resolution limit of the image [Hell *et al.*, 2007, Bates *et al.*, 2006], [Patterson et al., 2006]. Many super-resolution techniques use higher illumination powers as such as STED [Hell *et al.*, 2007] and Localization Microscopy (LM) [Patterson et al., 2006] and they can be damaging to live samples. Low power and fast imaging gives SIM [Gustofsson *et al.*, 2000] an advantage over other super resolution techniques. However, the sensitivity of SIM to the optical imperfection and aberrations of the sample makes it technically challenging and SIM is generally limited to two-fold resolution improvement. This forms the foundation for the idea to combine various imaging modalities into a system which can adapt to biological specimens.

Control of sample illumination and collection of emission light are the important elements in modern microscopy. Widefield microscopy and LM, including STORM and Photoactivated Localization Microscopy (PALM), use uniform light illumination while confocal microscopy, SIM and STED use patterned illumination. The mode of illumination of light and detection of fluorescence emission plays a crucial role in image resolution and sample invasion. This understanding is utilized with a DMD based illumination and detection system to deliver a versatile imaging platform which can combine various imaging techniques. The system allows us to combine low power widefield imaging, high power single molecule localization techniques and patterned illumination based confocal imaging.

Various imaging techniques are switched between each other at sub millisecond transition opening tremendous possibilities for adaptive biological investigations. To demonstrate this switching, various biological systems and imaging needs are addressed. The early mitosis stage in a Drosophila embryogenesis was studied with this versatile imaging platform. Low power widefield imaging was used initially to image the first few nuclear cycles, and at the specific nuclear cycle of interest, imaging was switched to a rapid confocal imaging modality. Using this rapid confocal data with the super resolution reconstruction algorithm Super Resolution Radial Fluctuation (SRRF), dynamics during splitting of centrosomes can be visualized in higher resolution. Rapid confocal technique was employed to get high resolution images of live amoeba cells undergoing phagocytosis. Imaging was switched from widefield to confocal when the cell was about to engulf nutrients from the medium.

Reconfigurable confocal detailed in this chapter is the final confocal development presented in this work. The technique was developed as an attempt to solve the fixed pinhole limitation of spinning disk microscope with fixed pinhole. One of the properties of a spinning disk system is the constant inter pinhole distance. When imaging thick samples, and when going deeper into the sample, emission light undergoes a higher degree of scattering which can hinder the image resolution at large sample depths. The Nipkov disk which is used in many commercial spinning disk microscopes has an inter pinhole distance of 2.5 µm. The effective inter pinhole distance in the sample plane depends on the objective used for imaging. At about 4-5 µm from focal plane, intensity of out-of-focus light associated with one pinhole passes through the nearest neighboring pinholes [Pawley, Chapter 10, book, third edition].

Yokogawa spinning disk systems have two Nipkov type disks, a microlens array disk to focus the laser beam and the pinhole disk. The use of a microlens array increases the through-put of excitation laser from 1-2% to nearly 50% .There are also spinning disk microscopes which allow the user to change the disk to a different inter pinhole distance. However, these require changing the hardware and this cannot be done during the experiment or during the acquisition of the image. The Andor company recently built a spinning disk microscope with larger inter pinhole distance with microlens array, called the ‘dragonfly’ which incorporated the SRRF algorithm to enhance the image resolution. The major disadvantage of the spinning disk microscope technology is the fixed pinhole limitation which does not allow the user to change between the optical sectioning and resolution depending on the sample or depending on the depth of the sample at which the image is being acquired.

A novel reconfigurable confocal microscope is presented in this chapter which has the ability to change the pinhole size and the inter pinhole distances. Reconfigurable confocal can change between different inter pinhole distances at sub millisecond transition even during an acquisition. A Spinacia Oleracea leaf was imaged using the reconfigurable confocal imaging modality to compare different inter pinhole distances. Deep imaging of up to 60 µm is presented in this work.

Reconfigurable confocal imaging was used to locate the position of stromal lamellae in the chloroplast in plant tissue. The structure of chloroplasts in plants tissue has been revealed over many years and studied extensively using electron microscopes [Staehelin *et al.*, 2011]. Chloroplasts in plant tissue contain grana stacks which are connected by stroma lamella. Since the thickness of stroma lamella is at the nanometer scale, it was never visualized with a confocal microscope. Attempts have been made to visualize these structures using a SIM system. One of the drawbacks of a SIM system is that it is limited by depth of imaging and the maximum depth achieved previously on live cells in a conventional SIM is 6 µm [Gustafsson *et al.*, 2011]. With this drawback it was difficult to confirm the visualization of these structures in the chloroplast using optical microscopy. In this work, reconfigurable confocal modality with enhanced deep imaging capabilities followed by deconvolution allowed the visualization of the sample in a 3D perspective revealing stroma lamella which is visualized in an optical microscope with this resolution and image clarity for the first time.

6.3. Results

6.3.1. Sub millisecond switching between point based and widefield based imaging

In this section, the ability of the system to swap between different imaging modalities is demonstrated. Widefield and rapid confocal images are taken at 10 msec camera exposure time for 1,000 frames on a 100 nm bead sample. Imaging is changed between widefield and confocal randomly using the custom Graphical User Interface (GUI) discussed in Chapter 2. This is achieved by preloading the widefield and the confocal sequences on to the onboard memory of the DMD. Widefield sequence is a uniform white (or 255 in Most Significant Bit (MSB)) pattern created by turning all the DMD pixels to +12 degrees towards the illumination laser light pathway in the optical setup. Confocal pattern with 3x3 pinhole size and 3x5 inter pinhole distance is chosen as a pattern for this experiment. The pinhole size is 408 nm and the inter pinhole distance is 2,048 nm in sample space (using a 100x objective).

The first 100 frames of the camera acquisition are widefield imaging. **Figure 6.1(a)** shows the summed image of the first 100 frames in the 1,000 frame sequence summed. Imaging is then switched to the confocal pattern by clicking the 'Start' button in the GUI for the second sequence which starts projecting a confocal pattern at sub millisecond transition (between 44 µsec and number of frames in a sequence*44 µsec). **Figure 6.1(b)** shows frames 421 to 520 summed**.** Green square marked in **figure 6.1(a)** and **(b)** shows the improvement of resolution in confocal image when compared to widefield. The resolution improvement in confocal mode can be attributed to out-of-focus light subtraction to render an optically sectioned image on this densely distributed sample area, even though it is a 100 nm bead sample, in **figure 6.1(b)** compared to **figure 6.1 (a)**.

Figure 6.1(c) shows a plot of intensity against frame number for 100 camera frames. The curve at high intensity represents widefield and the curve at low intensity represents confocal. It can be noted here that high illumination (widefield) shows a higher reduction in fluorescence intensity due to photobleaching and low intensity (confocal) has less photobleaching as visualized by **figures 6.1 (d)** and **(e)**. These are zoomed-in sections of **figure 6.1(c)** and are signified by the black arrows. It can be seen in **figure 6.1(d)** that there is an intensity decrease from 705.5 to 703 in widefield imaging during 100 frames at 10 msec exposure time. The distinct pattern present in the signal could be arising because of DMD and camera frame resets.

In confocal imaging, the intensity decrease is significantly less changing from 103.55 to 103.5 during 100 frames at 10 msec exposure time (**figure 6.1(e)**). In **figure 6.1(d)**, photobleaching can be visualised with a decrease in the overall intensity after acquired 100 frames. A gradual decline in the intensity can be noted here. While in **figure 6.1(e)**, reduction in photobleaching cannot be visualised as clearly as it is in the range of noise intensity and is mixed with noise signal.

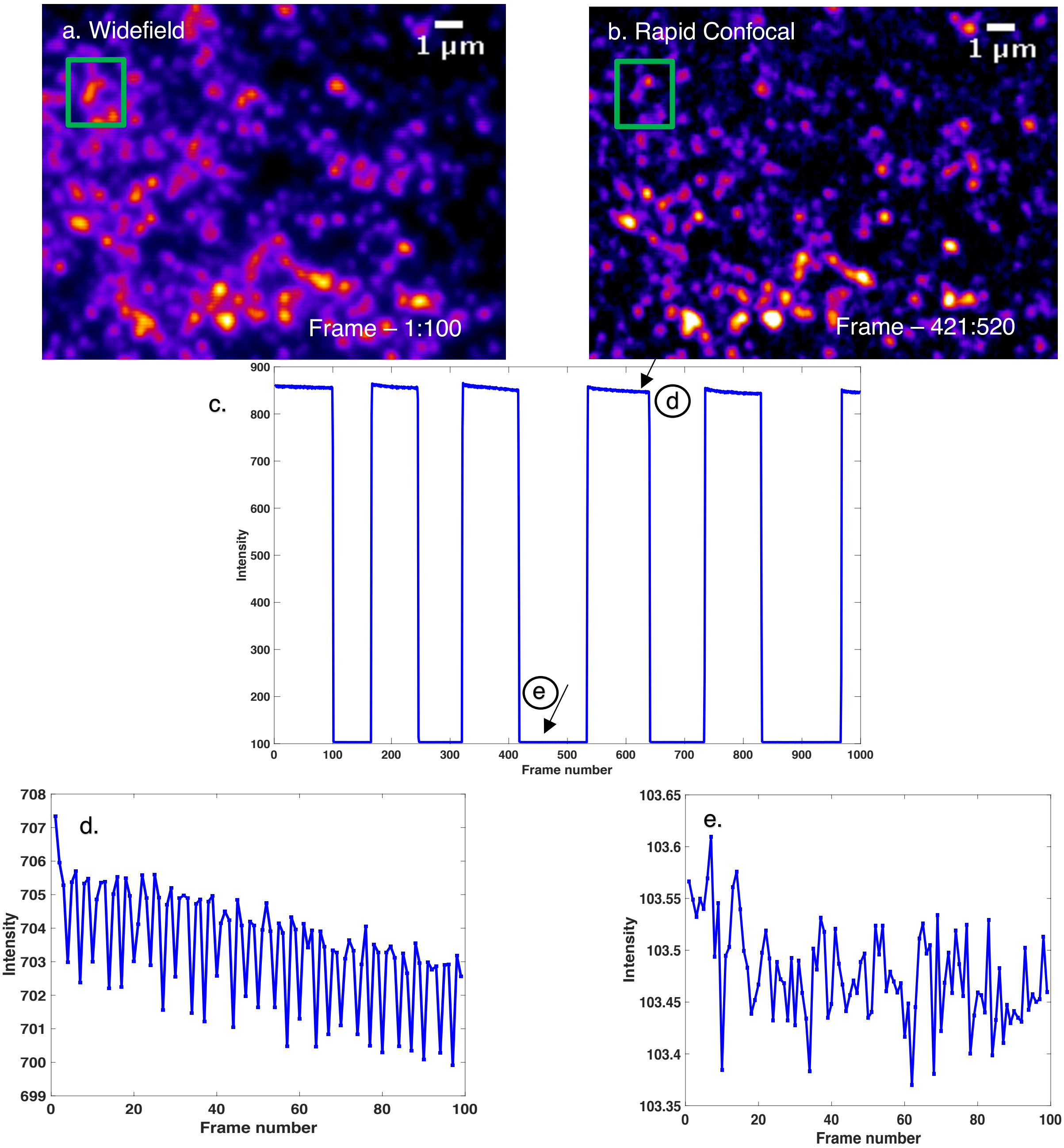

Fig. 6. 1. Sub millisecond swapping of widefield and confocal imaging. (a) Summed projection of first 100 widefield frames. **(b)** Summed projection of 100 confocal frames (421-520). **(c)** Intensity vs frame number for 1,000 frames for continuous camera acquisition showing sub millisecond transitions between widefield and confocal. **(d)** and **(e)** show zoomed-in sections of (c), marked by arrows. **(d)** shows a higher drop in intensity than (e). They both show summed images of 100 frames taken at 10 msec exposure time.

During this experiment, illumination power at the DMD is constant and the camera exposure time is also constant for widefield and confocal data acquisition. Widefield and confocal sequences are pre-loaded on to the DMD's onboard memory. 1,000 frames are taken as one camera sequence having the same camera exposure time. For the same camera exposure time, the signal-to-noise ratio of confocal is less than widefield. This is because the power delivered to the sample is reduced in confocal as only a subset of DMD pixels are ON at any point in time. In widefield illumination, the power delivered is higher as all DMD pixels are ON. This is detailed in Chapter 2. The number of pixels on per frame is less in confocal when compared to widefield. This decreases the power delivered to the sample at a specific time point. For a 3x3 pinhole size and 3x5 inter pinhole distance confocal pattern, the power delivered to the sample will be 1/0.04 ($\frac{1}{9/225}$) times less than the power delivered to the sample with all the DMD pixels on.

If both the sequences are in binary format internally set to run at the DMD's maximum speed, the range of time required to change between two sequences is between 44 µsec and the number of frames in the sequence multiplied by 44 µsec. This is because, the DMD completes the projection of all the frames in the first sequence before starting to project the second sequence if the 'Start' button on the GUI for the second sequence is pressed. This experiment shows that imaging modalities can be switched in less than 10 msec transition time.

To demonstrate that versatile imaging with switching between widefield and confocal results in lower photobleaching than continuous confocal imaging, two data sets are taken on Amoeba cells and are compared. First is a continuous confocal data taken for 300 seconds. Second is the versatile imaging performed by imaging in lower power widefield modality for 300 seconds and taking confocal snapshots at regular intervals. After 27 seconds of widefield imaging, imaging modality is switched to confocal for 1 second and then back to lower power widefield. When the imaging modality is switched to confocal, it is marked with a yellow square as shown in **figure 6.2 (b)**. **Figure 6.2 (a)** is a snapshot at the 123rd second and **figure 6.2 (b)** is the snapshot at the 124th second. **Figure 6.2 (c)** is the plot of mean intensity vs frame number for the continuous confocal data and **figure 6.2 (d)** is the mean intensity vs frame number for the versatile imaging data. It can be noted that mean intensity decreases through 300 seconds continuous confocal imaging while mean intensity of versatile imaging is constant. When the

DMD and camera frame rates are not synced, there can be a mix of widefield and confocal imaging. They are mixed and acquired in a single frame as can be seen in the frame succeeding the yellow square marked confocal frame.

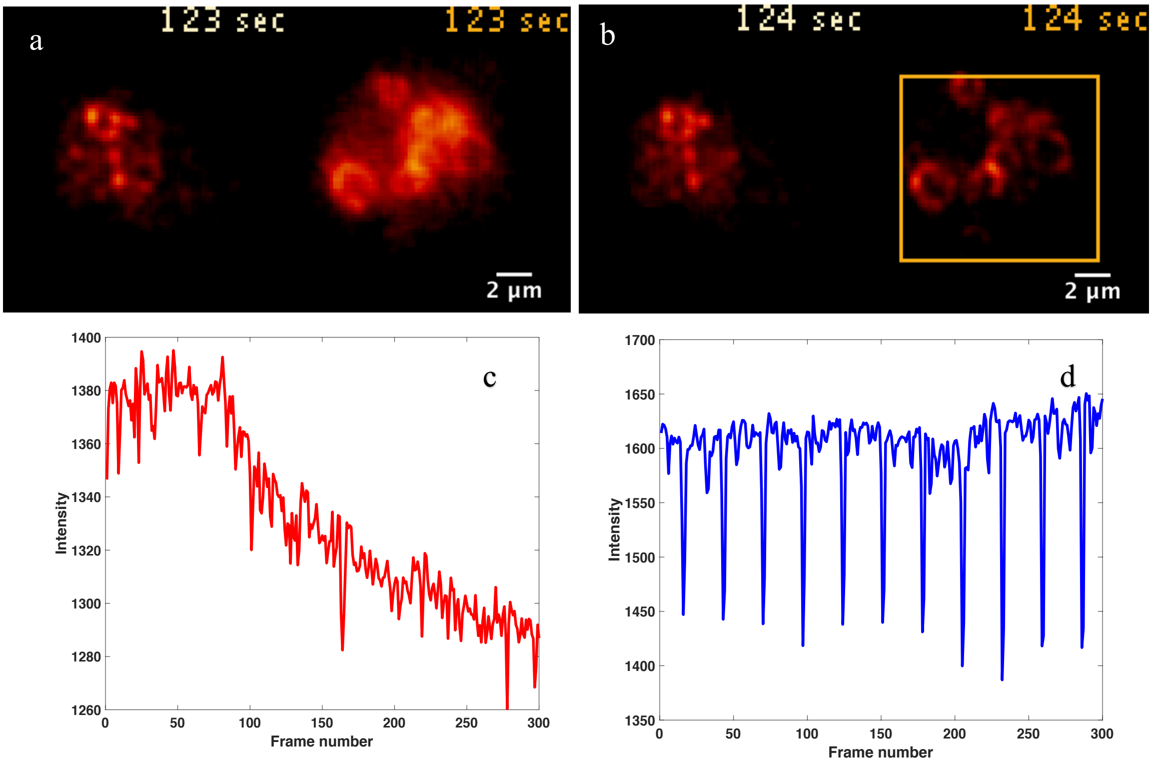

Fig. 6. 2. Photobleaching experiment. Two data are taken, one with continuous confocal and second with versatile imaging platform by changing between widefield and confocal imaging modalities. **(a)** 123th frame of the data. **(b)** 124th fame of the data. **(c)** Intensity profile of continuous confocal decreasing due to photobleaching. **(d)** Intensity profile do not show a decrease compared to (c).

For confocal imaging, 3x3 pinhole and 3x5 inter pinhole distance multifocal patterns are used. With this pattern 4% (9/225) of the laser power hitting the DMD chip is delivered to the sample. Widefield image is taken by controlling DMD micromirror flipping such that 0.4% (1/255) laser projected onto the DMD chip is delivered to the sample. For the second data, we automated the system to take 1 second confocal data after every 27 seconds low power widefield imaging. This can be changed to suit the sample type and investigation needs using the GUI provided. This example is programmed such that the VIP decreases the power delivered to the sample by approximately 10%. By employing versatile imaging, images with higher power or higher resolution can be acquired at the time point of interest during the lifetime of a biological investigation as demonstrated by imaging the mitosis in Drosophila embryo.

6.3.2. Combining widefield, confocal and STORM in one field of view

As discussed previously, widefield and STORM are based on uniform illumination of the sample. SIM, confocal and STED are based on structured illumination on the sample. Most of the imaging modalities are dependent on sample characteristics. For example, STORM is mostly performed on fixed samples because the membranes in live cells are impermeable to antibodies during immunolabelling. High illumination powers and long image acquisition time hinders the ability of a STORM microscope to visualize living cells. High resolution techniques such as STED and STORM require high power illumination and are sample invasive. Epi-fluorescence widefield imaging is a low power imaging technique, however it is diffraction limited. Confocal projects higher excitation illumination power than widefield and it renders optically sectioned images. However, conventional confocal is also a diffraction limited microscope. The development of versatile imaging presented here combines different imaging modalities in one field of view. This section explores the ability of the system to perform widefield, confocal and LM imaging in a single field of view.

Fixed 3T3 cells were immunolabelled with Alexa Flour (AF) 647 to visualize F-actin filaments. Sample preparation method for this section involves cell culture, fixation and immunolabelling techniques. The sample preparation methodology followed in this section is discussed previously in Chapter 4. A laser with a 647 nm peak illumination wavelength and an LED with 625 nm peak illumination wavelength are attached to the two sides of the optical setup. The laser and LED illumination are swapped between each other by changing the direction of DMD micromirrors. In this section the term ‘ON’ is used for the micromirrors turned towards laser pathway and the term ‘OFF’ is used for the micromirrors turned towards LED pathway of the system. For data acquisition, initially a widefield image was taken with all the DMD pixels ON at low light intensities as shown in **Figure 6.3(a).** A heart pattern is projected on to the DMD. The heart pattern was chosen as it is a known shape that has both corners and curved edges. However, any pattern such as a mask of a single cell or a subcellular structure can be used depending on the biological experimental requirements.

Figure 6.3 shows images of the same area using various imaging techniques: widefield shown in **figure 6.3(a)** and **(f),** targeted widefield shown in **figure 6.3(b)** and **6.3(c),** confocal shown in **figure 6.3(d),** and STORM shown in **figure 6.3(e)**. When the heart pattern was projected on to the DMD, **figure 6.3(b)** shows the image acquired in ON camera and **figure 6.3(c)** shows the image acquired in OFF camera. It is to be noted that this experiment was performed during the initial developments of confocal which is apparent from the quality of confocal image in **figure 6.3(d)**.

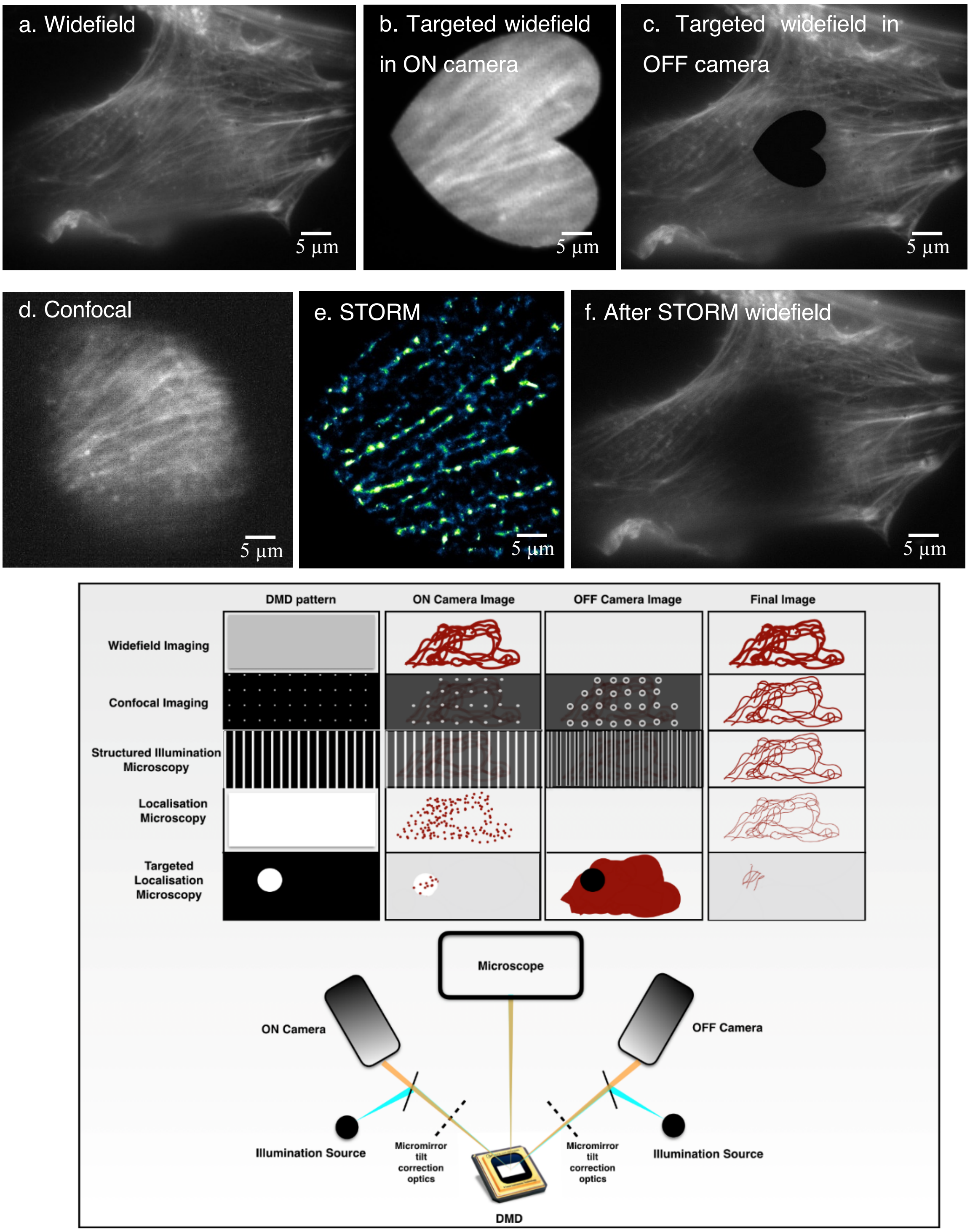

Fig. 6. 3. Combining widefield, confocal and STORM in NIH 3T3 cells. (a) Widefield phalloidin AF647 staining F-actin of NIH 3T3 cells. **(b)** ON camera widefield image of the targeted illumination. **(c)** OFF camera widefield (scattered light) image of the targeted illumination. **(d)** Confocal of the targeted area. **(e)** Reconstructed STORM image of the targeted area using ThunderSTORM. **(f)** Widefield image after STORM showing that only the targeted area and some area around this is photobleached. **(d)** Key aspects for implimenting multimodal adaptive super resolution confocal microscope.

During this stage of the confocal development there were several issue including DMD camera syncing problems and requirement for long imaging times resulting in photobleaching of the sample. Since then, confocal imaging has developed as given in Chapter 2 and 3. **Figure 6.3(f)** shows a widefield image taken after STORM, showing that only the targeted area and the area around this is photobleached. Area around the targeted area is photobleached due to scattering around the edges of the pattern. Widefield and confocal images were taken with LED illuminated through the OFF pathway and STORM is taken with laser illuminated through the ON pathway. [Tkaczyk *et al.*, 2010].

6.3.3. Versatile imaging platform in live Drosophila embryos

In versatile imaging mode, the imaging modalities can be switched seemlessly; in less than 10 msec. This was demonstrated by switching between widefield and rapid confocal on a fluorescent bead sample in section 6.3.1. To explore the potential of versatile imaging platform and to apply this to adapt the machine to suit the imaging requirements of biological systems, live Drosophila embryos were imaged in the syncytial blastoderm stage of their development.

Drosophila is a model organism widely employed to understand the development of single cells into multicellular complex organisms and the molecular basis of physiological mechanisms. Embryonic development in Drosophila is a rapid process where, after fertilization, a single cellular embryo develops into the cellular blastoderm consisting of 6,000-8,000 cells with a specific morphology and pattern formation which determine the future spatial organization of the fly's body. Imaging techniques of various kind have been employed in the study of this process. For example, electron microscopy has provided high resolution information of specific time points in fixed tissues [Mahowald *et al.*, 1979], while spinning disk and light sheet microscopy have been used to image changes in living cells as development proceeds [Basler *et al.*, 2016], [Tomer *et al.*, 2012].

Among the critically important cellular processes occurring between zygote formation and the cellular blastoderm are the multiple mitotic nuclear divisions of the syncytial blastoderm, but light exposure or photodamage can slow down this mitotic division limiting our ability to study this process in real time [Kelkar *et al.*, 2003]. To study the dynamic cellular processes in live cell imaging with minimal photodamage, the versatile imaging platform presented here can change between the low invasive widefield modality to the more invasive, but higher resolution, confocal imaging at sub millisecond transition at the start of a nuclear cycle of interest until the end of that nuclear division. The rapid switching between low power widefield to higher power confocal reduce the overall photobleaching in the sample. The dynamics of mitotic division are studied by imaging centrosomes which are the major microtubule organizing centres of the cell regulating the cell cycle progression. With this experiment, the system is adapted to image a live cellular (embryo) process with low power and the machine is transformed to adapt to the imaging requirements of a specific subcellular (centrosome) phenomenon.

Figures, 6.4(a), 6.4(b), 6.4(c) are images with low light exposure minimally invasive widefield microscopy at the early mitotic division nuclear cycles. At the onset of the desired nuclear cycle of interest, just before the centrosomes split, rapid confocal images are acquired until one cycle of division is completed. Rapid confocal images are taken using a 60x water objective at 1 sec exposure time in ON camera for 100 seconds for one cycle of centrosome division. **Figure 6.4(d)** is the 70th frame of the 100 frame video. Raw data were deconvoluted with Huygens software using classical maximum likelihood deconvolution.

SRRF images are reconstructed from rapid confocal data using ten rapid confocal raw images to generate each SRRF frame. **Figure 6.4(e)** is the 7th frame of the ten frame SRRF data. **Figures 6.4(d1-d5)** are the white square section of **figure 6.4(d)** zoomed-in, to visualize the images at various time points of centrosomes splitting in one nuclear cycle. **Figures 6.4(e1-e5)** are the white square of **figure 6.4(e)** zoomed-in. **Figures 6.4(e1-e5)** show higher resolution than **Figure 6.4(d1-d5).**

High resolution dynamics of the splitting of sub diffraction centrosomes is observed at specific time points in the syncytial blastoderm stage of embryo development. This sub millisecond switching of imaging modalities reduces the overall photodamage to the embryos. The rapid confocal data can then be used with the SRRF algorithm to provide high resolution data. The switching of imaging modalities to visualize the dynamics of centrosome division provides higher resolution. The versatility to rapidly switch between imaging modalities reduces photodamage during embryonic development.

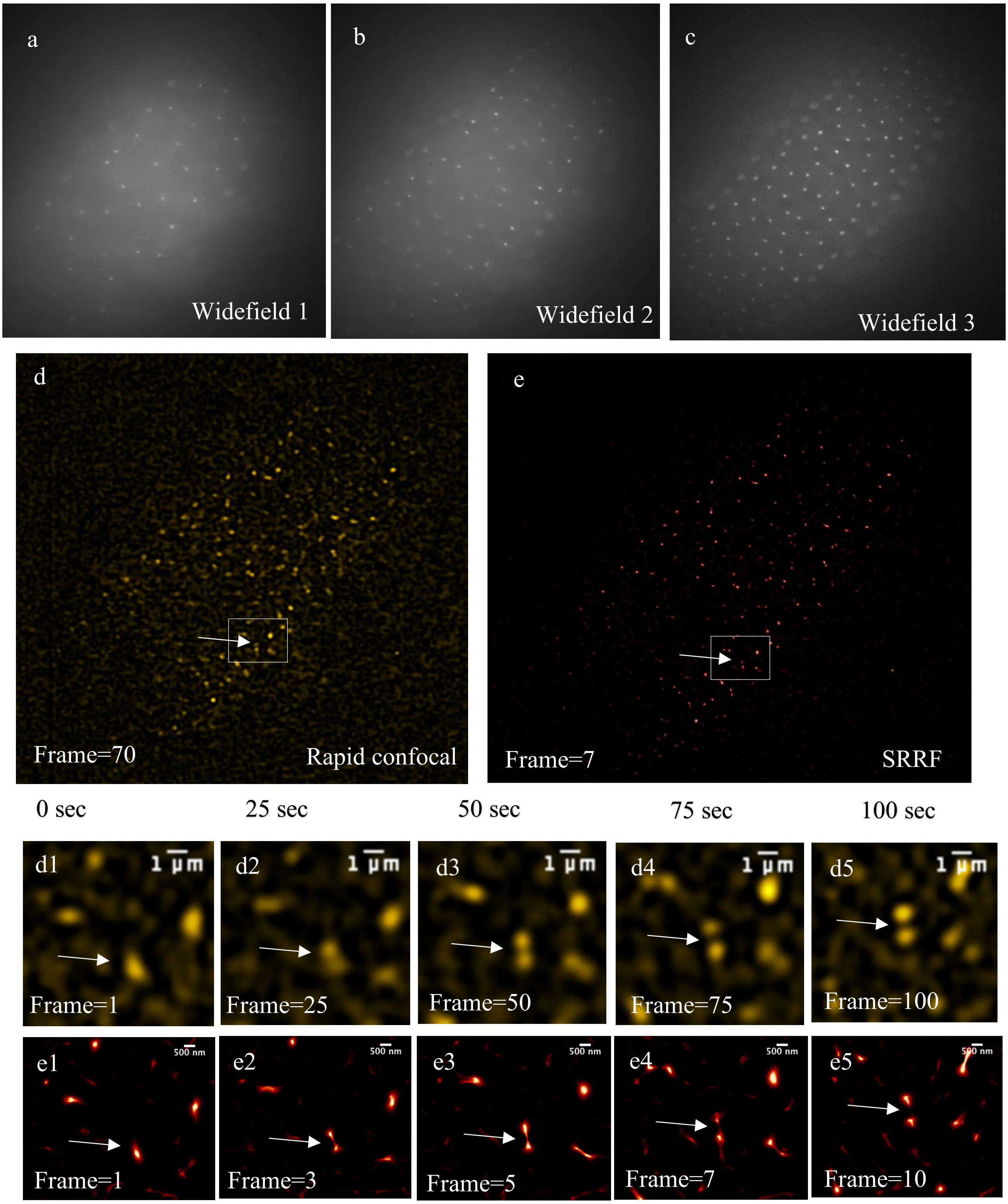

Fig. 6. 4. Early mitosis stage in Drosophila embryogenesis in super resolution. (a-c) Widefield images of early mitotic divisions. Mitotic division is visualized with the division of centrosomes. **(d)** Frame 70 of rapid confocal. **(e)** Frame 7 of SRRF reconstruction of rapid confocal data. **(d1-d5)** Zoomed-in rapid confocal images for a single centrosome splitting. **(e1-e5)** Zoomed-in SRRF images for a single centrosome splitting. **(d1-d5)** and **(e1-e5)** are frames at 0th, 25th, 50th, 75th, 100th time points.

To further analyse the error and resolution of these images, SQUIRREL analysis [Culley *et al.*, 2018] which is based on the FRC (Fourier Ring Correlation) method is employed. **Figure 6.5** shows the SQUIRREL analysis of mitotic division of centrosomes in shown **figure 6.4**. **Figures 6.5 (f1-f5)** show the error maps with reference frames as **figures 6.4 (d1-d5)** and super resolution frames as **figures 6.4 (e1-e5)**. As mentioned previously, to reconstruct a SRRF image with good signal-to-noise ratio, 10 raw confocal data were used. During the acquisition of the 10 confocal frames, centrosomes move inside the cell. This error in the reconstructed SRRF images can be visualized using the error map.

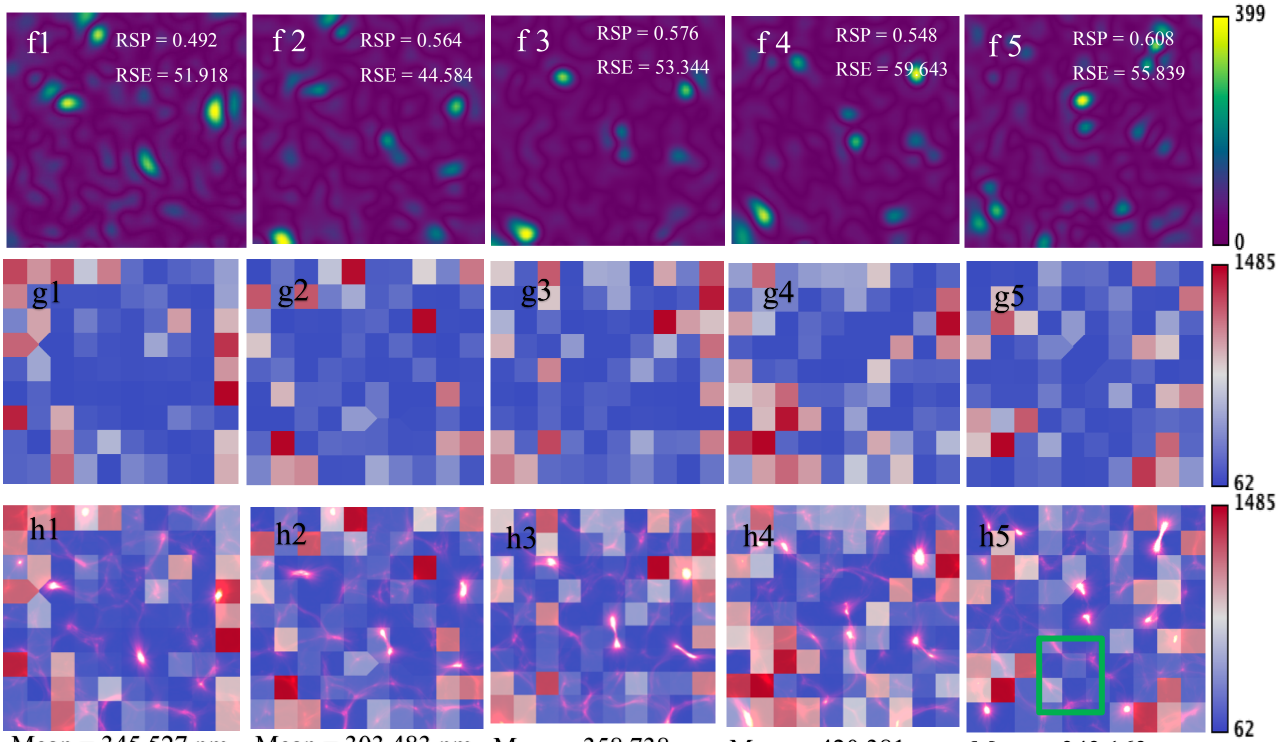

Mean = 345.527 nm Mean = 303.483 nm Mean = 358.738 nm Mean = 420.381 nm Mean = 343.163 nm

Min. = 59.584 nm Min. = 64.484 nm Min. = 65.029 nm Min. = 66.717 nm Min. = 61.540 nm

Fig. 6. 5. SQUIRREL analysis of figure 6.3. (**f1-f5**) Error map between **figure 6.3 (d1-d5)** and SRRF **figure 6.3 (e1-e5)** images. **(g1-g5)** FCR map between **figure 6.3 (d1-d5)** and SRRF **figure 6.3 (e1-e5)** images. **(h1-h5)** Overlay of SRRF and FCR map.

Figures 6.5 (g1-g5) show the FRC maps between **figures 6.4 (d1-d5)** and **figures 6.4 (e1-e5)**. **Figures 6.5 (h1-h5)** show the overlay between **figures 6.4 (e1-e5)** and **figures 6.5 (g1-g5)**. **Figures 6.5 (h1-h5)** is an overlay of the SRRF image and the FRC map. The green square marked in **figure 6.4 (h5)** is highlighted. This is to show the FRC values of the two centrosomes in the 100th frame of the acquired data. **Figures 6.5 (h1-h5)** show the regions of higher resolution (blue) and lower resolution (red). FCR scale bars are in nanometres. Dark red squares in the FRC map could be noise as the error map of the image area corresponding to red squares does not show substantial error.

6.3.4. Amoeba phagocytosis in high resolution

Another example for versatile imaging platform is demonstrated by visualizing the dynamics of amoeba undergoing phagocytosis. An amoeba is a eukaryotic single cellular organism. Amoeba are used as model organisms to phagocytic cells such as macrophages and neutrophils. They are used in various studies including cancer research, disease and infection, chemotaxis, thermotaxis and gene knockout [Gerstenmaier *et al.*, 2015, Buckley *et al.*, 2016]. Amoeba are light sensitive organisms. They tend to move away from bright light source. Here, amoeba (soil amoeba, Dictyostelium discoideum) is imaged with widefield to study the movement of the organism under low light illumination and imaging modality is switched to rapid confocal at the beginning of a cellular process of interest.

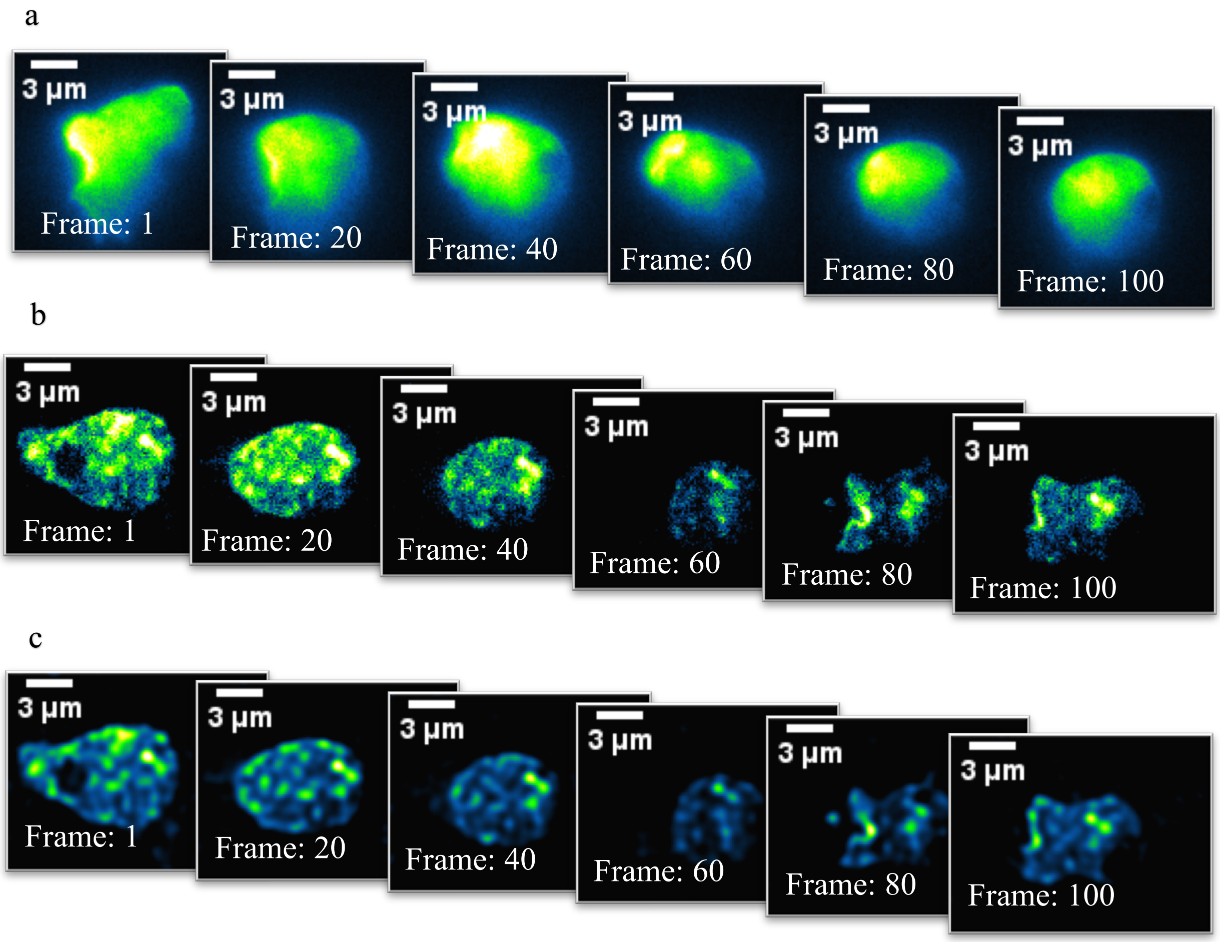

Fig. 6. 6. Widefield and confocal imaging for amoeba cells undergoing phagocytosis. (a), (b) Frames 1, 20, 40, 60, 80, 100 of a 100 frame continuous camera acquisition using widefield and confocal imaging modalities respectively. **(c),** deconvolution of **figure 6.4(b)** confocal data using Huygens classical maximum likelihood estimation method with 10 iterations.

Figure 6.6(a) shows frames 1, 20, 40, 60, 80, 100 of a 100 frame continuous camera acquisition using widefield imaging. Imaging modality is switched to rapid confocal **(figure 6.6(b))** at the onset of phagocytosis. During this phagocytotic process, the cell engulf nutrients from the media as can be seen in the confocal image. Images were acquired with 2x2 binning with 0.5 sec camera exposure time. The confocal pattern used was a 3x3 pinhole size and 3x5 inter pinhole distance multifocal modulation pattern.

The cell is visualised in widefield with low power until the beginning of a phagocytotic process. Imaging was switched from widefield to confocal at the onset of phagocytosis. This rapid switching reduces the overall photobleaching in the sample. The illumination intensity of the laser is increased when switching from widefield to confocal. Confocal imaging requires higher illumination intensity compared to widefield to render high signal-to-noise ratio images. The requirement of higher intensity for confocal imaging is to compensate for the reduction in sample projection intensity due to patterned illumination. **Figure 6.6(c)** shows the deconvoluted images of **figure 6.6(b)**. Deconvolution is performed with Huygens software using classical maximum likelihood estimation with 10 iterations. **Figure 6.6(c)** shows high resolution dynamics of phagocytosis in the amoeba cell.

6.3.5. Reconfigurable confocal modality for deep imaging

Chloroplasts in Spinacia Oleracea leaf disks are visualised in situ in rapid confocal modality for investigating deep imaging. Leaf tissue was prepared from market-bought Spinacia Oleracea leaves. A small leaf disk was placed on a microscope slide and mounted in vectashield (Vectalabs) under a 0.15 mm thick coverslip. The ability to rapidly switch between confocal patterns was used to improve imaging quality in deep samples. Here a reconfigurable confocal imaging technique is presented in which the inter pinhole distances are changed during acquisition to aid deep imaging of a sample. This achieves a high level of control over image resolution and optical sectioning within the specimen. This is demonstrated by imaging grana in chloroplasts of plant tissue to reveal the location of stromal lamella, the links between the grana, obtaining high resolution and contrast, deep into the sample.

The adaptive patterning optics implemented with the DMD allows the distance between the pinholes to be changed which enhances the out-of-focus rejection capabilities compared to a spinning disk confocal microscope, or other diffraction limited point illumination based microscopes. This technique allows changes between different confocal patterns defined by different inter pinhole distances at sub millisecond transitions, during data acquisition.

In a conventional system with a constant inter pinhole distance, the intensity of out-of-focus light collected in the detector is high at large sample depth. This is because the emission light from deep planes undergo scattering when travelling through the sample, to be collected at the objective lens. This increases the cross talk between the nearest pinholes and the image loses resolution [Pawley, book, 2006]. One unique advantage of the system presented in this work is being able to switch to a larger inter pinhole distance at higher depths of the sample during acquisition. The adaptive patterning optics implemented with the DMD allows changes in the distance between the pinholes as a function of imaging depth which in turn enhances the out-of-focus rejection capabilities compared to a spinning disk confocal microscope or other diffraction limited point illumination-based microscopes.

A leaf disk is imaged in rapid confocal mode with a 100x oil 1.49 objective, 488 nm laser illumination and emission light collected using a 488/562 nm dichroic with a dual band FITC/Cy3 collection filter. To demonstrate the improvement that can be achieved by altering the inter pinhole distances, two image sequences were collected deep into the sample using confocal patterns of different inter pinhole distances; 2,040 nm and 4,080 nm (distance in the image plane). These are shown as green and yellow respectively from now on. **Figure 6.7(a)** is a projection view through the 60 µm Z-stack data. Image is a 3D Z-projection in 30° perspective of the data in **figure 6.7(b)** which is the 180th frame of the 200-slice Z-stack with a step size of 300 nm. **Figure 6.7(b)** shows several isolated chloroplasts. Rapid confocal raw data are deconvoluted using AutoQuant software with ten iterations and minimum noise setting in adaptive Point Spread Function (PSF) (blind) deconvolution. Brightness and contrast of both images for different inter pinhole sizes have been adjusted to be on the same scale.

Figures 6.7(c) and **(d)** show zoomed-in areas indicated by the red boxes in **figure 6.7(b).** It can be seen from these images that there is an improved resolution obtained with the wider confocal pattern. **Figure 6.7(e)** shows the normalized intensity profile through the chloroplasts shown in **figures 6.7(c)** and **(d)** as blue and red lines respectively. When using a confocal pattern which has larger inter pinhole distance, images show a higher differentiation of chloroplast structure at a deep plane of the sample.

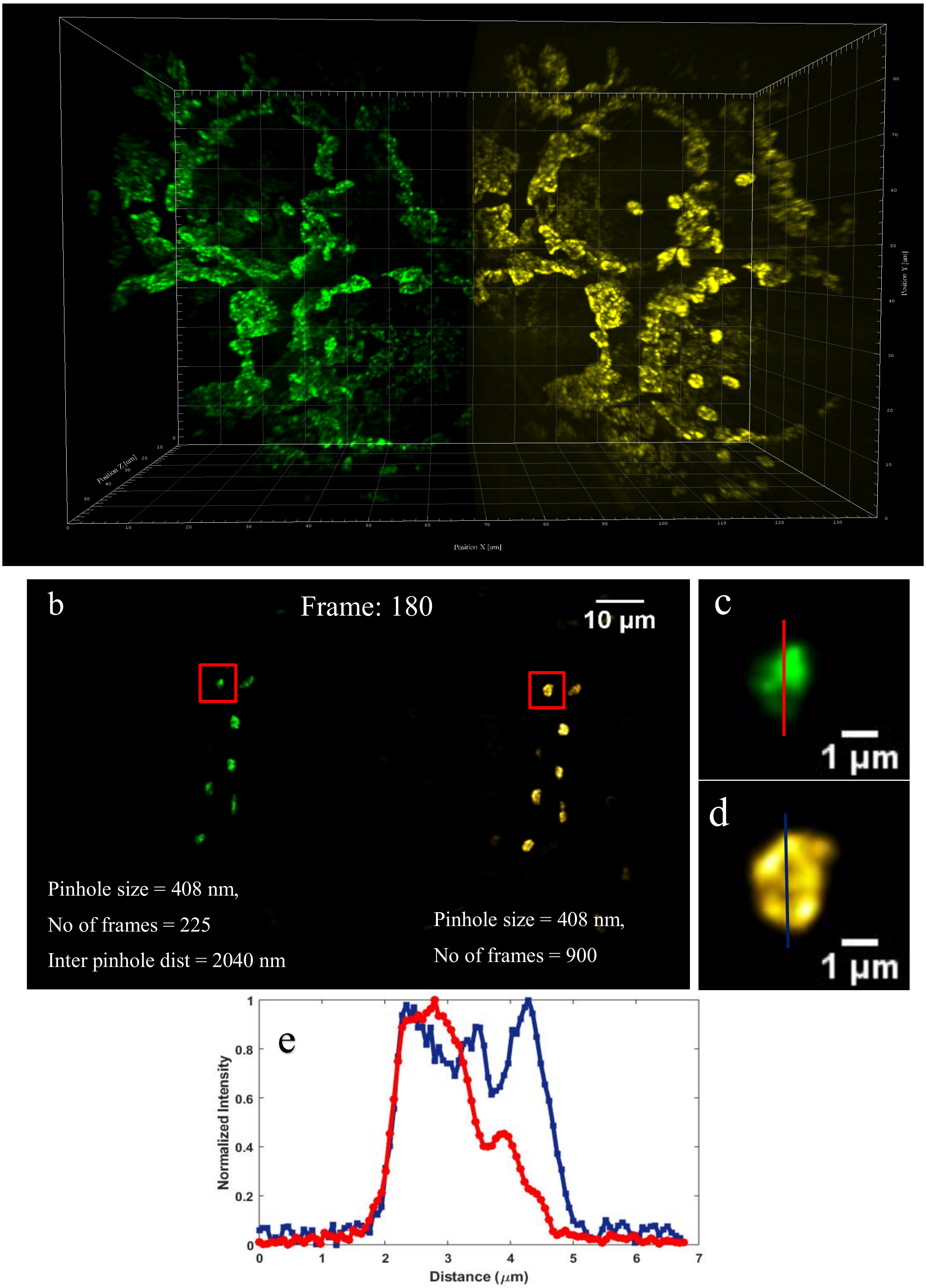

Fig. 6. 7. Reconfigurable confocal with different inter pinhole distances on plant tissue. (**a**) 30° perspective view of 3D Z-projection of rapid confocal for 200 slices with 60 µm depth. Green LUT is given for inter pinhole distance 2,040 nm and yellow LUT is given for inter pinhole distance 4,080 nm. (**b**) Frame 180 of figure (**a**). **(c)**,**(d)** Selected areas of **(b)** zoomed-in. (**e**) Plot of normalized intensity of line profile for lines shown as red and blue in (**c**) and (**d**) respectively.

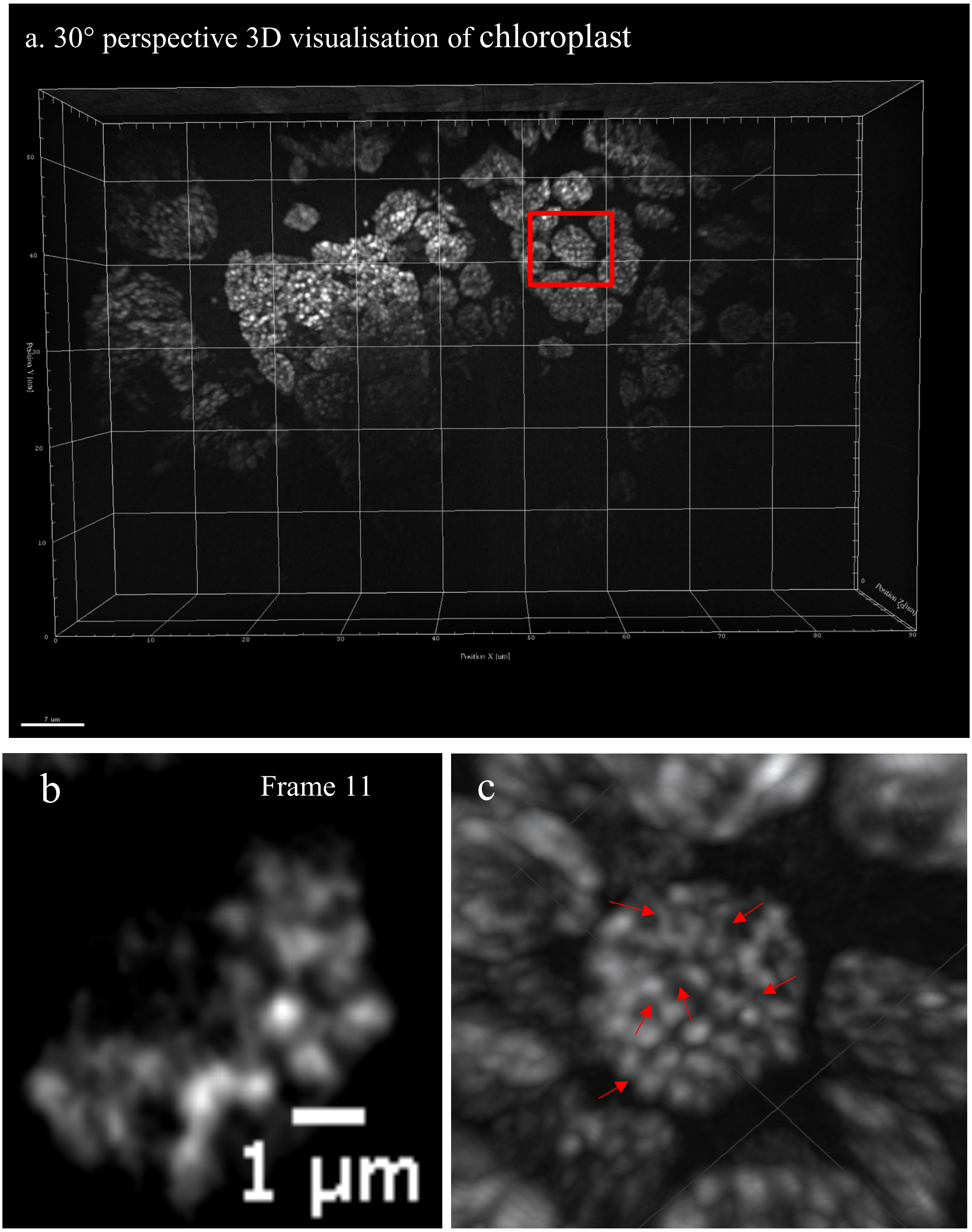

Fig. 6. 8. Reconfigurable confocal modality for deep imaging and revealing the grana and stroma lamellae of chloroplasts in situ in a leaf disk. (a) 30° perspective view 3D Z-projection of rapid confocal for 50 slices with 15 µm depth. (b) Frame 11 of the selected chloroplast of figure (a). (c) Red square of (a) zoomed-in. Red arrows indicate the stroma lamellae of the chloroplast.

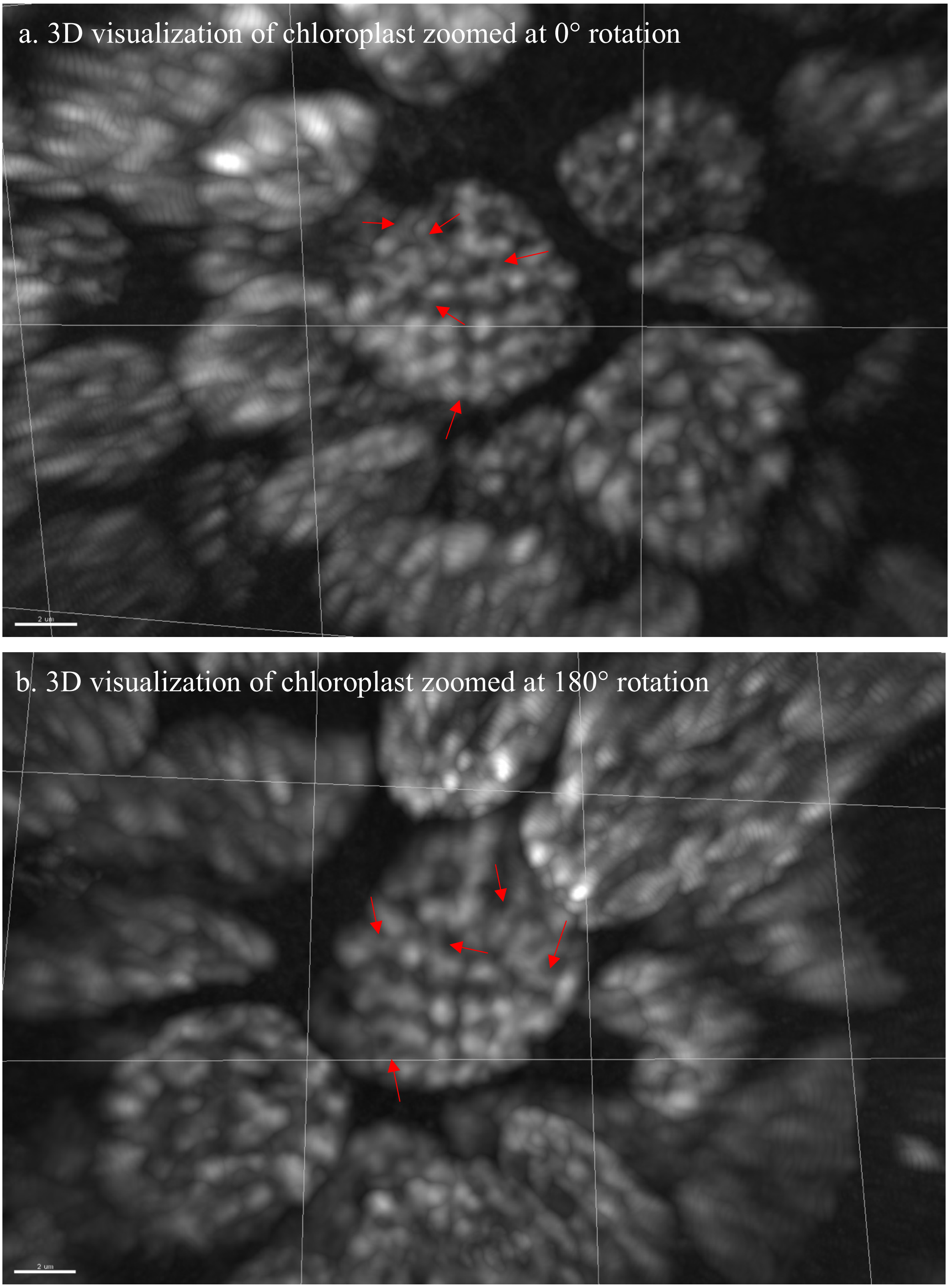

Fig. 6. 9. 3D view of chloroplasts at 0° and 180° perspective. (**a**) 0° perspective view of the chloroplast selected in red circle in **figure 6.7(a).** (**b**) 180° perspective view of the chloroplast selected in red circle in **figure 6.7(a).**

Figure 6.8(a) is a 30° perspective of 3D visualisation of chloroplasts in a deep Spinacia Oleracea leaf tissue. The image is 15 µm deep and was formed using 50 slices taking by rapid confocal at higher laser intensities. **Figure 6.8 (b)** is a single Z-slice (frame 11) of one chloroplast which reveals the locations of the grana. The 3D Z-projection allows us to locate the stroma lamellae which are the links between grana. These are marked by red arrows in **figure 6.8 (c)** which is a zoomed-in section of **figure 6.8(a)** (red box). With a single slice of the chloroplast, location of grana can be visualized (**figure 6.8 (b)**) and 3D projection with 23 slices through one chloroplast (**figure 6.8 (c)**) shows the precise localisation of stromal lamella which are links between the grana in the chloroplast.

Figure 6.9(a) and **(b)** are snapshots at 0° and 180° rotation respectively. The red arrows indicate the location of stroma lamella. Scale bar is 2 µm. Stromal lamellae are diffraction limited structures, which are only few nanometres thick as visualized in electron microscopes previously [Staehelin *et al.*, 2011]. Due to their size and location it has been extremely difficult to visualize these with SIM which has limited axial depth [Gustofsson *et al.*, 2000, Yokono *et al.*, 2016], [Johnson *et al.*, 2015], and conventional confocal microscopy which is limited by deep imaging and resolution. Although the structure has been imaged with an electron microscopes previously, this work reports the precise localization of these structures achieved with optical microscopy.

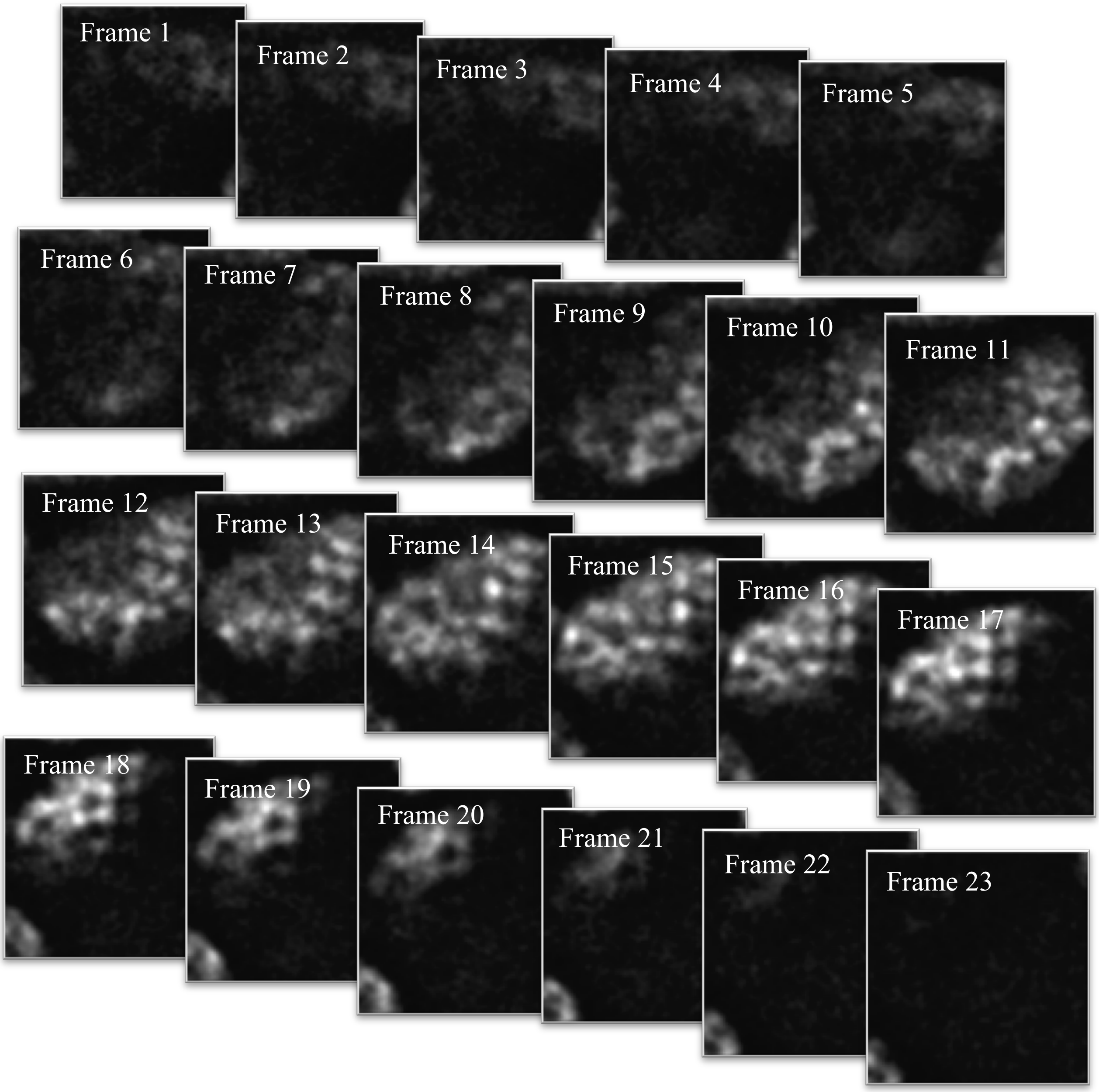

Fig. 6. 10. Z-axis slice of a single chloroplast. These are 23 slices of the selected chloroplast shown in this **figure 6.7(a)**. Step size between two slices is 300 nm. This is the image of the chloroplast selected in figure 6.7 (a) in red square.

Figure 6.10 is the z-axis slices of the chloroplasts indicated by red square in **figure 6.8(a)**. 23 frames of Z-stack through the chloroplast is shown in this figure. Z-stack is moved 300 nm between each slice. The adaptive deep imaging modality presented in this work demonstrated the imaging of chloroplasts and stroma lamellae at 60 µm depth. Localization of stromal lamellae in chloroplast, to the best of our knowledge, is not visualised previously at this clarity with an optical microscope.

6.4. Discussion

The system presented here combines the advantages of single molecule localization with low power fast imaging. This will open many possibilities for biological imaging experiments. Imaging modalities are switched by preloading sequences to the on-board memory of the DMD, prior to starting the image acquisition, this is demonstrated by changing between widefield and confocal with the developed custom GUI. The system can be further developed by real time image analysis and feedback to automated pattern generation. The software development for confocal in general (also for reconfigurable confocal) discussed in Chapter 2 can be extended to perform automate feedback control, depending on the biological investigation needs. Widefield, confocal and STORM images were acquired sequentially for NIH 3T3 cells to image the known actin structure in one field of view establishing versatile imaging.

Drosophila embryo are sensitive to light exposure and photodamage can increase the time for mitotic division in these embryos. Early mitosis in embryogenesis was visualized in higher resolution by combining low power widefield with rapid confocal to reduce photodamage and to image the dynamics of nuclear divisions at higher resolutions. This is an example of how versatile imaging developed here is adaptable to various imaging requirements and sample characteristics. Light sensitive organism, amoeba, was imaged by switching between low power widefield to follow the cells movements and imaging was switched to confocal at the beginning of a phagocytic process.

One of the major disadvantages of a spinning disk system is the fixed pinhole size and inter pinhole distances restricting its ability to perform deep imaging. The versatile imaging system presented here with reconfigurable confocal imaging has the ability to change the pinhole size and inter pinhole distance using the software during image acquisition. This reduces cross-talk at larger sample depths. The technique is software based, which is provided with this work. Deep imaging allows 3-D visualization of chloroplasts in plant tissue. The links between grana, which are termed as stroma lamellae, are only few layers thick. It has been proved to be extremely difficult to image these using conventional confocal microscopes or even a conventional grid based SIM system, due to the imaging techniques' restrictions on deep imaging capabilities and high degree of light scattering in plant tissues. Reconfigurable confocal imaging presented here can visualise chloroplasts in a 3-D perspective, localising the position of these structures.

Application in of the system to transform and adapt to the imaging requirements of different biological systems are presented in this chapter. This is demonstrated by investigating a variety of different types of biological systems such as, NIH 3T3 cells, Drosophila, Ameoba and Spinacia Oleracea samples.

Chapter 7

Conclusion

The complexity and fragility of biological systems in nature hinders the ability of the current state of the art imaging techniques to follow a live cellular process and adapt or transform to meet imaging requirements of specific time points of a subcellular phenomenon. The optical system presented here can adapt to meet the imaging requirements of specific time points within a sub-cellular phenomenon.

In modern microscopy, the mode of illumination and the mechanism by which the emitted light is detected play a crucial role in image resolution and photodamage to the sample. In this work, a Digital Micro-mirror Device (DMD) based illumination and detection system is utilized to deliver a versatile-imaging system which can switch between imaging modalities at sub-millisecond timescales allowing multimodal imaging to combine low power widefield, structured illumination based imaging and high power single molecule localization microscopy into a single microscope. The pathway to a multimodal imaging platform presented here allows biological processes to be followed through time using a range of imaging techniques.

There are six stages for confocal development presented in this work: digital pinholing confocal microscope, Background Corrected Confocal Microscope (BCCM), rapid confocal microscope, Super Resolution-Background Corrected Microscope (SR-BCM), AiryImaging and reconfigurable confocal for deep imaging. This work also provides ready-to-implement illumination patterns and power control software for sample illumination and reconstruction algorithms for all the confocal developments. Digital pinholing confocal microscope rejects the out-of-focus light digitally during post processing. BCCM collects the in-focus and out-of-focus data in two separate cameras. The post processing algorithm for BCCM subtracts the blead through of intensity from in-focus planes by utilising the light collected from out-of-focus planes of the sample.

SR-BCM (confocal based structured illumination) modality outlined here achieves the resolution improvement in a manner similar to previous elegant implementations such as SIM, MSIM, instant SIM, and CSD-ISM, while SR-BCM utilises the emission intensity effectively to improve the resolution and signal-to-noise ratio by employing out-of-focus light efficiently. SR-BCM presented shows superior background correction. Point based patterned illumination was chosen in this implementation to increase the spatial frequencies passing through the objective and to combine it with the implementation of digital light processing by utilizing the out-of-focus emission information. Enhanced background rejection of this system, to achieve higher signal-to-noise ratio and resolution, is compared with several other recently developed confocal based super resolution techniques. It was been shown that the efficient capture and control of light on the emission pathway allows the application of a number of enhanced resolutions techniques based on confocal microscopy, such as AiryImaging.

The adaptive nature of the system allows us not only to change the imaging modality but also to adapt a modality in real time to suit the sample. For example, one of the major disadvantages of a spinning disk system is the fixed pinhole restricting its ability to perform deep imaging. The reconfigurable confocal microscopy development allows us to solve the fixed pinhole limitation of a conventional spinning disk microscope. The versatile imaging platform presented here with reconfigurable confocal has the ability to change the pinhole size and the inter pinhole distance in real time during image acquisition implementing reconfigurable confocal for deep imaging reducing cross-talk at larger sample depths. The ability to choose various confocal imaging parameters such as the pinhole size and the inter pinhole distance to suit a sample's brightness and thickness, followed by the ability to change these confocal imaging parameters during an image acquisition through the sample as a function of depth without substantial loss of resolution is a unique advantage of this adaptive system.

Switching between modalities to either optimise for reduced photo-toxicity or resolution is also applied to super-resolution using localisation microscopy (LM). For the highest resolution achievable, localisation microscopy in the form of STORM was implemented in the system. This effectively allows system to tune resolution as a function of photo-toxicity. In chapter 4 and 5, the application of epi-fluorescence to locate areas of interest for imaging followed by LM is demonstrated to image those areas in the highest resolution possible. The software for targeted illumination development can be easily modified to any selective illumination experiments. Targeted localisation microscopy has been implemented to targeted specific regions for super resolution imaging and to reduce the overall photobleaching in the sample. The system can also target specific sections of the sample to image them with different imaging modalities.

To demonstrate the ability to switch between a low invasive/resolution and a higher invasive/resolution modality, embryogenesis in Drosophila was followed through their initial nuclear divisions in the syncytial blastoderm stage of their development using low power widefield imaging. The imaging modality is switched to visualize higher resolution dynamics of the splitting of centrosomes at a specific time point. The adaptive imaging modality was used to reduce the overall photobleaching of light sensitive biological systems such as Drosophila and Amoeba. Amoeba tend to move away from bright light source. This versatile multimodal imaging system can wait until the start of an event of interest using low illumination intensity imaging and switch to higher power imaging as demonstrated by switch to confocal at the onset of phagocytosis in Amoeba.

The systems ability to adapt to a wide range of sample characteristics opens wide possibilities for designing adaptive biological investigations. The flexibility of the system means that in a single field of view, processes occurring on different time scales can be addressed with different techniques, such that one area could be investigated using LM while a second using SR-BCM and a third using widefield microscopy. Biology is moving away from the model of a single imaging modality to multimodal imaging. It has been demonstrated in this work that we can study a specific process and follow those processes using the most suitable method available during the lifetime of the investigation.

References

1. Jaboski, A. Efficiency of Anti- Stokes Fluorescence in Dyes. *Nature* **131**, 839 (1933).
2. Abbe, E. Beiträge zur Theorie des Mikroskops und der mikroskopischen Wahrnehmung. *Archiv für mikroskopische Anatomie* **9**, 456-468 (1873).
3. Airy, G.B., Vol. 5 283–291 (Trans. Cambridge Phil. Soc, 1835).
4. Alberts, B. Molecular biology of the cell, Edn. 4th ed / Bruce Alberts .. [*et al.*]. (New York : Garland Science, 2002, New York; 2002).
5. Axelrod, D. Cell- substrate contacts illuminated by total internal reflection fluorescence. *Journal of Cell Biology* **89**, 141-145 (1981).
6. Axelrod, D., Koppel, D.E., Schlessinger, J., Elson, E. & Webb, W.W. Mobility measurement by analysis of fluorescence photobleaching recovery kinetics. *Biophysical Journal* **16**, 1055-1069 (1976).
7. Bansal, V., Patel, S. & Saggau, P., Vol. spie-5324. (ed. V. Bansal) 47-54 (2004).
8. Bansal, V., Patel, S. & Saggau, P. High- speed addressable confocal microscopy for functional imaging of cellular activity. *Journal of Biomedical Optics* **11**, 034003-034009 (2006).
9. Barbierato, M., Argentini, C. & Skaper, S.D. Indirect immunofluorescence staining of cultured neural cells. *Methods in Molecular Biology* **846**, 235-246 (2012).
10. Basler, K., Restrepo, S. & Basler, K. Drosophila wing imaginal discs respond to mechanical injury via slow InsP3R-mediated intercellular calcium waves. *Nature communications.* **7**, 12450 (2016).
11. Bass, M., Optical Society of, A., Osa, O.S.A & Optical, S. Handbook of optics, Edn. 2nd ed. (New York ; London : McGraw-Hill, 2001, New York ; London; 2001).
12. Bates, M., Zhuang, X., Rust, M.J., Bates, M. & Zhuang, X. Sub-diffraction-limit imaging by stochastic optical reconstruction microscopy (STORM). *Nature methods.* **3**, 793-796 (2006).
13. Bates, M., Huang, B., Dempsey, G.T. & Zhuang, X. Multicolor Super- Resolution Imaging with Photo- Switchable Fluorescent Probes. *Science* **317**, 1749-1753 (2007).
14. Betzig, E. *et al.* Imaging intracellular fluorescent proteins at nanometer resolution. *Science* **313**, 1642-1645 (2006).
15. Borden, W., Hoffmann, R., Stuyver, T. & Chen, B. Dioxygen: What Makes This Triplet Diradical Kinetically Persistent? *J. Am. Chem. Soc.* **139**, 9010-9018 (2017).
16. Buckley, C. *et al.* WASH drives early recycling from macropinosomes and phagosomes to maintain surface phagocytic receptors. *Proceedings of the National Academy of Sciences of the United States of America* **113**, E5906 (2016).
17. C.J.R, Shepphard. Super Resolution Confocal Microscope *Optik - International Journal for Light and Electron Optics* 80(2):53 (1988).
18. Caarls, W. *et al.* Minimizing light exposure with the programmable array microscope. *Journal of Microscopy* **241**, 101-110 (2010).
19. Chakrova, N., Heintzmann, R., Rieger, B. & Stallinga, S. Studying different illumination patterns for resolution improvement in fluorescence microscopy. *Opt. Express* **23**, 31367-31383 (2015).
20. Chakrova, N., Rieger, B. & Stallinga, S., Development of a DMD-based fluorescence microscope *Proc. Of SPIE* Vol. 9330 (2015).
21. Chalfie, M., Euskirchen, G., Ward, W.W. & Prasher, D.C. Green fluorescent protein as a marker for gene expression. *Science* **263**, 802 (1994).

22. Chen, X. *et al.* Diffraction of digital micromirror device gratings and its effect on properties of tunable fiber lasers. *Applied Optics* **51**, 7214-7220 (2012).
23. Cheng, L.C. *et al.* Nonlinear structured- illumination enhanced temporal focusing multiphoton excitation microscopy with a digital micromirror device. *Biomedical Optics Express* **5**, 2526-2536 (2014).
24. Conacci-Sorrell, M.E. *et al.* Nr- CAM is a target gene of the beta - catenin/ LEF- 1 pathway in melanoma and colon cancer and its expression enhances motility and confers tumorigenesis. *Genes & Development* **16**, 2058-2072 (2002).
25. Cox, G. Optical imaging techniques in cell biology. (Boca Raton : CRC/Taylor & Francis, 2007, Boca Raton; 2007).
26. Culley, S. *et al.* Quantitative mapping and minimization of super- resolution optical imaging artifacts. *Nat. Methods* **15**, 263-+ (2018).
27. Curd, A. *et al.* Construction of an instant structured illumination microscope. *Methods* **88**, 37-47 (2015).
28. Damisah, E.C. *et al.* Targeted two-photon chemical apoptotic ablation of defined cell types *in vivo*. *Nature communications.* **8**, 15837 (2017).
29. Dan, D. *et al.* DMD-based LED-illumination super-resolution and optical sectioning microscopy. *Sci Rep* **3**, 1116 (2013).
30. Dan, D., Yao, B. & Lei, M. Structured illumination microscopy for super- resolution and optical sectioning. *Chinese Science Bulletin* **59**, 1291-1307 (2014).
31. Dang, P., Smythe, E. & Furley, A.J. TAG1 regulates the endocytic trafficking and signaling of the semaphorin3A receptor complex. *J Neurosci* **32**, 10370-10382 (2012).
32. Davey, F., Hill, M., Falk, J., Sans, N. & Gunn-Moore, F.J. Synapse associated protein 102 is a novel binding partner to the cytoplasmic terminus of neurone- glial related cell adhesion molecule. *Journal of Neurochemistry* **94**, 1243-1253 (2005).
33. David, A.A. & John, W.S. Three- dimensional architecture of a polytene nucleus. *Nature* **302**, 676 (1983).
34. De Beule, P.A.A., de Vries, A.H.B., Arndt-Jovin, D.J. & Jovin, T.M., Vol. 7932 79320G-79320G-79310 (2011).
35. de Vries, A.H.B., Cook, N.P., Kramer, S., Arndt-Jovin, D.J. & Jovin, T.M., Vol. 9376 93760C-93760C-93715 (2015).
36. Dempsey, G., Vaughan, J., Chen, K., Bates, M. & Zhuang, X. Evaluation of fluorophores for optimal performance in localization- based super- resolution imaging. *Nature Methods* **8**, 1027-1036 (2011).
37. Denk, W., Strickler, J. & Webb, W. Two- Photon Laser Scanning Fluorescence Microscopy. *Science* **248**, 73 (1990).
38. Dudley, D., Duncan, W.M. & Slaughter, J., Vol. 4985 14-25 (2003).
39. Egger, M.D. & Petráń, M. New Reflected- Light Microscope for Viewing Unstained Brain and Ganglion Cells. *Science* **157**, 305-307 (1967).
40. Engelbrecht, C.J. & Stelzer, E.H.K. Resolution enhancement in a light- sheet- based microscope (SPIM). *Optics Letters* **31**, 1477-1479 (2006).
41. Fay, F.S., Carrington, W. & Fogarty, K.E. Three- dimensional molecular distribution in single cells analysed using the digital imaging microscope. *Journal of Microscopy* **153**, Pt 2/ (1989).
42. Feng, G. *et al.* Next-Generation Optical Technologies for Illuminating Genetically Targeted Brain Circuits. *The journal of neuroscience : the official journal of the Society for Neuroscience.* **26**, 10380-10386 (2006).
43. Davey, F. (Journal of Neurochemistry, 2005).
44. Fox-Roberts, P. *et al.* Local dimensionality determines imaging speed in localization microscopy. *Nat Commun* **8**, 13558 (2017).

45. Fukano, T. & Miyawaki, A. Whole- field fluorescence microscope with digital micromirror device: Imaging of biological samples. *Applied Optics* **42**, 4119-4124 (2003).
46. Fukano, T., Sawano, A., Ohba, Y., Matsuda, M. & Miyawaki, A. Differential Ras Activation between Caveolae/ Raft and Non- Raft Microdomains. *Cell Structure and Function* **32**, 9 (2007).
47. Fulwyler, M. *et al.* Selective photoreactions in a programmable array microscope (PAM): Photoinitiated polymerization, photodecaging, and photochromic conversion. *Cytometry Part A* **67**, 68-75 (2005).
48. Guemez-Gamboa, A., Coufal, Nicole g. & Gleeson, Joseph g. Primary Cilia in the Developing and Mature Brain. *Neuron* **82**, 511-521 (2014).
49. Guo, M. *et al.* Single-shot super-resolution total internal reflection fluorescence microscopy. *Nat Methods* (2018).
50. Gustafsson, M.G. Nonlinear structured-illumination microscopy: wide-field fluorescence imaging with theoretically unlimited resolution. *Proc Natl Acad Sci U S A* **102**, 13081-13086 (2005).
51. Gustafsson, N. *et al.* Fast live-cell conventional fluorophore nanoscopy with ImageJ through super-resolution radial fluctuations. *Nature communications.* **7**, 12471 (2016).
52. Ha, T. & Tinnefeld, P. Photophysics of Fluorescent Probes for Single- Molecule Biophysics and Super- Resolution Imaging. *Annu. Rev. Phys. Chem.* **63**, 595-617 (2012).
53. Hagen, G. *et al.* Biological applications of an LCoS- Based programmable array microscope (PAM). *Biophys. J.*, 159A-159A (2007).
54. Hanley, Q., Verveer, P., Gemkow, M., Arndt-Jovin, D. & Jovin, T.M. An optical sectioning programmable array microscope implemented with a digital micromirror device. *J. Microsc.-Oxf.* **196**, 317-331 (1999).
55. Hanley, Q.S., Lidke, K.A., Heintzmann, R., Arndt-Jovin, D.J. & Jovin, T.M. Fluorescence lifetime imaging in an optically sectioning programmable array microscope (PAM. *Cytometry Part A* **67**, 112-118 (2005).
56. Hari, S. *et al.* Dual- color superresolution imaging of genetically expressed probes within individual adhesion complexes. *Proceedings of the National Academy of Sciences* **104**, 20308 (2007).
57. Eugene, H., Edn. 5 (Pearson Education, 2016).
58. O, H., Vol. 28 330–337 (Z *Wiss Mikrosk*, 1911).
59. Hein, B., Willig, K.I. & Hell, S.W. Stimulated emission depletion (STED) nanoscopy of a fluorescent protein-labeled organelle inside a living cell. *Proc Natl Acad Sci U S A* **105**, 14271-14276 (2008).
60. Heintzmann, R., Hanley, Q.S., Arndt-Jovin, D. & Jovin, T.M. A dual path programmable array microscope (PAM): simultaneous acquisition of conjugate and non-conjugate images. *J Microsc* **204**, 119-135 (2001).
61. Hell, S.W. Far-Field Optical Nanoscopy. *Science.* **316**, 1153-1158 (2007).
62. Hell, S. *et al.* in J. Phys. D-Appl. Phys., Vol. 48 (2015).
63. Henriques, R. *et al.* QuickPALM: 3D real-time photoactivation nanoscopy image processing in ImageJ. *Nat Methods* **7**, 339-340 (2010).
64. Hess, S.T., Girirajan, T.P. & Mason, M.D. Ultra-high resolution imaging by fluorescence photoactivation localization microscopy. *Biophys J* **91**, 4258-4272 (2006).
65. Hill, M. *et al.* Synapse associated protein 102 is a novel binding partner to the cytoplasmic terminus of neurone-glial related cell adhesion molecule. *Journal of neurochemistry.* **94**, 1243-1253 (2005).
66. Holden, S.J. *et al.* High throughput 3D super-resolution microscopy reveals Caulobacter crescentus *in vivo* Z-ring organization. *Proc Natl Acad Sci U S A* **111**, 4566-4571 (2014).

67. Hooke, R. Micrographia, or, Some physiological descriptions of minute bodies made by magnifying glasses [electronic resource] : with observations and inquiries thereupon. (London : Printed for James Allestry ... and are to be sold at his shop ..., MDCLXV11 [1667, London; 1667).
68. Huang, B., Babcock, H. & Zhuang, X. Breaking the Diffraction Barrier: Super-Resolution Imaging of Cells. *Cell* **143**, 1047-1058 (2010).
69. Huisken, J., Swoger, J., Del Bene, F. & Wittbrodt, J. Optical Sectioning Deep inside Live Embryos by Selective Plane Illumination Microscopy. *Science* **305**, 1007-1009 (2004).
70. Jan, K. *et al.* Macromolecular- scale resolution in biological fluorescence microscopy. *Proceedings of the National Academy of Sciences* **103**, 11440 (2006).
71. Jia, Q. *et al.* Full- color structured illumination optical sectioning microscopy. *Scientific Reports* **5** (2015).
72. Jiang, S. & Walker, J. Differential high- speed digital micromirror device based fluorescence speckle confocal microscopy. *Applied Optics* **49**, 497-504 (2010).
73. Jiang, S.-H. & Walker, J.G. Speckle- illuminated fluorescence confocal microscopy, using a digital micro- mirror device. *Measurement Science and Technology* **20**, 065501 (2009).
74. John, A. Application of patterned illumination using a DMD for optogenetic control of signaling. *Nature Methods* **14** (2017).
75. Johnson, M.P., Ruban, A.V. & Johnson, M.P. Visualizing the dynamic structure of the plant photosynthetic membrane. *Nature plants.* **1**, 15161 (2015).
76. Jones, S.A., Shim, S.H., He, J. & Zhuang, X. Fast, three-dimensional super-resolution imaging of live cells. *Nat Methods* **8**, 499-508 (2011).
77. José-Angel, C. & Jeff, W.L. Optical sectioning microscopy. *Nature Methods* **2**, 920 (2005).
78. Joseph, H. *et al.* The new 2D Superresolution mode for ZEISS Airyscan. *Nature Methods* **14** (2017).
79. Thomas, J. Patent, Programmable spatially light modulated microscope ND microscopy (2002).
80. Jovin, T. Oligomerization of epidermal growth factor receptors on A431 cells studied by time- resolved fluorescence imaging microscopy. A stereochemical model for tyrosine kinase receptor activation. *The Journal of Cell Biology* **129**, 1543 (1995).
81. Kelkar, A. & Theurkauf, W.E. Drosophila checkpoint kinase 2 couples centrosome function and spindle assembly to genomic integrity. *Cell.* **113**, 87-99 (2003).
82. Kohki, O. *et al.* Intracellular temperature mapping with a fluorescent polymeric thermometer and fluorescence lifetime imaging microscopy. *Nature Communications* **3**, 705 (2012).
83. Křžek, P., Raška, I. & Hagen, G.M. Flexible structured illumination microscope with a programmable illumination array. *Optics Express* **20**, 24585-24599 (2012).
84. Leeuwenhoek, A.v. The select works of Antony van Leeuwenhoek: containing his microscopical discoveries in many of the works of nature. (London: Whittingham and Arliss, 1816).
85. Lewis, G.N. & Kasha, M. Phosphorescence and the Triplet State. *Journal of the American Chemical Society* **66**, 2100-2116 (1944).
86. Liang, J. *et al.* Random- access optical- resolution photoacoustic microscopy using a digital micromirror device. *Optics Letters* **38**, 2683-2686 (2013).
87. Liang, M., Stehr, R.L. & Krause, A.W. Confocal pattern period in multiple- aperture confocal imaging systems with coherent illumination. *Optics Letters* **22**, 751-753 (1997).
88. Lilli, G. *et al.* The autophagic machinery ensures nonlytic transmission of mycobacteria. *Proceedings of the National Academy of Sciences* **112**, E687 (2015).

89. Gustafsson, M.G. Surpassing the lateral resolution limit by a factor of two using structured illumination microscopy. *Journal of microscopy.* **198**, 82-87 (2000).
90. Magde, D., Elson, E. & Webb, W.W. Thermodynamic fluctuations in a reacting system measurement by fluorescence correlation spectroscopy. *Physical Review Letters* **29**, 705-708 (1972).
91. Mahowald, A.P. Scanning electron microscopy of Drosophila melanogaster embryogenesis. III. Formation of the head and caudal segments. *Developmental biology.* **68**, 96-109 (1979).
92. Marco Castello, G.T., Mauro Buttafava, Takahiro Deguchi, Federica Villa, Sami Koho, Paolo Bianchini, & Colin J. R. Sheppard, A.D., Alberto Tosi , and Giuseppe Vicidomini. Image Scanning Microscopy with Single Photon Detection Array. bioRxiv (2018).
93. Martial, F. & Hartell, N. Programmable Illumination and High- Speed, Multi-Wavelength, Confocal Microscopy Using a Digital Micromirror. *PLoS One* **7**, e43942 (2012).
94. Masters, B.R. Confocal microscopy and multiphoton excitation microscopy [electronic resource] : the genesis of live cell imaging. (Bellingham, Wash. 1000 20th St. Bellingham WA 98225-6705 USA : SPIE, 2006, Bellingham, Wash. (1000 20th St. Bellingham WA 98225-6705 USA); 2006).
95. Michael, J.R., Mark, B. & Xiaowei, Z. Sub- diffraction- limit imaging by stochastic optical reconstruction microscopy (STORM). *Nature Methods* **3**, 793 (2006).
96. Müller, C.B. & Enderlein, J. Image Scanning Microscopy. *Physical review letters.* **104**, 198101 (2010).
97. Neil, M.A.A., Juškaitis, R. & Wilson, T. Method of obtaining optical sectioning by using structured light in a conventional microscope. *Optics Letters* **22**, 1905-1907 (1997).
98. Niederman, R., Amrein, P.C. & Hartwig, J. Three-dimensional structure of actin filaments and of an actin gel made with actin-binding protein. *J Cell Biol* **96**, 1400-1413 (1983).
99. Nieuwenhuizen, R.P. *et al.* Measuring image resolution in optical nanoscopy. *Nat Methods* **10**, 557-562 (2013).
100. Ovesný, M., Křížek, P., Borkovec, J., Švindrych, Z. & Hagen, G.M. ThunderSTORM: a comprehensive ImageJ plug-in for PALM and STORM data analysis and super-resolution imaging. *Bioinformatics* **30**, 2389-2390 (2014).
101. Patterson, G.H. *et al.* Imaging Intracellular Fluorescent Proteins at Nanometer Resolution. *Science.* **313**, 1642-1645 (2006).
102. Pawley, J.B. Handbook of biological confocal microscopy, Edn. 3rd ed. (New York, NY : Springer-Verlag, 2006, New York, NY; 2006).
103. Peixin, Z., Otto, F., Jennifer, S., Yan-Ping Zhang, S. & Rainer, W.F. High- resolution optical control of spatiotemporal neuronal activity patterns in zebrafish using a digital micromirror device. *Nature Protocols* **7**, 1410 (2012).
104. Peter, M. & Ameer-Beg, S.M. Imaging molecular interactions by multiphoton FLIM. *Biology of the Cell* **96**, 231-236 (2004).
105. Rayleigh, L. On the Theory of Optical Images, with special reference to the Microscope. *Journal of the Royal Microscopical Society* **23**, 474-482 (1903).
106. Fernandez, S.M. & Berlin, R.D. Cell surface distribution of lectin receptors determined by resonance energy transfer. *Nature* **264**, 411 (1976).
107. Saberianfar, R. *et al.* Green to red photoconversion of GFP for protein tracking *in vivo*. *Scientific reports.* **5**, 11771 (2015).
108. Sakurai, T. The role of NrCAM in neural development and disorders—Beyond a simple glue in the brain. *Molecular and Cellular Neuroscience* **49**, 351-363 (2012).

109. SCHERER, W.F., SYVERTON, J.T. & GEY, G.O. Studies on the propagation in vitro of poliomyelitis viruses. IV. Viral multiplication in a stable strain of human malignant epithelial cells (strain HeLa) derived from an epidermoid carcinoma of the cervix. *J Exp Med* **97**, 695-710 (1953).
110. Schulz, O. *et al.* Resolution doubling in fluorescence microscopy with confocal spinning-disk image scanning microscopy. *Proceedings of the National Academy of Sciences of the United States of America.* **110**, 21000-21005 (2013).
111. Seamus, J.H., Stephan, U. & Achillefs, N.K. DAOSTORM: an algorithm for high-density super-resolution microscopy. *Nature Methods* **8**, 279 (2011).
112. Shao, L. *et al.* Super-resolution 3D microscopy of live whole cells using structured illumination. *Nature methods.* **8**, 1044-1046 (2011).
113. Sheppard, C.J.R. & Wilson, T. The theory of the direct- view confocal microscope. *Journal of Microscopy* **124**, 107-117 (1981).
114. Shi, X., Lim, J. & Ha, T. Acidification of the oxygen scavenging system in single-molecule fluorescence studies: In situ sensing with a ratiometric dual- emission probe. *Analytical Chemistry* **82**, 6132-6138 (2010).
115. Smythe, E., Furley, A.J., Dang, P. & Furley, A.J.W. TAG1 Regulates the Endocytic Trafficking and Signaling of the Semaphorin3A Receptor Complex. *The journal of neuroscience : the official journal of the Society for Neuroscience.* **32**, 10370-10382 (2012).
116. Snapp, E., Kenworthy, A., Lippincott-Schwartz, J., Snapp, E. & Kenworthy, A. Studying protein dynamics in living cells. *Nature reviews.* **2**, 444-456 (2001).
117. Staehelin, L.A. & Austin, J.R. Three-Dimensional Architecture of Grana and Stroma Thylakoids of Higher Plants as Determined by Electron Tomography. *Plant physiology.* **155**, 1601-1611 (2011).
118. Steve, W. *et al.* rapidSTORM: accurate, fast open- source software for localization microscopy. *Nature Methods* **9**, 1040 (2012).
119. Strickler, J.H. & Webb, W.W. Two-photon laser scanning fluorescence microscopy. *Science.* **248**, 73-76 (1990).
120. Susan, C. *et al.* Bayesian localization microscopy reveals nanoscale podosome dynamics. *Nature Methods* **9**, 195 (2011).
121. Instrument, T., Using Lasers with DLP DMD Technology (2008).
122. Martin, T., Patent, Optical arrangement for digital micromirror device. US9625690B2 (2017)
123. Thomas, A.K., Stefan, J., Marcus, D., Alexander, E. & Stefan, W.H. Fluorescence microscopy with diffraction resolution barrier broken by stimulated emission. *Proceedings of the National Academy of Sciences of the United States of America* **97**, 8206 (2000).
124. Tkaczyk, T.S. Field guide to microscopy [electronic resource]. (Bellingham, Wash. 1000 20th St. Bellingham WA 98225-6705 USA : SPIE, c2010, Bellingham, Wash. (1000 20th St. Bellingham WA 98225-6705 USA); 2010).
125. Todaro, G.J. & Green, H. Quantitative studies of the growth of mouse embryo cells in culture and their development into established lines. *The Journal of cell biology* **17**, 299-313 (1963).
126. Tomer, R., Khairy, K., Amat, F. & Keller, P.J. Quantitative high-speed imaging of entire developing embryos with simultaneous multiview light-sheet microscopy. *Nat Methods* **9**, 755-763 (2012).
127. Tucker, R.W., Pardee, A.B. & Fujiwara, K. Centriole ciliation is related to quiescence and DNA synthesis in 3T3 cells. *Cell* **17**, 527-535 (1979).

128. Valeur, B. Molecular fluorescence : principles and applications. (Weinheim : Wiley-VCH, 2002, Weinheim; 2002).
129. Vaughan, J.C. *et al.* Evaluation of fluorophores for optimal performance in localization-based super-resolution imaging. *Nature methods.* **8**, 1027-1036 (2011).
130. Verveer, P.J., Gemkow, M.J. & Jovin, T.M. A comparison of image restoration approaches applied to three-dimensional confocal and wide- field fluorescence microscopy. *Journal of Microscopy* **193**, 50-61 (1999).
131. Verveer, P.J. & Jovin, T.M. Image restoration based on Good's roughness penalty with application to fluorescence microscopy. *Journal of the Optical Society of America A: Optics and Image Science, and Vision* **15**, 1077-1083 (1998).
132. Verveer, P.J. & Jovin, T.M. Improved restoration from multiple images of a single object: Application to fluorescence microscopy. *Applied Optics* **37**, 6240-6246 (1998).
133. Verveer, P., Hanley, Q., Verbeek, P., Van Vliet, L. & Jovin, T.M. Theory of confocal fluorescence imaging in the programmable array microscope (PAM). *J. Microsc.* **189**, 192-198 (1998).
134. Vincent, S. *et al.* Compressive fluorescence microscopy for biological and hyperspectral imaging. *Proceedings of the National Academy of Sciences* **109**, E1679 (2012).
135. Vogelsang, J. *et al.* A Reducing and Oxidizing System Minimizes Photobleaching and Blinking of Fluorescent Dyes. *Angewandte Chemie International Edition* **47**, 5465-5469 (2008).
136. Voie, A.H., Burns, D.H. & Spelman, F.A., Vol. 170 229-236 (Oxford, UK; 1993).
137. Voort, H.T.M. & Brakenhoff, G.J. 3- D image formation in high- aperture fluorescence confocal microscopy: a numerical analysis. *Journal of Microscopy* **158**, 43-54 (1990).
138. Wäldchen, S., Lehmann, J., Klein, T., van de Linde, S. & Sauer, M. Light-induced cell damage in live-cell super-resolution microscopy. *Sci Rep* **5**, 15348 (2015).
139. Wang, P. *et al.* Robust growth of Escherichia coli. *Curr Biol* **20**, 1099-1103 (2010).
140. Ward, E.N. & Pal, R. Image scanning microscopy: an overview. *Journal of Microscopy* **266**, 221-228 (2017).
141. Weiner, O.D. *et al.* Spatiotemporal control of cell signalling using a light-switchable protein interaction. *Nature.* **461**, 997-1001 (2009).
142. Westphal, V. & Hell, S.W. Nanoscale resolution in the focal plane of an optical microscope. *Physical Review Letters* **94**, (2005).
143. Winter, P.W. *et al.* Two-photon instant structured illumination microscopy improves the depth penetration of super-resolution imaging in thick scattering samples. *Optica* **1**, 181-191 (2014).
144. Wong, C.H., Chen, N.G. & Sheppard, C.J.R. 218-221 (2006).
145. Wu, Y., Ye, P., Mirza, I.O., Arce, G.R. & Prather, D.W. Experimental demonstration of an optical- sectioning compressive sensing microscope (CSM). *Optics Express* **18**, 24565-24578 (2010).
146. Yih, J.N. *et al.* Temporal focusing-based multiphoton excitation microscopy via digital micromirror device. *Opt Lett* **39**, 3134-3137 (2014).
147. Yokono, M. *et al.* Live-cell visualization of excitation energy dynamics in chloroplast thylakoid structures. *Scientific reports.* **6**, 29940 (2016).
148. York, A.G. *et al.* Instant super-resolution imaging in live cells and embryos via analog image processing. *Nature methods.* **10**, 1122-1126 (2013).
149. York, A.G. *et al.* Resolution doubling in live, multicellular organisms via multifocal structured illumination microscopy. *Nature methods.* **9**, 749-754 (2012).
150. Zernike, F. Phase contrast, a new method for the microscopic observation of transparent objects. *Physica* **9**, 686-698 (1942).